2020

Effect of multiple recurring weld repairs on the properties of a 690 MPa Quenched and Tempered steel

Suchinthana Pragathi Dissananayaka

UNIVERSITY
OF WOLLONGONG
AUSTRALIA

Effect of multiple recurring weld repairs on the properties of a 690 MPa Quenched and Tempered steel

By

Suchinthana Pragathi Dissananayaka

Supervisors:

Prof. Huijun Li, A/Prof. Stephen van Duin, Dr. Kristin Carpenter

This thesis is presented as part of the requirement for the conferral of the degree of

Doctor of Philosophy

This research has been conducted with the support of the Australian Government Research Training Program Scholarship

University of Wollongong

School of Mechanical, Materials Mechatronics and Biomedical Engineering

December 2020

ABSTRACT

Australia's Collins class submarines are made from a high strength quenched and tempered steel, BIS812 EMA. This steel has a minimum 690 MPa yield strength and it consists of a combination of macro and micro-alloying elements which contribute to both its high strength and high low-temperature toughness.

After long exposure to seawater environments, localised corrosion damage occurs and this can lead to a reduction of steel plate thickness which can adversely affect the structural integrity of the hull. Corrosion damage can be repaired by removing the damaged region and rebuilding the area with weld deposits. Over the life of a vessel, corrosion damage at the same location can occur and recurring repair welding is preferable to plate replacement, as it is a more cost effective and timely procedure. Additionally, recurring butt welds on the hull may be required for the long-term sustainment of the submarines. All these recurring multiple repair welds may have a detrimental effect on the mechanical properties of the base plate, that is, in the heat affected zone (HAZ).

There has been limited research published on the effects of multiple repair welds on the properties of steel. From the limited research that has been conducted, the nature of the weld repair, welding type and steel type having been identified as important factors affecting the mechanical properties of the HAZ. Besides, very few of these studies were specifically conducted on quenched and tempered steels. BIS812 EMA steel is a unique steel type; it is a quenched and tempered steel with macro-alloying elements (Cr, Mo, Ni) and microalloying additions (Nb, Ti, V and B). High strength submarine steels are generally macroalloyed and do not contain microalloying additions. As such, the limited research that has been conducted is not readily transferable to the recurring welding of BIS812 EMA steel. This research is focussed on analysing the effect of multiple repair welds on the steel and understanding the underlying mechanisms for the variation of mechanical properties and microstructure.

Specifically, the influence of the number of weld repairs (i.e. up to four repeated welds) on the microstructure and mechanical properties of a quenched and tempered (Q&T) steel was assessed. This assessment was undertaken through real (or actual) welds and Gleeble thermo-mechanical simulations, all with multiple thermal cycles. Thermal data measured from the real welds were used to ensure that the thermal simulations were representative as possible. Instrumented Charpy impact toughness, dynamic tear test, hardness tests and residual stress measurements were performed, followed by microstructural and fractographic analysis.

Thermal simulations allowed the toughness of specific regions of the HAZ to be evaluated, as the entire cross-section near the notch of Charpy test sample can be produced with specific microstructure related to each specific sub-HAZ. Results from this study found the (coarse-grained HAZ) CG HAZ and only a small region where the intercritical temperature is closer to lower transformation temperature in (intercritically reheated coarse-grained HAZ) ICCG HAZ showed low toughness. Application of a combination of multiple repeated simulated thermal cycles did not degrade the toughness further.

From a combination of studying the microstructure and instrumented Charpy fracture properties of HAZ simulated specimens, it was noted that Martensite-Austenite (MA) constituents formed along the PAG boundaries at lower IC temperatures within the ICCG regions. These were the key features responsible for the low toughness in the ICCG region. MA constituents acted as fracture initiation sites in the ICCG region, thus dramatically lowering the toughness. However, there was no evidence that the MA constituents affected the propagation of fracture. When the IC reheating temperature was just above the A_{c1}, low toughness was observed, even with the prior austenite grain size was small. As the IC temperature increased, the coarsening of MA along the grain boundaries diminished its ability to act as fracture initiation sites. In fact, EBSD characterisation showed that the coarser MA phase consisted of a relatively high fraction of high angle grain boundaries. High angle grain boundaries are known to hinder fracture propagation by deflecting the fracture path. Therefore, ICCG samples with higher IC showed higher toughness.

Real weld tests were conducted as Bead-on-Plate (BoP), pad repair welds and full penetration butt welds with single, double, triple and quadruple repair welds. For the real butt-welds, Charpy test samples were machined where the notch was placed at weld metal (WM), fusion line (FL) and 3 mm away from the fusion line (FL+3). In the above welds, it was found that the microstructure with low toughness (CG and ICGC HAZ) consisted of about 2% of the total HAZ. Therefore, toughness in real welds was considerably higher compared to the lower toughness observed in simulated specimens. Dynamic tear (DT) samples were machined with a notch placed in HAZ. All Charpy and DT tests showed that Charpy toughness and DT energy passed the design requirements for BIS812 EMA and were not adversely affected by the number of repair weld cycles.

In conducting both real weld tests and HAZ simulations, along with mechanical testing and microstructural characterisations, it was discovered that there were no significant changes to the properties or the microstructures during multiple repair welding, compared with single repair welding on BIS812 EMA steel. Ultimately, it can be concluded that in terms of toughness and hardness, multiple repair welding, of up to four cycles, may be conducted without affecting the structural integrity of BIS812 EMA steel.

ACKNOWLEDGEMENTS

I would like to express my sincere gratitude to my supervisors, Prof. Huijun Li, A/Prof. Stephen van Duin and Dr. Kristin Carpenter for all their support and guidance during the time of this research. Also, I am particularly thankful to project advisors Dr. Zoran Sterjovski and Mr. Joe Donato from the Defence Science and Technology Group (DST Group), and Mr. Daniel Miller and Mr. Mikael Johansson from ASC Pty Ltd for providing numerous supports for the project.

I would like to acknowledge the support given by DST Group and ASC Pty Ltd for their collaboration, expertise and access to their facilities for my experiments.

I am extremely thankful to have been provided a scholarship to support this project from the research training centre for naval design and manufacturing (RTCNDM). The RTCNDM is a University-Industry partnership established under the Australian Research Council Industry Transformation grant scheme (ARC IC140100003). This project would not be possible without this funding support.

I should mention about the support given by the staff of electron microscopy centre at the University of Wollongong for the success of this study. Special thanks should go to Dr. Mitchell Nancarrow and Dr. Azdiar Gazder for their support of and training for electron microscopes. I am thankful to Dr. Monika Wyszomirska for her support of preparation of FIB samples and Dr. Andrew Kostryzhev and Dr. Kristin Carpenter for their support of carrying out TEM studies. I would also like to express my thankfulness to Dr. Mark Reid for his support for the residual stress measurements at ANSTO.

All the technical staff at the University of Wollongong, including Mr. Matthew Franklin and Mr. Stuart Rodd, helped me, from equipment induction to sample preparation, which contributed to successfully completing the project.

This journey would not be enjoyable without my friends and colleagues at the University of Wollongong and my officemates, and especially those enjoyable conversations over morning coffee with Monika and Apsara.

This journey could not be possible without the wonderful support of my loving wife, Kaushi. I am so grateful to have all the support from you on this journey with all ups and downs. Also, I cannot thank enough for all the support from my loving family; mum, dad, brother and sister.

Finally, I would like to thank everyone which I could not mention above but supported me in this journey.

CERTIFICATION

I, Suchinthana Pragathi Dissanayaka, declare that this thesis submitted in fulfilment of the requirements for the conferral of the degree Doctor of Philosophy, from the University of Wollongong, is wholly my own work unless otherwise referenced or acknowledged. This document has not been submitted for qualifications at any other academic institution.

_____

Suchinthana Pragathi Dissanayaka

December 14, 2020

ABBREVIATIONS

BCC	Body Centred Cubic
BoP	Bead on Plate
CG HAZ	Coarse Grain Heat Affected Zone
DBTT	Ductile to Brittle Transformation Temperature
DT	Dynamic Tear
EDS	Energy Dispersive Spectroscopy
E_i	Fracture Initiation Energy
E_p	Fracture Propagation Energy
E_t	Total Energy
FCC	Face Centred Cubic
FG HAZ	Fine Grained Heat Affected Zone
FIB	Focussed Ion Beam
FL	Fusion Line
FL+3	3 mm away from the Fusion Line
HACC	Hydrogen Assisted Cold Cracking
HAGB	High Angle Grain Boundary
HAZ	Heat Affected Zone
HSLA	High Strength Low Alloy
IC HAZ	Intercritical Heat Affected Zone
ICCG	Intercritically Reheated Coarse Grain
ICFG	Intercritically Reheated Fine Grain
IPF	Inverse Pole Figure
LBZ	Local Brittle Zone
LW	Longitudinal to the Weld
MA	Martensite-Austenite
MMAW	Manual Metal Arc Welding
OM	Optical Microscopy
OR	Orientation Relationship
PAG	Prior Austenite Grain
PAGB	Prior Austenite Grain Boundary
PAGS	Prior Austenite Grain Size

PWHT	Post Weld Heat Treatment
Q&T	Quenched and Tempered
RA	Retained Austenite
SC	Sub Critical
SEM	Scanning Electron Microscopy
$t_{8/5}$	Cooling Time From 800°C to 500°C
TEM	Transmission Electron Microscopy
TIG	Tungsten Inert Gas
TW	Transverse to the Weld
UTS	Ultimate Tensile Strength
WM	Weld Metal
YS	Yield Strength

TABLE OF CONTENTS

ABSTRACT ..... **I**
ACKNOWLEDGEMENTS ..... **IV**
CERTIFICATION ..... **VI**
ABBREVIATIONS ..... **VII**
TABLE OF CONTENTS ..... **IX**
LIST OF FIGURES ..... **XIII**
LIST OF TABLES ..... **XXV**
1 INTRODUCTION **1**
1.1 Background 1
1.2 Objectives 3
1.3 Research methodology 4
1.4 Thesis outline 5
2 LITERATURE REVIEW **6**
2.1 Weldability of high strength Q & T steels 7
2.1.1 Hardenability and carbon equivalent effect on weld HAZ 8
2.2 Effects of welding thermal cycles on the base steel 9
2.2.1 Weld heat affected zone (HAZ) 9
2.2.2 Weld microstructures 13
2.2.3 HAZ hardenability 15
2.2.4 HAZ hardness 17
2.2.5 Hydrogen Assisted cold cracking 20
2.2.6 Elemental segregation affected by thermal cycles 21
2.2.7 Simulated HAZ vs real weld HAZ 22
2.2.8 Effects of multiple thermal cycles on microstructure 24
2.3 Repair welding 25
2.3.1 Repairing of corrosion damage 27
2.3.2 Repairing of butt weld joints 28
2.3.3 Effects of repair welds on residual stress 28
2.4.3 Improvement of HAZ toughness 49
2.5 Residual stresses in welds 52
2.6 Summary of the chapter 56
3 MATERIALS AND METHODS **59**

3.1 Material 59
3.2 Dilatometer studies 60
3.3 Welding trials and simulated HAZ 60
3.3.1 Real weld experiments 61
3.3.2 Thermal HAZ simulations 68
3.4 Mechanical testing 72
3.4.1 Hardness 72
3.4.2 Charpy impact testing 73
3.4.3 Dynamic tear testing 76
3.4.4 Residual stress analysis 78
3.5 Microstructure characterisation 83
3.5.1 Metallographic sample preparation 83
3.5.2 Optical microscopy 85
3.5.3 Scanning Electron Microscopy (SEM) 85
3.5.4 Electron Back Scattering Diffraction (EBSD) 85
3.5.5 Transmission Electron Microscopy (TEM) 86
3.5.6 TEM sample preparation with FIB 86
4 RESULTS 88
4.1 Transformation temperatures with high heating rates 88
4.2 Prior austenite grain sizes 89
4.3 Instrumented welding 93
4.4 Microstructural characterisation 95
4.4.1 Microstructure with multiple repeated thermal cycles 101
4.5 Real weld microstructures 103
4.5.1 BoP welds 103
4.5.2 Pad welds 107
4.6 Variation of Charpy Impact toughness in simulated HAZ and real welds 111
4.6.1 Variation of Charpy impact toughness of single and double simulated HAZs 112
4.6.2 Variation of Charpy impact toughness of multiple simulated thermal cycles 114

4.6.3 Variation of Charpy impact toughness of multiple repairs of real welds .. 115
4.7 Variation in hardness 117
4.8 Fractography 126
4.9 TEM analysis 133
4.9.1 TEM foils for simulated welds 133
4.9.2 TEM FIB samples for simulated and real welds 135
4.10 Dynamic tear testing 143
4.11 Residual stresses in pad welds 145
4.12 EBSD Analysis 151
4.12.1 EBSD of simulated HAZ specimens. 151
4.13 Summary of Results 157
5 DISCUSSION 158
5.1 Microstructure evolution in multiple repair welds 159
5.1.1 Characterisation of martensite matrix 162
5.1.2 Formation of MA constituents 162
5.2 Effect on PAG size on toughness in single cycle welds 167
5.3 Effects of PAG size on double cycle ICCG HAZ 168
5.4 Effect of IC temperature on toughness 171
5.5 HAZ Toughness with Multiple thermal cycles 175
5.6 Fracture behaviour of ICCG HAZ and CG HAZ 177
5.6.1 Influence by hardness 179
5.6.2 Influence by grain boundaries 180
5.7 Mechanism of fracture propagation in ICCG 181
5.8 Effect of weld repair cycle on residual stresses 183
5.9 Variation of hardness and hardness profile with weld repair cycles 185
6 CONCLUSIONS 188
6.1 Effect of PAG size on toughness in single cycle welds 188
6.2 Effect of PAG size on toughness for double thermal cycles with intercritical reheating 188
6.3 Effect on IC temperature on toughness 189
6.4 Effect of multiple thermal cycles on the toughness of simulated HAZ specimens 189

6.5 Factors affecting the toughness of intercritically reheated specimens..... 190
6.6 Influence of MA constituent on toughness 191
6.7 Difference between the simulated and real weld microstructures 191
6.8 Hardness of multiple repair welds for the real welds..... 191
6.9 The effects of multiple repairs on the mechanical properties of real welds... 191
6.10 Effect of recurring repair welds on residual stresses 192
6.11 Summary of the effects of recurring repair welds on the properties of BIS812EMA steel 192
6.12 Feasibility of multiple recurring weld repairs on BIS812 EMA steel 193
7 RECOMMENDATIONS 194
7.1 Careful control of the weld sequence 194
7.2 The effect of post-weld heat treatment (PWHT) for residual stress 194
7.3 In-situ studies of fracture behaviour of the ICCG region 194
REFERENCES 195
APPENDIX A: DILATOMETER MEASUREMENTS 206
APPENDIX B: REAL WELD THERMAL CYCLES 209
APPENDIX C: SIMULATED THERMAL CYCLES 212
APPENDIX D: FRACTURE SURFACES 223

LIST OF FIGURES

Figure 2-1: Total weld input relationship of Q & T steels [16]. 8
Figure 2-2: HAZ classification in the fusion weld [25]. 10
Figure 2-3: Various HAZ zones in single and two pass weld. Adapted from Kumar, et al. [26]. 11
Figure 2-4: Typical inter-critically reheated GC-HAZ in X70 grade pipeline steel [10]. 12
Figure 2-5: The variation of dislocation densities with prior austenite grain size (PAGS) in as-quenched (AsQ), low temperature tempering (LLT) and high temperature tempering (HTT) [39]. 16
Figure 2-6: The variation of Vickers micro hardness with PAGs in as-quenched (AsQ), low temperature tempering (LLT) and high temperature tempering (HTT) [31]. 16
Figure 2-7: Hardness gradient of 20 mm thick BIS60 plate welded with 5 kJ/mm heat input (SAW process with even-matched filler metal) [47]. 18
Figure 2-8: Variation of HAZ hardness with different peak temperature for two different heat input in HSLA-80 steel [43]. 19
Figure 2-9: The variation of hardness with peak temperature in different HAZ with simulated and real welds [42]. 20
Figure 2-10: Percentages of carbon content of austenite and ferrite measured from different quenching temperature [54]. 22
Figure 2-11: Comparison between simulated microstructure vs real weld microstructure of CG HAZ and SC HAZ of a quenched and tempered high strength armour steel. Microstructures were comparable to each other [42]. 23
Figure 2-12: Variation of grain size in CG HAZ, for real and simulated specimens, as a function of peak temperature in GMAW steel plate of HSLA-100 [48]. 24
Figure 2-13: Microstructure of single cycle CG HAZ and double cycle CG HAZ. Microstructures consisted of lath bainitic ferrite (BF). With 4% nital etch [33]. 25
Figure 2-14: Overlapping HAZ of pad weld repairs. Adopted from Sterjovski [5]. . 27

Figure 2-15: Residual stress distribution of original and repair welds of butt welds. (Org-original weld, SFR-single full repair, DFR-double full repair, SPR-single partial repair, DPR-double partial repair) [68]. 29
Figure 2-16: Changes in toughness with different sub-HAZ for a low carbon, Q & T steel. (HAZ consisted of AF, GB, and GBF) [80]. 30
Figure 2-17: Transition curves TMCP steel with 0.07% C, received, CGHAZ at 1250°C, ICCG at higher IC, CGHAZ at a slower cooling rate, and ICCG at lower IC. Adopted from [81]. 31
Figure 2-18: Variation of impact toughness with peak temperature [26] 33
Figure 2-19: MA islands formed along PAG boundaries in ICCG HAZ with original CG HAZ with bainitic microstructure [81]. 34
Figure 2-20: The effects of the application of a second reheat cycle to the CGHAZ on the MA constituent and hardness [53]. 35
Figure 2-21: Effect of MA with third cycle temperature (1350-750-300°C) [53]. (0.082C, 0.53Mn, 0.31Si, and Nb, Ti, V steel). 35
Figure 2-22: The effect of PAG size and martensite packet size on the impact strength of Hardox 450 steel. (tested at -40°C) [93]. 37
Figure 2-23: The variation of upper shelf Charpy energy and ductile to brittle transition temperature with two different PAG sizes [94]. 37
Figure 2-24: Variation of fracture initiation and propagation energies with temperature for two different PAG sizes. Both samples were tempered at 500°C [94]. 38
Figure 2-25: Evidence of de-cohesion where secondary fracture followed the boundary between MA and bainitic matrix [103]. 39
Figure 2-26: An evidence of MA island originated the cleavage fracture [81] 40
Figure 2-27: Variation of Charpy impact energy with the volume fraction of MA in X70 pipeline steel HAZ. Tested at -20°C [31]..... 42
Figure 2-28: Carbon and Silicon segregation on MA particle (500 MPa structural steel). (a) MA particle in the matrix and (b) Carbon and silicon concentration along the black line in ‘a’ [80]. 45
Figure 2-29: Effect of carbon content on MA constituent (For steels with different carbon content) [53]. 46

Figure 2-30: Grain boundary distribution of ultra-heavy plate of high strength steel [111] 47
Figure 2-31: Microstructural hierarchy of lath martensite [113, 115]. 48
Figure 2-32: Typical distribution of residual stress fields in butt-welded joints [127]. 52
Figure 2-33: Categories of residual stress fields [130] 53
Figure 2-34: Longitudinal residual stress measured for different welding techniques on a 4 mm thick plate. Adapted from Colegrove, et al. [131]. 54
Figure 2-35: Axial residual stress distribution with short girth weld on a pipe (a) with residual stress of original weld and (b) without existing residual stress [136]. . 55
Figure 2-36: Residual stress fields of (a) initial fabrication weld and (b) a short length weld repair with same external loading [64] 55
Figure 3-1: Pictures of dilatometer experiments (a) a thin K-type thermocouple welded to a sample for temperature measurement and control and (b) dilatometer set-up used for the experiment 60
Figure 3-2: Weld experiment data acquisition set-up (a) recording of temperature histories and (b) MMA welder and welding current and voltage measurement set-up 61
Figure 3-3: First two steps of BoP weld trials. (a) first set of 4 overlapping BoP welds (b) last three welds were ground back to the level of the base plate. (c) re-weld on top of ground 3 BoP welds. (d) last two welds were ground back to the level of the base plate. After eight steps of grinding and re-welding, the plate ended up with four BoP welds with four different weld repairs. 63
Figure 3-4: BoP welds (a) welded side with four different repair welds and (b) holes on the opposite side of the plate where thermocouples were imbedded. 63
Figure 3-5: Steps of pad weld repair. (a) First pad weld (b) Pad weld ground-off and dished-out about 2 mm below the plate surface (c) Re-deposited pad weld..... 65
Figure 3-6: Pad repair welds, where (a) Completed pad repair weld and (b) second repair weld where the first pad weld was ground and dished-out the middle part. 65
Figure 3-7: Cross section of the locations of holes for thermocouple placement for full penetration butt weld (dimensions are in millimetres). 66

Figure 3-8: The sequence of repair weld of full penetration butt welds. (a) 30 mm and 50 mm plates welded together with single bevel butt weld. (b) Filler metal was cut off along with the 30 mm plate and new 30 mm plate placed and (c) plates re-welded together (first repair weld). 67
Figure 3-9: Photos of the Gleeble thermo-mechanical simulator and a simulated HAZ sample during testing. 68
Figure 3-10: An example of temperature histories captured by three imbedded thermocouples in a real BoP weld. 69
Figure 3-11: An example of the temperature profile of a two-cycle thermal simulation with maximum peak temperatures of peak 1 (T_{p1}) and peak 2 (T_{p2}). 72
Figure 3-12: Example of test points for hardness mapping on a BoP weld sample... 73
Figure 3-13: Charpy impact test sample (a) full-size impact test sample and (b) detail of the notch 74
Figure 3-14: Charpy impact test equipment used for the study [143] 74
Figure 3-15: Typical load vs displacement curve of an instrumented Charpy test [144] 75
Figure 3-16: (a) Dynamic tear sample (b) detailed view of the pressed notch and (c) the drop weight tower used for dynamic tear testing (dimensions are in millimetres) 77
Figure 3-17: Close-up picture of the notch of dynamic tear test sample (a) the notch as machined and (b) pressed notch [143] 78
Figure 3-18: A pad weld sample being tested on KOWARI residual stress diffractometer 79
Figure 3-19: Sample for residual stress measurement with neutron diffraction (a) Pad weld with "X" and "Y" reference directions and (b) The array of points where residual stress was measured along the depth of the plate in X and Y directions. 80
Figure 3-20: Residual stress measurement points of pad weld samples (a) on the XZ plane and (b) on the YZ plane. Z-direction was taken as the thickness and 0,0,0 point is on the top side of the pad weld plate. 81
Figure 3-21: An illustration of Bragg's law and Principle of strain measurement with neutron diffraction [146]. 82

Figure 3-22: Neutron interaction with the material and definition of scattering vector Q 82
Figure 3-23: Simulated HAZ samples (a) the location of the sample was cut for the metallurgical characterisation and (b) a mounted sample 84
Figure 3-24: TEM sample preparation with FIB (a) the location of where the sample was taken is shown by the red box. The length was about 15µm and the sample was cut into the material. (b) finalised sample with electron transparent region. 87
Figure 4-1: Lower and upper transition temperatures (Ac_1 and Ac_3) of BIS812 EMA steel at different heating rates. 88
Figure 4-2: Etched samples with saturated picric acid for measurement of Prior Austenite Grain (PAG) sizes for different peak temperatures. From (a) to (e), Base metal, at 1100°C, at 1200°C, at 1300°C and at 1350°C, respectively. 90
Figure 4-3: The variation of average PAG size in the simulated HAZ specimens with different peak temperatures. 91
Figure 4-4: Typical microstructure of BIS812 EMA steel with 2% Nital etch. 92
Figure 4-5: Microstructural changes in with intercritical reheating. (a) and (b) are single thermal cycles at 1350°C and 1100°C peak temperatures and (c) and (d) are double thermal cycles with subsequent heating up to 750°C (just above the A_{c1} temperature), after the first thermal cycle. (2% nital etch for 5 s)..... 93
Figure 4-6: Temperature histories of BoP welds (a) first weld and (b) second weld (first repair weld), at 2.5 mm and 4 mm below the surface under weld beads. . 94
Figure 4-7 Cross sections of BoP welds through the plug where the thermocouples were mounted, where (a) 2.5 mm and (b) 4 mm (Actual distances measured from fusion line to thermocouples were 1.4 and 2.5 mm) 94
Figure 4-8: The comparison between simulated and real weld microstructures (a) and (c) are real weld HAZ microstructures of CG and ICCG regions and, (b) and (d) are CG (1350°C) and ICCG (1350-750°C) simulated samples (with 2% natal etch). 95
Figure 4-9: Microstructures of base material and simulated HAZ with 2% Nital etch. (a) unaffected base material and, single thermal cycles with (b) 1350°C peak, (c) 1200°C peak and (d) 1100°C peak. 96

Figure 4-10: Optical micrographs of series of two cycle simulated HAZ specimens with 2% Nital etch, where; (a)1350-750°C, (b) 1350-800°C, (c) 1350°C-850°C, (d) 1200-750°C, (e) 1200-800°C, (f) 1200-850°C, (g) 1100-750°C, (h) 1100-800°C and (i) 1100-850°C. 99
Figure 4-11: Secondary electron images of simulated single and double thermal cycles (a) Single thermal cycle at 1350°C peak (b) and (c) 1350-750°C, (d) and (e) 1350-850°C. 100
Figure 4-12: Comparison of CG HAZ (1350°C) from; (a) single CG cycle, (b) double CG cycles, (c) three CG cycles and (d) four CG cycles. (with 2% Nital etch). 101
Figure 4-13: Comparison of different of CG and IC thermal cycle tested, where CG - 1350°C and IC - 750°C. (a) to (c) were CG-IC cycles with only the CG cycle repeated, (d) to (e) were CG-IC cycles with only the IC cycle repeated and (f) was a CG-IC×2 cycle. (2% Nital etch). 102
Figure 4-14: Macrographs of BoP repair welds. Macrographs (a), (b), (c) and (d) are BoP1, BoP2, BoP3 and BoP4, respectively. BoP 1 is first weld and BoP 4 is forth weld (third repair weld). The first-pass of the weld is on the left side and the second-pass was on right side. 104
Figure 4-15: Stitched Micrograph showing the varying microstructure of a real HAZ, showing a transition from CG and CG-IC to FG and FG-IC microstructures, for BoP 1. 105
Figure 4-16: Typical optical images of specific HAZ microstructure for BoP 1 where; (a) CG region, (b) ICCG region, (c) FG region and (d) ICFG region.. 106
Figure 4-17: Typical optical images of specific HAZ microstructure for BoP 4 where; (a) CG region, (b) ICCG region, (c) FG region and (d) ICFG region.. 107
Figure 4-18: Macro-image of the cross section of the HAZ in pad repair weld 1, where (b) and (c) show two regions comprised of the low toughness ICCG microstructure. 108
Figure 4-19: Typical examples of the different sub regions in the HAZ of pad weld repair 1, where (a) CG, (b) ICCG, (c) FG and (d) ICFG. 109
Figure 4-20: Macro-image of the cross section of the HAZ in pad repair weld 4, where (b) and (c) show two regions comprised of the low toughness ICCG microstructure. 110

Figure 4-21: Typical examples of the different sub regions in the HAZ of pad weld repair 4, where (a) CG, (b) ICCG, (c) FG and (d) ICFG. 111
Figure 4-22: The variation of Charpy impact toughness with different peak temperatures, where the initial peak temperature, T_{p1} is shown on the bottom X-axis and the intercritical reheat temperature, T_{p2}, is shown in the legend. The upper X axis represents PAG sizes associated to peak temperatures on bottom axis. (test temperature was -20°C). 112
Figure 4-23: Instrumented impact test results (with curve smoothing) of simulated HAZ samples with single (1350°C) and double thermal cycles (1350-750°C and 1350-800°C), tested at -20ºC. Curve soothing was applied to eliminate noise. 113
Figure 4-24: Effect of different thermal cycles on the toughness of simulated HAZ. Red columns are single, double and triple CG thermal cycles (1350°C) and blue columns are the samples with IC thermal cycle of 750°C followed by the previous respective combination of CG cycles. 114
Figure 4-25: Load vs displacement curves from instrumented impact toughness testing for full penetration butt welds with weld 1 and weld 4, where samples were taken from fusion line (FL) and FL + 3 mm (FL+3). (tested at -18°C). . 115
Figure 4-26: Load vs displacement curves from instrumented impact toughness testing for full penetration butt welds with weld 1 and weld 4 where samples were taken from fusion line (FL) and 3 mm into HAZ from FL (FL+3). (tested at -51°C). 116
Figure 4-27: Variation of the hardness of single and double thermal cycles. 118
Figure 4-28: Variation of micro hardness of samples with different second cycle IC and PAG size temperatures for different PAG sizes. 118
Figure 4-29: Variation of hardness with multiple CG (1350ºC) thermal cycles and multiple CG (1350ºC) cycles with a final IC (750ºC) cycle (HV5). 119
Figure 4-30: The variation of micro hardness of single and multiple repairs of BoP welds, where BoP 1 to 4 is from top to bottom (HV0.5). 120
Figure 4-31: Hardness maps of pad repair welds. (a) and (c) are hardness in longitudinal direction to the weld from pad repair 1 and pad repair 2 respectively. (b) and (d) are hardness in transverse direction to the weld of pad 1 and pad 2, respectively (HV0.5). 122

Figure 4-32: Hardness maps of pad repair welds. (a) and (c) are hardness in longitudinal direction to the weld from pad repair 3 and pad repair 4 respectively. (b) and (d) are hardness in transverse direction to the weld of pad 3 and pad 4, respectively (HV0.5). 123
Figure 4-33: Comparison of hardness distribution between full penetration butt weld repair 1 and repair 4. The only 50 mm plate on left side of the weld have gone through all 4 weld cycles in the weld repair 4. The 30 mm plate was replaced with a new one in each weld repair. 124
Figure 4-34: Nano hardness indentations of (a) 1350-750°C and (b)1350-800°C specimens. 125
Figure 4-35: SEM fractograph of simulated HAZ where (a) and (b) are 1100°C peak temperature (FG HAZ), (c) and (d) 1100 - 750°C double cycle and (e) and (f) 1100 - 850°C double cycle. 127
Figure 4-36: SEM fractographs of simulated HAZ, where (a) and (b) are 1200°C peak temperature (CG-HAZ), (c) and (d) 1200 - 750°C double cycle, (e) and (f) 1200 - 850°C double cycle. 128
Figure 4-37: SEM fractographs of simulated HAZ where, (a) and (b) are peak temperature 1350°C (CG HAZ), (c) and (d) 1350 - 750°C double cycle, (e) and (f) 1350 - 850°C double cycle. 129
Figure 4-38: SEM fractographs of simulated HAZ of double CG thermal cycle (1350-1350°C) 130
Figure 4-39: SEM fractographs of simulated HAZ with three thermal cycles, CG-CG-IC (1350-1350-750°C) 130
Figure 4-40: SEM fractographs of simulated HAZ with three thermal cycles CG-IC-IC (1350-750-750°C) 131
Figure 4-41: SEM fractographs of simulated HAZ with four thermal cycles CG-CG-CG-IC (1350-1350-1350-750°C) 131
Figure 4-42: Metallography of fracture cross sections with 2% nital etch. (a) and (b) double cycle simulation 1350 - 850°C and (c) and (d) double cycle simulation 1100 - 850°C (Nickel coated on 1350-850°C to preserve the edge). 132
Figure 4-43: TEM micrograph of Martensite laths in the base metal 133
Figure 4-44: TEM images of simulated HAZ of single and double thermal cycles (a) 1350ºC and (b) 1350 - 750°C 134

Figure 4-45: TEM images of simulated HAZ. (a) 1350 - 750°C and (b) 1350 - 800°C 134
Figure 4-46: TEM images of simulated HAZ. (a) 1100 - 750°C and (b) 1100 - 800°C 134
Figure 4-47: FIB sample taken from CGIC region on pad weld repair 1. (a) CGIC region where the fib sample was taken, (b) the magnified image of the location where sample cut out and (c) the FIB lamellar after final preparation. 135
Figure 4-48: TEM images from the MA constituent in GCIC region of single repair pad weld sample. Where (a) Fine lath structure with high dislocations and retained austenite, (b) Dark field image of (a) where cementite particles can be seen in white and retained austenite as grey and (c) the diffraction pattern with FCC spots, obtained from location A, confirmed the presence of RA. 136
Figure 4-49: TEM images from the tempered matrix of pad repair 1. Where (a) a large grain with 011 orientation, (b) carbide particles along the grain boundaries and (c) Diffraction pattern from the large grain showing [011] zone axis orientation. 137
Figure 4-50: TEM images from the same grain shown in Figure 4-49, showing (a) presence of high dislocation density and small carbide particles and (b) diffraction from area "C", showing 011 BCC matrix with spots in between (arrowed) from cementite. 138
Figure 4-51: FIB sample taken from an ICCG region of repair 4, pad weld. Where (a) region of selected ICCG HAZ, (b) location of the FIB sample and (c) the FIB lamellar after final preparation. Image (c) is a 30 kV transmission electron image of where the centre is the second phase of ICCG and the edge is the matrix region. 139
Figure 4-52: TEM images of pad 4. (a) low magnification image of centre ICCG region, (b) dislocations in ICCG region in 'a' tilted to 001 zone axis, (c) low magnification image of edge, (d) dislocations and cementite of lath 1 in 'c' tilted to 001 and (e) diffraction from above ‘d’ and extra spots are from cementite. 140
Figure 4-53: TEM image of retained austenite particles from the ICCG region of pad weld repair x4, where the diffraction pattern from “A” contains spots from an FCC phase, is shown in the inset. 141

Figure 4-54: TEM image and diffraction patterns of the matrix region of pad repair weld ×4, where (a) TEM image from the matrix region showing dark grains of retained austenite and (b) and (c) show diffraction patterns from locations D and E, respectively, with evidence of FCC spots, indicating retained austenite. ... 142
Figure 4-55: Macro images of dynamic tear test samples..... 144
Figure 4-56: Longitudinal residual stress distribution along the longitudinal direction of the weld (shaded is weld region) 145
Figure 4-57: Transverse residual stress distribution along the longitudinal direction of the weld (shaded is weld region) 146
Figure 4-58: Normal residual stress distribution along the longitudinal direction of the weld 146
Figure 4-59: The variation of residual stresses in longitudinal and transverse directions of pad repair weld 1 and pad repair weld 4. 147
Figure 4-60: Comparison of residual stress changes in pad repair 1 between the original weld and after the weld capping was ground back to 1 mm above the plate surface. 148
Figure 4-61: Distribution of residual stresses below the pad weld repair 1 (a) Longitudinal stresses longitudinal to the weld (b) longitudinal stresses transverse to the weld, (c) transverse stresses longitudinal to the weld and (d) transverse stresses transverse to the weld 149
Figure 4-62: Distribution of residual stresses below the pad weld repair 2 (a) Longitudinal stresses longitudinal to the weld (b) longitudinal stresses transverse to the weld, (c) transverse stresses longitudinal to the weld and (d) transverse stresses transverse to the weld 149
Figure 4-63: Distribution of residual stresses below the pad weld repair 3 (a) Longitudinal stresses longitudinal to the weld (b) longitudinal stresses transverse to the weld, (c) transverse stresses longitudinal to the weld and (d) transverse stresses transverse to the weld 150
Figure 4-64: Distribution of residual stresses below the pad weld repair 4 (a) Longitudinal stresses longitudinal to the weld (b) longitudinal stresses transverse to the weld, (c) transverse stresses longitudinal to the weld and (d) transverse stresses transverse to the weld 150

Figure 4-65: Band contrast map for the simulated HAZ of 1350-750°C sample. MA particles formed along the prior austenite grain boundaries during the second intercritical heating can be seen as darker regions. 151
Figure 4-66: (a) IPF colour map for the simulated ICCG sample with 1350-750°C thermal cycles and (b) is the higher magnification from the inset of a. (Black lines are the grain boundaries with more than 15° of misorientation). 152
Figure 4-67: Band contrast map with grain boundaries of simulated HAZ with double thermal cycles (1350-750ºC). Darker grey areas represent newly formed MA constituents. Dark lines show high angle grain boundaries (θ>15º) and green lines are low angle grain boundaries (15º>θ>2º). 153
Figure 4-68: Phase map of simulated HAZ with double thermal cycles (1350-750°C). Red is BCC steel and Blue is FCC. Dark lines show high angle grain boundaries (θ>15º) and green lines are low angle grain boundaries (15º>θ>2º)..... 154
Figure 4-69: Band contrast map for the simulated HAZ of 1350-800°C sample. MA particles formed along the prior austenite grain boundaries during the second intercritical heating can be seen as darker regions. 155
Figure 4-70: IPF colour map for the simulated ICCG sample with 1350-800°C thermal cycles. (Black lines are grain boundaries with more than 15° of misorientation). 156
Figure 5-1 Continuous cooling transformation (CCT) diagram of BIS812 EMA steel with the sample austenised at 1250°C for 13 s before cooling [21]. 159
Figure 5-2 SEM images showing (a) low magnification image of 1350-850°C, showing second phase formed on grain boundaries, (b) higher magnification image of (a) and (c) image of 1350-750°C specimen at the same magnification as (b). 163
Figure 5-3: High magnification secondary electron image of an MA particle in above Figure 5-2(c) image shows lath structure inside MA. 164
Figure 5-4: Grain misorientation map of simulated 1350-750°C sample. Confirming that MA grows into neighbouring grain while keeping specific OR. θ is the misorientation angle. (misorientation along line AB presented in Figure 5-5). 165
Figure 5-5: Misorientation profile of 1350-750ºC sample through a MA particle along the line A to B shown in Figure 5-4. 165

Figure 5-6: Grain misorientation map of simulated 1350-800°C sample. Confirming that MA grows into neighbouring grain while keeping specific OR. θ is the misorientation angle. (misorientation along line AB presented in Figure 5-7). 166
Figure 5-7: Misorientation profile of 1350-800ºC sample through a MA particle along the line A to B shown in Figure 5-6. 166
Figure 5-8: Characterization of the microstructure of ICCG HAZ and M-A constituent. (a) OM micrograph (etched by 4% nital), (b) OM micrograph (etched by LePera etchant), (c) SEM micrograph and (d) TEM micrograph of blocky type M-A constituent 170
Figure 5-9: Instrumented Charpy impact energies of single cycle FG (1100°C) and CG (1350°C) samples and, double cycle ICFG (1100-750°C) and ICCG (1350-750°C) samples. 171
Figure 5-10: The variation of toughness due to IC cycle compared with single thermal cycle for different PAG sizes. 173
Figure 5-11: The proposed mechanism of fracture behaviour in low and high IC reheating where; (a) at low IC temperature (750ºC) and (b) at high IC temperature (800ºC). 179
Figure 5-12: Evidence of high density of HAGB in MA at higher IC temperature. (a) region with MA at PAGB and (b) matrix. Dark lines – High angle grain boundaries (>15°) and Green lines – Low angle grain boundaries (2°<θ<15°). Simulated HAZ sample with 1350-800°C thermal cycle. 180
Figure 5-13: Evidence of fracture arrests by high angle grain boundaries (HAGB's) of MA produced in high IC thermal cycles. Simulated sample with 1350-800°C thermal cycle. Grain boundaries with misorientation >15° shown in black lines. 181
Figure 5-14: Distribution of residual stress field and hardness in longitudinal direction of weld under the toe of pad weld repair 2. Circled areas show regions with high tensile stress and higher hardness. 184
Figure 5-15: The comparison of variation of hardness across the HAZ region on pad weld 1 187

LIST OF TABLES

Table 2-1: Estimated solubility temperatures of particles in steel [44]. 17
Table 2-2: Carbon concentration of MA for the samples quenched from 400°C. Carbon percentage in ferrite was 0.02% [54]..... 44
Table 2-3: Orientation relationship in steel..... 48
Table 2-4: Principals and techniques for improving the HAZ toughness under high heat input welding [119]. 50
Table 2-5: Effects of alloying elements for the toughness of HAZ in steel [44, 125]51
Table 3-1: Chemical composition (wt%) and carbon equivalent of BIS812 EMA steel [139] 59
Table 3-2: Typical mechanical properties of BIS812 EMA steel [139] 59
Table 3-3: Pad weld sizes with different repair cycles. See Figure 3-5. 64
Table 3-4: Characteristics of thermal cycles used to simulate different HAZs 69
Table 3-5: Properties of the material used for the HAZ simulations 70
Table 3-6: Tested thermal cycles with Gleeble thermo-mechanical simulator..... 71
Table 3-7: Steps of sample preparation for the optical microscopy and SEM..... 84
Table 3-8: Steps of etching for revealing of PAGs 84
Table 3-9: Steps of LePera's etchant used for revealing MA particles 85
Table 4-1: Average prior austenite grain sizes achieved with different peak heating temperatures (from minimum of 50 grains). 91
Table 4-2: Instrumented Charpy fracture energies of simulated HAZ samples with single and double thermal cycles, tested at -20°C 113
Table 4-3: Variation of toughness with short tempering cycle. (Tempering cycle was applied on ICCG (1350-750) sample. 115
Table 4-4: Fracture initiation (E_i), propagation (E_p) and total (E_t) energies of real weld samples with different repair weld cycles. 117
Table 4-5: Nano indentation hardness measured on simulated HAZ specimens. Location numbers are corresponding to Figure 4-34. 125
Table 4-6: Dynamic tear test results of HAZ samples taken from full penetration butt joints with four cycles of repair welding..... 143
Table 5-1: PAG sizes with single and consecutive multiple thermal cycles. All CG cycles were 1350ºC peak, 0.5 s at peak and 4.3 s to cool from 800 to 500ºC. 161

Table 5-2: Percentage of MA measured in different thermal cycles. 161
Table 5-3: toughness of samples with multiple thermal simulations and similarities to single and double thermal simulations in terms of toughness..... 176
Table 5-4: Summery of average hardness on the MA and the matrix measured with nano indentation. 180
Table 5-5: Average area of the hardness higher than 400HV0.5 with different repair weld cycles in pad weld repairs. (The average area is the average hardness of longitudinal and transverse sections). See figures 4-30 and 4-31 for visual representation of hardness. 186
Table 6-1 The toughness equivalent of the multiple thermal cycles to a single or double thermal cycle. 190

1 INTRODUCTION

1.1 Background

BIS812 EMA is a micro-alloyed quenched and tempered steel, with a minimum yield strength of 690 MPa, which is used for the pressure hull of the Collins Class submarines [1, 2]. There has been extensive research on the weldability of BIS812 EMA steel [2-4] so, effective procedures for primary fabrication and welding have been developed and qualified. However, the effects of multiple welding cycles at the same location on the base steel properties have not been comprehensively investigated.

Corrosion is an unavoidable degradation process faced by steel structures that are exposed to seawater. There are corrosion protection systems in place to safeguard against corrosion, but due to various reasons, these systems can be compromised. Corrosion can occur as a result of inadequate cathodic protection, coating degradation and/or the presence of sulphur reducing bacteria in seawater [5].

Welding is one of the most efficient methods to repair corrosion damage. In addition, it may be necessary to remove and reinstall sections of the hull for maintenance purposes and again, re-welding is required. Over the lifetime of the vessel, it is feasible that a previously repaired area is again subjected to corrosion damage, or the removal and reinstallment of a section of the hull for maintenance purposes are required several times. Few studies have been conducted to determine if the same area can be repaired multiple times by welding. The objective of this work is to determine the effects of multiple welds on the material properties of the parent plate of the Collins Class submarines. The outcomes of this research will be used to inform the long-term maintenance schedule of Collins Class submarines and reduce their cost of ownership.

Three types of weld repairs were considered; bead-on-plate (BoP) welds, pad welds and full penetration butt welds. BoP welds represent the welding of attachments onto a submarine’s pressure hull for maintenance applications. These temporary attachments are typically fillet welded in place, and then taken off at the end of the maintenance work. Pad welds are remediation of corrosion damage (generally

pitting) to the hull or ballast tanks. Full penetration butt welds represent circumferential welds on the submarine hull. For maintenance requirements, it is necessary to cut-open the pressure hull to access internal machinery and components.

BoP welds were introduced to capture the microstructural changes due to fillet welds. Even though the weld geometry is different, BoP welds were more suitable for investigating the effects of multiple thermal cycles of repair welds on the parent plate.

Pad welding is used to repair the corrosion damage in high strength steel hulls in naval vessels. The repair dimensions are typically 10-30% of the plate thickness and 50-200 mm in diameter [5]. The repair welding procedures should be designed to avoid introducing any adverse effects on base material properties or the structural integrity of the hull [5]. For example, shorter weld runs in repair welding can result in higher non-uniformity in temperature fields, which leads to non-uniformity in microstructure [5, 6], and this produces undesirable mechanical properties, so should be avoided.

Full penetration butt welds are longitudinal and circumferential welds on the submarine pressure hull. When major maintenance is scheduled, it is required to cut-open the pressure hull for internal access. The pressure hull is usually cut along an existing weld seam [7]. In the event of re-welding the hull back together, the existing heat affected zone (HAZ) is removed, and the edges are buttered-up with weld deposits to compensate the length removed. The buttered ends are prepared to the correct weld geometry to allow full penetration butt welds to reinstall the pressure hull together. This technique also ensures that the new HAZ does not overlap the existing HAZ of the weld seam.

In multi-pass welds, the thermal cycle generated by each pass affects the HAZ from previous weld runs. Due to the relatively transient thermal gradient of a weld run, the impact of one run to surrounding weld runs is restricted to a narrow region. For recurring repair welds, mismatch between the previous HAZ and the new welds can create combinations of thermal cycles that cannot be achieved for multi-pass welds.

Furthermore, when multiple recurring welds are made at the same location, multiple variations of repeated thermal cycles can be experienced by the base plate. In a real weld, it is difficult to determine which kind of thermal cycles a particular area experienced, except for the final cycle. Therefore, combinations of simulated sub-HAZ regions are required to study the effects of multiple cycles at the same location.

Currently, there is insufficient research and data available to understand the impact of recurring weld thermal cycles on the mechanical properties and understand the underlying mechanisms at play to support the safe practice of applying recurring repair welds on BIS812 EMA steel. This research will provide data for the industry partner to enable them to determine if multiple weld repairs are feasible. This could result in cost-savings and time-savings for the maintenance of marine vessels.

1.2 Objectives

As outlined in the introduction, the main objective of this research is to provide evidence to determine if multiple weld repairs can be carried out on the steel used for the Collins Class submarines, BIS812 EMA. The sub-objectives set up to achieve the main objective are;

- One of the main objectives is to examine the microstructural changes with multiple thermal cycles on the parent material. The HAZ generated with different thermal cycles is expected to consist of different microstructures. The initial tests were designed to identify the effect of multiple thermal cycles in specific sub-regions of HAZs. This objective was achieved by simulating HAZ with Gleeble thermo-mechanical simulator.
- Study of the extent of microstructural changes on mechanical properties in HAZ with multiple thermal cycles on BIS812 EMA steel. This was achieved by Identifying sub HAZ regions with low toughness and investigated in detail.
- Investigate the fracture properties and related microstructural features of sub-HAZ regions identified as having low toughness, for both recurring real welds and simulated HAZ specimens.

- Examine the changes in residual stresses with multiple repeated weld repair cycles of real welds. This is to assist in determining if multiple pad repairs affect the structural integrity of the hull. (Note: Residual stresses in full penetration butt welds for BIS812 EMA steel has previously been studied, so will not be included in this thesis [8]).
- Determine the "worse-case scenario" for base metal properties subjected to multiple recurring thermal cycles.

1.3 Research methodology

In order to investigate the effect of multiple recurring thermal cycles on the properties of BIS 812 EMA steel, a series of experiments were designed including instrumented welding and testing, HAZ simulations, microstructural analysis, mechanical testing and residual stress analysis. Welds were conducted with imbedded thermocouples in the parent plate to record thermal histories at a different distance from the weld fusion zone. Four different weld repair cycles were carried out with qualified weld procedures and qualified welders.

Temperature histories of instrumented welds were used to design the HAZ simulations. Key parameters were the heating rate, peak temperatures and cooling rate from 800°C to 500°C ($t_{8/5}$). Simulations were used to isolate different sub-regions of the HAZ for single and multiple thermal cycles, which is otherwise not possible on real welds, for conducting impact testing and metallography. Dilatometer tests were conducted at high heating rates to identify lower and upper transformation temperatures of the steel, which were used to design the simulation experiments for the intercritically reheated specimens.

Mechanical testing and metallography were conducted on both real welds and simulated HAZ samples to determine the effects of multiple repair welds on the parent plate properties.

1.4 Thesis outline

Chapter 1 gives the general background on the topic "Effects of mechanical properties of 690 MPa quenched and tempered steel with multiple repair welding". Chapter 2 consists of an in-depth literature review on welding of high strength microalloyed and quenched and tempered (Q&T) steels with respect to changes in microstructure and mechanical properties. This chapter provides details on weldability of high strength steels, effects of welding thermal cycles, repair welding, toughness in weld HAZ and residual stresses in welds. The summary at the end of the chapter specifies important aspects in the literature review and summarises gaps in the current body of knowledge.

Chapter 3 provides all the relevant details of materials used in the current research and the experimental methods. Starting with the base material and its properties, followed by the manufacturing of test samples with thermal simulations and then the welding procedures and setup are explained. Microanalytical characterisation with optical microscopy, SEM, TEM and EBSD is discussed. Mechanical test procedures, such as Charpy V-notch impact tests, Vickers hardness testing and measurements of residual stresses, are also discussed in this chapter.

The main results of this research are presented in Chapter 4. Optical micrographs and SEM images are presented in providing an understanding of the microstructural behaviour with thermal cycles. Charpy impact toughness, hardness tests and residual stress results are provided with reference to different thermal cycles. TEM and EBSD results demonstrate microstructural and crystallographic properties, which, when combined together, provide powerful support for understanding the properties of the HAZ.

Chapter 5 discusses the results of current research in combination with comparing the existing body of knowledge. Microstructure evolution of BIS812 EMA steel with multiple recurring repair welds is discussed. Changes in mechanical properties are discussed from the point of view of providing a better understanding of the effects of multiple recurring repair welding on mechanical properties of high strength microalloyed Q&T steel. The outcomes of the residual stress component of the thesis are also discussed.

Chapter 6 provides the overall conclusions drawn from the research and includes suggestions and recommendations for further studies.

2 LITERATURE REVIEW

This literature review provides an overview of the welding of high strength quenched and tempered (Q&T) microalloyed steels and the adverse effects of welding on microstructural and mechanical properties. The key aim is to provide an in-depth review of how single and multi-pass welds, with a focus on multiple recurring repair welds, affects the microstructure and properties of parent material of different steel types.

Precise control of welding parameters, such as welding heat input, preheat temperature, inter-pass temperature and welding sequence is crucial due to the degradation of parent materials properties by the thermal energy of the welding process. Thermal cycles in welding can weaken the microstructure and degrade mechanical properties of the HAZ. Multiple pass welds create more complex HAZ than in single-pass welds and multiple repair welds can create complex interactions between multiple HAZ's, which can significantly influence the mechanical properties. The coarse grain heat affected zone (CG HAZ) and intercritically reheated coarse grain heat affected zone (ICCG HAZ; Also abbreviated as CG-IC HAZ) are known to have low toughness in a weld [9, 10].

Microstructure within the HAZ largely depends on the hardenability of the base material for a given welding condition. Heat input of the weld as well as micro and macro alloying elements, both influence the microstructural evolution of the HAZ. Prior austenite grain (PAG) size is well known to significantly affect the strength and toughness of the HAZ [11, 12]. Large PAG size promotes low toughness microstructures, in which it is easier to propagate cleavage fracture. The martensite-austenite (MA) constituent is one of the main microstructural components that can affect the toughness of the HAZ. Consequently, the formation of MA in the ICCG and CG HAZ regions has been a focal point within the literature. In particular, the link between fracture toughness and MA constituents, which can initiate fracture and lower toughness, continues to receive on-going attention. Therefore, the focus of this literature review will be on the above area.

Residual stresses associated with welding can affect the overall stress distribution of a structure or a component. Residual stress is described as the stress remaining in the component after completion of the thermal cycle. Repair welds can introduce different stresses compared to original fabrication weld and can alter the overall stress distribution. A part of this research examined the influence of multiple repair weld on the residual stresses for pad welds, so a brief review of the effects for welding on residual stresses is also included.

2.1 Weldability of high strength Q & T steels

High strength quenched and tempered steels were designed to meet specific mechanical property requirements, which were traditionally difficult to meet by thermo-mechanical processing. The microstructure of Q&T steels predominately consists of tempered martensite. In thermo-mechanically processed steels, martensitic microstructures are usually avoided, in preference for bainitic, ferrite + pearlite or acicular ferrite microstructures. As such, the weldability of Q&T steels presents different challenges compared to thermo-mechanically processed grades. Low carbon, Q&T steels commonly have a lath martensite microstructure, which can have excellent strength and toughness, when a suitable heat treatment is performed, so are widely used within the industry [13, 14].

Due to the degradation of original material properties by the thermal energy of the welding process, the precise control of welding parameters is crucial. Among the various welding parameters, preheat temperature and arc energy input have a predominant effect on the efficiency of the weld joint (Figure 2-1). Welding parameters and weld heat input must be closely controlled in certain limits to achieve required properties. Higher heat input leads to slower cooling rates leading to coarser grains, which reduce strength and toughness. On the other hand, low heat inputs leads to higher cooling rates and may result in a brittle microstructure [15].

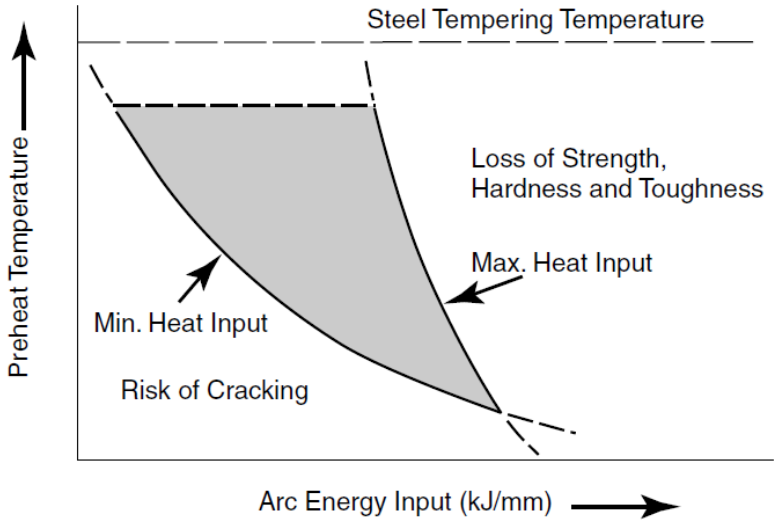

Figure 2-1: Total weld input relationship of Q & T steels [16].

2.1.1 Hardenability and carbon equivalent effect on weld HAZ

Hardenability of a steel is directly correlated to the hardenability of the HAZ, so is an important indicator of expected final microstructure and HAZ properties. The hardenability of steel is expressed as the ability to form martensite upon quenching. Alloys with higher hardenability can achieve a fully martensitic microstructure at slower cooling rates. To achieve a fully martensitic structure, the hardenability must be sufficient to avoid decomposition of austenite to ferrite, perlite or bainite. The ability to achieve a fully martensitic structure depends on cooling rate, geometry and composition [17]. Formation of fine low temperature transformation phases, such as bainite, can be minimised by adding appropriate alloying elements [18].

Hardenability can be estimated from the carbon equivalent, after the introduction of empirical formula's to describe the critical cooling rate for full martensite transformation in steel [19]. The carbon equivalent was originally used as an index for cold cracking susceptibility, as the latter is closely related to HAZ hardness. The effect of various alloying elements on hardness is taken into account in order to assess the hardenability. The carbon equivalent used by the International Institute of Welding (IIW) is one of the most widely used equations, as shown below [20];

$$CE_{IIW} = C + \frac{Mn}{6} + \frac{Cr + Mo + V}{5} + \frac{Cu + Ni}{15} \quad (1)$$

However, IIW carbon equivalent equation does not take into account some of the alloying elements used for modern high strength low alloy (HSLA) steels. Therefore, an improved formula to use for HSLA steels was proposed by Ito and Bessyo [21];

$$P_{cm} = C + \frac{Mn + Cu + Cr}{20} + \frac{Si}{30} + \frac{Ni}{60} + \frac{Mo}{15} + \frac{V}{10} + 5B \quad (2)$$

Quantities for equations 1 and 2 are to be inserted as wt%

2.2 Effects of welding thermal cycles on the base steel

Thermal cycles in welding can change the microstructure and weaken the mechanical properties of materials. In particular, the combination of high strength and toughness of Q&T steel can be degraded in the HAZ because of weld thermal cycles [9, 22, 23]. During the fusion welding processes, because of the application of localised thermal energy in order to melt the steel, the surrounding microstructure is exposed to a significantly different thermal cycle compared to the production process. As such, the resulting microstructure and mechanical properties of the steel affected by the weld thermal cycle, the HAZ, can be substantially altered compared with the original microstructure and properties [24]. Therefore, the welding process should be carefully controlled in order to retain the required microstructural and mechanical properties of the component or structure.

2.2.1 Weld heat affected zone (HAZ)

A typical HAZ of a single-pass weld is illustrated in Figure 2-2. The HAZ is not uniform; it contains four sub-zones, depending on peak temperature and cooling rate; a coarse grain zone (CG), fine grain zone (FG), intercritical zone (IC) and subcritical (SC) or tempered zone. Different sub-zones possess different mechanical properties.

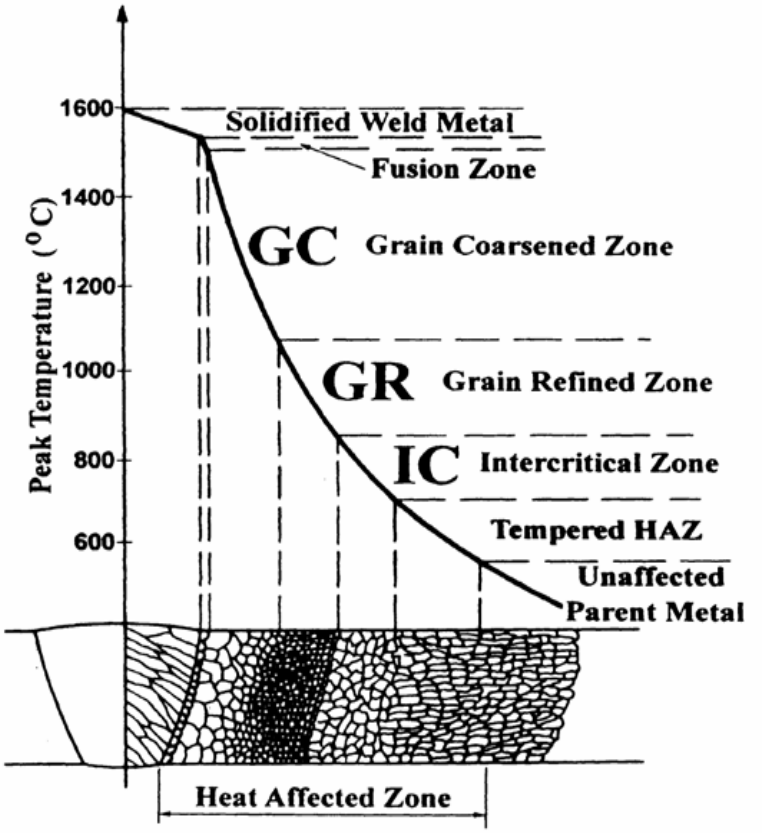

Figure 2-2: HAZ classification in the fusion weld [25].

Multi-pass welds create a more complex HAZ, as shown in Figure 2-3. Due to the generation of more complex microstructures, multiple repair welds can have a strong influence on mechanical properties. When the HAZ from a single weld cycle is subjected to multiple weld cycles, four additional HAZ sub-zones are created due to the reheating of the pre-existing HAZ [19, 22, 23]. These are; unaltered CGHAZ (UA CGHAZ), supercritically reheated CGHAZ (SCR CGHAZ), inter critically reheated CGHAZ (IC CGHAZ) and sub critically reheated CGHAZ (SC CGHAZ) [26-28].

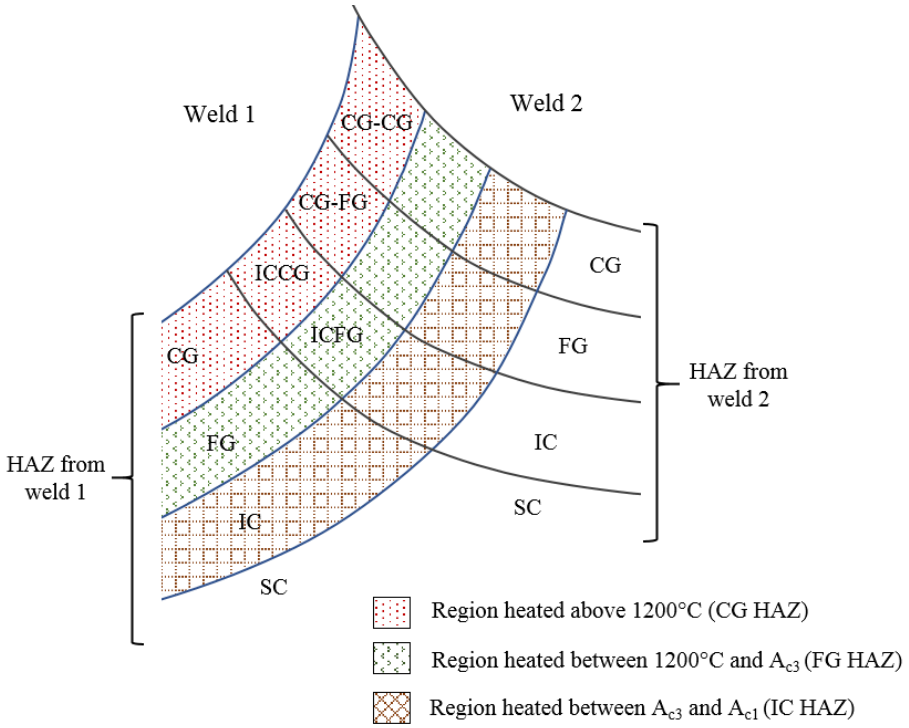

Figure 2-3: Various HAZ zones in single and two pass weld. Adapted from Kumar, et al. [26].

It has been observed that these subzones can have poor mechanical properties and the failure of welded structures can often be attributed due to the formation of such brittle zones [26]. Brittle crack initiation in these local brittle zones is related to the high hardness and low toughness microstructures. These regions of higher hardness are also prone to HACC and additional stresses and fatigue loads can lead to failure of the weld.

2.2.1.1 Coarse grain HAZ (CG HAZ)

Coarse grain HAZ is the zone heated above the austenite transformation temperature to a temperature high enough to cause significant grain coarsening. When the cooling rate is high, which is often the case during the thermal cycle in welding, this zone will become hardened because of the formation of hard phases such as martensite and bainite. Thus, the toughness of the material in this region deteriorates, as it is prone to HAZ embrittlement due to high hardness [29].

2.2.1.2 Fine grain HAZ (FG HAZ)

Fine grain HAZ is the zone next to the CG HAZ, which experiences temperature above upper critical temperature (A_3), but are low enough to prevent significant grain growth. Grain refinement in the FG HAZ can lead to a softer, tougher microstructure compared to the CG HAZ.

2.2.1.3 Intercritical HAZ (IC HAZ)

In this region, the material becomes austenite in part because of heating to the temperature between lower critical temperature (A_1) and A_3 points. In multi-pass welds, the FGHAZ and CG HAZ can be intercritically reheated, ICFG HAZ and ICCG HAZ, respectively. The CG HAZ and ICCG HAZ are well known to be regions with low toughness in a weld due to transformation of low toughness microstructures such as coarse martensite, coarse bainite which relates back to larger PAG size [30-32]. Furthermore, the ICCG HAZ has been shown to have the highest susceptibility to hydrogen embrittlement followed by CG HAZ [33]. Therefore, researchers have focused on the study and characterisation of the above two regions. The microstructure of typical ICCG HAZ with large PAGs and fine bainitic ferrite laths with secondary martensite-austenite (MA) constituent along grain boundaries is shown in Figure 2-4.

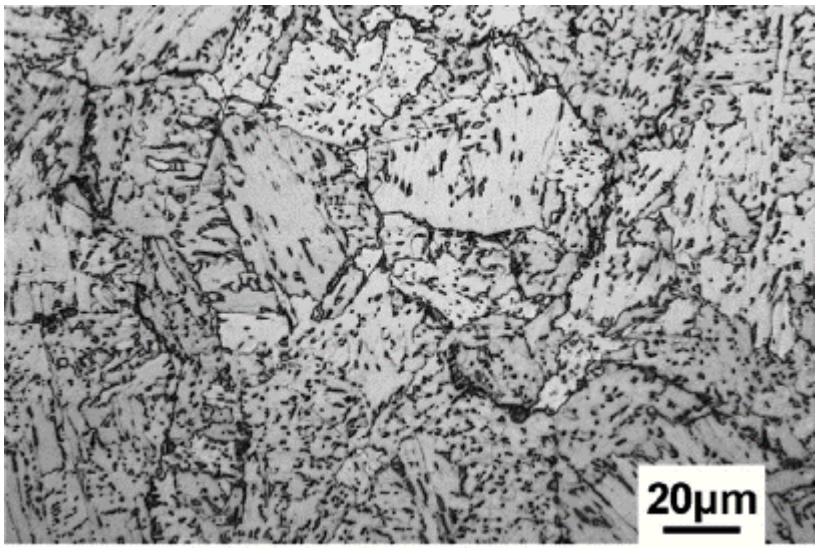

Figure 2-4: Typical inter-critically reheated GC-HAZ in X70 grade pipeline steel [10].

It was commonly reported that with the second thermal cycle in the intercritical range, the HAZ develops a second phase along the grain boundaries and sometimes inside the grains. This phase is referred to as martensite-austenite (MA) constituent [34]. The formation of MA constituent and its effect on properties is described in Section 2.4

2.2.1.4 Subcritical HAZ (SC HAZ)

This is the zone which is heated below A_{c1} point and it is often difficult to distinguish between SC HAZ and the parent metal under the optical microscope. The microstructure has been slightly tempered, decreasing hardness compared to the base metal.

2.2.1.5 Unaltered CG HAZ

As mentioned earlier, several researchers have separated the unaltered GC HAZ two ways. The first is when an existing CG HAZ is reheated again into the CG temperature region or secondly, when the existing CG region is not reheated at all. However, researchers [26] assumed that there are no microstructural changes from the second weld CG thermal cycle, in order to call it an un-affected (unaltered) CG HAZ.

2.2.2 Weld microstructures

The weld microstructure varies within the weld region depending on the peak temperature experienced by the material and cooling rate. The transformation of several microstructures is possible on the cooling of austenite.

2.2.2.1 Ferrite

Three main ferritic components can be found mainly in the weld metals. Namely, Allotrimorphic ferrite, Widmanstätten ferrite and Acicular ferrite. Generally, allotrimorphic ferrite and Widmanstätten ferrite are not observed in high strength steel weld metals. The microstructure of acicular ferrite can be seen as needle-like structures and generally recognised as three-dimensional structure of lenticular plates.

The plates of acicular ferrite nucleate on small non-metallic inclusions inside the austenite grains and radiate in many different directions. This gives the chaotic ordering and gives superior mechanical properties; especially the toughness [17].

2.2.2.2 Martensite

Martensite is a very hard microstructure that forms during rapid cooling from austenite to room temperature in steels. To obtain martensite, the cooling rate must be sufficiently fast enough to avoid the solid-state transformations. For the plain carbon steels, this rate is very high but for the alloyed steels containing austenite stabilising elements, the rate is much slower.

Strength of martensite depends mainly on its carbon content and the yield strength of martensite increases linearly with its carbon content [35]. Substitution alloying elements such as Mn and Si also strengthen the martensite [24]. Because the martensite transformation is diffusion-less, martensite has the exact same composition as parent austenite although this is dependent on the alloy composition and valid up to 2 % carbon concentration [36].

In microstructural observations, martensite is often identified as a needle-like microstructure in two dimensions. However, the crystals have lath or plane shape in three dimensions [36]. Martensite is not an equilibrium phase and can easily be altered applying the heat and is used for the stress relieving. However, this property can adversely affect the welding of martensitic steels because of over-softening of some regions and brittleness of other regions.

2.2.2.3 Bainite

Time temperature transformation (TTT) diagrams show that the pearlite reaction occurs at high temperature and the martensite formation starts at relatively lower temperatures. In between these two temperatures, an intermediate microstructure may form, called bainite. Bainite transformation occurs when cooling rate is too high to form perlite and too slow to form martensite. Mainly there are two forms of bainite; upper bainite (550-400˚C) and lower bainite (400-250˚C) [17].

2.2.3 HAZ hardenability

The final microstructure after the heating and cooling cycle, for the given welding parameters, depends on the hardenability of the base material. As an example, in welding of ferrite/pearlite steels, the HAZ microstructure (mainly CG HAZ) can transform to bainite, or with higher hardenability, to a martensitic microstructure.

2.2.3.1 Grain size control in welding

In the strengthening of steels, refining the grain size plays a vital role. In the early 1950s, E.O. Hall and N.J. Petch revealed by scientific analysis, the relationship between yield strength and grain size, which is represented in the Hall-Petch relationship in Equation 3 [37].

$$\sigma = \sigma_0 + kd^{-1/2} \quad (3)$$

Where, σ_0 is the lattice friction stress required to move individual dislocations, k is a constant, which depends on the material (known as Hall-Petch slope), and d is the grain size.

The effect of grain size on yield strength is described as dislocations within crystals travel and pile-up at the grain boundary and cause stress to be generated in the adjacent grain. With large grains, high concentration of stress is generated because of the higher number of dislocations in larger grains. With a higher concentration of stress, it is easier for the propagation of yielding [17]. Therefore, smaller grain size leads to increased strength of the material. Furthermore, it was found that the microstructure refinement is more effective in improving impact toughness than improving tensile strength [38] in research on 0.17% carbon Q&T steel. Due to the significance of grain size on strength and toughness, controlling the grain size has become an important aspect of the heat treatment and the welding of Q&T steel.

Grain size and tempering conditions have been shown to influence the dislocation density in Q&T steels, which in turn influences the mechanical properties. Kennet [39] examined the effects of PAG size and tempering temperature on dislocation density and microhardness of a low carbon, microalloyed steel. It was noted that in the quenched and low temperature tempering (LTT) conditions, dislocation densities decreased with increasing PAG size, as shown in Figure 2-5. However, after high

temperature tempering (HTT), dislocation densities increased with increasing PAG size. The overall dislocation density was much lower compared to the as-quenched and LTT conditions. As hardness is closely related to dislocation density, the above trends were also observed in the hardness results, see Figure 2-6.

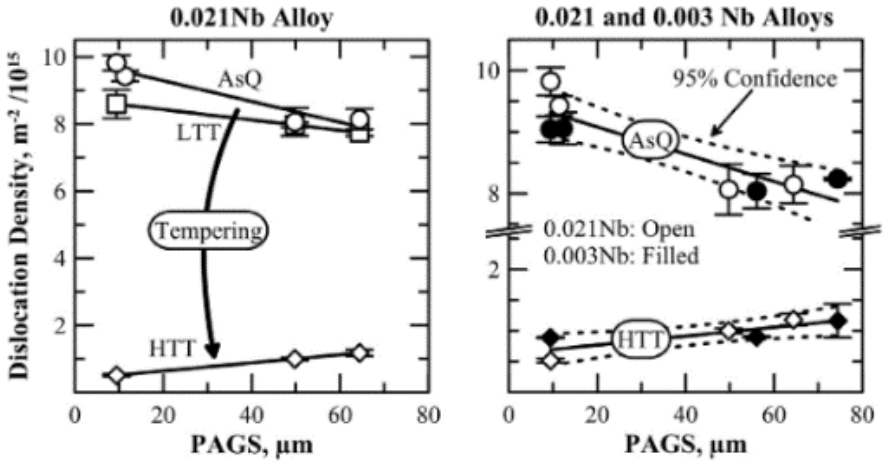

Figure 2-5: The variation of dislocation densities with prior austenite grain size (PAGS) in as-quenched (AsQ), low temperature tempering (LLT) and high temperature tempering (HTT) [39].

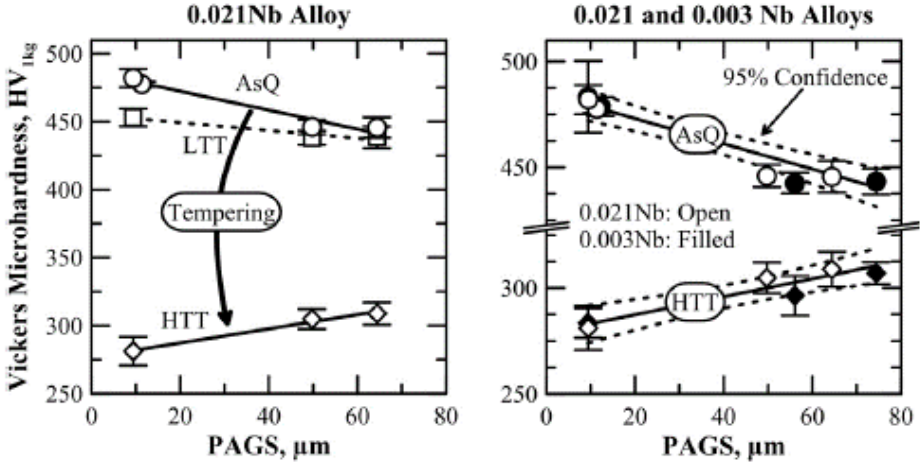

Figure 2-6: The variation of Vickers micro hardness with PAGs in as-quenched (AsQ), low temperature tempering (LLT) and high temperature tempering (HTT) [31].

The excessive grain growth in the CG region leads to the formation of microstructures with unfavourable mechanical properties. One of the best methods to control the grain size of steel subjected to welding is to add certain alloying elements

during the steel manufacturing process [40]. The addition of microalloying elements (such as Ti, B, V, Mo, and W) can form carbides and nitrides to pin grain boundaries and reduce grain growth via control grain boundary mitigation [40, 41]. Furthermore, hardenability is increased by larger grain sizes because the martensite start (Ms) temperature increases [42], which can also influence the final microstructure.

TiN is a common grain refiner, especially for the CGHAZ because of the stability of TiN particles at high temperatures. In research with HSLA-80 and HSLA-100 steels, it was noted that the grain size grew rapidly beyond 1100°C, primarily due to the dissolution of Nb (CN) precipitates [43]. Some common compounds, which are used in grain refinement and their solubility temperatures, are listed in Table 2-1.

Table 2-1: Estimated solubility temperatures of particles in steel [44].

Compound	**Estimated solubility temperature (°C)**
VN	1050
NbC	1100
AlN	1150
TiN	>1450

When grain boundaries are pinned by carbides or nitrides, the grain growth can be expressed in Equation 4 [45]. With larger pinning force, the grain coarsening rate will become smaller.

$$\frac{d\emptyset}{dt} = A\{f(\emptyset) - P[T(t)]\}\, exp - \left(\frac{Q}{RT(t)}\right) \quad (4)$$

Where, $\emptyset$ is the grain size, t is time, A is a constant, T is temperature, P is pinning force, Q is activation energy and R is the gas constant.

2.2.4 HAZ hardness

HAZ hardness provides a useful indication of HAZ strength, toughness and hardenability of a steel [46]. A high hardness HAZ is often associated with high

cracking susceptibility of the welded structure, so welding procedures/standards often prescribe a maximum hardness value. HAZ hardness is controlled by the welding process (cooling rate) and steel composition (hardenability). The typical trend of hardness gradient in the weld metal and HAZ is shown in Figure 2-7.

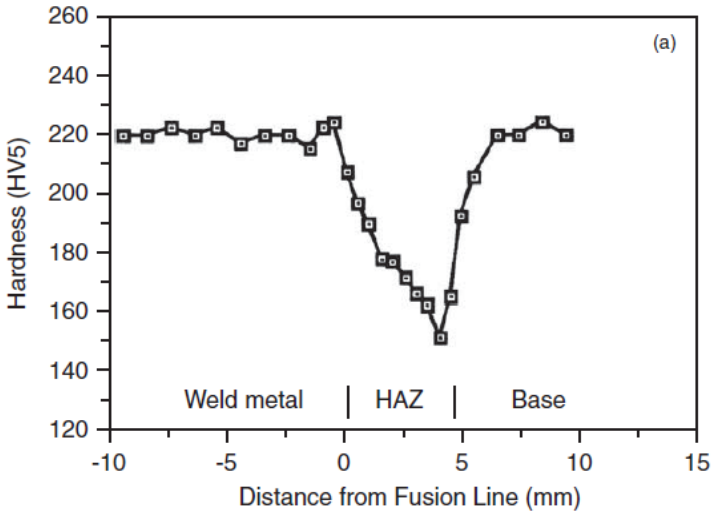

Figure 2-7: Hardness gradient of 20 mm thick BIS60 plate welded with 5 kJ/mm heat input (SAW process with even-matched filler metal) [47].

Most high strength steels, like HSLA-80 and HSLA-100, the maximum hardness in the HAZ was in the CGHAZ [43, 48]. The lower hardness in FG region (Figure 2-8) in HSLA-80 steel was due to the presence of allotriomorphic ferrite and acicular ferrite, and in CG region showed higher hardness because of the presence of lath martensite [43]. A similar trend was reported for HSLA-100 steel by Shome [48]. In general, hardness typically increases with increasing peak temperature for single pass welds due to the increasing likelihood of the formation of bainite and/or martensite and the formation of hard MA constituents. In multi-pass welding, the hardness of the CG HAZ can decrease if it is reheated within the fine grained regions, where lower hardness microstructures can form [26].

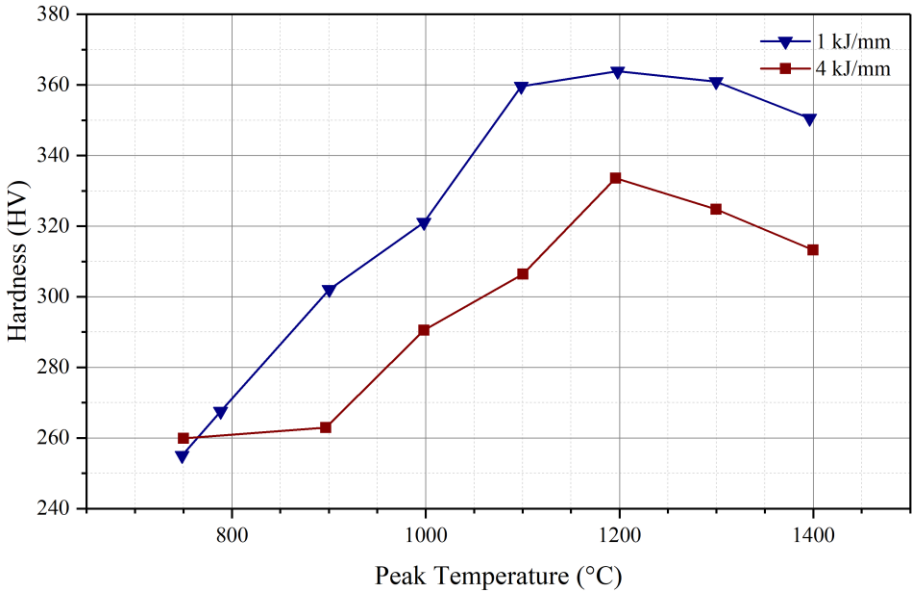

Figure 2-8: Variation of HAZ hardness with different peak temperature for two different heat input in HSLA-80 steel [43].

It was reported that in high strength Q & T armour steel, the highest hardness was at the FG HAZ, as shown in Figure 2-9. The hardness profile of the HAZ, shown in Figure 2-9, was a comparison of simulation and real weld hardness' for hybrid laser-arc welding. Falkenreck, et al. [42] reported that similar behaviour was observed in the welding of S690QL steel by Zhang [49], where the increase of hardness of the FGHAZ was attributed to the presence of carbides and precipitation strengthening, as the steel contained Ti and V microalloying elements. Falkenreck considered that for their armour steel, the relatively high levels of Cr, Ni and Mo, which have a strong effect on hardenability, may have caused the higher hardness in FGHAZ [42]. The decrease in hardness of the ICHAZ was caused by transformation to a softer phase and over tempering of the SCHAZ resulted in lower hardness compared with the base steel, which had a low tempering temperature.

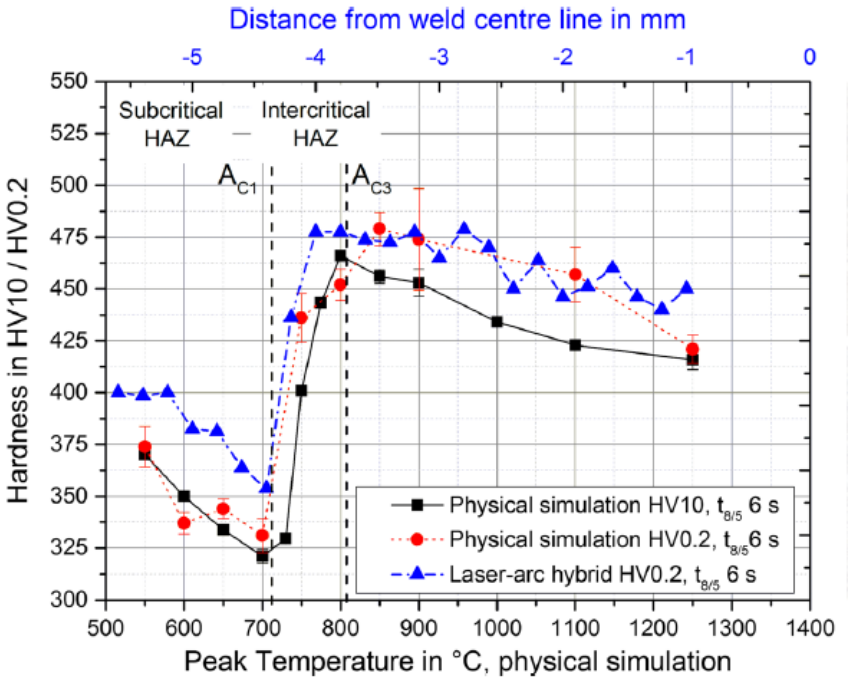

Figure 2-9: The variation of hardness with peak temperature in different HAZ with simulated and real welds [42].

2.2.5 Hydrogen Assisted cold cracking

Hydrogen assisted cold cracking (HACC), which is also known as cold cracking or delayed cracking, can be a significant mode of failure in the welding industry[5, 33, 50]. The main contributor for HACC has been identified as entrapped hydrogen within the weld material or surrounding area. This type of failure can occur after several hours, or even after several days, after welding.

HACC is considered as the most crucial failure risk in Q & T steel welding. To avoid or reduce HACC, the common practice is to introduce sufficient pre-heat temperature and carry out post-weld heat treatments. The preheating is necessary to reduce the cooling rate and give adequate time to diffuse hydrogen out of the joint. There are several methods to determine the preheat temperature to ensure avoidance of HACC (ISO/TR 17844) [51]. The use of pre-heat temperatures and maintaining inter-pass temperatures within welding procedures has the drawback of decreasing the welding efficiency [51].

In the current study, HACC was not investigated because the welding procedures used in this study were developed to minimise HACC.

2.2.6 Elemental segregation affected by thermal cycles

In welding, in some regions of the HAZ, the microstructure is completely or partially austenised at the peak of the thermal cycle. Elements have a solubility difference in ferrite and austenite, so when austenite begins to form, segregation of certain elements into the austenite can occur. In equilibrium cooling, most of the elements in a material can redistribute evenly minimising any segregation, because of the adequate time is given for diffusion of elements. However, due to the high cooling rate of welding, there is insufficient time for elements to diffuse upon cooling and elemental segregation is expected in HAZ. Elements with higher diffusivity have a higher probability to segregate than elements with low diffusivity. In steel, carbon is considered as one of the most diffusive elements. Therefore, carbon segregation can be visible in the regions where steel is partially austenised. The MA constituents in ICCG region can possess higher concentrations of highly diffusive elements. An atom probe study by Li [52], found both C and Mn had segregated to the MA constituent in the ICCG HAZ of high strength pipeline steel. As an example, it was reported that the carbon content in MA is almost independent from the carbon content in base metal because of higher solubility of carbon in austenite. However, the area fraction of MA increases with the increase of carbon content [53]. Higher carbon content was reported in austenite compared to the rest of the matrix as 0.6% carbon (which can be transformed into MA upon cooling) compared to the 0.02% in ferrite as shown in Figure 2-10.

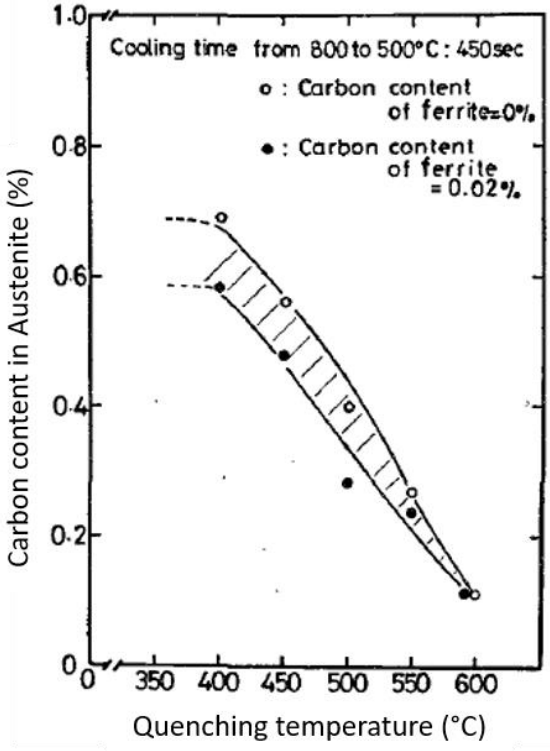

Figure 2-10: Percentages of carbon content of austenite and ferrite measured from different quenching temperature [54].

2.2.7 Simulated HAZ vs real weld HAZ

The HAZ generated in real welds consists of a relatively narrow zone with a wide range of final microstructures, due to the sharp temperature gradient (see Figure 2-2). Due to the narrow size of each sub-zone, it is difficult to isolate a particular zone for mechanical testing. Weld HAZ simulation is an effective method to study HAZ sub-zones in real welds, as a sample large enough to carry out mechanical testing (such as hardness and impact toughness) can be produced. The aim of weld simulations is to replicate the thermal cycle experienced by any sub-region of HAZ as closely as possible. When the thermal conditions for a real weld are correctly simulated, the resultant microstructure should be reasonably similar to that of the real weld. This has shown to be the case in this research and a few examples from the literature demonstrates that accurate representations of the welded microstructures can be simulated [42, 48]. In Figure 2-11, the simulated microstructures vs real weld microstructures of the CG HAZ and SC HAZ of a quenched and tempered high strength armour steel are shown to be comparable to each other [42].

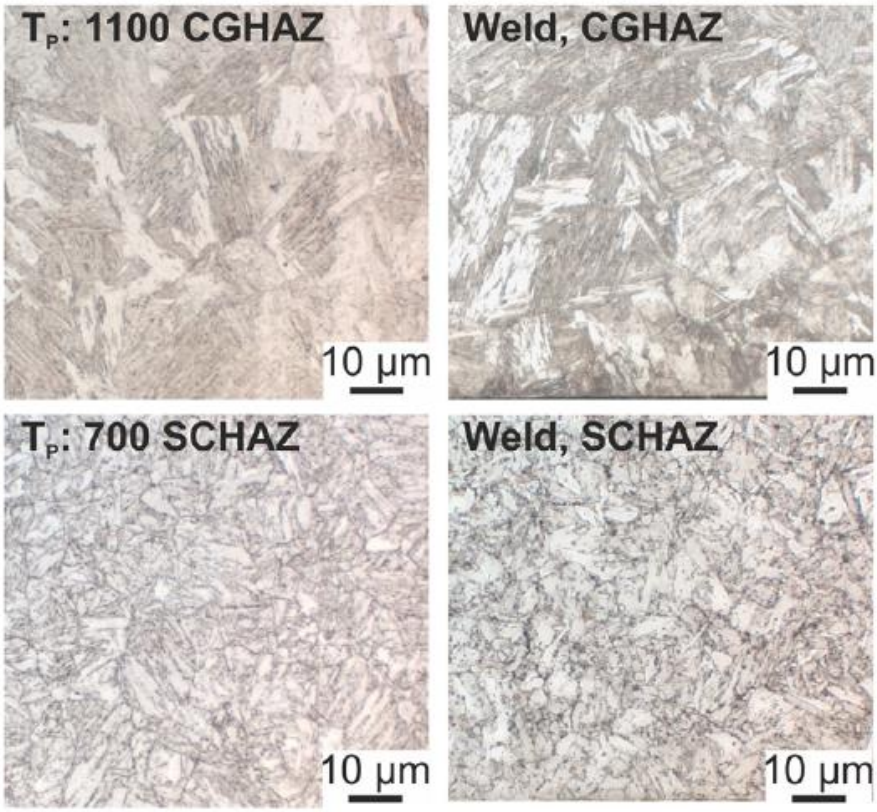

Figure 2-11: Comparison between simulated microstructure vs real weld microstructure of CG HAZ and SC HAZ of a quenched and tempered high strength armour steel. Microstructures were comparable to each other [42].

In Figure 2-12, the variation of grain size in CG HAZ for real and simulated specimens, as a function of peak temperature in GMAW steel plate of HSLA-100, is shown [48]. The simulated HAZ were designed with identical heat inputs to the real welds and closely match to the grain sizes for the CG HAZ was observed.

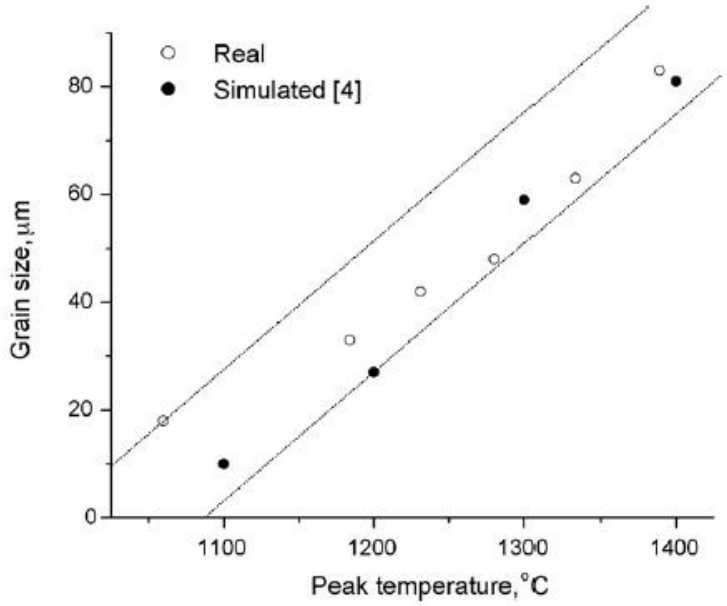

Figure 2-12: Variation of grain size in CG HAZ, for real and simulated specimens, as a function of peak temperature in GMAW steel plate of HSLA-100 [48].

2.2.8 Effects of multiple thermal cycles on microstructure

As discussed in Section 2.2, welding thermal cycles alter the microstructure in the base metal and result in heterogeneous microstructures due to the temperature gradient. When multiple repair welding is considered, complex thermal cycles at the same location may affect the final microstructures. In a study with X80 pipeline steel, in two-cycle CG thermal simulations (CG HAZ (1350°C) and double CG HAZ (1350-1350°C)), metallographic examination showed that there were no visible changes in microstructural features, as shown in Figure 2-13. However, the tensile strength was 5% (762 to 723 MPa) lower with the application of a second CG cycle [33]. This was due to minor grain growth with secondary reheating, as the grain size of the single CG was 30-50 μm, but the average was higher than 50μm for double CG sample.

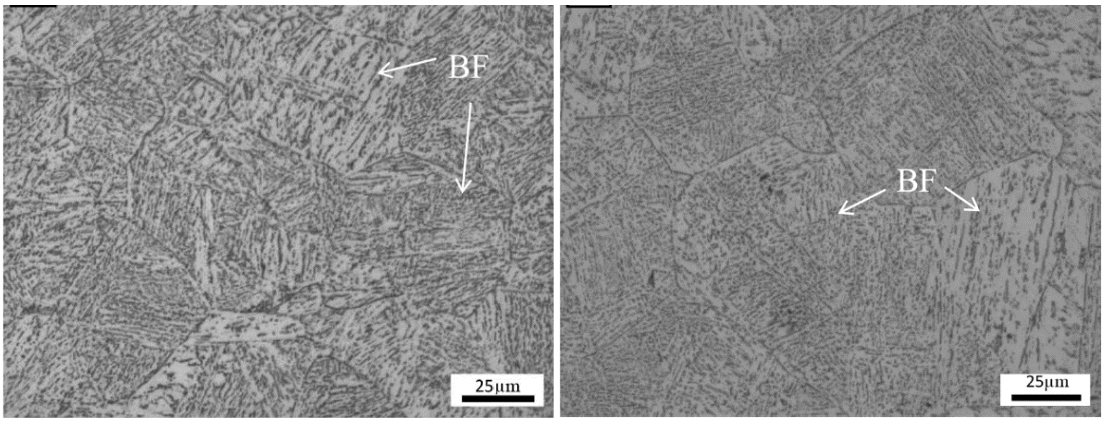

(a) 1350°C (b) 1350-1350°C

Figure 2-13: Microstructure of single cycle CG HAZ and double cycle CG HAZ. Microstructures consisted of lath bainitic ferrite (BF). With 4% nital etch [33].

2.3 Repair welding

Corrosion damage is one of the main factors that can affect the structural integrity of sea-going vessels and must be repaired [5]. Repair by welding involves removal of defective areas and replacement by depositing sound weld material with similar properties. Typically, the weld repair is conducted to an approved welding procedure, by qualified welders and followed by non-destructive inspections. Welding repair is a more economical approach in comparison with replacement, especially in a complex structure, where replacement is difficult, or even impossible. It is common that a repaired region may suffer corrosion damage again and it is preferable to carry out a second or third weld repair instead of hull section replacement due to economic viabilities and time restrictions. Repair welds involve multi-pass welds and in recurring repair welds, there is a possibility of the base plate experiencing multiple overlapping thermal cycles in combinations that are not possible in multi-pass welds. Therefore, an understanding of the effects of multiple repair welds on base plate properties is important.

A review of standards found that there is limited information regarding the number of times the same region can be repaired. AS/NZS 1554.1 and AS/NZS 1554.4 cover repairing of defects on welds which involve removing of defective weld metal and refilling the gap with filler material. The standard specifies that the weld repairs must be examined to ensure it is complying with the standard's requirements. However,

both these standards only address the repair of defective welds and these standards are not applicable for the application of BIS812 EMA steel. Also, there is no maximum number of recurring repairs specified [55, 56]. AS/NZS 3992:2015 specifies that repair welding can be carried out on the deteriorated region with acceptable weld procedure, but the specific details on the repair procedure and maximum allowed repairs were not mentioned [57]. A standard for structural and pressure vessel steel plates, AS/NZS 3597-2008, allows repair welding to be applied to rectify surface imperfections within strict parameters where the repair area should not be more than 2% of the plate surface and where no more than 20% of the thickness should be removed. Again, there is no information on recurring repair welding [58]. AS/NZS 2885.2 allowed repairs to repair welds with the approval from a welding engineer on a case-by-case basis (i.e. for the repair of an unacceptable weld). The standard states, if the base material is microalloyed or heat-treated, the effect from multiple heat cycles needs to be physically assessed [59].

The military standard, MIL-STD-1689, allows welding repair on high-strength shipbuilding steels [60]. This standard requires the length of such repairs not to exceed 6 inches and adjacent repairs within the same weld joint are required to be more than 3 feet apart. The later rule suggests that multiple repairs are not allowed, as repairs must be separated. The DNV standard on submarine pipeline system, Appendix C, Subsection G 300 specifies that only two repair welds in the same area are allowed [61].

According to the TWI [62], the allowed number of times a weld can be repaired depends on the type of material being welded and the welding process. Materials that are metallurgically sensitive to heat input are not recommended to be re-welded due to the increased risk of the degradation of HAZ properties. Materials such as mild, low carbon and carbon-manganese steels are considered to be very tolerant to heat input and may accept at least two or more welding repair operations. Vega, et al. [63] researched the effects of multi-welding repairs on high strength line pipe steels. A significant reduction in Charpy-V impact toughness was observed with an increased number of weld repairs; when the notch location was in the intersection of the fusion line with the specimen mid-thickness. A significant increase in the Vickers hardness

was observed in the heat affected zone after the first repair and a gradual decrease in the Vickers hardness occurred as the number of repairs increased [63].

2.3.1 Repairing of corrosion damage

The loss of thickness of steel plates due to corrosion damage can be rectified by pad repair welds. Pad welds are overlapping weld beads usually with short weld lengths that cover a small region of a plate or structure. Welding procedures are similar to ordinary butt weld joints [5], but due to the shorter length of weld runs and the alignment of weld start-stops, there is a greater risk of altering the microstructural features and residual stress fields [5, 6]. Pad weld repair dimensions are typically 10-30% of the plate thickness and 50-200 mm in diameter [5]. The repair welding procedure should be designed to avoid introducing any adverse effect on parent material properties and overall structural integrity [5].

The recurring pad weld repair adds increased complexity to the microstructure and residual stresses because the HAZ of second repair weld overlaps the pre-existing HAZ of the first repair, as illustrated in Figure 2-14.

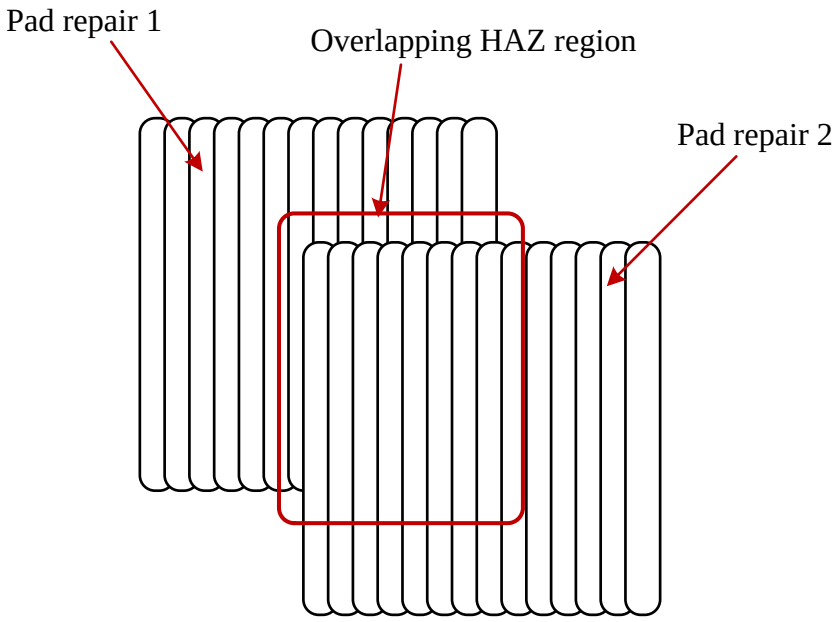

Figure 2-14: Overlapping HAZ of pad weld repairs. Adopted from Sterjovski [5].

2.3.2 Repairing of butt weld joints

Repair welding of butt weld joints is typically understood as a repair to rectify weld defects, such as porosity, lack of fusion, insufficient crown height or undercut, rather than examining the effects of overlapping multiple HAZ's on base plate properties. Consequently, there is limited research carried out on the effect of multiple repair welding on the existing HAZ on the base material, even though the HAZ of repair weld will usually overlap with the pre-existing HAZ. Samardzic and Siewert [6] suggested that in high strength steels, the failure rate due to stress corrosion cracking may be higher in repair welds than original fabrication weld; hence the welding process should be controlled carefully.

2.3.3 Effects of repair welds on residual stress

Residual stresses in repair welding is a major factor to be considered because repair welds can introduce completely different residual stresses (including amplitude and distribution) to the component than initial weld due to high restraint conditions [64, 65]. Therefore, it is recommended that the weld repair procedures should be carefully controlled as the residual stresses generated may affect the structural integrity of the component [64, 66]. Dong [64] stated that elevated stress levels in repair welds could increase the fracture driving force significantly by increasing the stress intensity factor (K). The type of repair weld can range from shallow localised repairs to deep excavations that can be a significant portion of the structure; hence the residual stresses can vary markedly [67]. To minimise the effect of residual stresses due to repair welds, the preferred repair weld geometry should be longer, shallower and narrower weld runs [64].

The residual stresses from the repair of pipeline girth welds were investigated by Bouchard, et al. [67] who state that the axial stresses in the HAZ at the mid-length of the longer repair are less than the stresses for the shorter repair.

In repair welding of butt weld joints (X52 pipeline steel, 13 mm thick), high tensile residual stresses occurred for the original weld, single repair and double repair welds, at the fusion line, which were close to the yield stress of the material, as shown in Figure 2-15. However, the different repair welds all showed higher tensile residual stresses further away from the weld centre line.

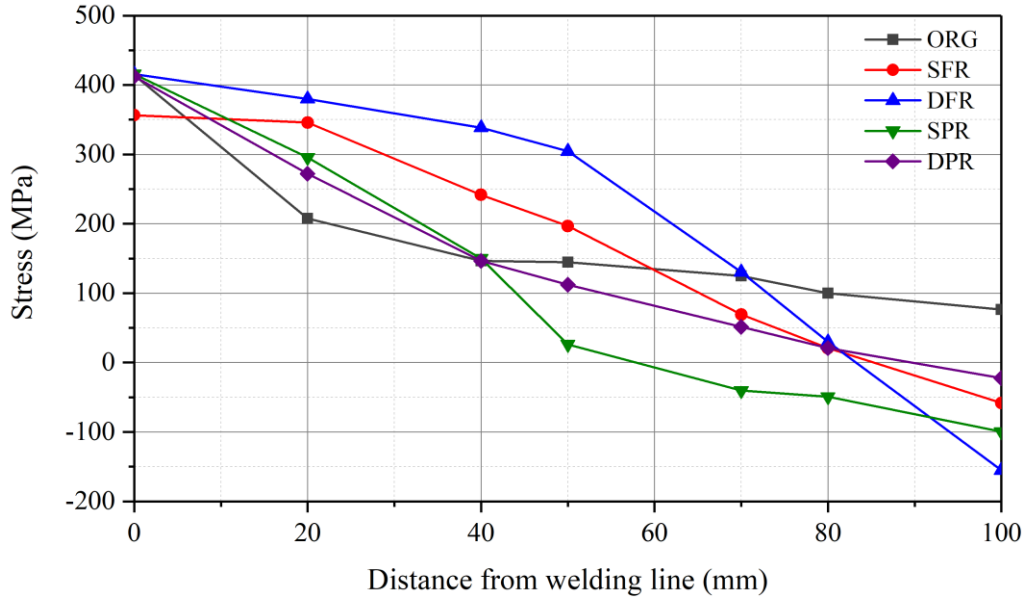

Figure 2-15: Residual stress distribution of original and repair welds of butt welds. (Org-original weld, SFR-single full repair, DFR-double full repair, SPR-single partial repair, DPR-double partial repair) [68].

2.4 Toughness and Fracture mechanics of HAZ

The toughness is identified as the material's ability to absorb energy by plastic deformation. The combination of high strength and high toughness of steel can be at risk due to repetitive weld thermal cycles that decrease toughness in the heat affected zone (HAZ) [9, 22, 23]. The coarse grain heat affected zone (CG HAZ) and intercritically reheated coarse grain zone (ICCG HAZ) can have significantly reduced toughness, so these subzones are referred to as 'local brittle zones' (LBZ) [26, 69-79]. In some cases, the formation of upper bainite and Widmanstätten ferrite also contributes to deleterious impact toughness [23, 71, 77, 78]. The following examples highlight the substantial decrease in toughness observed in the above-mentioned zones.

The variation of toughness of different sub-zones of the HAZ is shown in Figure 2-16 for a Q&T steel with weld simulation (0.07C, 0.15Si, 1.55Mn and with microalloying elements (Ti and Nb), C_{eq}=0.41) [80]. The lowest toughness was in the IRCG HAZ (commonly referred to as ICCG HAZ) and SRCG HAZ due to formation

of MA. Another method to show the variation in the toughness of sub-zones of a HAZ is by Charpy transition curves. The ductile to brittle transition temperature (DBTT) varied significantly between the different zones in HAZ for a thermo-mechanically controlled processed (TMCP), HSLA Steel (0.07%C, 1.5%Mn, 0.12%Mo, 0.47%Ni, 0.16%Cu and 0.014%Nb), as shown in Figure 2-17 [81]. The DBTT curve shifted to the right from as-received to CG HAZ to ICCG HAZ. The slow cooling rate of CG HAZ lowered the toughness due to microstructure transformation into upper bainite instead of martensite.

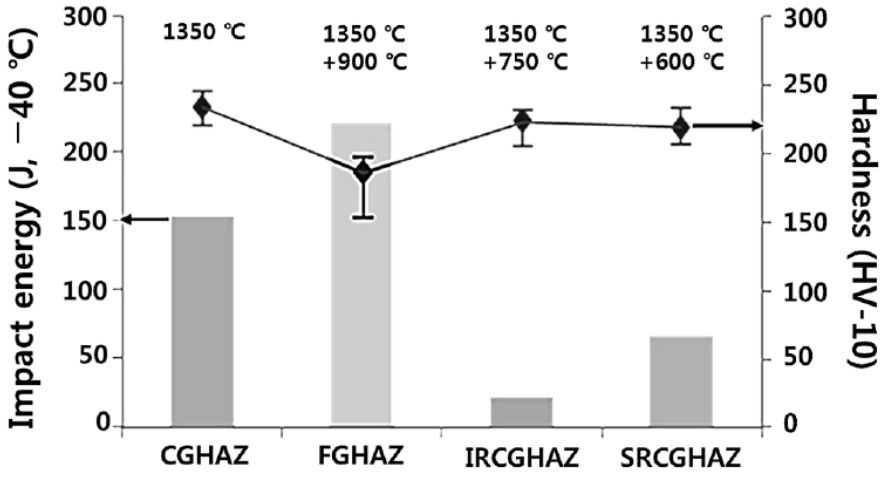

Figure 2-16: Changes in toughness with different sub-HAZ for a low carbon, Q & T steel. (HAZ consisted of AF, GB, and GBF) [80].

The ICCG region showed the worst performance in low temperature toughness compared to the base material as shown in Figure 2-17 where DBTT was pushed towards room temperature [81].

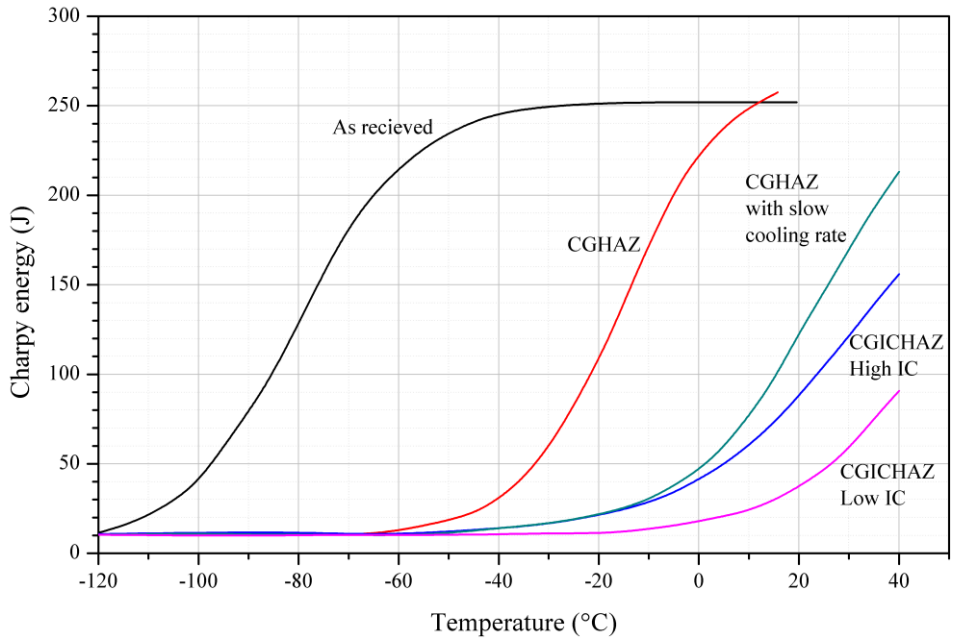

Figure 2-17: Transition curves TMCP steel with 0.07% C, received, CGHAZ at 1250°C, ICCG at higher IC, CGHAZ at a slower cooling rate, and ICCG at lower IC. Adopted from [81].

Similar to the results of the above study, Kumar, et al. [26] showed there was a degradation of toughness with higher temperatures with single thermal cycles where 1300°C showed the lowest toughness, as shown in Figure 2-18. With the application of a second thermal cycle, toughness was slightly improved but the lowest toughness with a second thermal cycle was observed with a low IC temperature. Due to the low toughness that is typically observed in the CG HAZ and ICCG HAZ, a significant body of research has been conducted examining the factors affecting the toughness of these two regions. Fracture mechanisms in these two regions play an impotent role in the toughness.

2.4.1 Fracture Mechanisms

Failure of a component can occur in many ways, however, failure due to brittle fracture is considered as the most critical scenario. In metals, brittle fracture typically occurs via the cleavage fracture mechanism [82, 83]. Fracture can be divided into two categories, ductile and brittle. Ductile fracture shows extensive plastic deformation before fracture takes place, while for brittle fracture, there is little-to-no

plastic deformation prior to fracture. In crystalline materials, brittle fracture can occur by cleavage. Failure by cleavage fracture can be divided into three stages. In the first stage, micro-cracks initiate at particles or inclusions in the solid body (crack nucleation). The second stage is cleavage crack propagation into adjacent grains along cleavage planes. The third stage is the unstable fracture propagation into neighbouring grains, leading to failure [84].

The basic equation of fracture mechanics is [85],

$$K = \sigma\sqrt{\pi a} \quad (5)$$

Where, *K* is the stress intensity that describes the stress field around the crack (stress intensity factor), 'a' is the half-length of the crack and 'σ' is total stress at the defect. To prevent unstable crack propagation, the stress intensity factor *K* should be less than the fracture toughness, K_{Ic}. From Equation 5, K will increase with increasing applied load and increasing crack length. The fracture toughness depends on the material, temperature and the loading rate [86]. Considering the fracture of weld HAZ, the half crack length, 'a' of the equation can be taken as half-length of MA particles or inclusions [86]; assuming that the particle cracks under the applied load (as fracture initiation sites), than larger particles are more detrimental to fracture toughness.

2.4.2 Toughness of the CG HAZ and ICCG HAZ

The low toughness of the CG HAZ is mainly due to the transformation of low toughness microstructures, such as martensite or coarse grained bainite, from the large prior austenite grains. In section 2.2.3, it was already established that large grain size is strongly related to poor toughness. However, the morphology of the microstructure also influences the toughness. The formation of upper bainite and Widmanstätten ferrite can contribute to deleterious impact toughness of the CG HAZ [23, 71, 77, 78]. Research carried out by Kumar, et al. [26] showed that fracture properties changed from ductile to brittle and impact energy decreased with peak temperature increased from 600 to 1300ºC in single thermal cycle (see Figure 2-18). This observation was mainly due to increased grain growth with increasing peak temperature. Brittle fracture was observed for the 1300ºC specimen, due to the formation of very coarse acicular bainite and martensite microstructure. When

CGHAZ (1300ºC) was reheated to between 1100ºC to 900ºC, toughness improved significantly at the highest reheat temperature, due to the significant refinement of the microstructure, while at 800ºC, (intercritical reheat) toughness decreased due to formation of MA. At the sub-critical reheat temperature of 700°C, there was no transformation, so the coarse grain size remained and the tempering of the on microstructure led to a slight improvement of toughness [26].

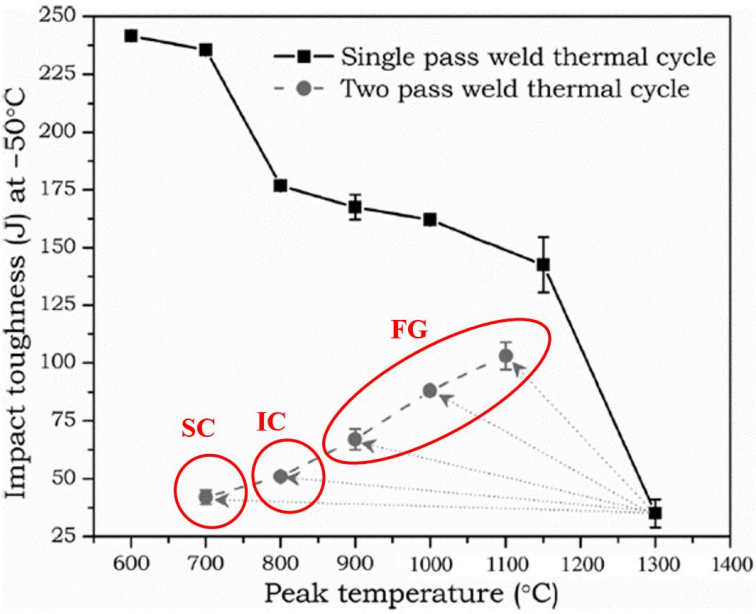

Figure 2-18: Variation of impact toughness with peak temperature [26]

The toughness of the CG-IC region is controlled by both the large grain size and martensite-austenite constituents [23]. Martensite-Austenite typically consists of high carbon martensite with some retained austenite and the characteristic of MA constituents will be reviewed in more detail in the following sections. When the CG HAZ is reheated into the two-phase region, MA constituents can form at the prior austenite grain boundaries, particularly when the reheat temperature is just above A_{c1}, as shown in Figure 2-19. As proposed by many researchers, the main reason for the significant loss of the toughness of ICCG HAZ is due to the formation of MA constituents along the PAGB [22, 28, 77, 87]. The neckless-like MA constituent develops because austenite re-nucleates, during reheating to peak temperatures between the A_{c1} and A_{c3}, and then grows along large prior austenite grain boundaries. Austenite islands created along prior austenite grain boundaries are enriched with carbon, due to the high diffusivity of carbon and high solubility of carbon in

austenite, which can transform into martensite-austenite (MA) constituents during cooling [23, 34, 77, 88, 89].

A study conducted by Zeng, et al. [90] on X70 pipeline steel showed that the low temperature toughness depended on effective grain size and other microstructural features, such as MA constituents and precipitates. The ICCG HAZ which is called as MA typically consists of high carbon martensite with some retained austenite and typically appear along the grain boundaries [34, 81, 88], as shown in Figure 2-19.

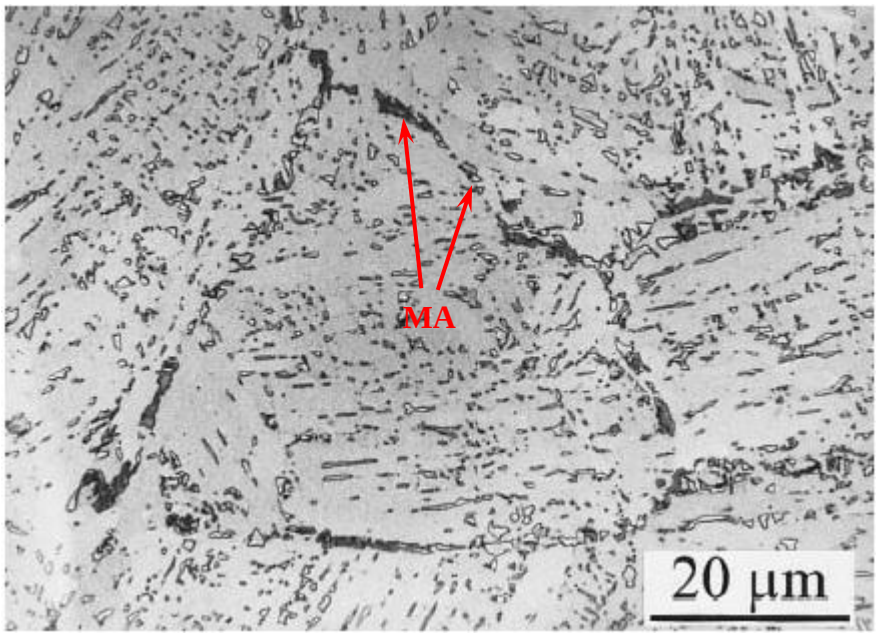

Figure 2-19: MA islands formed along PAG boundaries in ICCG HAZ with original CG HAZ with bainitic microstructure [81].

Research by Bayraktar and Kaplan [53], showed that the area fraction of MA constituent, formed due to reheating of the CG HAZ, peaked at a temperature 15-20°C above the A_{C1}, then rapidly declined, as shown in Figure 2-20. The application of a third thermal cycle, which was less than the A_{C1} temperature, decreased the hardness and area fraction of MA due to the decomposition of the MA into ferrite and carbide products.

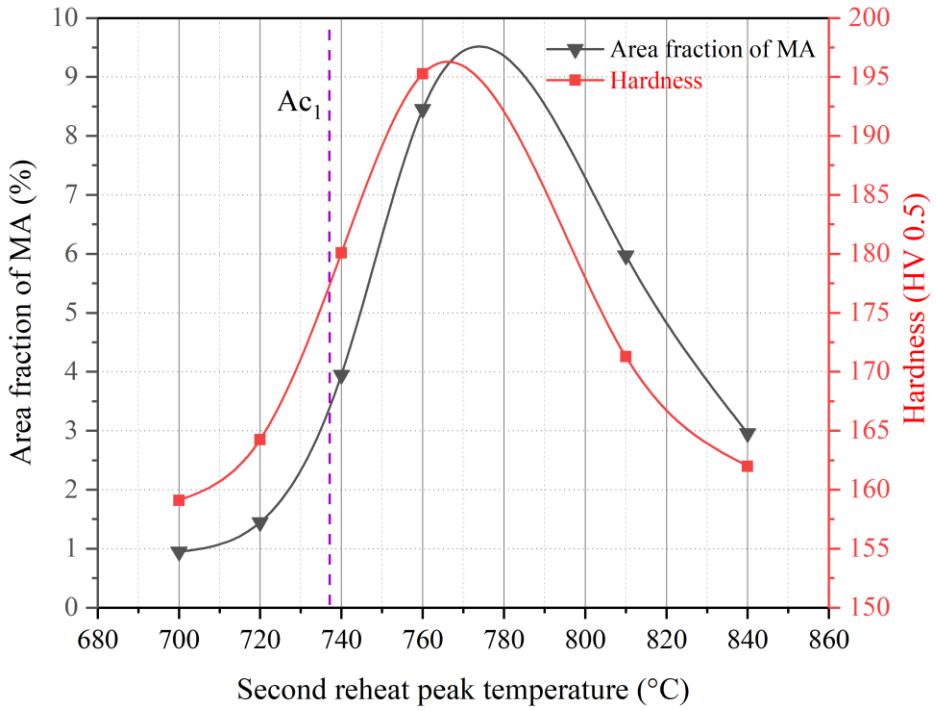

Figure 2-20: The effects of the application of a second reheat cycle to the CGHAZ on the MA constituent and hardness [53].

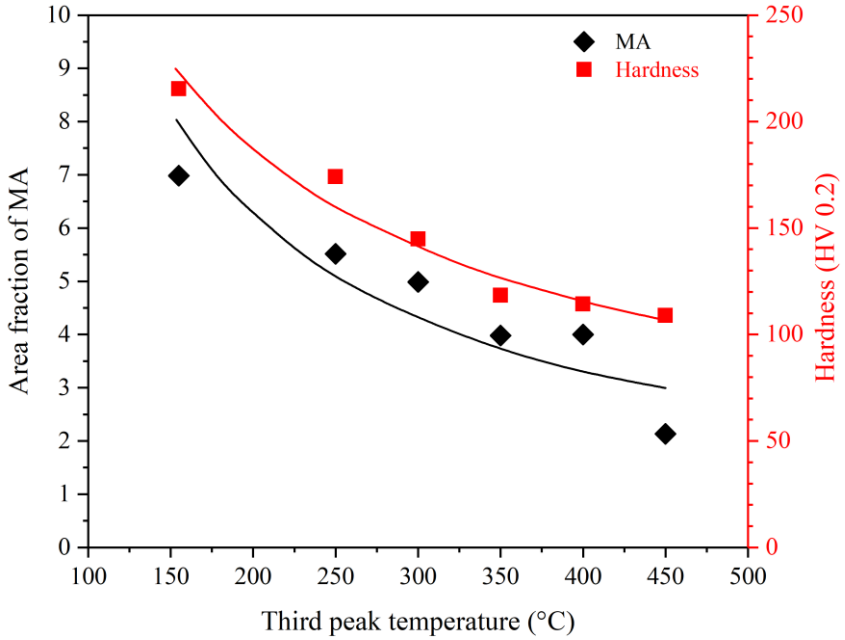

Figure 2-21: Effect of MA with third cycle temperature (1350-750-300°C) [53]. (0.082C, 0.53Mn, 0.31Si, and Nb, Ti, V steel).

2.4.2.1 Variation of toughness with multiple thermal cycles

The effect of multiple repeated thermal cycles on high strength Q & T steels has not been comprehensively studied, but some recent work has been conducted on HSLA steels. In a study with HSLA-100 steel, Duch and Dupont [91] concluded that multiple applications of CG thermal cycles (up to 3 cycles at 1300°C) did not affect toughness, but toughness decreased with multiple IC cycles (at 750°C). In multiple CG thermal cycles, the last thermal cycle will replace the existing microstructures, so it can be expected that toughness of multiple CG cycles will be similar to the single cycle, as a similar microstructure can be expected. However, the reason for the decrease of toughness with multiple IC cycles was not clear in the above research.

Simulated samples with triple thermal cycles showed improved toughness after application of SC thermal cycle on ICCG sample [53]. The increase of toughness was mainly due to a decrease of MA constituent by the dissolution of small particles.

2.4.2.2 Effect of PAG size

It has been well established that low temperature toughness has a strong dependency on PAG size. The low fracture toughness in LBZs (CGHAZ and ICGCHAZ) was largely attributed to large PAG sizes, as reported by several researchers [22, 26, 81, 87]. Li et al. [92] investigated the effect of PAG size on ICGCHAZ, where the initial peak temperatures were 1100, 1200 and 1300ºC followed by a second peak temperature at 760ºC (low intercritical temperature), resulting in PAG sizes of 17, 27 and 68μm and average Charpy energy values of 191, 59 and 43 J, respectively. The low toughness of the intercritically reheated HAZ was substantially improved by decreasing the PAG size.

Research by Bialobrzeska [93] found a significant decrease in impact energy with increasing PAG size and packet size for Hardox 450 steel, as shown in Figure 2-22. Takebayashi et al. investigated the effects of PAG size on toughness for high carbon (C%) martensitic steel [94]. As shown in Figure 2-23, when the PAG size was refined, both the upper-self energy and DBTT were improved. Takebayashi et al. [94] separated the total absorbed energy into the fracture initiation energy and

propagation energy, as shown in Figure 2-24. The fracture initiation energies increased slightly for the smaller PAG size, but a large difference in fracture propagation energies was recorded. Toughness improved due to the increase in grain boundary area, which provided effective obstacles for fracture propagation, leading to increased plastic deformation and toughness.

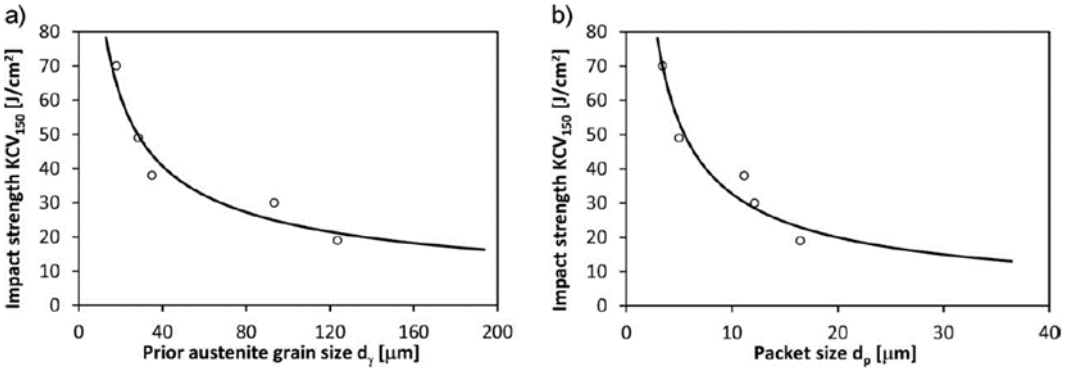

Figure 2-22: The effect of PAG size and martensite packet size on the impact strength of Hardox 450 steel. (tested at -40°C) [93].

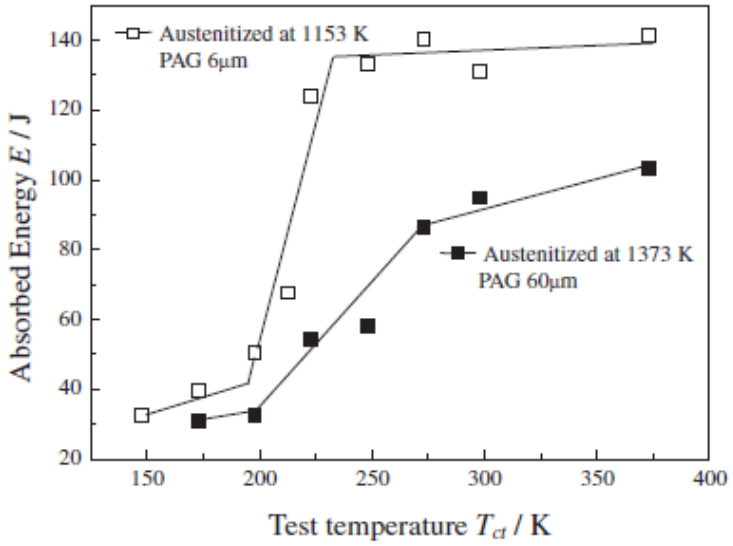

Figure 2-23: The variation of upper shelf Charpy energy and ductile to brittle transition temperature with two different PAG sizes [94].

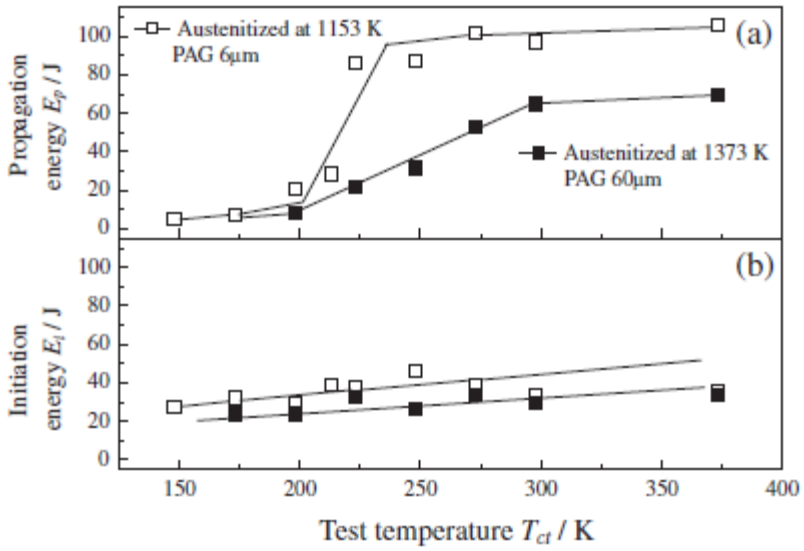

Figure 2-24: Variation of fracture initiation and propagation energies with temperature for two different PAG sizes. Both samples were tempered at 500°C [94].

2.4.2.3 Effect of MA constituent on HAZ toughness

It has been established that the formation of MA constituents with the HAZ is detrimental to toughness [87, 95]. This section of the literature review is focused on research into the impact of MA constituents on HAZ toughness. As there are a variety of steel types, welding processes (which affects heating and cooling rates) and different peak inter-critical temperatures, MA constituents will vary in morphology, size, volume fraction, location (i.e. along PAG boundaries or in-between laths) and chemistry (such as carbon content) [10, 22, 28, 30, 70, 72, 73, 75, 77, 87, 88, 92, 95-99]. All these above mentioned factors will influence the sensitivity of toughness to the presence of MA constituents and need to be reviewed.

There are two main mechanisms proposed in the literature for the reason why MA constituents cause a reduction in toughness; in the first mechanism, it is proposed the harder MA constituent fractures in a brittle manner under the applied stress and this micro-crack then propagates into the matrix [26, 28, 32, 87, 95]. The second mechanism proposed that a micro-crack is formed due to de-bonding of the MA constituent with the matrix (interfacial de-cohesion), as high stress concentrations are anticipated at this interface [28, 70, 76, 77, 95, 100]. In the first mechanism, the size of the MA constituents was important [28, 87, 101], where coarser particles were

related to lower toughness. This was previously explained using Griffith crack theory [73, 96], where the critical stress value required to propagate fracture will decrease as the crack size (cracked MA constituent) increases. When the critical stress value is below the applied stress, then the existing micro-crack will propagate, leading to failure. In the second mechanism, researchers [28, 70, 76, 77, 95, 102] have observed MA constituent at the fracture initiation sites for cleavage de-cohesion. An example of de-cohesion of MA particles with fracture propagation is shown in Figure 2-25.

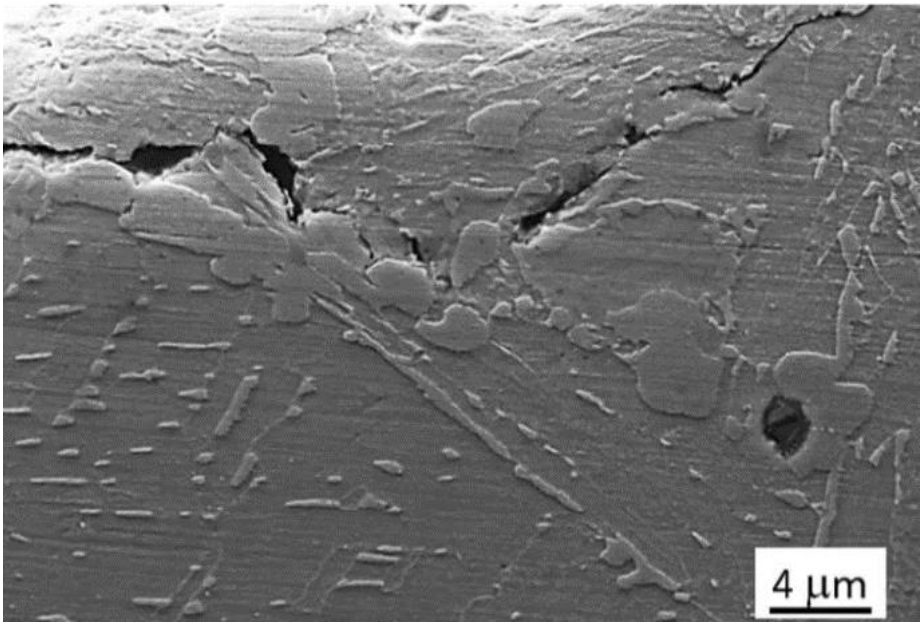

Figure 2-25: Evidence of de-cohesion where secondary fracture followed the boundary between MA and bainitic matrix [103].

As previously discussed, several researchers found evidence that MA particles act as fracture initiation sites. An example of fracture initiation at MA particle is shown in Figure 2-26 [81], where the arrow shows the particle at which fracture was initiated.

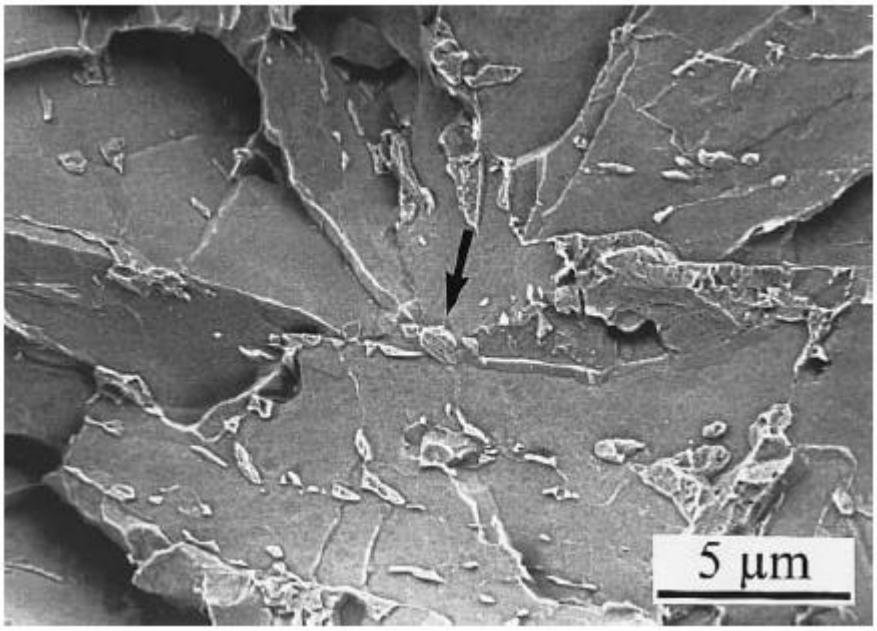

Figure 2-26: An evidence of MA island originated the cleavage fracture [81]

In the above two mechanisms, MA size was shown to be a critical parameter, so this will be reviewed in more detail. Moeinifar studied the impact toughness of weldments (TSAW) in X80 line-pipe steel and found that a CGHAZ reheated to mid-inter-critical temperature of 800°C had the lowest impact toughness compared to subcritical (700°C) and supercritical (900°) reheating temperatures, due to the formation of blocky MA constituents [83]. The size of MA strongly influenced toughness as MA facilitates early void formation [95]. This observation was backed up with the research on HT80 steel by Chen, et al. [87], who found the controlling factor for cleavage fracture in CGHAZ was the size of MA constituent, where the larger MA size (7 μm verse 3 μm), lowered the crack nucleation energy. Chen also conducted room temperature impact tests, where high toughness was observed. Large strain led to deformation of the ferrite matrix and fracture occurred (via debonding) at the interface of the soft ferrite grains and hard M-A constituents. Lan, et al. [100] found that MA constituents larger than 3μm contributed to the initiation of micro cracking, which substantially reduced toughness in ICCG HAZ of low-carbon bainitic steels. Jia, et al. [96] reported that upper shelf Charpy impact energy decreased with increasing MA size in high strength microalloyed steel. The above-mentioned study was conducted on steel with thermomechanical processing, but not the application of weld thermal cycles. While the presence of MA was due to the

thermal processing, the toughness behaviour was similar to the effect of MA found in HAZ regions (i.e. acted as crack initiators).

The size of the MA constituents is not the only factor affecting toughness, volume fraction, morphology and location also play an important role. In research with a range of micro and macro alloyed steels, it was noted by Bayraktar and Kaplan [53] that area fraction of MA (mainly related to massive, or blocky MA) and the impact toughness has an inverse relationship, where toughness decreased as MA percentage increased. In [31], a similar relationship in X70 steels was shown, where toughness decrease with an increased volume fraction of MA, as shown in Figure 2-27. Di's research also found that the location of MA constituents was important, as the lowest toughness was observed when MA constituents formed the necklace like structure along the PAGB. Zhu et. al. [10] report that higher volume fractions of MA particles formed along the prior austenite grain boundaries (also location related), were unfavourable for toughness in the ICCG HAZ of X70 line-pipe steel weldments. Davis and King [70] concluded that the HAZ impact toughness of HSLA steels was not always compromised by the presence of MA constituents. It was proposed that debonding at isolated MA particles was insufficient to cause failure [26]. Consequently, they proposed that a connected grain boundary network of MA was required to achieve very low toughness, the so-called "neck-lace" morphology.

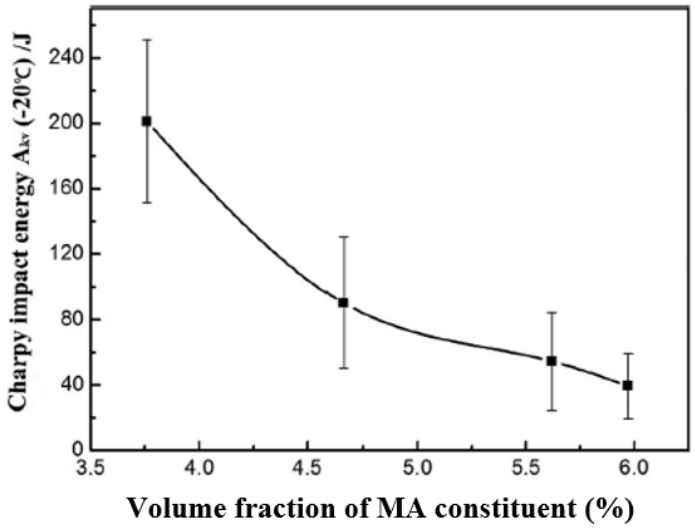

Figure 2-27: Variation of Charpy impact energy with the volume fraction of MA in X70 pipeline steel HAZ. Tested at -20°C [31]

There are several morphologies of MA such as massive or blocky slender (lath-like) and small round, or granular, particles. Cleavage cracking behaviour is sensitive to these morphologies of MA [28, 104]. The adverse effects of small granular MA on toughness was found to be less compared to larger nubby (coarse lump-like) MA [90] on research on X70 and X80 pipeline steel with drop-weight tear test (DWTT). The above research also found that the lath-like MA deteriorates toughness more than the smaller granular MA. The slender MA fractured more easily than massive MA in steel welds [31], while blocky MA could promote fracture initiation and propagation via decohesion. Li and Baker [95] investigated the influence of the morphology of MA constituents on cleavage fracture and found that elongated MA constituents were more likely to de-bond from the matrix, whereas 'blocky' constituents were more likely to embrittle and propagate cleavage fracture.

As already discussed, it has been established that toughness of the ICCG HAZ is typically the lowest when the reheating temperature was just above the A_{c1}. Therefore, a range of toughness occurs within the intercritically reheated zone. In research by Li [89], found a significant improvement in toughness with increasing intercritical temperature for X100 Pipeline steel. However, research by Zhu, et al. [10] on X70 pipeline steels, found only a small improvement in toughness with

increasing IC temperatures. Both found small MA constituents scattered in the microstructure at the higher intercritical temperature (Li 1.9 µm, Zhu <0.1 µm), but the matrix microstructures were different, where the X100 steel had a refined ferrite, acicular ferrite and bainite microstructure and the X70 steel had a coarser bainitic ferrite microstructure. It appears that X100 steel had a tougher matrix microstructure and hence, improved toughness. Li [88], reviewed why the toughness improved with increasing intercritical reheating temperature and found; 1) at low IC temperature, coarse MA formed a necklace-like structure along PAGB's, 2) at intermediate IC temperature, coarse MA was still present but now had larger interspacing and 3) at high IC temperature, MA size was small and a tougher, refined matrix stabilized the toughness.

Research on low carbon bainitic steels by Kumar [26], found that the ICCG HAZ subjected to a mid-intercritical reheat temperature had improved toughness compared to the CG HAZ (1300°C peak temperature). This was attributed to a refinement of the final grain size of the regions that cycled through the austenite transformation. Kumar did not investigate the influence of lower initial peak temperatures on the toughness of the ICHAZ.

In a previous study with HSLA-100 steel, Duch and Dupont [91] reported that toughness of ICCG (at lower IC) was almost similar to the toughness of CG but hardness was considerably higher. Similarly, TMCP steel showed a significant reduction in toughness by 83% (150 J to 25 J) when CG followed by an IC cycle. The reduction of toughness was found to be attributed to the presence of acicular ferrite (AF) and bainitic ferrite (BF) and MA in the microstructure of ICCG compared to AF and BF in CG [80].

2.4.2.4 Factors affecting the formation of MA constituents

In a review by Matsuda, the carbon content of MA was found to be relatively independent of the average carbon concentration of the steel, but volume fraction of MA increased with increasing carbon content of the steel [105]. This indicates that the hardness ratio between MA and matrix can be higher in steels with lower carbon concentration, potentially leading to lower toughness due to a greater mismatch

between the hardness of the matrix and MA particle. Bhadeshia argued that during the final period of transformation (of ferritic or bainitic phases), the residual austenite can be high in carbon and transform into an MA constituent and the hardness of the MA phase would be expected to decrease if a larger volume fraction of MA formed [34]. The carbon content of MA was found to change with the cooling rate, where the carbon concentration decreased with slower faster cooling rates, as shown in Table 2-2 [54]. A higher carbon percentage in MA is expected to contribute to the brittleness of the MA constituents, which promotes the formation of micro-cracks due to particle cracking.

Table 2-2: Carbon concentration of MA for the samples quenched from 400°C. Carbon percentage in ferrite was 0.02% [54].

Cooling time Δt (s)	**Carbon in MA constituent (%wt)**
85	0.73-0.87
170	0.57-0.65
450	0.58-0.69
870	0.49-0.53

The formation of MA found to be influenced by the alloying elements present in the base material. The elements such as Si, Al, Cr, Mo, Nb and V along with C are the most effective in changing MA formation and properties [53]. Among them, Si and Al were found to increase the amount of MA the most [53]. Silicon was also found to segregate to the MA due to the lower solubility of Si in BCC steel. The evidence of carbon and silicon segregation in MA is shown in Figure 2-28 [80].

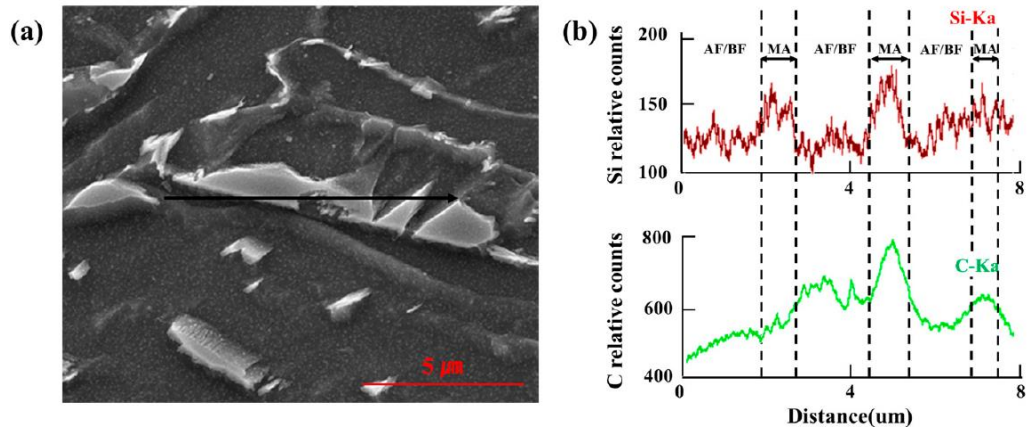

Figure 2-28: Carbon and Silicon segregation on MA particle (500 MPa structural steel). (a) MA particle in the matrix and (b) Carbon and silicon concentration along the black line in 'a' [80].

It was found that the volume percentage of MA exhibit a relationship with carbon percentage of the steel. Figure 2-29 shows the measured MA percentages of similar steels with different carbon contents. As a general trend, it was noted that a high percentage of MA was produced when the carbon level of the grade was higher. Therefore, it is possible to predict the carbon percentage of MA based on the carbon percentage of base metal for a given heat treatment condition. Bayraktar and Kaplan [53] proposed a formula for maximum MA percentage in ICCG with 760°C IC reheating, based on the chemistry range of the steels they studied, as given in Equation 6. The volume fraction of MA was found to be a function of carbon, Mn and Nb content.

$$MA_{max} = 86 \times \%C + 5 \times \%Mn + 134 \times \%Nb - 10 \quad (6)$$

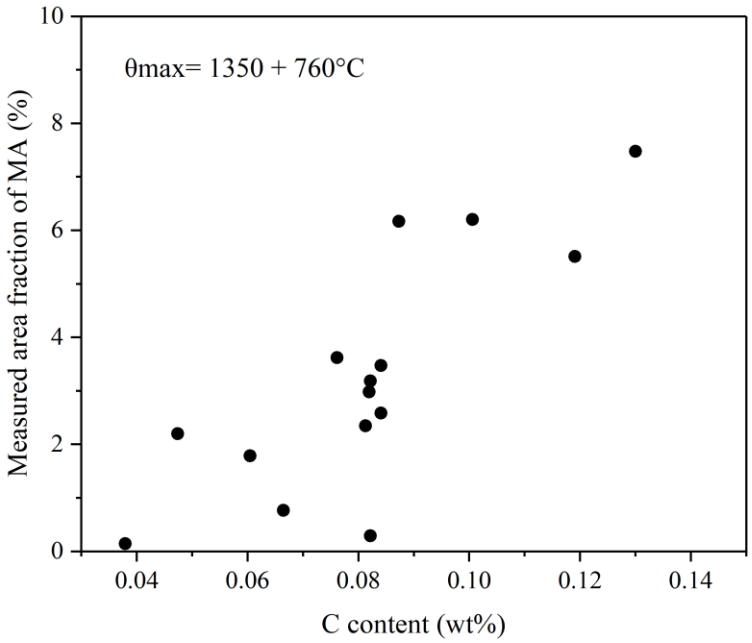

Figure 2-29: Effect of carbon content on MA constituent (For steels with different carbon content) [53].

2.4.2.5 Other microstructural features affecting the toughness

In the previous sections, the toughness of the HAZ was reviewed. However, other factors that can influence the toughness of steel, other than what was discussed above. Numerous studies have shown that the effective grain size is the main microstructural feature that controls the low temperature toughness [92, 106, 107]. Wang, et al. [108] reported that the fraction of high angle grain boundaries (HAGB) had a strong correlation to low temperature toughness for TMCP pipeline steels, so argued that the fraction of HAGB's should be considered, rather than just the effective grain size. It has been shown that cleavage fracture direction changes when the fracture front meets a HAGB's, thus smaller effective grain size provide high resistance to fracture propagation [90, 109, 110]. Typically, divisions of crystallographic domains, which are greater than 15°, is used to define HABG's and to calculate effective grain size [90, 109].

Grain boundary distribution of an ultra-heavy (in regards to thickness), high strength steel, is shown in Figure 2-30 and shows a general distribution of high and low angle boundaries. The toughness of steel has a close relationship with HAGB so that the distribution of high and low angle boundaries is important for mechanical properties.

Grain boundaries in white show lath boundaries, PAG boundaries in black and packet and block boundaries in yellow.

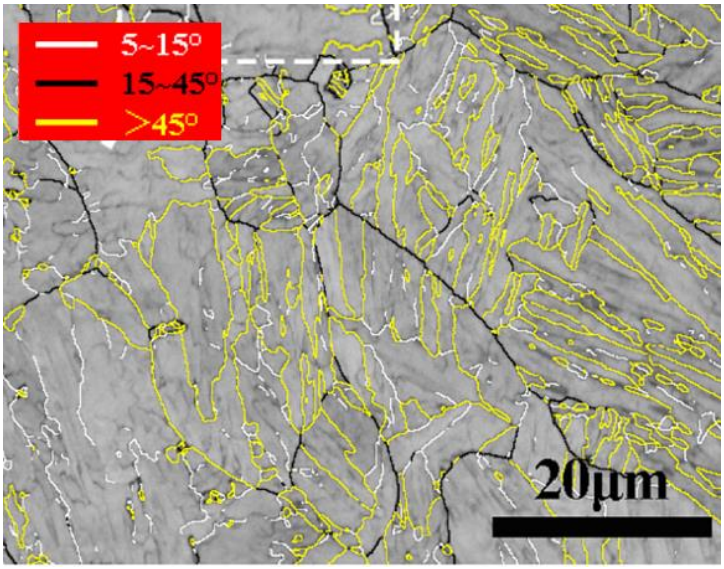

Figure 2-30: Grain boundary distribution of ultra-heavy plate of high strength steel [111]

Zeng, et al. [90], who studied X70 pipeline steel showed that low temperature fracture toughness does not always depend on HAGBs, but also on other microstructural features like MA particles and precipitates. Therefore, relying on effective grain size to determine low temperature toughness was not sufficient and the combined effects of microstructural features with effective grain size must be considered. In X80 steel, the densities of high angle grain boundaries (<15°) were higher in sample reheated to subcritical temperature (35.8%) compared to CGIC at mid IC (23.2%) and single CG (17.8%) [33]. Higher densities of high angle grain boundaries generally showed higher toughness.

Lath martensite formed in low carbon steels exhibits a microstructural hierarchy, comprising of PAGs, packets, blocks and laths, in descending order of size [112, 113]. PAG of lath martensite can consist of several packets with approximately $\{111\}_{\gamma}$ habit plane. A packet contains strip-shaped blocks run parallel to each other and a block contains laths with similar crystallographic orientation [114, 115].

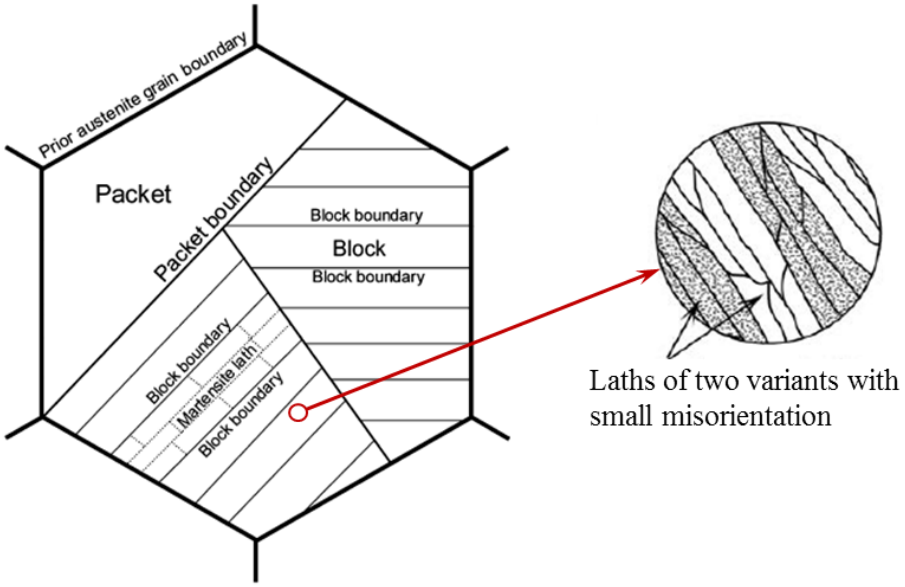

Figure 2-31: Microstructural hierarchy of lath martensite [113, 115].

The substructure of martensite depends on the carbon content of the base material. In low carbon steels (0-0.4% C), the neighbouring laths in a block were found to be in two different variants, with small misorientation between each other [113], as shown in the inset of Figure 2-31.

Martensite or ferrite holds specific orientation relationships (OR) in transformation with respect to its parent austenite. Understanding this relationship between austenite and martensite has great importance, as it can assist in explaining material behaviour. There are five different OR found in steel, which are shown in Table 2-3.

Table 2-3: Orientation relationship in steel

Orientation relationship	**Parallelism**
Pitsch (P)	$\{100\}_{\gamma}//\{011\}_{\alpha}$, $<011>_{\gamma}//<111>_{\alpha}$
Nishiyama-Wasserman (N-W)	$\{111\}_{\gamma}//\{110\}_{\alpha}$, $<112>_{\gamma}//<110>_{\alpha}$
Kurdjumov-Sachs (K-S),	$\{111\}_{\gamma}//\{011\}_{\alpha}$, $<110>_{\gamma}//<111>_{\alpha}$
Greninger-Troiano (G-T)	$\{111\}_{\gamma}//\{110\}_{\alpha}$, $<123>_{\gamma}//<133>_{\alpha}$
Greninger-Troiano′(G-T′)	$\{110\}_{\gamma}//\{111\}_{\alpha}$, $<133>_{\gamma}//<123>_{\alpha}$

Most low carbon steels show OR closer to K-S and N-W. Among those two, K-S OR ($\{111\}_\alpha$ //$\{011\}_\gamma$, $<101>_\alpha$//$<111>_\gamma$) between fcc (α) and bcc (γ) is the most common in most modern steels [111, 116, 117].

In lath martensite, laths are the fundamental crystallographic unit and there are 24 different lath variants that may develop from a parent austenite grain with K-S orientation relationship [11] during transformation (i.e. four different parallel plans and each with six parallel directions). These 24 variants can be constitutes as 15 kinds of variant pairs [117]. The boundary between variant 1 (V1-$(111)_\alpha$//$(011)_\gamma$, $[\bar{1}01]_\alpha$//$[\bar{1}\bar{1}1]_\gamma$) and variant 4 (V4-$(111)_\alpha$//$(011)_\gamma$, $[10\bar{1}]_\alpha$//$[\bar{1}1\bar{1}]_\gamma$) (sub-block) belongs to low angle boundaries. Twin related V1/V2 (V2-$(111)_\alpha$//$(011)_\gamma$, $[\bar{1}01]_\alpha$//$[\bar{1}1\bar{1}]_\gamma$) pair (which belong to block boundaries with angle/axis of 60.2°/[11-1]) [118]) are associated with increased cooling rates [111]. The density of block boundaries determines the toughness [111]. Higher the cooling rate, higher the V1/V2 pairs [111]. A high density of high angle grain boundaries (HAGB); especially V1/V2 variant pair help to hinder crack propagation hence improve toughness [111].

2.4.3 Improvement of HAZ toughness

To improve the mechanical properties; especially, toughness in HAZ, two main measures that have been proposed. One is to reduce the carbon content which prevents the formation of MA constituents and the other is to add special alloying elements to form fine, high melting point oxide inclusions (Titanium, Zirconium, Calcium) to inhibit austenite grain coarsening [32].

There are several methods used for improving HAZ toughness for high heat input welding for low temperature toughness applications for steel. A review conducted by Pan and Lee [119] outlined methods for improving toughness and shown in Table 2-4. Toughness of sub HAZ regions of can be controlled by PAG size, inclusion engineering to generate the formation of intergranular acicular ferrite (IAF), reducing hard phases and particles or improving the toughness of the matrix.

Table 2-4: Principals and techniques for improving the HAZ toughness under high heat input welding [119].

Method	Principles	Techniques
Refining austenite grain size	• Preventing grain growth of austenite by the presence of fine TiN and AlN particles	• Adding Ti, controlling Ti/N ratio • Increasing Al and lowering N
Sectioning austenite grain	• Sectioning the austenite grain into many small grain colonies by the formation of IAF	• Ti-killing to form TiO, Ti_2O, TiO_2 • Ca treating to form CaO-MnS • Adding REM to form REM oxides • Adding B to form $Fe_{23}(C,B)_4$
Modifying HAZ structure	• Decreasing hard second phase such as MA in upper bainite • Changing hard second phase into pseudo particles	• Lowering carbon equivalent by controlled cooling or TMCP • Ca-treating to reduce amount of elongated MnS present • Reducing N content
Increasing matrix toughness	• Reducing elements which can harden the ferrite matrix • Adding elements which can increase the matrix toughness	• Reducing N and C content • Adding Ti, B, Al to reduce free N • Adding Ni

IAF - Intergranular acicular ferrite
MA - Martensite-austenite
REM - Rare earth metals

The addition of alloying elements to the base metal has a strong influence on the evolution of the HAZ microstructure and resultant mechanical properties, so controlled alloying addition can be used to improve HAZ toughness. The grain growth and transformation characteristics of the HAZ can be controlled by the additional alloying elements, such as; Nb, V and Ti. These elements can all form fine stable precipitates at high temperature (carbides or nitrides), that can impede grain growth by grain boundary pinning during the thermal cycles of welding [45, 120]. If the microalloying precipitates are dissolved during heating, they can re-precipitate as fine carbides and/or nitrides during cooling and can also inhibit grain growth [121]. The presence of stable microalloying precipitates can promote intergranular ferrite nucleation, which increases the grain density, thus improving the toughness [122, 123]. Boron nitride (BN) and Ca sulphides act as nucleation sites for $\gamma \rightarrow \alpha$ transformation thus smaller grains can be achieved [124]. Alloying elements that form solid solutions in steel can change the transformation temperature and provide

matrix hardening [121]. The balance of Mn-Cu-Ni was found critical to achieve low temperature toughness while maintaining the joint strength [124]. The effect of some alloying element on HAZ toughness is listed in Table 2-5.

Table 2-5: Effects of alloying elements for the toughness of HAZ in steel [44, 125]

Alloying element	**HAZ toughness**
Ti	Fine dispersion of TiN precipitates can hinder austenite grain growth in the HAZ
Nb	Up to 0.11wt% of Nb can improve HAZ toughness with medium heat input (3 kJ/mm), but for low Nb levels, there is minimal effect on toughness
V	Higher levels are detrimental to the toughness, but lower levels (<0.08wt%) there is minimal effect.
B	Increase the hardenability. Therefore, beneficial for strengthening of thick plates.
Ni	Increase the toughness without affecting much increase of strength.

Hu et al. [23] showed that impact toughness depends on both the initiation and propagation energy of micro-cracks in low carbon microalloyed steels. In a steel designed to produce V(C,N) precipitates, the presence of such particles reduced the carbon concentration at PAGB's, which avoided the formation of large and hard MA constituents, which act a crack initiation sites. Secondly, the formation of fine-grained ferrite along the PAGB's with high angle boundaries improved crack propagation energy. Thus, the ICCG HAZ toughness of the V-N steel was significantly improved compared to Nb-Ti steel

Controlling of formation and properties of MA can directly influence the toughness of ICCG region. It was observed that V (C, N) precipitates significantly affected the impact toughness in the ICCG HAZ region. The V (C, N) precipitates acted as nucleation sites for ferrite, which lead to fine grained ferrite to form along the PAGB's, instead of MA constituents, so toughness can be improved [23]. The Si content was directly related to MA formation, as in multilayer welds, lower Si content reduces MA content [124].

2.5 Residual stresses in welds

Residual stresses are classified as the stresses that remain in the structure, as a result of a weld (or a thermal cycle) and restraint of the structure, after all externally applied factors are removed [126]. The typical distribution of residual stresses around a butt weld joint is shown in Figure 2-32. Development of residual stresses occur during heating and cooling cycles of a weld and develop due to thermal expansion, contraction and volume changes associated with phase changes.

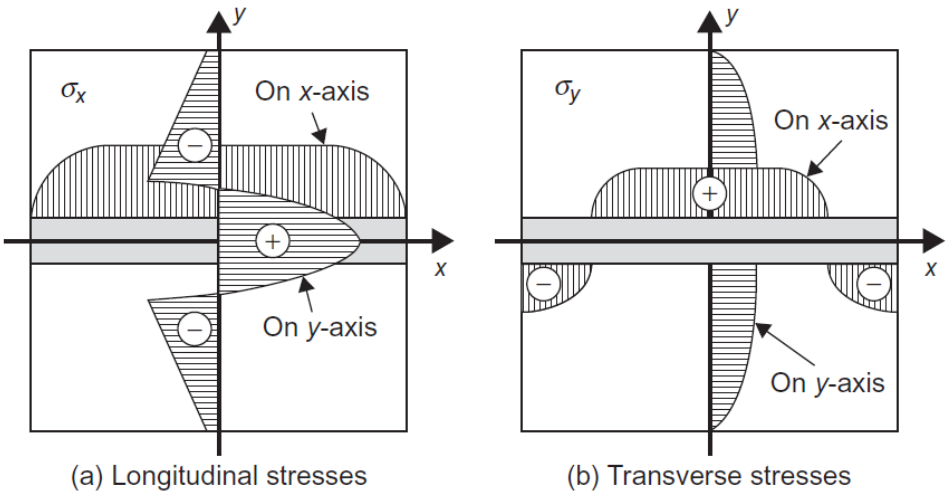

Figure 2-32: Typical distribution of residual stress fields in butt-welded joints [127].

The structure's stress response to an applied load is influenced by residual stress. Depending on the magnitude, direction and geometry of the residual stress field, it can positively or adversely affect the performance of the structure. In welds, residual tensile stresses are generally considered as unfavourable due to the effect of promoting fracture by initiation and acceleration of crack growth [128]. On the other hand, compressive residual stresses can be beneficial by slowing-down fracture propagation or by delaying crack initiation.

In most cases, residual stress is represented in a single direction. However, stress distribution in three dimensions in a solid body generates complex triaxial stress. Therefore, triaxial stress measurement is important in to understand the complete effect of residual stresses a component. The Australian standard AS/NZS 2885.2 states that the residual stresses associated with repair welding are higher than the original weld, so a higher preheat temperature is likely to be required [59].

Residual stresses are categorised by the length scale that the stress acts upon, which is separated into Types 1, 2 and 3. The Type 1 stress is a macro stress, which acts over length scales of multiple grains and is considered as the average stress at a location. Type 2 stress is intergranular stress which acts in single grains and will vary from grain to grain Type 2 stresses are typically in the micrometre range and the averages of type 2 stress are used in producing type 1 stress. Type 3 stress is also an intergranular stress, but acts within a grain at the scale range of several atomic scales. It is related to stress fields around atomic defects [129]. Type 1, 2 and 3 residual stresses are schematically shown in Figure 2-33.

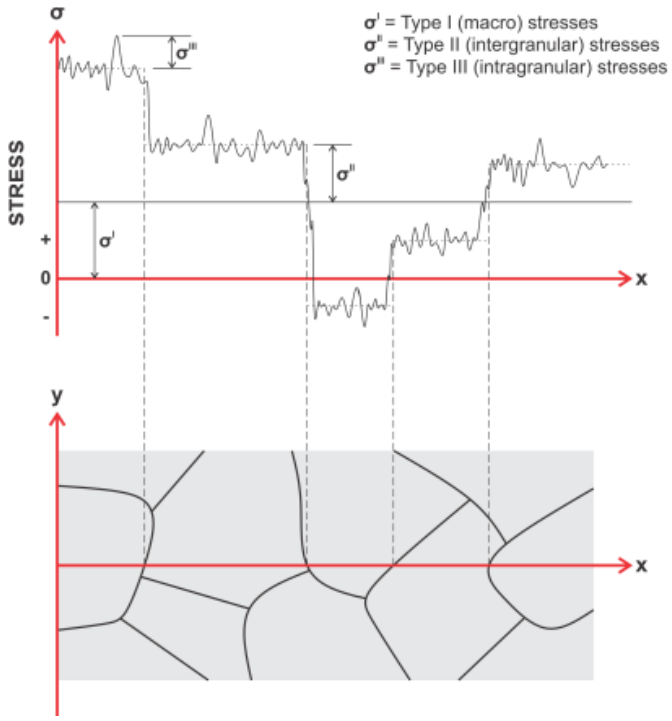

Figure 2-33: Categories of residual stress fields [130]

Type 1 stress is the most important component for engineering structures as it has the most influence on fracture and stress corrosion behaviour [129].

The magnitude and distribution of residual stress are controlled by physical restrains of the component, material properties and welding process. Figure 2-34 compares residual stresses introduced by different welding processes in welding a 4 mm thick shipbuilding steel plate [124]. The welding processes with lower heat input generally produce smaller stresses as well as a shorter distribution, showing that heat input is an important parameter affecting residual stresses and distortion.

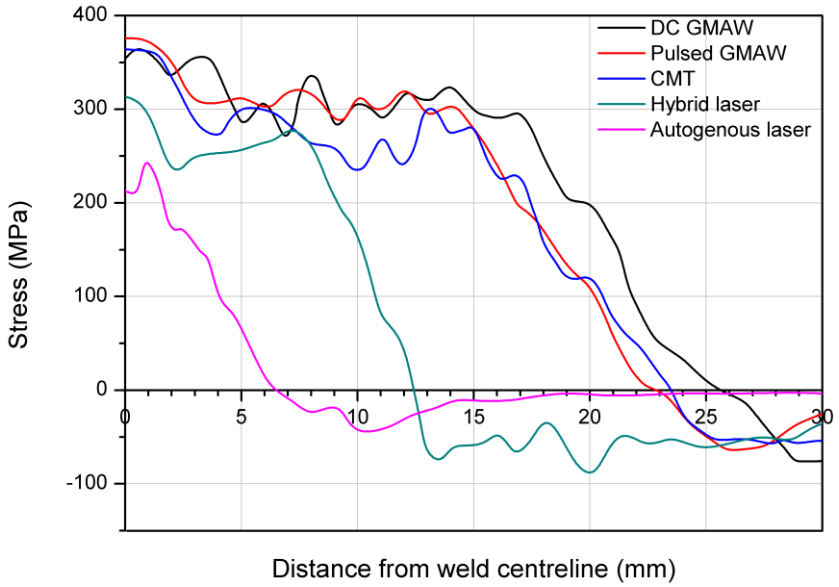

Figure 2-34: Longitudinal residual stress measured for different welding techniques on a 4 mm thick plate. Adapted from Colegrove, et al. [131].

Weld residual stresses may adversely influence properties such as brittle fracture, fatigue, stress corrosion cracking and buckling [127]. In most cases, compressive residual stresses are considered favourable for welded structures [132]. Tensile residual stresses, especially when the magnitude of the stress is close to the yield strength, can deteriorate fracture toughness by increasing the crack growth rate [133]. The influence of residual stresses can shorten the life-time integrity of a structure, particularly in harsh environments, such as for nuclear components [134, 135] or in ships and seagoing vessels, where residual stresses can have a detrimental effect on fatigue and fracture [133].

2.5.1.1 Residual stress in repair welds

The characteristics of the residual stress field in a repair weld can be significantly different from the original fabrication welds. Residual stress field of a repair weld depends on many factors including, weld geometry, repair length, repair depth, weld procedure [136].

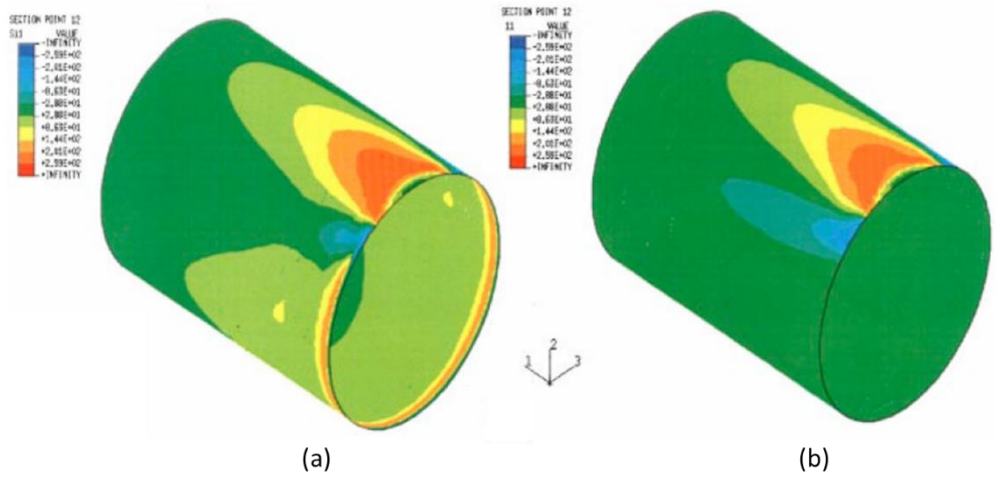

Figure 2-35: Axial residual stress distribution with short girth weld on a pipe (a) with residual stress of original weld and (b) without existing residual stress [136].

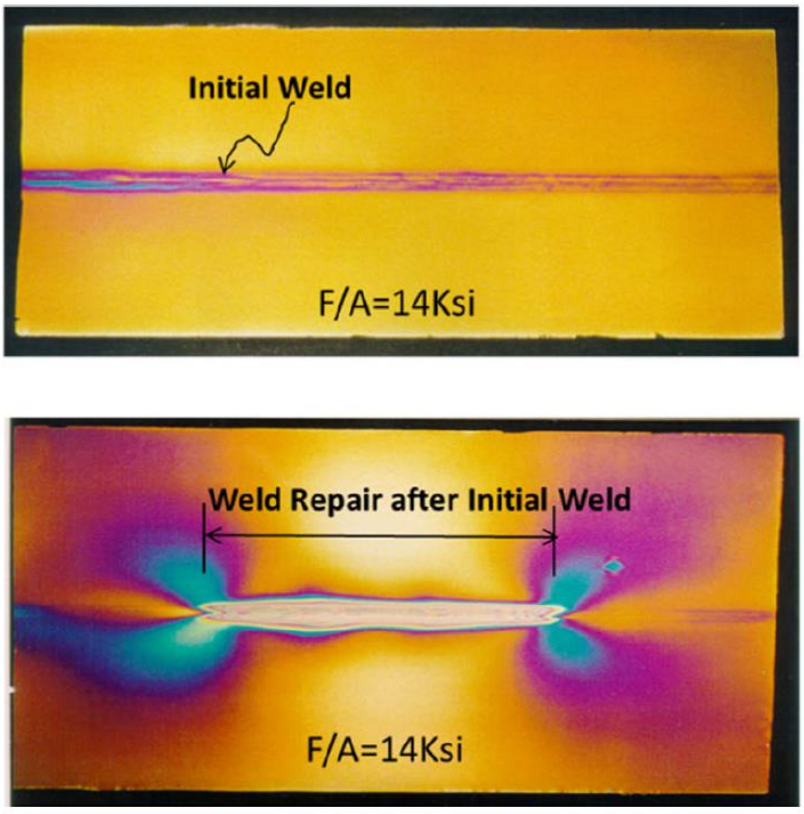

Figure 2-36: Residual stress fields of (a) initial fabrication weld and (b) a short length weld repair with same external loading [64]

In research on stainless steel pipeline girth welds, it was found that the pre-existing stress fields in the original girth welds had minimal effects on the residual stresses of the repair girth weld [136] (see Figure 2-35). Dong [64] investigated the repair length of repair welds, high residual stresses occurred at the weld start and the end locations, as shown in Figure 2-36. The maximum stress occurred at arc start-stop locations. George, et al. [137] found in their research on repair welds on pipes, that a shallower repair weld introduced higher hoop stress and lower axial stress compared to deeper weld repairs. Bouchard [67] examined the residual stresses for long and short weld repairs in a manual metal arc (MMA), J-preparation girth weld in a stainless steel pipe, using neutron diffraction, deep-hole and surface-hole techniques. The repairs were axially offset from the original girth weld to limit further degeneration of the original HAZ and the potential for lack of side-wall fusion. The measured axial residual stresses in the short repair were found to be higher compared to the long repair. Repair welds can significantly alter the residual stress fields, particularly at the start/stop locations. A common finding is the length of a weld repair is an important consideration, where shorter repairs typically result in greater residual stresses compared to longer repairs.

2.6 Summary of the chapter

This literature review provided an overview of the welding of high strength steels, where important aspects relating to welding Q&T steels were reviewed. The main topic of this research is the effect of multiple recurring repair welding on the effect of mechanical properties of BIS812 EMA steel. A review of factors affecting HAZ toughness of steels was conducted, with consideration given for literature investigating the effects of multiple weld repairs or simulated HAZ cycles. The key aim was to gather and understand the technical details to enable a critical assessment of the impact of multiple repair welds on HAZ properties of steel.

During the welding of steels, a HAZ is always produced and local brittle zones (LBZ) are identified as regions with low toughness present within the HAZ. Previous research identified the CG HAZ and ICCG HAZ are the regions with the lowest toughness in the HAZ. The main reason for lower toughness in the CG region was

due to large PAG size, which produces a low toughness microstructure with a low grain boundary density and fewer obstacles to fracture propagation. In CG-IC HAZ (or ICCG HAZ), the lower toughness was attributed to both larger PAG size and MA constituents, which can act as fracture initiation sites and thereby lower the fracture initiation energy. While it is known that there exists a variation of toughness within the ICCG HAZ relative to the IC temperature, this variation depends on the steel type. The failure mechanism (MA constituent cracking or MA constituent/matrix debonding) in the low toughness sub-HAZ regions varied with steel type and welding parameters and there is limited research conducted on quench and tempered steels. Therefore, it is important to examine the toughness of the CG HAZ and ICCG HAZ for BIS812 EMA steel, which is quite unique as it is a Q&T steel with solid solution strengthening, microalloying hardening and a boron addition.

Key points in the literature review are outlined below;

- Previous research examined the effects of PAGS on the toughness of the ICCG HAZ and the toughness gradient in the ICCG HAZ, but there is limited knowledge on the combined effects of PAGS and temperature gradient on intercritically reheated HAZ; particularly for Q & T steels.
- Effects of multiple simulated HAZ cycles on properties have rarely been studied for different alloy designs but not for Q & T steels.
    - The effect of multiple repeated thermal cycles on high strength Q & T steels has not been comprehensively studied, only some recent work has conducted on HSLA steels. In a study with HSLA-100 steel, Duch and Dupont [91] concluded that multiple applications of CG thermal cycles did not affect toughness, but toughness decreased with multiple IC cycles.
    - In the current research, a significant effort was given to analyse the fracture behaviour in double cycle welds, as it was understood the ICCG HAZ showed the lowest toughness for multi-pass welds. This knowledge can be compared with the finding for multiple repair welds to help understand the effects of multiple thermal cycles on the mechanical properties of the base plate.

- While the residual stresses generated in butt welded joints have received wide attention, an understanding of the variation of residual stresses in multiple pad welds has not been conducted. Therefore, a component of this research was to study the effects of multiple pad repair welds on residual stress behaviour using the neutron diffraction technique.
- Welding Standards and Standards for specific grades of steel rarely provide guidelines on how many times repair welds can be performed at one location. If they do, the number of repairs is often limited. Furthermore, weld repairs are traditionally restricted to the repair of defective welds or imperfection on a base plate (rolling damage, corrosion etc.) and pay no attention to the effects of multiple weld thermal cycles to the base plate properties. Such scenarios are significantly different from the methods used in this thesis in examining the effects of multiple welds to the same location during recurring maintenance routines for the long-term sustainability of the Collins Class Submarines.
- Repair welds of defective weld regions are typically subjected to severe restraint conditions, which is not the case for pad repair welds and full penetration butt welds, where the entire weld was removed. The most similar research was that by Vega et al [63], who assessed the effects of multiple repairs in girth welds for API X52 pipeline steel, using shielded metal arc welding (SMAW). The mechanical properties and microstructures for one, two, three and four SMAW repairs in the same area were evaluated. Their results found that after multiple repair welds the microstructural constituents of the HAZ had not significantly changed, but grain growth in the HAZ at the mid-thickness did result in a deterioration of toughness properties. Again, girth welds are quite different to pad or full penetration butt welds and chemical composition and properties of X52 is significantly different from BIS812 EMA steel.

Therefore, the main focus in this thesis is to study the microstructure and mechanical properties of BIS812 EMA steel subjected to a range of weld thermal cycles in simulated HAZ specimens and for real weld tests. Combining results from simulated HAZ experiments with carefully designed weld tests will enable both the weld HAZ properties and mechanisms behind the variation in properties for multiple weld repairs to be understood.

3 MATERIALS AND METHODS

3.1 Material

The material used in this investigation was microalloyed Quenched and Tempered (Q & T) steel produced in Australia for the pressure hull of the Collins class submarines. The steel was produced with basic oxygen steelmaking process with secondary ladle treatment, then continuous casting to produce 220 mm slabs, reheat soaking at 1200°C for hot rolling to the required thickness [138]. The Q&T heat treatment was then carried-out using roller quench equipment, with austenising at about 900°C, quenching and then tempering at about 650°C [138]. The typical chemical composition and typical mechanical properties of the steel are shown in Table 3-1 and Table 3-2 respectively.

Table 3-1: Chemical composition (wt%) and carbon equivalent of BIS812 EMA steel [139]

C	**Si**	**Mn**	**P**	**S**	**Cr**	**Ni**	**Mo**	**V**	**Ti**
0.13	0.24	0.93	0.011	0.002	0.48	1.28	0.39	0.02	0.01
Cu	**Al**	**Nb**	**B**	**N**	**Ca**	**O**	**Fe**	**CE_N**	**P_{cm}**
0.21	0.07	0.01	0.0066	-	≤3ppm	0.009	Bal.	0.495	0.301

The steel was produced with low sulphur and phosphorous to minimise the non-metallic inclusions. Chromium, nickel and molybdenum were added to improve the hardenability, with Ni addition for improvement of low temperature toughness. Boron was added for additional hardenability [138].

Table 3-2: Typical mechanical properties of BIS812 EMA steel [139]

0.2% Proof stress	**UTS (MPa)**	**Yield stress (MPa)**	**% Elongation**	**Charpy impact energy (J)**	
				at -18˚C	**at -60˚C**
754	845	690	18	90	75

The base material consisted of lath martensite with an average prior austenite grain size of 18 µm.

3.2 Dilatometer studies

Dilatometer experiments were conducted to identify critical transition temperatures of the steel. Hollow cylindrical samples were machined from a 30 mm thick plate to the size of 10 mm long, 5 mm OD and 3.5 mm ID.

A range of heating rates was applied to different samples to identify if there were any differences in transformation temperatures with heating rate. Heating rates of 5 ºC/s, 50 ºC/s, 100 ºC/s, 150 ºC/s and 200 ºC/s were applied for three samples per heating rate. Figure 3-1 shows a thermocouple attached to a typical dilatometer sample and the dilatometer used (Theta industries Dilatronic® dilatometer).

(a) (b)

Figure 3-1: Pictures of dilatometer experiments (a) a thin K-type thermocouple welded to a sample for temperature measurement and control and (b) dilatometer set-up used for the experiment

3.3 Welding trials and simulated HAZ

This study focused on the effect of multiple repair welding on the mechanical properties of the parent steel. Therefore, experiments were designed to study the changes in microstructure and mechanical properties with the application of multiple thermal cycles at the same location on the base plate. There were two primary components of the experimental program; 1) investigation of Simulated Heat affected zones (HAZ) and, 2) investigation of the HAZ of real welds.

3.3.1 Real weld experiments

Three different welding scenarios were considered for this study; namely, Bead on Plate (BoP) weld, pad weld and full penetration butt weld. Weld experiments were designed to replicate the real-world repair welding practices on Collins class submarine hulls. Each scenario will be explained in more detail in the relevant section. The research was aimed to target up to 3 instances of recurring welding repairs with a similar heat input (one original/design weld and three repair welds, equally four welds in total for the three different welding scenarios).

For all three welding scenarios, instrumented welds were conducted to record temperature histories and real-time current and voltage measurements. The temperature was measured with imbedded K-type thermocouples which were placed as close as possible to the heat affected zone and were spaced at incremental distances (1.5 mm, 3 mm and 5 mm) from the fusion line (FL) to allow accurate measurement of temperature. Thermocouples were first welded to the flat surface of 3 mm diameter cylindrical steel pieces (corresponding to the above three lengths) and then pushed into holes on the base plate. Temperatures were recorded in real-time with a data logger (National Instrument's CompactRio controller) attached to a computer.

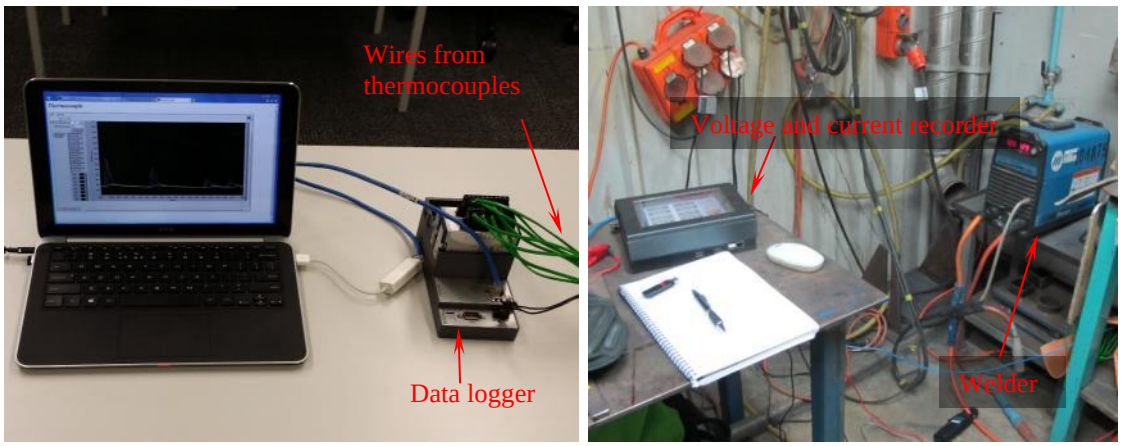

(a) (b)

Figure 3-2: Weld experiment data acquisition set-up (a) recording of temperature histories and (b) MMA welder and welding current and voltage measurement set-up

Weld repairs were conducted using manual metal arc welding process (MMA) with DC power source (Miller Maxstar 200), high strength low-hydrogen electrodes (Atom arc E120.18 M2) and relatively high preheat and interpass temperatures were used to prevent any possible occurrence of delayed hydrogen induced cracking (process parameters are shown in the appendix A). Weld arc energy was maintained at around 1 kJ/mm. Weld bead removal for repair welding was carried out by grinding with a hand-held grinder to replicate the real-word repair situation of submarine hull weld repairs. This process minimises the unnecessary thermal application to weld region in comparison with arc gouging. Completed welds were sectioned, and the microstructure, hardness and residual stresses were examined. Only the critical sub-zones were selected for detailed investigations for microstructure and mechanical properties.

3.3.1.1 Bead-on-Plate welds

Bead-on-Plate (BoP) welds were used to replicate fillet welds of structures that are typically used for welding of steel profiles to hull plates; in most cases, as temporary attachments. BoP welds were used to adequately capture the effects to the parent metal due to a fillet weld, but without the complications of joint preparation. Welding was conducted with four different welding cycles on 250×250×30 mm plate. In the first step, four sets of BoP welds were deposited, where each consisted of two overlapping welds. Next round, three sets of welds were ground back to the parent plate, and three sets of BoP welds were deposited over the top, as per the same procedure for the first round. In the third round, two sets of previously deposited welds were ground back to the parent plate, and two BoP welds were redeposited over the top. In the last step, the last weld was ground back to the parent plate and redeposited. A schematic illustration of the first two steps of the welding process is shown in Figure 3-3. Real BoP repair weld sample and the holes on the back of the weld side for mounting thermocouples are shown in Figure 3-4 (a) and (b).

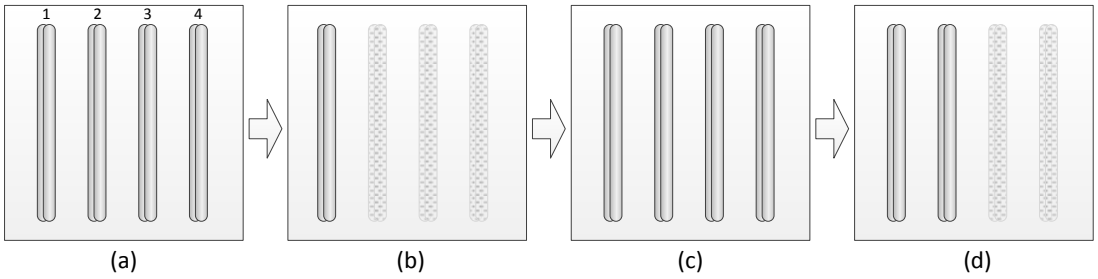

Figure 3-3: First two steps of BoP weld trials. (a) first set of 4 overlapping BoP welds (b) last three welds were ground back to the level of the base plate. (c) re-weld on top of ground 3 BoP welds. (d) last two welds were ground back to the level of the base plate. After eight steps of grinding and re-welding, the plate ended up with four BoP welds with four different weld repairs.

(a) (b)

Figure 3-4: BoP welds (a) welded side with four different repair welds and (b) holes on the opposite side of the plate where thermocouples were imbedded.

3.3.1.2 Pad Welds

Pad welds comprise of a series of weld beads placed next to each other to form a rectangle weld region to rectify the loss of thickness of a plate; such as for repairing corrosion damage. In order to replicate the rectification of corrosion damage, a 3 mm deep dish, 50 mm in circumference, was ground into the base plate. To study multiple welds, previous pads were ground back to a clean, uniform profile, to about 1 mm proud of the original surface. The effects of re-welding on parent metal properties were focused mainly in this study.

Deposited pad welds varied in size depending on the repair cycle. The first weld (first repair weld to rectify the damage of parent plate) was 60×60 mm in size and the second weld (second repair weld to rectify the damage to first repair weld) was 50×50 mm. Next two repair welds were 40×40 mm. All dimensions of pad welds are summarised in Table 3-3.

Table 3-3: Pad weld sizes with different repair cycles. See Figure 3-5.

Repair cycle	**Pad weld size (a × a) /mm**	**"c" Ground back from the previous pad weld/mm**
1	60 × 60	-
2	50 × 50	~1
3	40 × 40	~1.5
4	40 × 40	~2

Four identical base plates with 250×250×30 mm were used to prepare pad welds with four different repair welds. First, pad welds were deposited at an area of 60×60 mm on all four plates on the centre of the plate. For the second cycle, three plates were ground back to 1 mm above the plate surface and dished-out in the middle to about 3 mm below the top of the ground pad. Then, 50×50 mm pads were deposited on the three plates. For the third weld cycle, only two weld samples with second repair pads were ground back to around 1.5 mm above the plate surface. The middle part was dished-out to about 3 mm below the top of the ground pad and then the third weld repair layer was applied. For the final step, one plate with three repair weld was ground back to around 2 mm above the original plate surface and the centre was dished-out as before. Then the fourth repair pad weld was laid down at an area of 40×40 mm. With the above steps, four different samples were made with four different repair weld cycles; original repair, 2×, 3× and 4× repairs. Figure 3-5 is a schematic showing the repair weld process for the original and 2× repair welds. Photographs of the pad weld first repair and second repair are shown in Figure 3-6 (a) and (b), respectively.

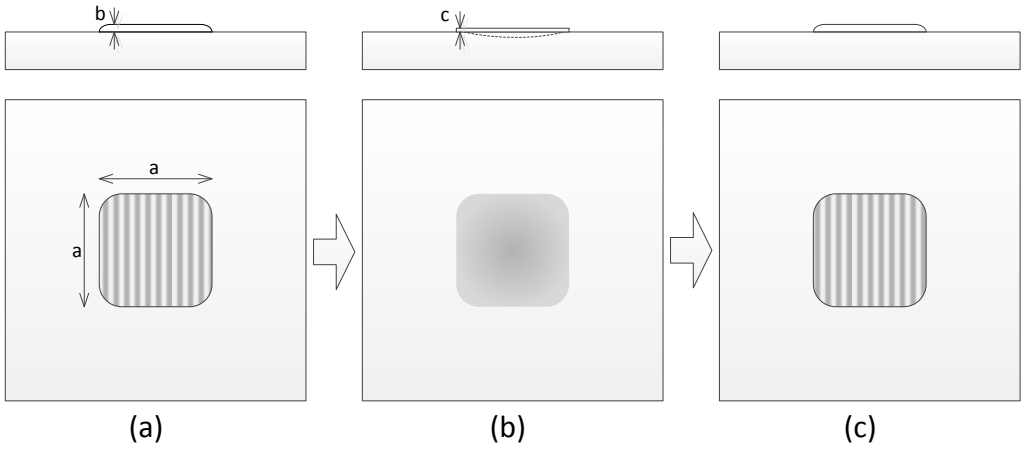

Figure 3-5: Steps of pad weld repair. (a) First pad weld (b) Pad weld ground-off and dished-out about 2 mm below the plate surface (c) Re-deposited pad weld.

The first set of pad welds were instrumented in order to capture the thermal histories and welding parameters. Therefore, a set of thermocouples were imbedded into plates from the opposite side of the weld. A set of duplicate pad repair plates were made without imbedded thermocouples. Pad welds with thermocouples were used for microstructural characterisation and hardness testing. To examine the effect of re-welding on the previous weld sites, the interface between the original surface and the weld was examined in detail. Weld samples without thermocouples were used for residual stress measurements.

(a) (b)

Figure 3-6: Pad repair welds, where (a) Completed pad repair weld and (b) second repair weld where the first pad weld was ground and dished-out the middle part.

3.3.1.3 Full penetration butt Welds

Full penetration butt welds are mainly pressure hull circumferential welds that have been cut to separate the hull to facilitate internal access for machinery, equipment repair and upgrades. Cuts to the main hull are generally made along an existing weld seam. To reassemble, the hull edges are then ground back, welds are used to 'butter-up' the edges to restore the double bevel weld preparation, then the hull is re-welded back together.

Single bevel joint design was chosen for this study to obtain a fairly straight HAZ along the thickness of the plate to allow the sectioning of test samples for subsequent mechanical testing. Furthermore, this design allows the repair weld HAZ to overlap the existing HAZ, so the effects of re-welding on parent metal could be examined. 30 mm and 50 mm thick plates were prepared for the weld, with 45° bevel machined on the edge of 30 mm plate. On 50 mm plate, a straight edge was machined. The welding sequence was designed to obtain a HAZ as straight as possible down the edge of the 50 mm plate. An array of thermocouples was imbedded at incremental distances from the HAZ to allow accurate measurement of the thermal cycles. Fig 3-7 is a schematic of the weld set up and thermocouple placements.

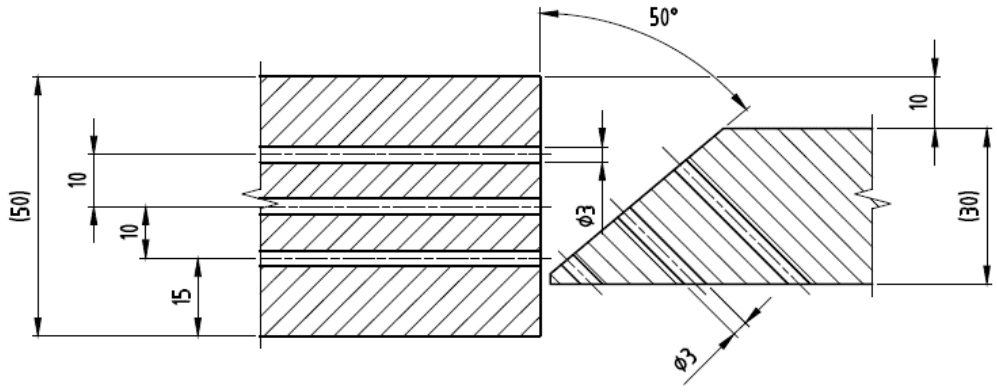

Figure 3-7: Cross section of the locations of holes for thermocouple placement for full penetration butt weld (dimensions are in millimetres).

Four representative welded samples were created to study the effects of multiple welds on the parent plate properties; the original/fabrication weld, first repair weld, second repair weld and third repair weld. To enable consecutive weld repairs, the

weld metal was saw-cut adjacent to the 50 mm plate and machined back to the original surface. Then a new 30 mm plate was welded to the existing 50 mm plate, as shown in Figure 3-8.

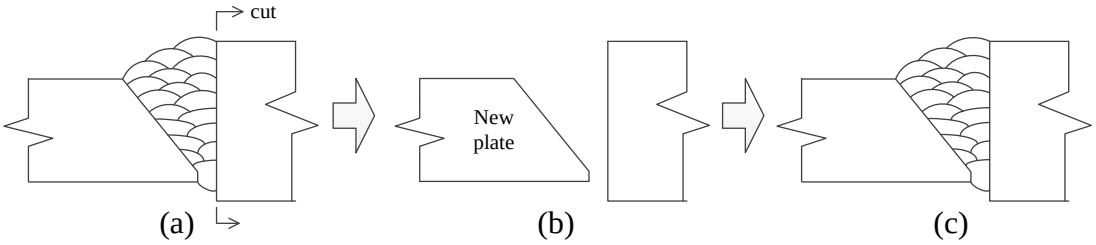

Figure 3-8: The sequence of repair weld of full penetration butt welds. (a) 30 mm and 50 mm plates welded together with single bevel butt weld. (b) Filler metal was cut off along with the 30 mm plate and new 30 mm plate placed and (c) plates re-welded together (first repair weld).

This process was repeated until three weld repairs (4 welds in total) were completed using one 50 mm plate.

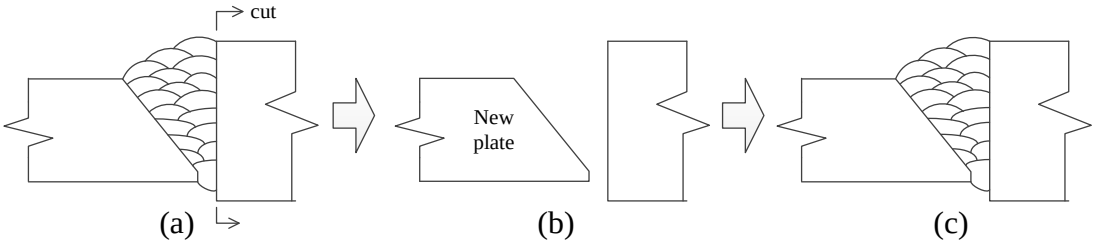

Figure 3-8: The sequence of repair weld of full penetration butt welds. (a) 30 mm and 50 mm plates welded together with single bevel butt weld. (b) Filler metal was cut off along with the 30 mm plate and new 30 mm plate placed and (c) plates re-welded together (first repair weld).

Metallurgical analysis and mechanical tests were conducted as discussed in Section 3.5.

3.3.2 Thermal HAZ simulations

Thermal HAZ simulations were conducted to replicate the effect of thermal cycles in real welds in order to isolate and test the mechanical properties of different HAZ microstructures, such as the CG HAZ and ICCG HAZ, to establish the significance of each HAZ for BIS812 EMA steel. Thermal cycles were applied in Gleeble 3500 thermo-mechanical simulator with resistance heating. Figure 3-9 shows the Gleeble simulator and a HAZ simulation in progress.

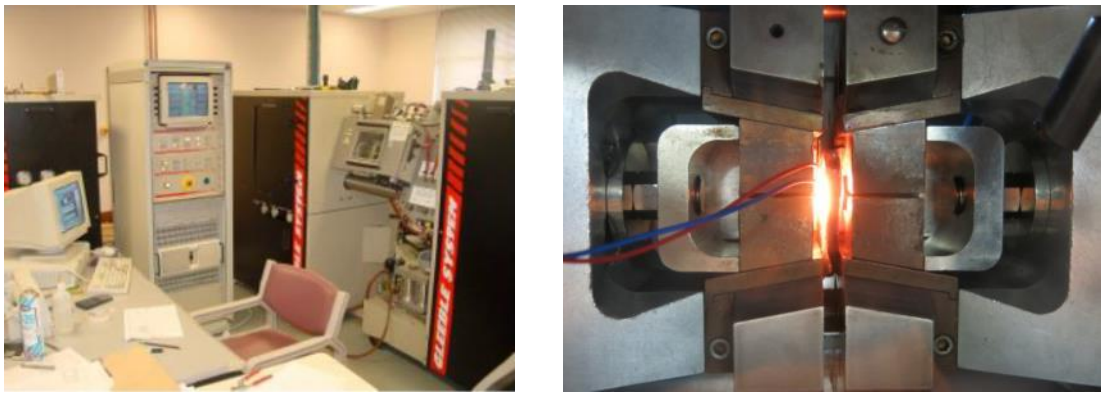

Figure 3-9: Photos of the Gleeble thermo-mechanical simulator and a simulated HAZ sample during testing.

Simulated HAZ samples were 11×11×80 mm in size (to allow full-sized Charpy samples) and were cut from the long-transverse (LT) direction from 30 mm thick plate. A thin K-type thermocouple was spot welded at the middle on one facet to control and monitor the temperature. Samples were heated with resistance heating in a vacuum ($\approx 95\times10^{-5}$ bar). The gap between clamps was maintained at 15 mm for all test pieces to produce a uniform HAZ at the mid-section and pressurised air was used to maintain the required cooling rate.

Temperature profiles obtained from instrumented BoP welding trials were used to define the experimental variables for simulations (see Figure 3-10). Three different temperature ranges were chosen to simulate different regions of the HAZ as shown in Table 3-4. All samples were pre-heated to 150°C before applying the actual thermal cycle which replicates preheat in a real weld. The cooling rate from 800°C to 500°C ($t_{8/5}$) gives an important control of temperature control for transformation microstructures during welding [15]. Therefore, cooling curves were simulated with a Rykalin-3D mathematical model, which is used to simulate the welding of thick

plates, based on the $t_{8/5}$. Thermal properties of the material used for the simulation is shown in Table 3-5. When the temperature of the cooling process was less than 160°C, the temperature control was switched off and specimens were either left to cool to room temperature or the next cycle was started. This cut-off temperature was chosen to limit test time and any microstructural changes below this temperature are negligible. At least three samples for each thermal cycle were prepared for subsequent Charpy impact testing.

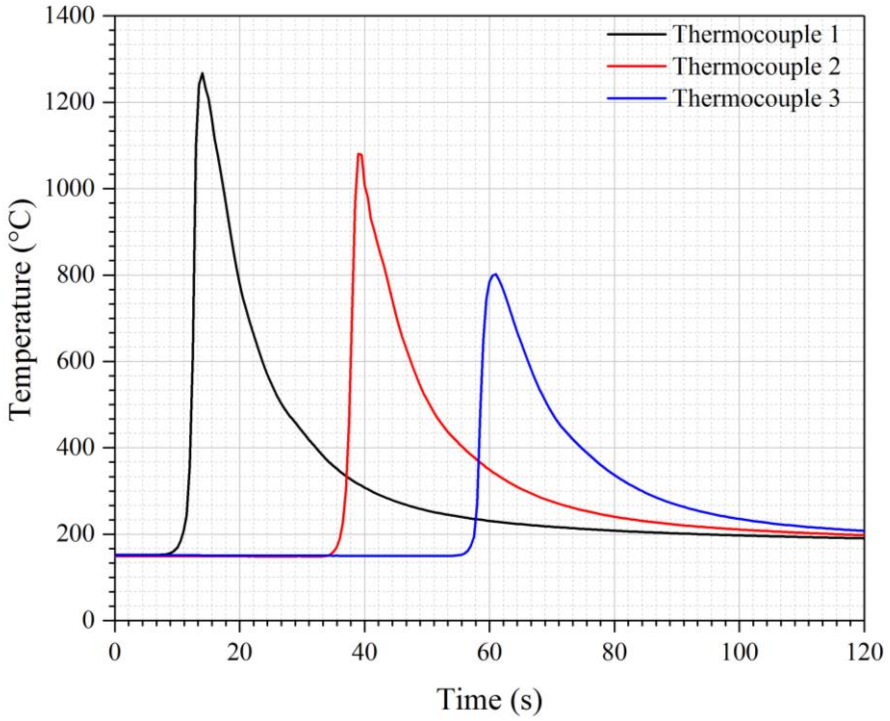

Figure 3-10: An example of temperature histories captured by three imbedded thermocouples in a real BoP weld.

Table 3-4: Characteristics of thermal cycles used to simulate different HAZs

Simulating HAZ region	**Maximum temperature of a cycle/ °C**	**Heating rate/(°C/s)**	**$t_{8/5}$ /s**	**Hold time at max temp/s**
CG	$1350 \leq \theta < 1100$	200	4.3	0.5
FG	$1100 \leq \theta < 850$	200	4.3	0.5
IC	$850 \leq \theta \leq 750$	130	6.7	0.5

To produce different PAG sizes, four different temperatures were chosen, 1000°C and 1100°C for the FG region and 1200°C, and 1350°C for the CG region. A wide range of thermal cycles was applied to simulate the different HAZ combinations and

multiple thermal cycles were used to simulate repeated repair welding. All combinations of thermal cycles tested on samples are listed in Table 3-6.

Table 3-5: Properties of the material used for the HAZ simulations

Density/ (kg/m^3)	**Specific heat capacity/ (J/kg.°C)**	**Thermal conductivity/ (W/m.°C)**
7800	592	41.0

From dilatometer experiments, lower and upper transformation temperatures (A_{c1} and A_{c3}) for slow and fast heating rates were established. For BIS812 EMA steels, the A_{c1} and A_{c3} temperatures were 740°C and 860°C respectively, at the heating rate of 150 °C/s. Therefore, for the simulation of intercritical temperature, three temperatures were chosen based on A_{c1} and A_{c3} temperatures; 750°C (just above A_{c1}), 800°C (mid-intercritical temperature) and 860°C (just below A_{c3} temperature). The thermal cycle of an intercritically reheated sample is shown in Figure 3-11.

Table 3-6: Tested thermal cycles with Gleeble thermo-mechanical simulator

No of thermal cycles	Description	Simulation region	Maximum temperature/°C			
			1st cycle	2nd cycle	3rd cycle	4th cycle
1	Single HAZ cycles	CG	1350	Not applied	Not applied	Not applied
		FG	1100			
		IC	800			
2	CG or FG cycle followed by lower IC cycle	FG-IC	1000	750		
		FG-IC	1100	750		
		FG-IC	1200	750		
		CG-IC	1300	750		
		CG-IC	1350	750		
	CG or FG cycle followed by mid IC cycle	FG-IC	1000	800		
		FG-IC	1100	800		
		FG-IC	1200	800		
		CG-IC	1350	800		
	CG or FG cycle followed by high IC cycle	FG-IC	1000	850		
		FG-IC	1100	850		
		FG-IC	1200	850		
		CG-IC	1350	850		
	IC followed by CG	IC-CG	750	1300		
	Double CG	CG-CG	1350	1350		
	CG followed by FG	CG-FG	1350	1200		
3	Two CG followed by IC, FG or CG cycle	CG-CG-IC	1350	1350	750	
		CG-CG-FG	1350	1350	1100	
		CG-CG-CG	1350	1350	1350	
	CG followed by different combinations of FG and IC cycles	CG-FG-IC	1350	1100	750	
		CG-FG-FG	1350	1100	1100	
		CG-IC-FG	1350	750	1100	
	CG-IC cycle followed by tempering cycle	CG-IC-TM	1350	750	300	
		CG-IC-TM	1350	750	400	
		CG-IC-TM	1350	750	500	
4	Different combinations of IC, FG and CG cycles	CG-CG-IC-IC	1350	1350	750	750
		CG-IC-CG-IC	1350	750	1350	750
		FG-IC-CG-IC	1100	750	1350	750
		CG-IC-IC-IC	1350	750	750	750

CG – Course Grained HAZ

FG – Fine Grained HAZ

IC – Inter Critical HAZ

TM – tempering cycle (sub-critical temperature)

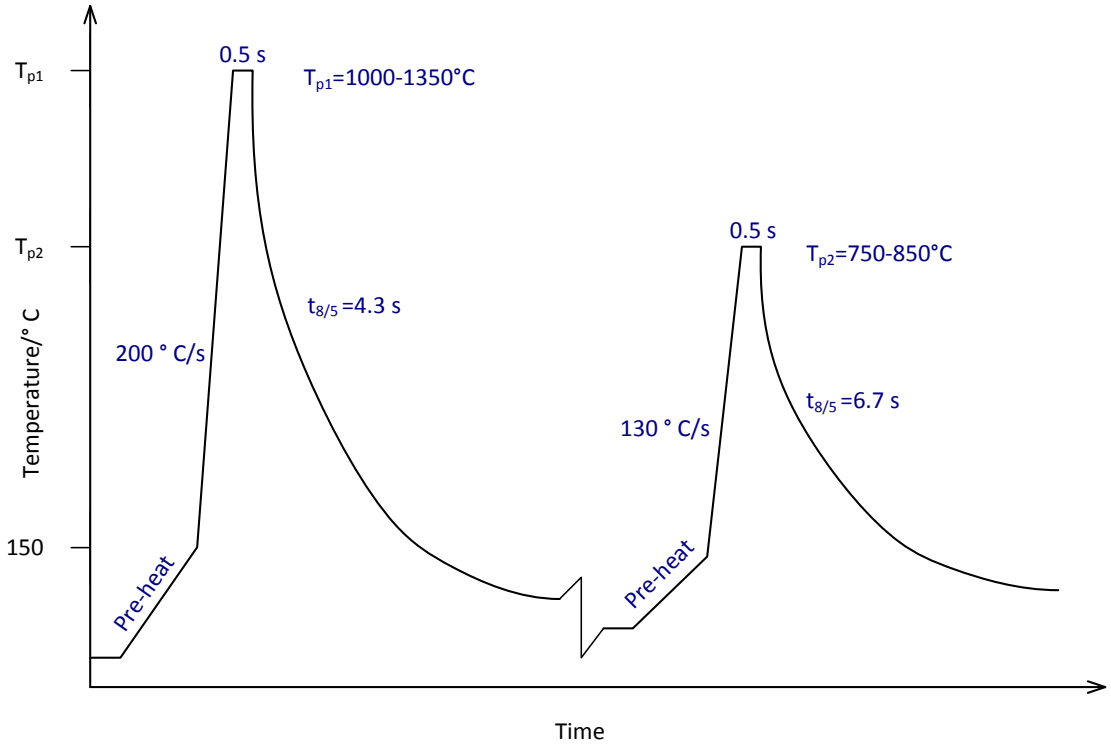

Figure 3-11: An example of the temperature profile of a two-cycle thermal simulation with maximum peak temperatures of peak 1 (T_{p1}) and peak 2 (T_{p2}).

3.4 Mechanical testing

3.4.1 Hardness

Hardness testing was conducted with Matsuzawa Via-F automatic Vickers hardness tester. For measuring of hardness profiles across welds, a standard load of 5 kg was used as per the Australian Standard AS 2205.6.1 [140] and for hardness mapping, 0.5 kg load was used, with a matrix of points spaced 0.5×0.5 mm to cover the weld, HAZ and parent plate, as shown schematically in Figure 3-12.

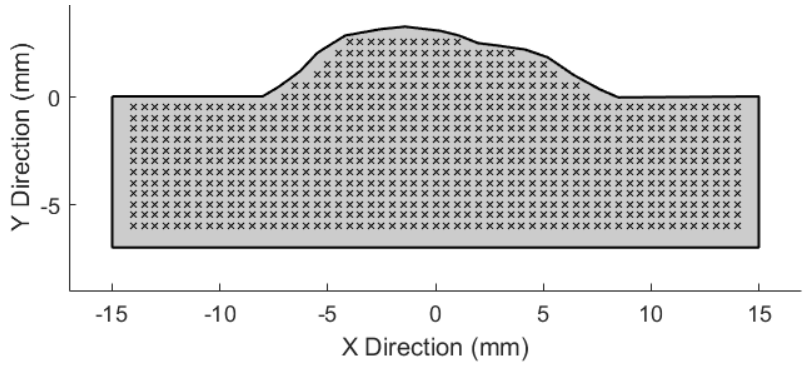

Figure 3-12: Example of test points for hardness mapping on a BoP weld sample.

The Vickers hardness number is calculated as follows [141],

$$HV = \frac{F}{A}$$

$$HV = \frac{F \times 2Sin(136°/2)}{d^2}$$

$$HV = \frac{1.854F}{d^2} \quad (7)$$

Where,

F – Force (kgf)

A – Surface area of the resulting indentation (mm^2)

d – Diagonal length of the imprint from the indenter (mm)

Hardness measurement on targeted phases was performed with Nano-indentation on a Hysitron Nanoindentation machine, located at University of Wollongong's Tribology Lab. On double cycle thermal simulated samples, indentations were placed on both MA phase and the matrix. Nano-scale hardness was measured with 10 mN applied force at targeted locations using a Berkovich indenter.

3.4.2 Charpy impact testing

Full size, standard Charpy impact test samples were machined from simulated HAZ samples, where the notch was placed at the middle of the HAZ, as shown in Figure 3-13. For real welds, full-size Charpy specimens were taken from the weld metal (WM), fusion line (FL) and FL+3 mm locations. Charpy tests were conducted according to AS 1544.2:2003 [142] at -20°C. The temperature of specimens was

controlled with immersing in an Ethanol bath and adding the required amount of liquid Nitrogen. Samples were kept at the test temperature for at least 15 minutes before testing. Samples were broken within 5s after removal from the bath (Charpy impact test machine used is shown in Figure 3-14). The absorbed energy from the impact was measured. Fracture facet was examined visually (percentage fibrosity) and further analysis was done by optical microscopy and SEM.

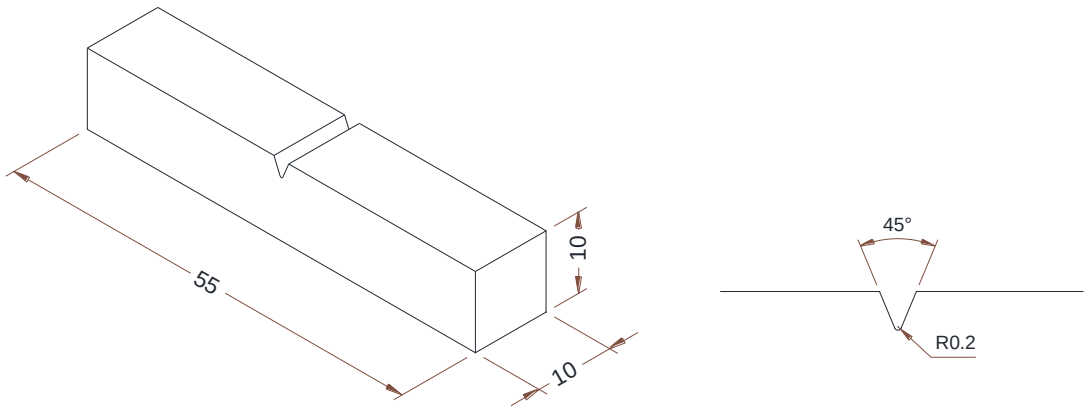

(a) (b)

Figure 3-13: Charpy impact test sample (a) full-size impact test sample and (b) detail of the notch

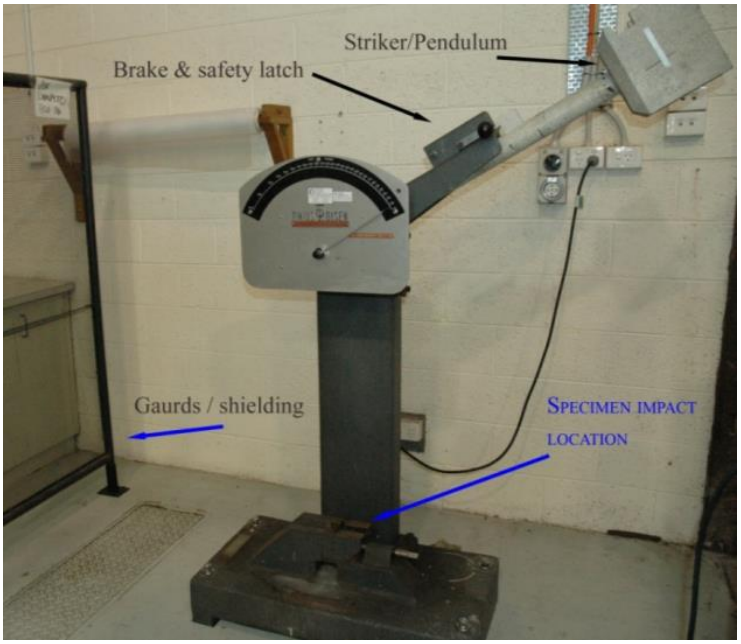

Figure 3-14: Charpy impact test equipment used for the study [143]

Instrumented Charpy impact tests were conducted with the same procedure as described above, on an Instron MPX 750. With the instrumented Charpy impact test, the variation of load with displacement data was obtained along with the total absorbed energy. The fracture initiation and propagation energies were calculated from load vs displacement curves. The total absorbed energy was calculated with two methods; as the sum of fracture initiation and propagation energies (i.e. total area under the curve) and with the potential energy difference between initial and final positions of the pendulum after breaking the sample. An example of a typical force vs displacement curve is shown in Figure 3-15.

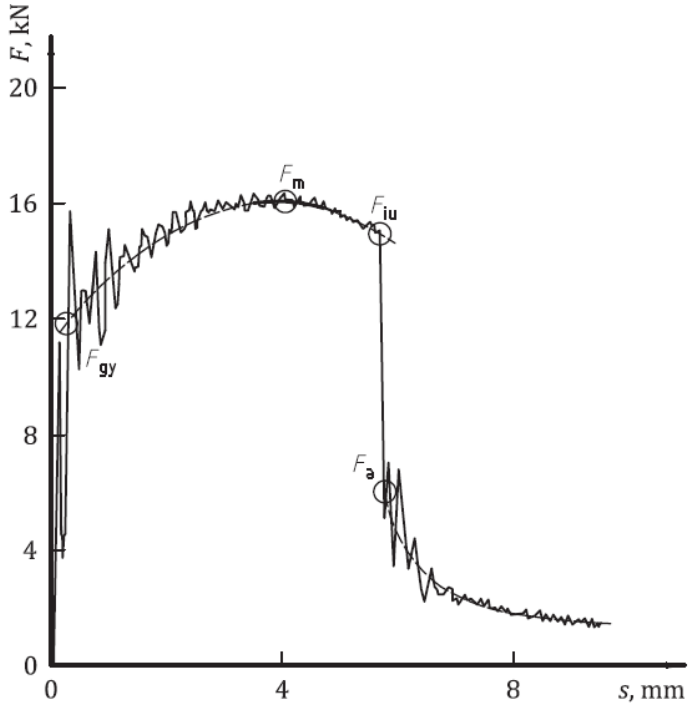

Figure 3-15: Typical load vs displacement curve of an instrumented Charpy test [144]

The different force categories that can be obtained from instrumented Charpy data, as labelled on Figure 3-15, are listed below;

F_{gy} - Force at the end of the elastic limit

F_m - Maximum force

F_{iu} - Force at where the unstable crack initiating

F_a - Force at crack arrest

Displacement was not directly measured from the instrument, so it was calculated with equations 8 and 9.

$$V(t) = V_0 - \frac{1}{m}\int_{t_0}^{t} F(t)dt \tag{8}$$

$$S(t) = \int_{t_0}^{t} V(t)dt \tag{9}$$

Where, m is the effective mass of the pendulum, V_0 is the initial impact velocity, t_0 is the beginning of the deformation and S is the final deformation after time, t.

Instrumented data can be used to separate different regions of the load-displacement curve and the energy for that region is calculated by integrating the area below the curve, see Figure 3-15. The unstable crack initiation energy was calculated by integrating the area under the curve from 0 to F_{iu}. The fracture propagation energy was the area under the curve from F_{iu} to the sample is completely broken.

3.4.3 Dynamic tear testing

The Dynamic Tear (DT) energy value is a measure of the specimen's resistance to rapid progressive fracture. The test was performed according to ASTM E604 [145]. Test samples were prepared with full penetration butt weld plates where the notch was placed in the HAZ of the weld. There were four test samples taken from the weld zone of the three repair weld plate (giving a total of four welds when the original weld is counted). The DT machine used for the experiment was located at the Defence Science and Technology Group, Fishermen's Bend site. Details of the test sample and a photo of the instrument are shown in Figure 3-16.

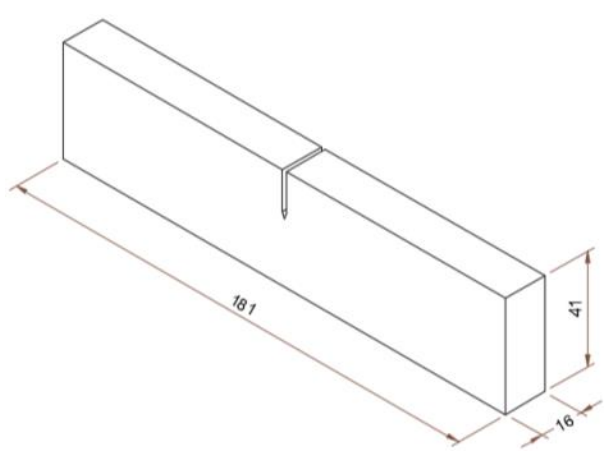

(a)

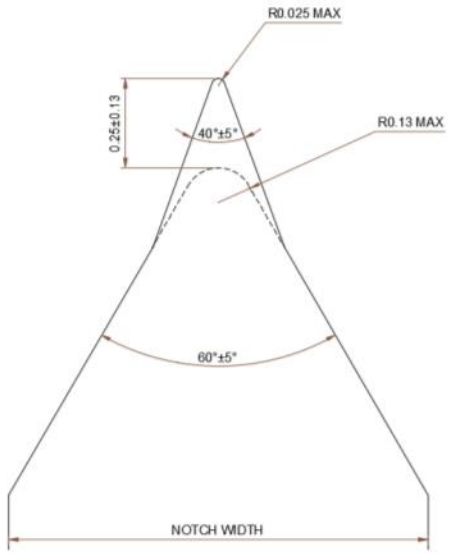

(b)

(c)

Figure 3-16: (a) Dynamic tear sample (b) detailed view of the pressed notch and (c) the drop weight tower used for dynamic tear testing (dimensions are in millimetres)

The machined notch was sharpened by a notch-pressing knife prior to testing. The depth of the pressed notch was measured using a microscope with a micrometre stage at 20× magnification.

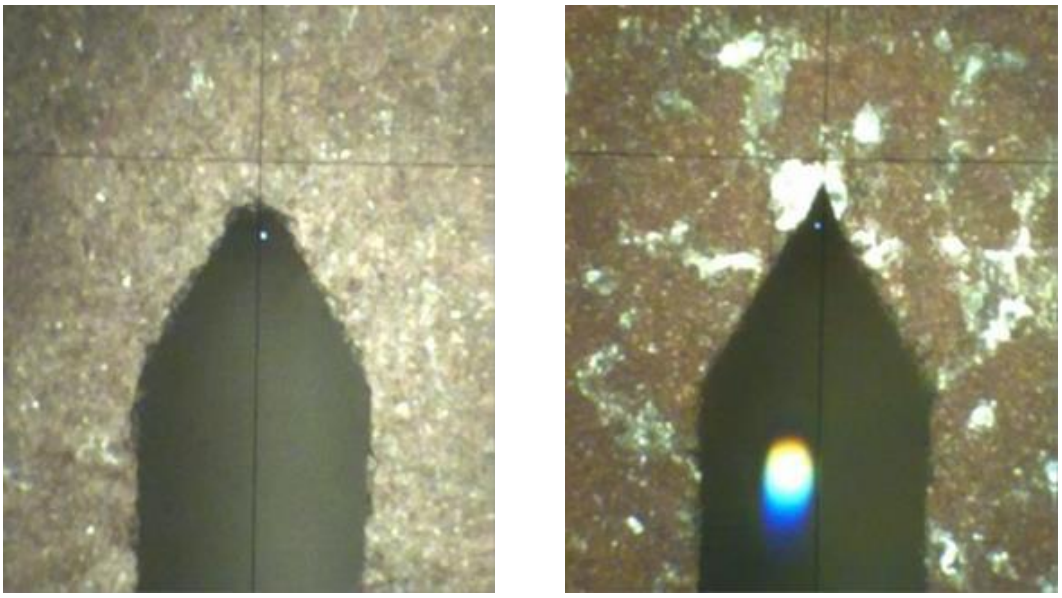

(a) (b)

Figure 3-17: Close-up picture of the notch of dynamic tear test sample (a) the notch as machined and (b) pressed notch [143]

3.4.4 Residual stress analysis

Residual stresses in pad weld specimens were measured with neutron diffraction technique. As-weld samples were used for the measurements. Experiments were conducted using the KOWARI residual stress diffractometer, located at the Australian Nuclear Science and Technology Organisation (ANSTO) at Lucas Heights, Australia.

Figure 3-18: A pad weld sample being tested on KOWARI residual stress diffractometer

Weld samples were fixed on the sample stage as shown in Figure 3-18 and scanned in the through-thickness direction and in the longitudinal and transverse direction to weld direction. The middle of the pad was taken as 0, 0 point. Because of the symmetry of pad weld (I.e. square), only half of the weld was scanned to reduce the required beam time. Directions and planes which neutron scan was conducted are shown in Figure 3-19 and the matrix of points on XZ and YZ planes are shown in Figure 3-20.

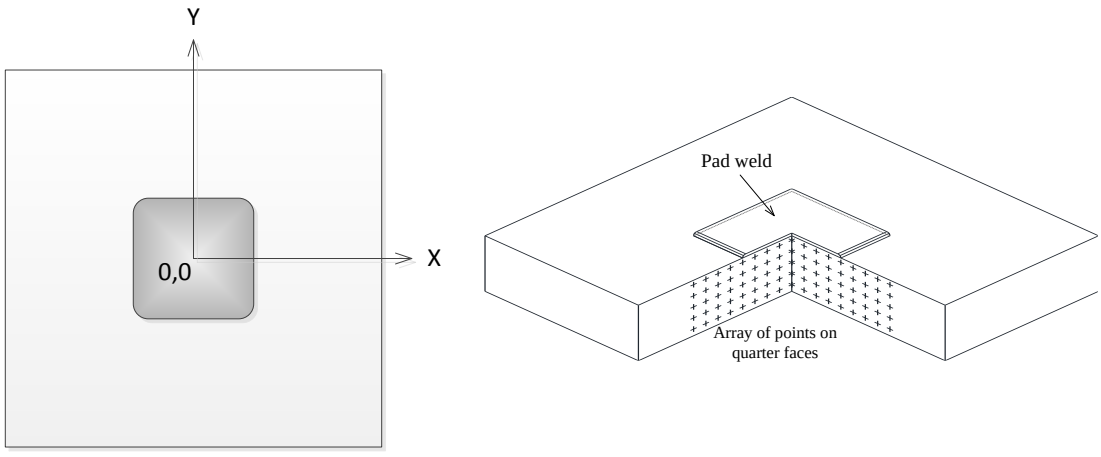

(a) (b)

Figure 3-19: Sample for residual stress measurement with neutron diffraction (a) Pad weld with "X" and "Y" reference directions and (b) The array of points where residual stress was measured along the depth of the plate in X and Y directions.

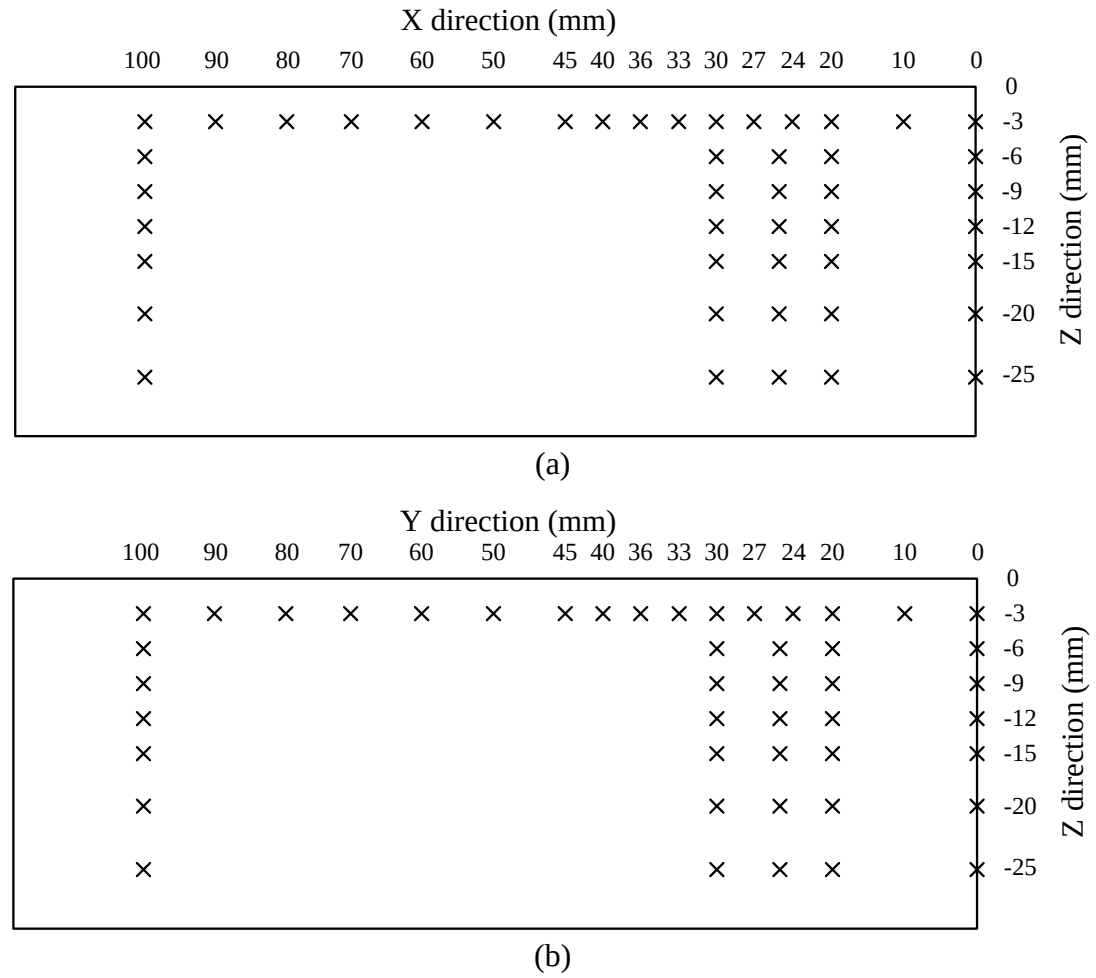

Figure 3-20: Residual stress measurement points of pad weld samples (a) on the XZ plane and (b) on the YZ plane. Z-direction was taken as the thickness and 0,0,0 point is on the top side of the pad weld plate.

Braggs low provides the theoretical foundation for measuring residual stresses of crystalline materials. According to Bragg's law, the spacing between atomic plans can be measured by knowing the diffraction angle and incident wavelength as shown in Figure 3-21 and Equation 10.

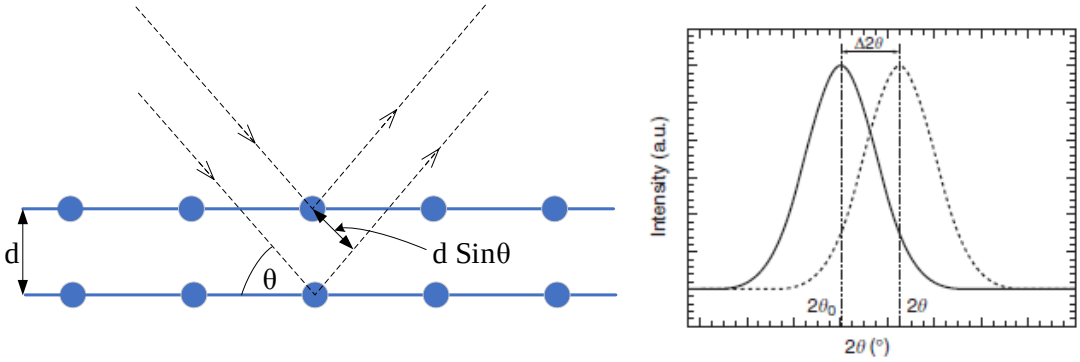

Figure 3-21: An illustration of Bragg's law and Principle of strain measurement with neutron diffraction [146].

$$\lambda = 2d\,Sin\theta \tag{10}$$

λ - Wavelength of the beam
d - Distance between crystal lattice
θ - Incident beam angle

The shifting of diffraction peaks is directly related to the changes of the inter-planner distance of crystal planes, hence the lattice strain can be determined.

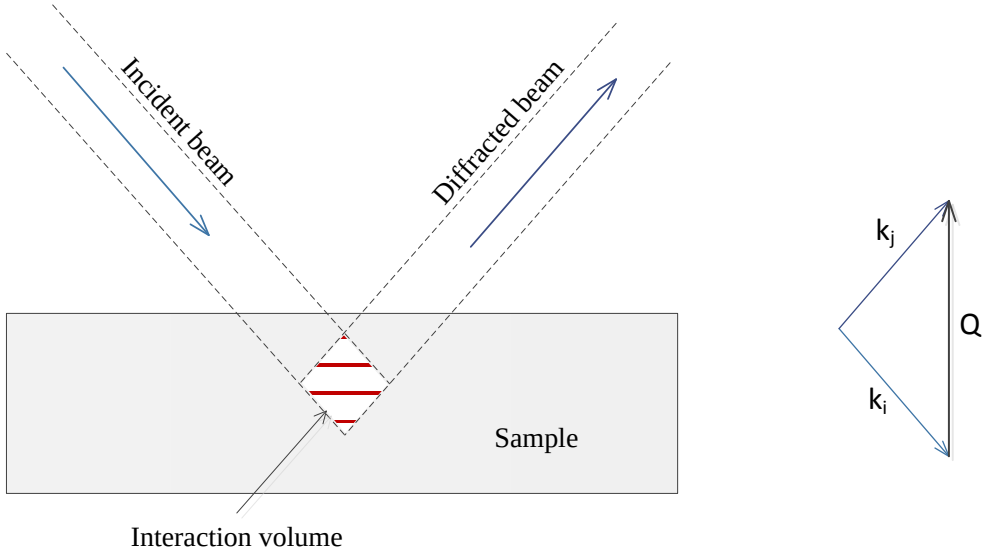

Figure 3-22: Neutron interaction with the material and definition of scattering vector Q

The elastic strain in "X" direction can be calculated by knowing the deformed lattice spacing in X direction, d_{xx} and unstressed lattice spacing, d_0 as described in Equation 11.

$$e_{xx} = \frac{(d_{xx} - d_0)}{d_0} \tag{11}$$

Stress can be calculated using Hooke's law as shown in Equation 12. Usual notations are used in the equation as E-Young's modulus, ν-Poison's ratio, ε_{xx}, ε_{yy} *and* ε_{zz} - elastic strain in three principal axes.

$$\sigma_{xx} = \frac{E}{(1+\nu)(1-2\nu)}[(1-\nu)\varepsilon_{xx} + \nu(\varepsilon_{yy} + \varepsilon_{zz})] \tag{12}$$

3.5 Microstructure characterisation

Microstructural characterisations were conducted with samples that were mounted in Bakelite, as well as with unmounted samples. Microstructural analysis was performed by optical microscopy, scanning electron microscopy (SEM) and transmission electron microscopy (TEM). Fracture analysis was performed with SEM. Electron Back Scattering Diffraction (EBSD) studies were conducted for characterisation of fracture propagation and, to study the effect of martensite packets and blocks for the impact toughness.

3.5.1 Metallographic sample preparation

Gleeble simulated HAZ samples were cut from the middle part of the HAZ and mounted in conductive Bakelite for optical micrography and SEM analysis, as shown in Figure 3-23. All real weld samples (BoP, pad and full penetration butt welds) were prepared unmounted by attaching the samples with double-sided tape to platens and using automated polishing machines. Specimens were machined beforehand to obtain flat, parallel faces. A series of grinding and polishing steps were used for samples, which varied depending on the characterisation method. Detail of sample preparation is described in Table 3-7. Additional steps for specific characterisation techniques are described in relevant sections.

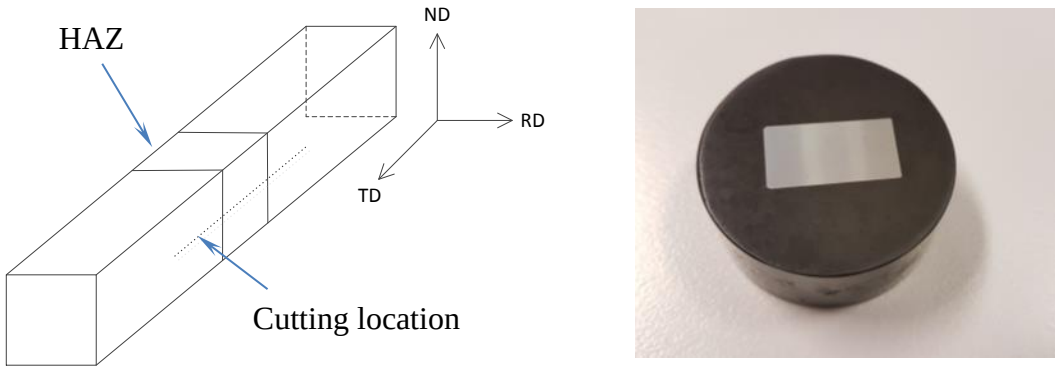

(a) (b)

Figure 3-23: Simulated HAZ samples (a) the location of the sample was cut for the metallurgical characterisation and (b) a mounted sample

Table 3-7: Steps of sample preparation for the optical microscopy and SEM

Step No.	**Grinding/Polishing method**	**rpm**	**Time/min**	**Force/N**
Step 1	240 Grit SiC paper	150	2	26
Step 2	600 Grit SiC paper	150	2	26
Step 3	1200 Grit SiC paper	150	2	22
Step 4	9 µm Diamond	150	5	22
Step 5	3 µm Diamond	150	5	22
Step 6	1 µm Diamond	150	5	22

Optical microscopy and SEM samples were etched with 2% Nital solution. To reveal prior austenite grain boundaries, selected samples were etched with saturated picric acid solution. Steps which were followed for picrel etching are described in Table 3-8. To identify MA particles, samples were etched with LePera's solution and steps for the LePera's etching is shown in Table 3-9.

Table 3-8: Steps of etching for revealing of PAGs

Step 1	Polish sample with 1 µm diamond
Step 2	Wash with soap and then with ethanol and dry
Step 3	Immerse in freshly prepared aqueous saturated picric solution with 4 drops of wetting agent (for 100 ml solution) for 2 minutes at room temperature
Step 4	Clean the black smudge with water and soap and quickly wash with 100% ethanol and dry

Table 3-9: Steps of LePera's etchant used for revealing MA particles

Step 1	Polish sample with 1 µm diamond
Step 2	Wash with soap and then with ethanol and dry
Step 3	Immerse in freshly prepared LePera's solution for 90 s. (1% aqueous solution of sodium metabisulfite ($Na_2S_2O_5$) and 4% picric acid ($C_6H_2(NO_2)_3OH$) in ethanol.
Step 4	Clean the sample with distilled water and then with ethanol and dry

3.5.2 Optical microscopy

Optical micrography was conducted on Leica DM6000 optical microscope, equipped with facilities for image stitching and focus-stacking. Bright field imaging technique was used for the majority of samples and bright field imaging with polarised light was used for some selected samples.

3.5.3 Scanning Electron Microscopy (SEM)

A scanning electron microscope was used for characterisation of both polished and fractured samples. SEM studies were conducted at Electron Microscopy Centre (EMC) at the University of Wollongong using a JEOL JSM-6490LV and a JEOL JSM-7001F and at Defence Science and Technology (DST) Group, Melbourne, using a JEOL JSM-6490LV. The JEOL JSM-6490 machines are 30 kV SEMs with conventional tungsten filament and JEOL JSM-7001F is equipped with thermal field emission gun.

3.5.4 Electron Back Scattering Diffraction (EBSD)

In EBSD, diffraction patterns provide crystallographic information related to their location of origin in on the specimen [14]. For EBSD, mounted samples with 12 mm diameter mounts were prepared to allow samples to be small enough to facilitate 15 mm working distance for EBDS/EDS mapping. For sample preparation, all above steps described in Table 3-7 was followed with the additional steps of 0.25 µm diamond polish for 3 min and 50% diluted OP-S polishing for 2 mins.

EBSD experiments were conducted to obtain crystallographic information in HAZ samples with single and multiple thermal cycles. JEOL JSM-7001F equipped with Oxford Instruments Nordlys II(S) high-resolution EBSD camera was used for this study. All EBSD maps were obtained with steps of 0.1 µm and 0.15 µm. 15 kV,

~2 nA and 15 mm working distance was maintained for all samples and EDS and EBSD maps were obtained simultaneously.

Post-processing of EBSD data was carried out in HKL-Channel 5 software suite. Wild orientation spikes and zero solution sites were removed with extrapolation of up to four neighbouring pixels to clean the data.

3.5.5 Transmission Electron Microscopy (TEM)

Transmission electron microscope studies were conducted with JOEL-JSM 2010, 200 kV, LaB_6 transmission electron microscope to identify martensite laths and finer precipitates in the HAZ.

Thin foils were prepared from simulated HAZ specimens by using a precision cut-off machine (Accutom-50) to slice thin disks of approximately 150-250 µm thick. The thin slices were ground down to below 100 µm using a Struers Accustop specimen holder and 1200 grit SiC paper. 3 mm disks were punched out of the slices and ground down, using 1200 grit and 4000 grit paper, to between 70-80µm, the optimal thickness for electro-polishing steel TEM samples.

Electro-polishing was conducted using a Struers Tenupol-5, Twin jet electro-polishing unit. A sample holder clamps on the rim of the 3 mm disks and is placed between two jet nozzles. The sample acts as the anode and the nozzles act as the cathode and both are submerged in an electrolyte. A 10% Perchloric, 90% ethanol electrolyte was used at temperatures below -30^{o}C. The electrolyte is pumped against both sides of the disk, leading to thinning at the centre. Once a hole forms, a light sensor shuts off the polishing and the sample holder is immediately removed from the unit and rinsed in two baths of ethanol. The electro-polishing settings were; 22-23.5 V, initial pump 20 (0 sec), final pump 10 (12 sec) and light stop of 12.

3.5.6 TEM sample preparation with FIB

Focussed Ion Beam (FIB) was used to obtain a thin sample from a targeted area on ICCG region of real weld samples. TEM sample was prepared with FEI Helios

NanoLab G3 CX scanning electron microscope equipped with a focussed ion beam. An example of an ICCG region identified on single repair pad weld sample is shown in Figure 3-24(a) and image (b) shows the FIB TEM sample, ready for removal.

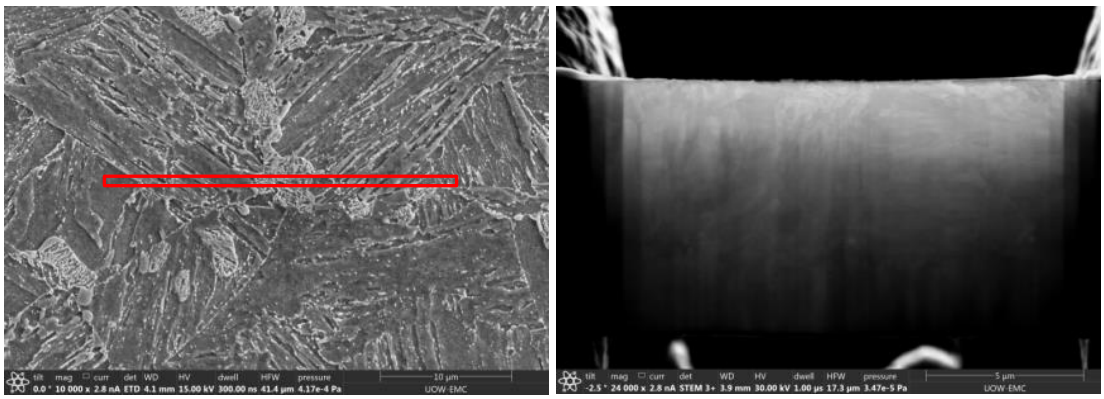

(a) (b)

Figure 3-24: TEM sample preparation with FIB (a) the location of where the sample was taken is shown by the red box. The length was about 15µm and the sample was cut into the material. (b) finalised sample with electron transparent region.

4 RESULTS

This section contains all the results of the research obtained in order to support the conclusions of the project. Results from dilatometer studies and microstructural characterisations of multiple repairs of real and simulated welds are discussed in Sections from 4.1 to 4.5. Charpy impact toughness tests with analysis of instrumented Charpy results are presented in Section 4.6. Hardness, fractography, TEM, dynamic tear and residuals stress results are presented in Sections from 4.7 to 4.11. The last section (4.12) provides the results from EBSD analysis.

4.1 Transformation temperatures with high heating rates

Phase transformation temperatures of BIS812 EMA steel at different heating rates were measured using dilatometry and are showed in Figure 4-1. These transformation temperatures were used for designing the heating and cooling cycles in Gleeble HAZ simulations as discussed in section 3.2.

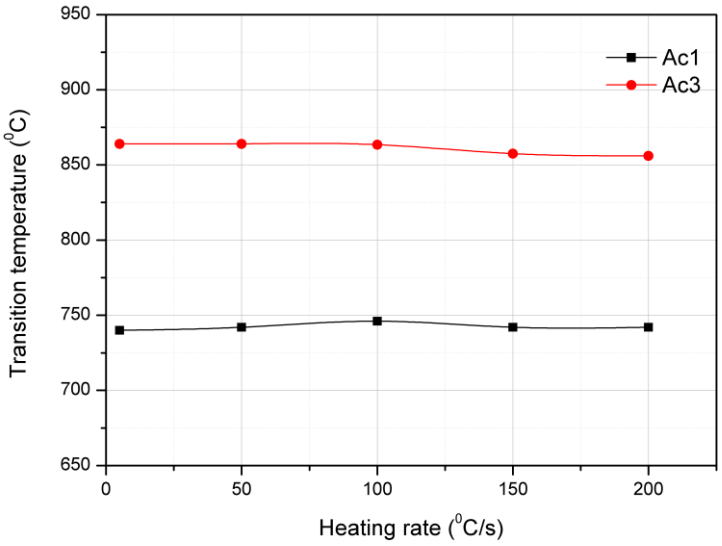

Figure 4-1: Lower and upper transition temperatures (Ac_1 and Ac_3) of BIS812 EMA steel at different heating rates.

At the heating rate of 200 °C/s, the lower and upper transformation temperatures were 740°C and 860°C, respectively. These temperatures were used to design the intercritical test temperatures use in HAZ simulations. The transformation temperature of martensitic steel has previously been studied and it was found that there was a slight increase of transformation temperature with increased heating rate [15]. The transformation temperatures of BIS812 EMA steel was relatively stable in

the heating rates between 5 ºC/s and 200 °C/s. Higher heating rates were not tested due to the limitations of the dilatometer equipment.

4.2 Prior austenite grain sizes

In fusion welding, the microstructure will vary, depending on the thermal cycle experienced by the parent metal. The largest grain size can be found near to the fusion line and as the temperature decreases, so also does the Prior Austenite Grain Size (PAGS).

To produce different PAG sizes, which represent the CG to FGHAZ region, a Gleeble simulator was used, as described in section 3.3.3. The prior austenite grains were revealed with Picral etching (section 3.5.1). The micrographs obtained after etching are shown in Figure 4-2. The variation of PAG size with the maximum temperature is shown in Table 4-1. The peak temperatures of 1000ºC and 1100ºC represent the fine grain (FGHAZ) region of a real weld HAZ and temperatures 1200ºC, 1300ºC and 1350ºC represent the coarse grain (CGHAZ) region in a real weld.

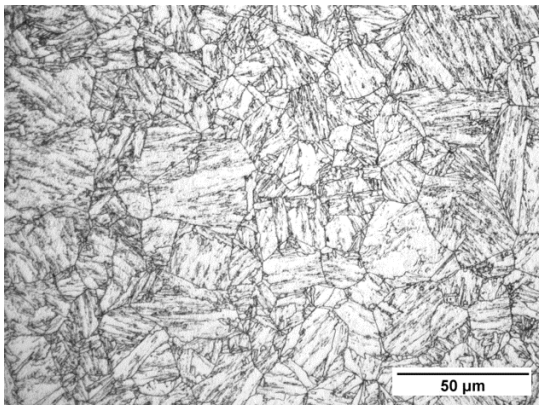

(a)

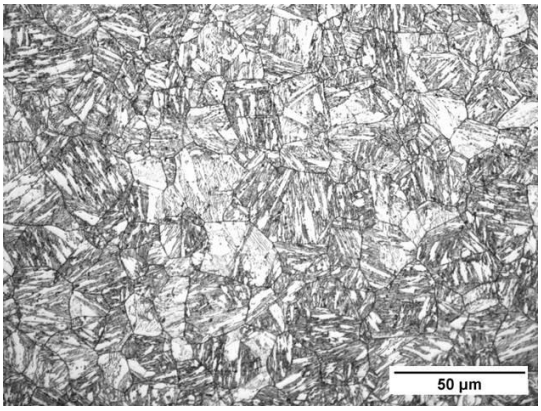

(b)

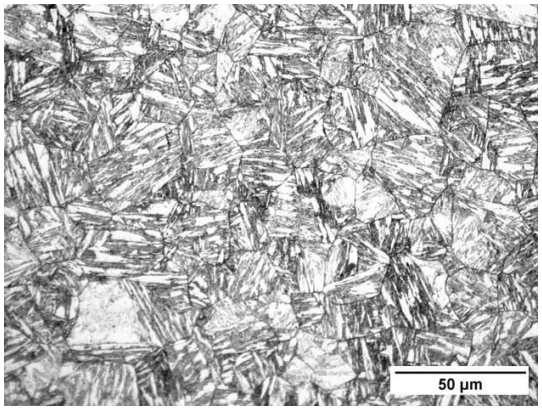

(c)

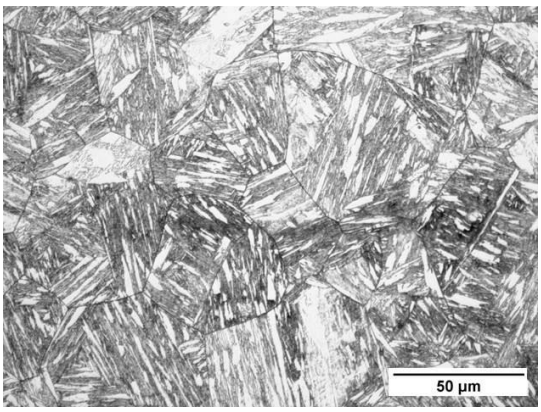

(d)

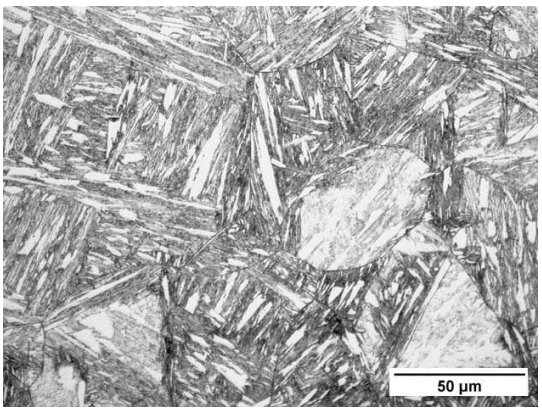

(e)

Figure 4-2: Etched samples with saturated picric acid for measurement of Prior Austenite Grain (PAG) sizes for different peak temperatures. From (a) to (e), Base metal, at 1100°C, at 1200°C, at 1300°C and at 1350°C, respectively.

Table 4-1: Average prior austenite grain sizes achieved with different peak heating temperatures (from minimum of 50 grains).

Maximum temperature of the first cycle/ °C	**Parent metal**	**1000**	**1100**	**1200**	**1350**
Average PAG size/µm	18±7	11±5	15±5	27±13	64±18

Figure 4-3: shows the variation of average PAG size with heating temperature. The average grain size increased, as the peak temperature increased.

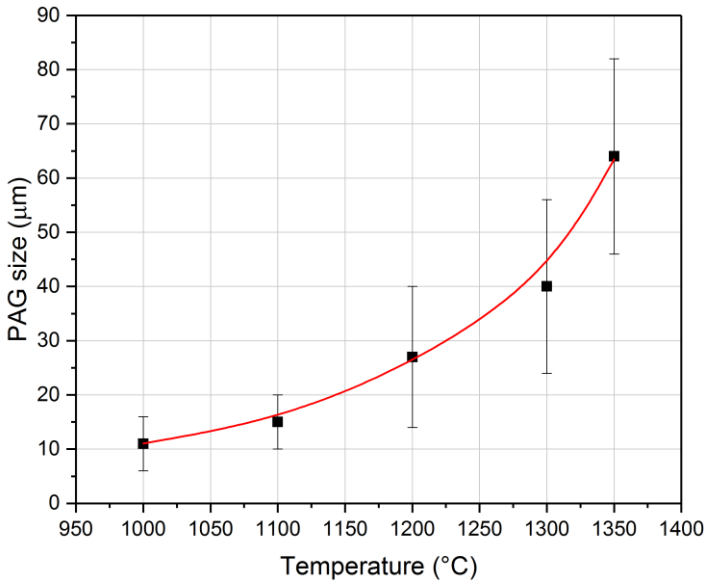

Figure 4-3: The variation of average PAG size in the simulated HAZ specimens with different peak temperatures.

Figure 4-4 shows the typical microstructure of BIS812 EMA base material. The microstructure predominantly consisted of tempered martensite. The 2% Nital etch revealed the typical lath-like structure of martensite. The size of martensite packets varied with the variation of PAG sizes.

Figure 4-4: Typical microstructure of BIS812 EMA steel with 2% Nital etch.

In multi-pass welds, the HAZ generated by the first weld is reheated by the second weld. Therefore, more complex microstructure is present in the regions where the two thermal cycles overlap, as was described in Section 2.2. The microstructures produced with single and double thermal cycle simulation using the Gleeble are shown in Figure 4-5. Microstructures related to CGHAZ and FGHAZ are shown in Figure 4-5 (a-b), which were reheated by a second thermal cycle, within the inter-critical temperature, as shown in c) and d) respectively. Formation of MA phase along the prior austenite grain boundaries can be seen in the reheated samples, as highlighted by the arrow in Figure 4-5(c).

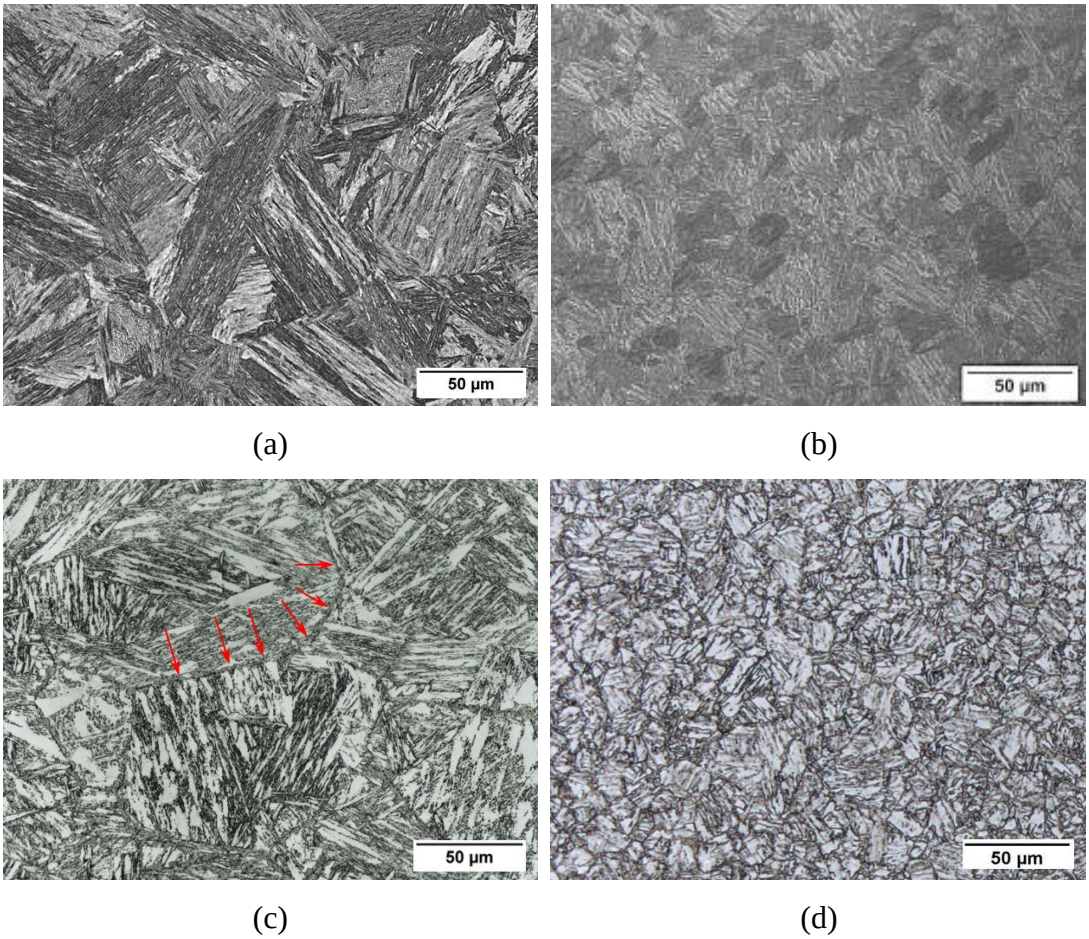

Figure 4-5: Microstructural changes in with intercritical reheating. (a) and (b) are single thermal cycles at 1350°C and 1100°C peak temperatures and (c) and (d) are double thermal cycles with subsequent heating up to 750°C (just above the A_{c1} temperature), after the first thermal cycle. (2% nital etch for 5 s).

4.3 Instrumented welding

Thermal profiles of BoP, pad and full penetration butt welds were recorded with imbedded thermocouples, at 2.5 mm and 4 mm below the surface. Thermal profiles for first and second BoP welds are shown in Figure 4-6 (a) and (b), respectively.

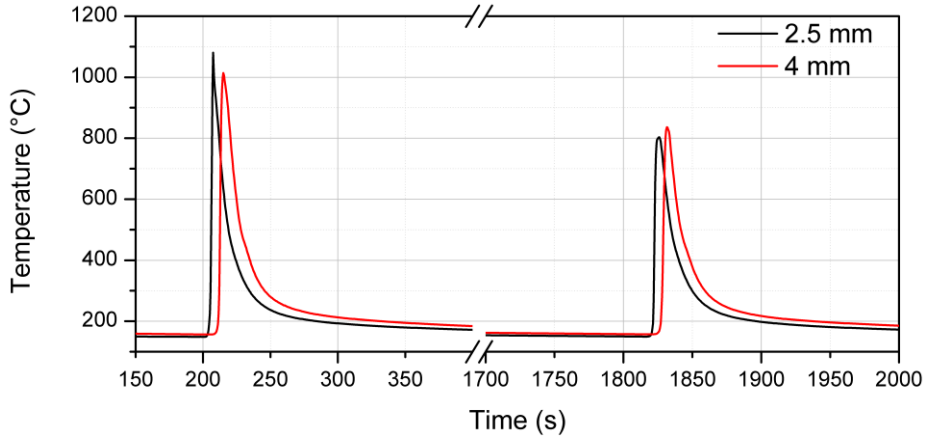

(a)

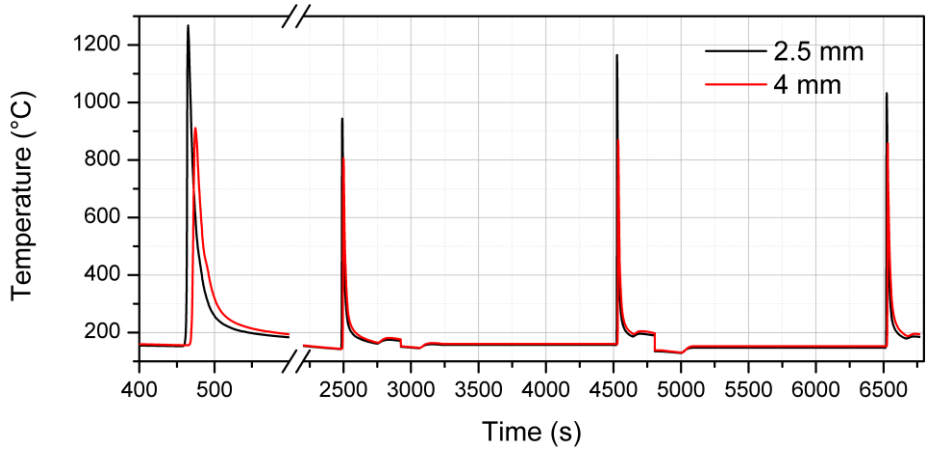

(b)

Figure 4-6: Temperature histories of BoP welds (a) first weld and (b) second weld (first repair weld), at 2.5 mm and 4 mm below the surface under weld beads.

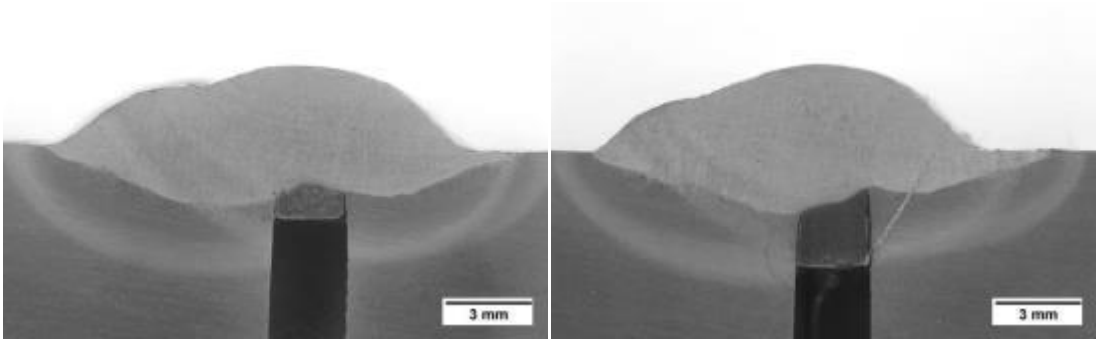

(a) (b)

Figure 4-7 Cross sections of BoP welds through the plug where the thermocouples were mounted, where (a) 2.5 mm and (b) 4 mm (Actual distances measured from fusion line to thermocouples were 1.4 and 2.5 mm)

Cross sections of completed welds were observed to allow more accurate measurements of the distance from the fusion line to the thermocouple. A cross section view of two BoP welds through the thermocouple locations are shown in Figure 4-7.

4.4 Microstructural characterisation

Microstructures of both simulated HAZ and real weld specimens were observed with an optical microscope and SEM. The comparison between real and simulated HAZ is shown for two different regions are shown in Figure 4-8. For microstructure characterisations, the microstructures of the simulated HAZ specimens will be presented first.

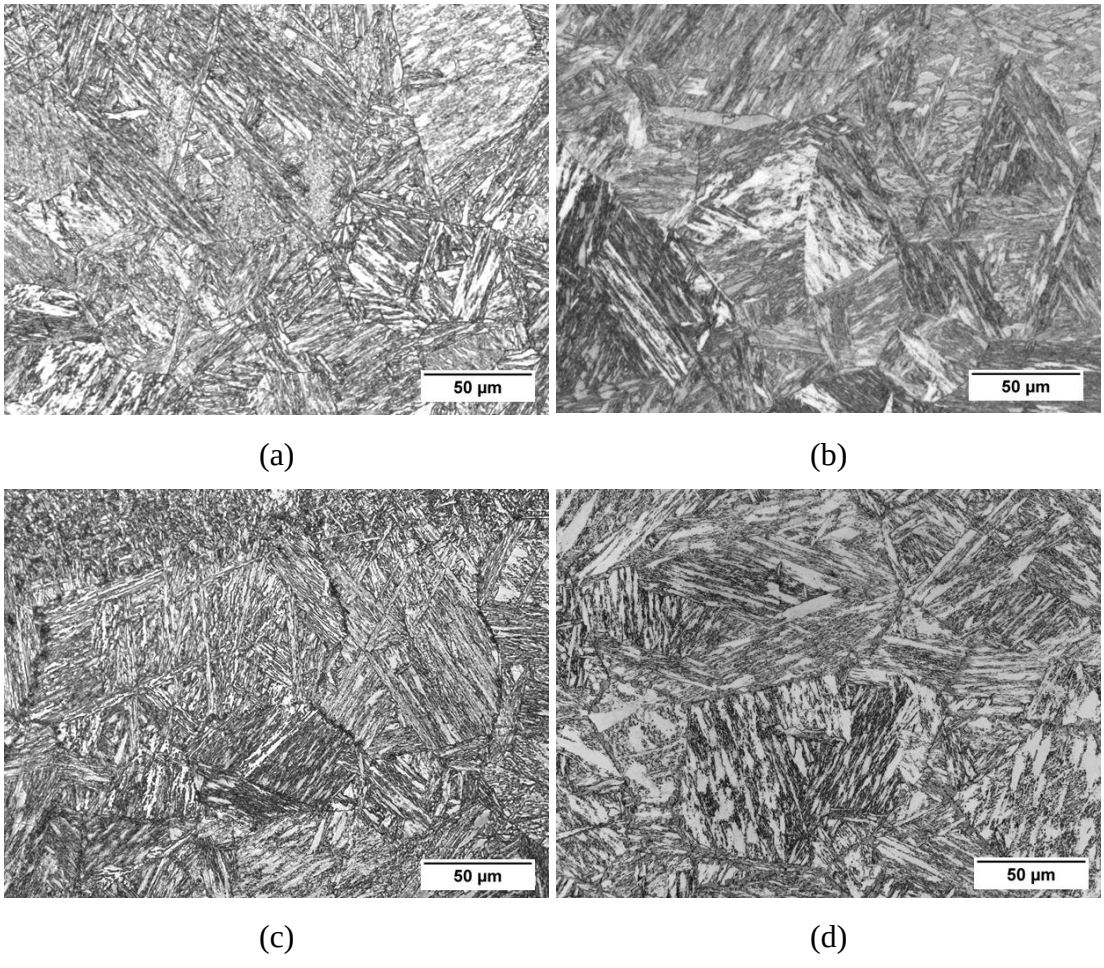

Figure 4-8: The comparison between simulated and real weld microstructures (a) and (c) are real weld HAZ microstructures of CG and ICCG regions and, (b) and (d) are CG (1350°C) and ICCG (1350-750°C) simulated samples (with 2% natal etch).

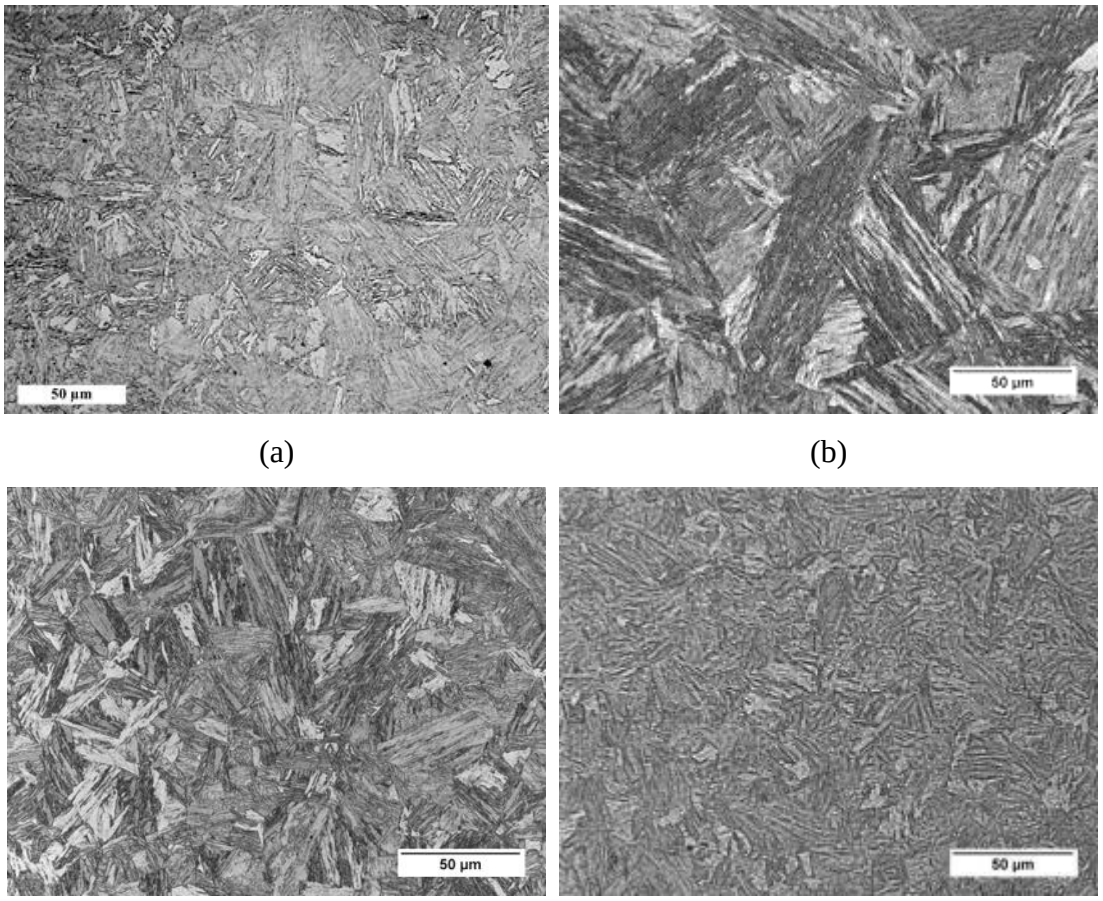

Figure 4-9: Microstructures of base material and simulated HAZ with 2% Nital etch. (a) unaffected base material and, single thermal cycles with (b) 1350°C peak, (c) 1200°C peak and (d) 1100°C peak.

Micrographs of unaffected parent metal and single-cycle thermal simulated HAZ's are shown in Figure 4-9. The parent microstructure mainly consisted of tempered martensite with an average PAG size of 18 µm. Single-cycle simulated samples showed martensitic structure, where the PAG size, block and packet sizes decreased as the peak temperature decreased.

Double-cycle simulated HAZ's, where the second thermal cycles were in the intercritical range, are shown in Figure 4-10. All samples showed secondary MA phase along grain boundaries with thinner MA at 750°C and broader MA at 850°C cycles. At the highest IC cycles, the degree of transformation was substantial, so the 'MA' phase, is now newly formed lath martensite, however, the term 'MA' is still used for consistency.

Secondary electron images taken with an SEM of double cycle simulated HAZ, with the IC temperatures of 750°C and 850°C, showed differences between the size and distribution of MA phases. As shown in Figure 4-11, the ICCG with IC at 750°C, showed thin, non-continuous MA phase along grain boundaries. The ICCG samples with higher IC temperatures, 800 and 850°C, showed continuous and increasingly wider MA phase. Furthermore, the amount of MA phase at each intercritical temperature, increased as the peak initial temperature decreased (CG to FGHAZ).

At higher magnifications, (Figure 4-11(e)) formation of secondary laths was observable within the MA phase.

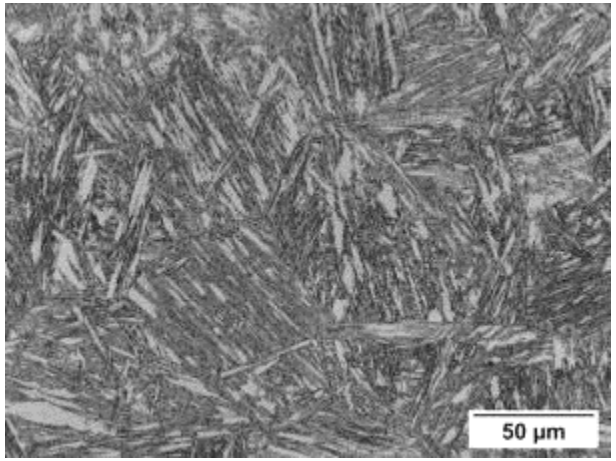

(a)

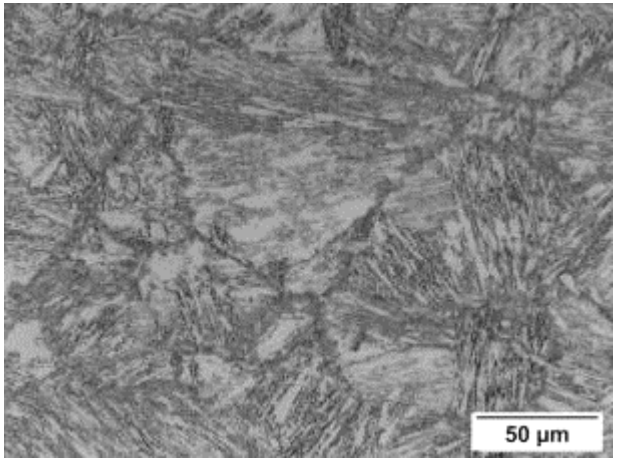

(b)

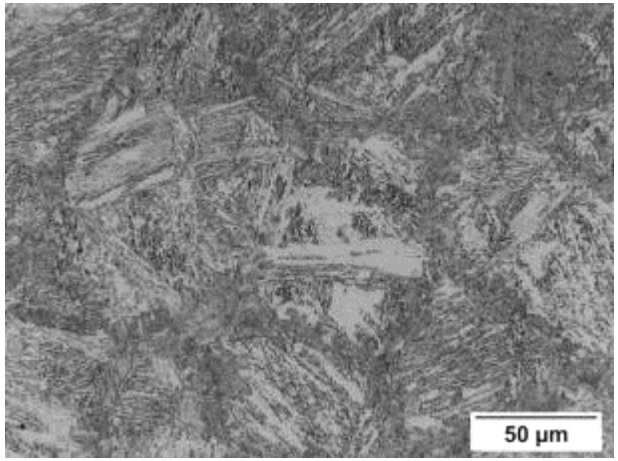

(c)

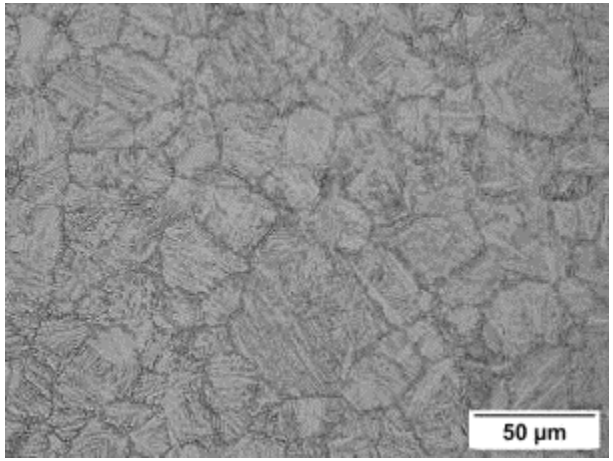

(d)

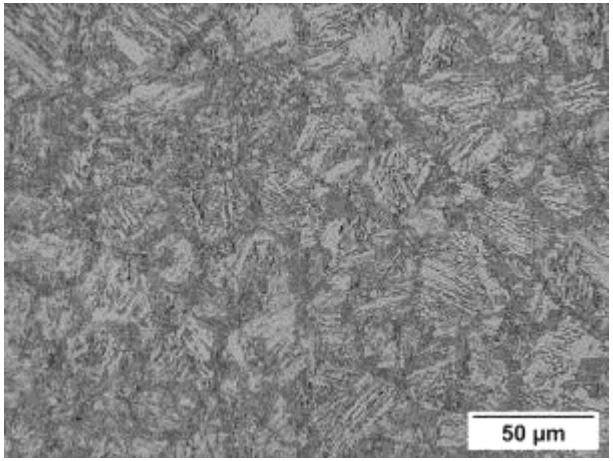

(e)

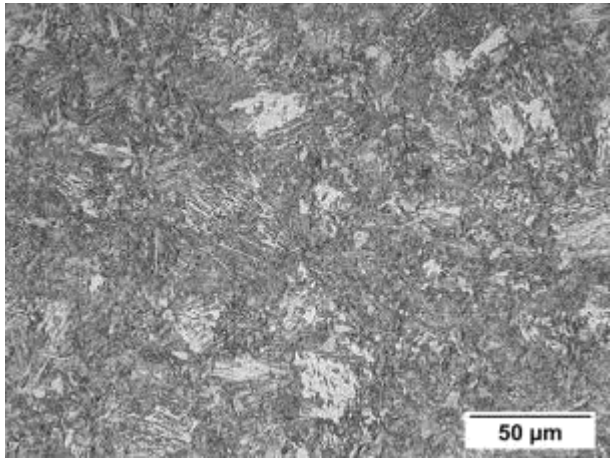

(f)

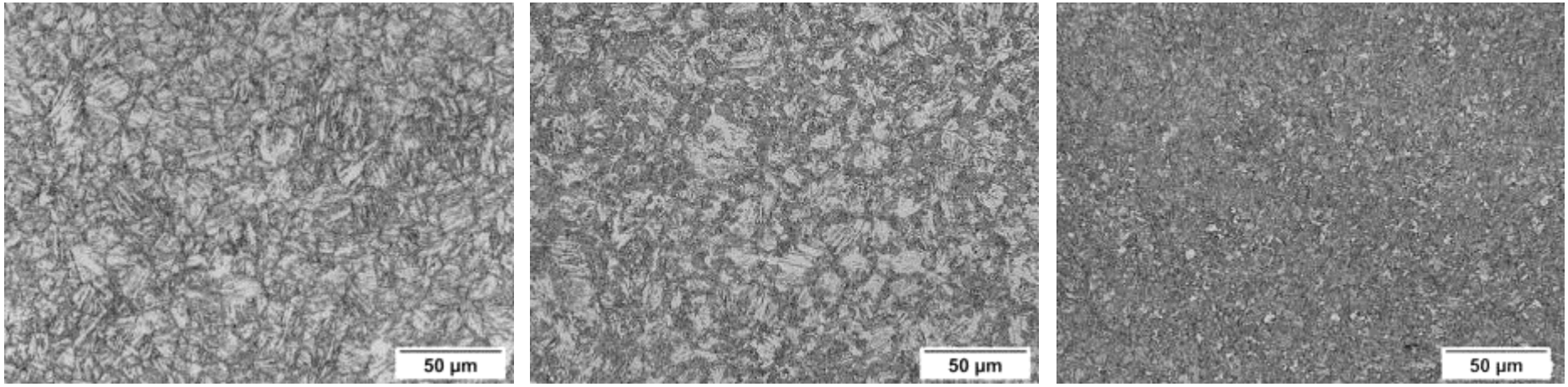

(g) (h) (i)

Figure 4-10: Optical micrographs of series of two cycle simulated HAZ specimens with 2% Nital etch, where; (a)1350-750°C, (b) 1350-800°C, (c) 1350°C-850°C, (d) 1200-750°C, (e) 1200-800°C, (f) 1200-850°C, (g) 1100-750°C, (h) 1100-800°C and (i) 1100-850°C.

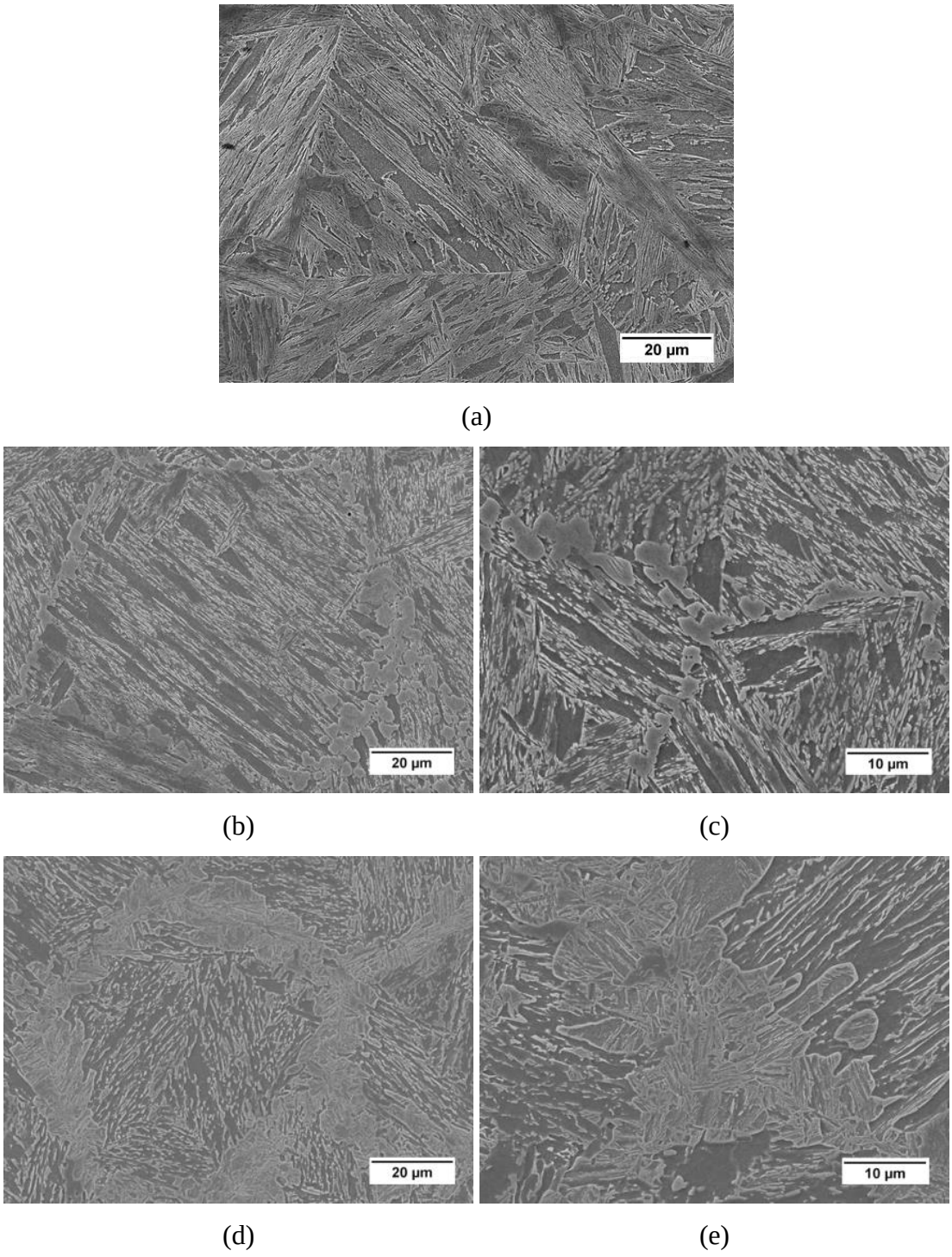

Figure 4-11: Secondary electron images of simulated single and double thermal cycles (a) Single thermal cycle at 1350°C peak (b) and (c) 1350-750°C, (d) and (e) 1350-850°C.

4.4.1 Microstructure with multiple repeated thermal cycles

Microstructures of multiple repeated thermal cycle simulated samples were analysed under an optical microscope. Multiple thermal cycles consisted of repeating either a single HAZ cycle, such as CG-CG-CG-CG (CG×4; four consecutive CG cycles) or repeating double intercritical HAZ cycles, such as CG-IC-CG-IC-CG-IC-CG-IC ((CG-IC)×4; four CG-IC cycles). Repeat cycles were compared with single cycles.

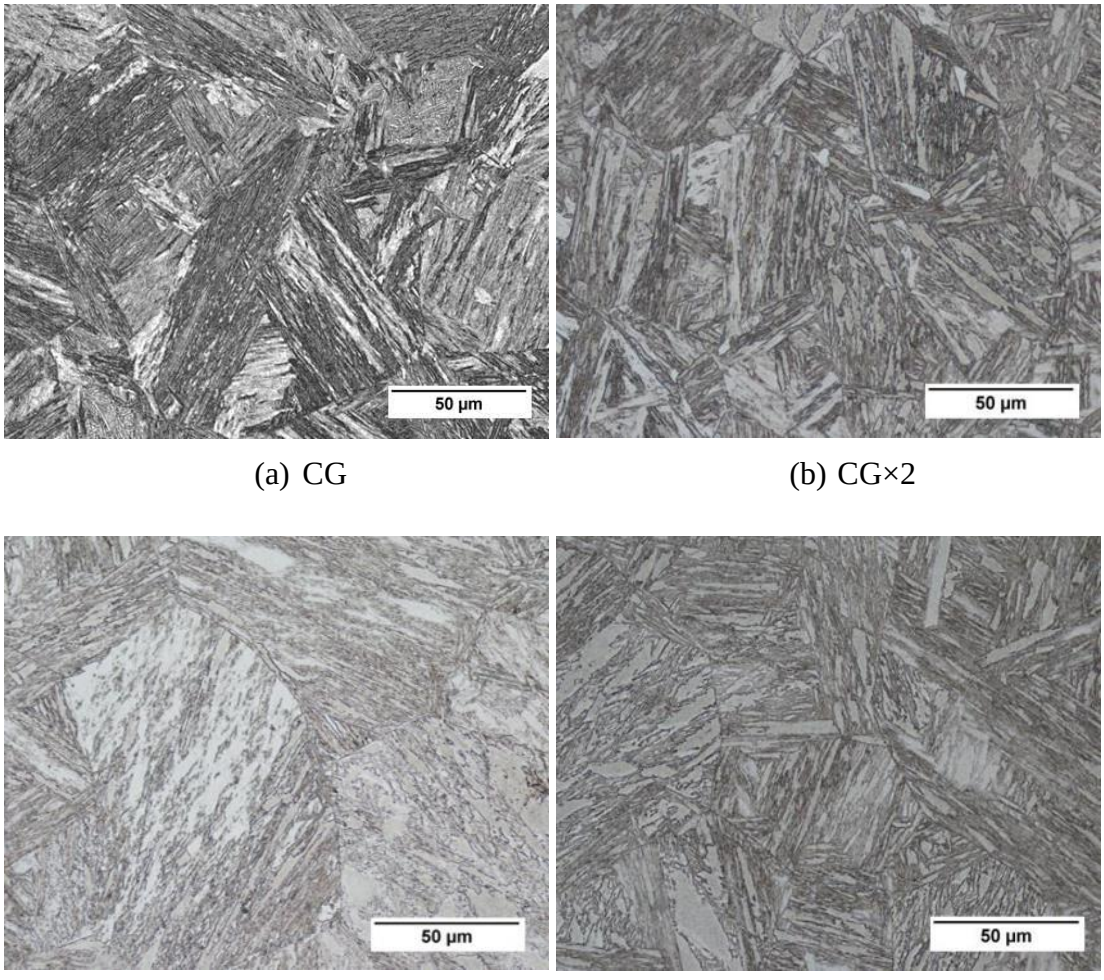

(a) CG (b) CG×2

(c) CG×3 (d) CG×4

Figure 4-12: Comparison of CG HAZ (1350°C) from; (a) single CG cycle, (b) double CG cycles, (c) three CG cycles and (d) four CG cycles. (with 2% Nital etch).

In Figure 4-12, the microstructures for (a) CG, (b) CG×2, (c) CG×3 and (d) CG×4 are shown. Irrespective of the number CG cycles, all samples showed lath martensite microstructure, with a similar average PAG size varied between 64-69 µm. This

indicated that the previous CG microstructure was replaced by a new, but similar, CG microstructure.

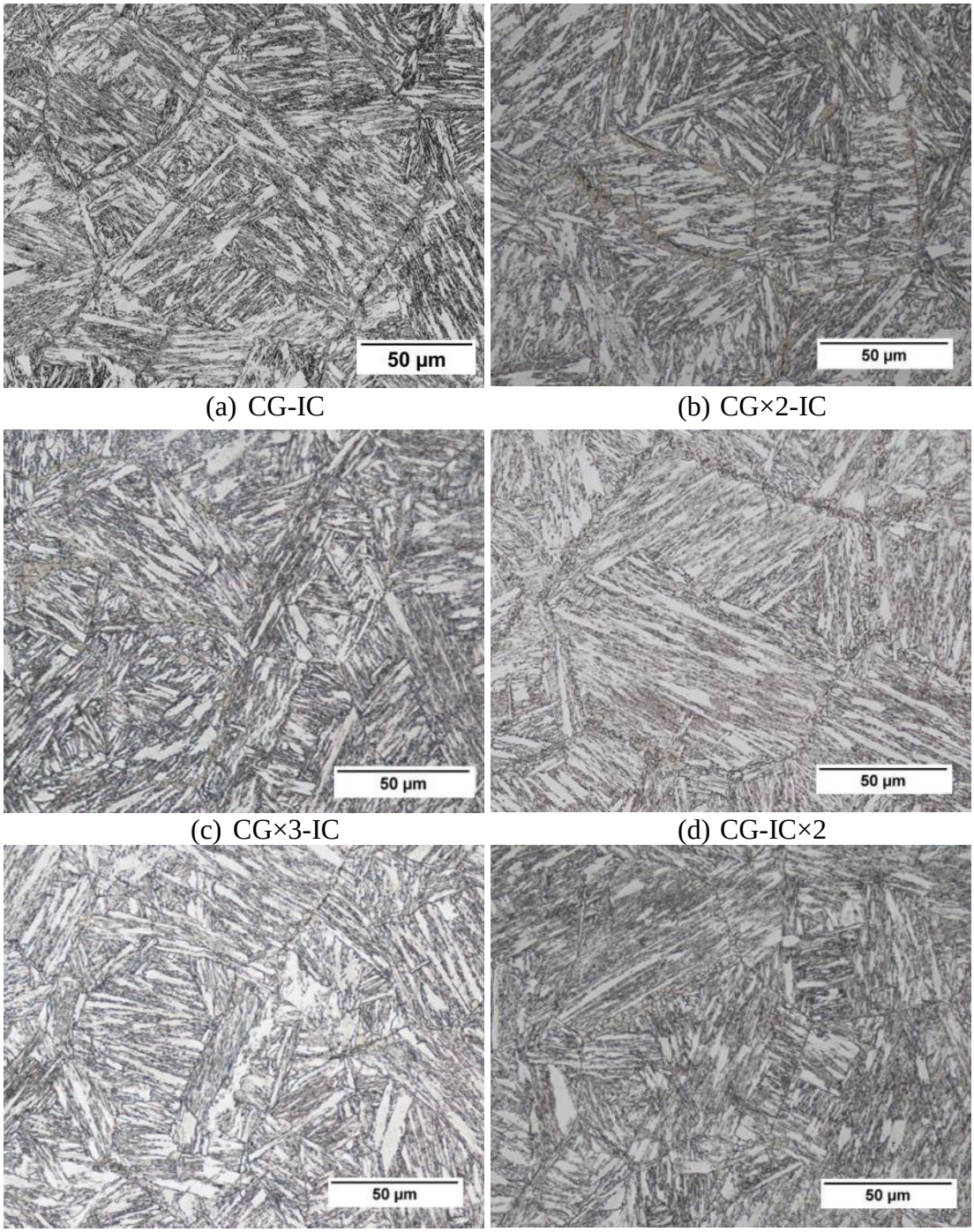

(a) CG-IC (b) CG×2-IC

(c) CG×3-IC (d) CG-IC×2

(e) CG-IC×3 (f) (CG-IC)×2

Figure 4-13: Comparison of different of CG and IC thermal cycle tested, where CG - 1350°C and IC - 750°C. (a) to (c) were CG-IC cycles with only the CG cycle repeated, (d) to (e) were CG-IC cycles with only the IC cycle repeated and (f) was a CG-IC×2 cycle. (2% Nital etch).

Samples with CG and IC thermal cycles, where the intercritical cycle was 750°C, did now show a noticeable variation of the microstructure, as shown in Figure 4-13. In Figure 4-13, (a) to (c) were CG-IC cycles with only the CG cycle repeated, (d) to (e) were CG-IC cycles with only the IC cycle repeated and (f) was a CG-IC×2 cycle. All samples finished with a 750°C IC cycle and the amount and distribution of secondary MA phase present was similar. Even with two or three IC cycles on top of a CG thermal cycle, did not change the size and distribution of MA. This is probably due to the high heating and cooling rates and very short hold time (0.5 s) at the peak temperature, limiting the time available for microstructural changes.

4.5 Real weld microstructures

4.5.1 BoP welds

BoP welds were sectioned, and the microstructure investigated for initial weld (or 1st weld) to repair 4 (or 4th weld). All four repair weld samples had similar weld and HAZ morphology, as shown in the macrographs of Figure 4-14. The first, second, third and fourth repair welds are referred to as BoP1, BoP2, BoP3 and BoP4, respectively.

The BoP welds consisted of two weld beads, so reheated HAZ microstructures were observed for all four repair welds. Unlike the simulated HAZ specimens, real welds consist of the full spectrum of heat affected zones. An example of this is shown in Figure 4-15, which is a composite image of the intercritically reheated region (between the two weld beads), showing a transition from CG and CG-IC to FG and FG-IC microstructures, for BoP repair 1. In Figure 4-16, typical images of the microstructures of CG, CG-IC, FG-IC and FG regions for the BoP repair 1 sample are shown. As the equivalent sub-HAZ microstructures were similar for all four BoP repairs, only images from repair 1 and repair 4 are shown. The same HAZ microstructures shown for BoP 1 are shown in Figure 4-17 for BoP 4. There was no noticeable difference in the microstructures of repair 1 and repair 4. The result was consistent with similar microstructures observed for the simulated HAZ samples with multiple thermal cycles.

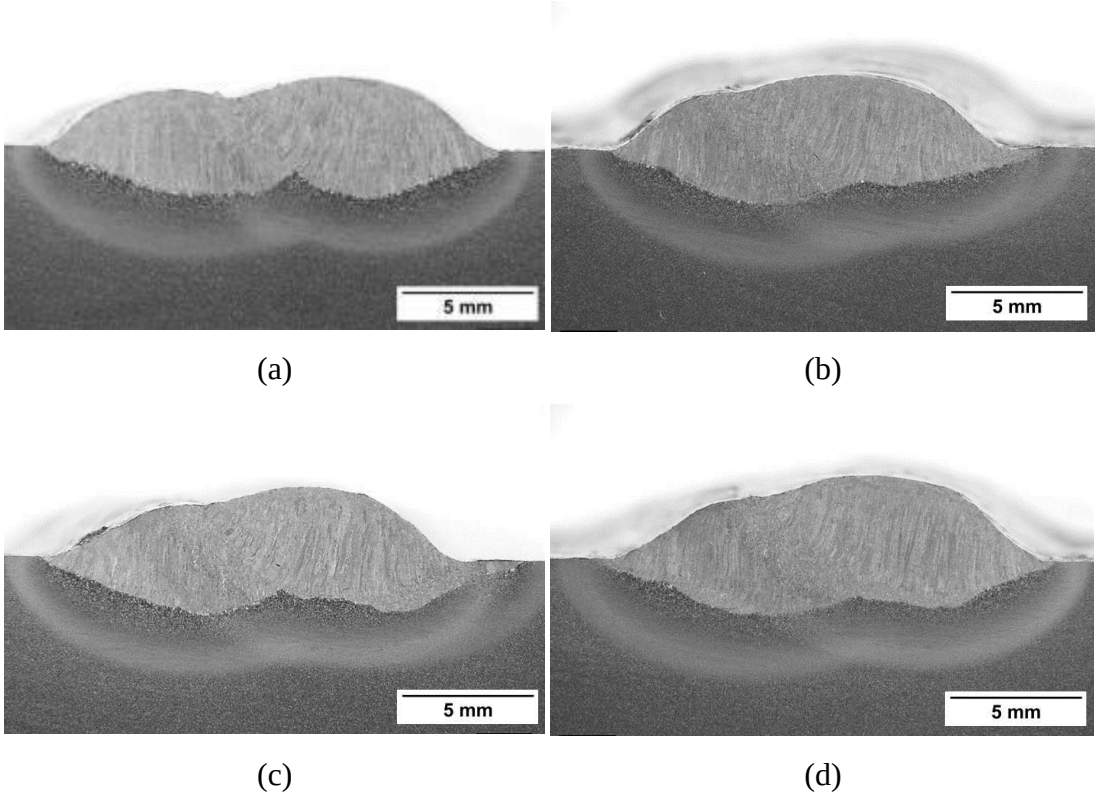

Figure 4-14: Macrographs of BoP repair welds. Macrographs (a), (b), (c) and (d) are BoP1, BoP2, BoP3 and BoP4, respectively. BoP 1 is first weld and BoP 4 is forth weld (third repair weld). The first-pass of the weld is on the left side and the second-pass was on right side.

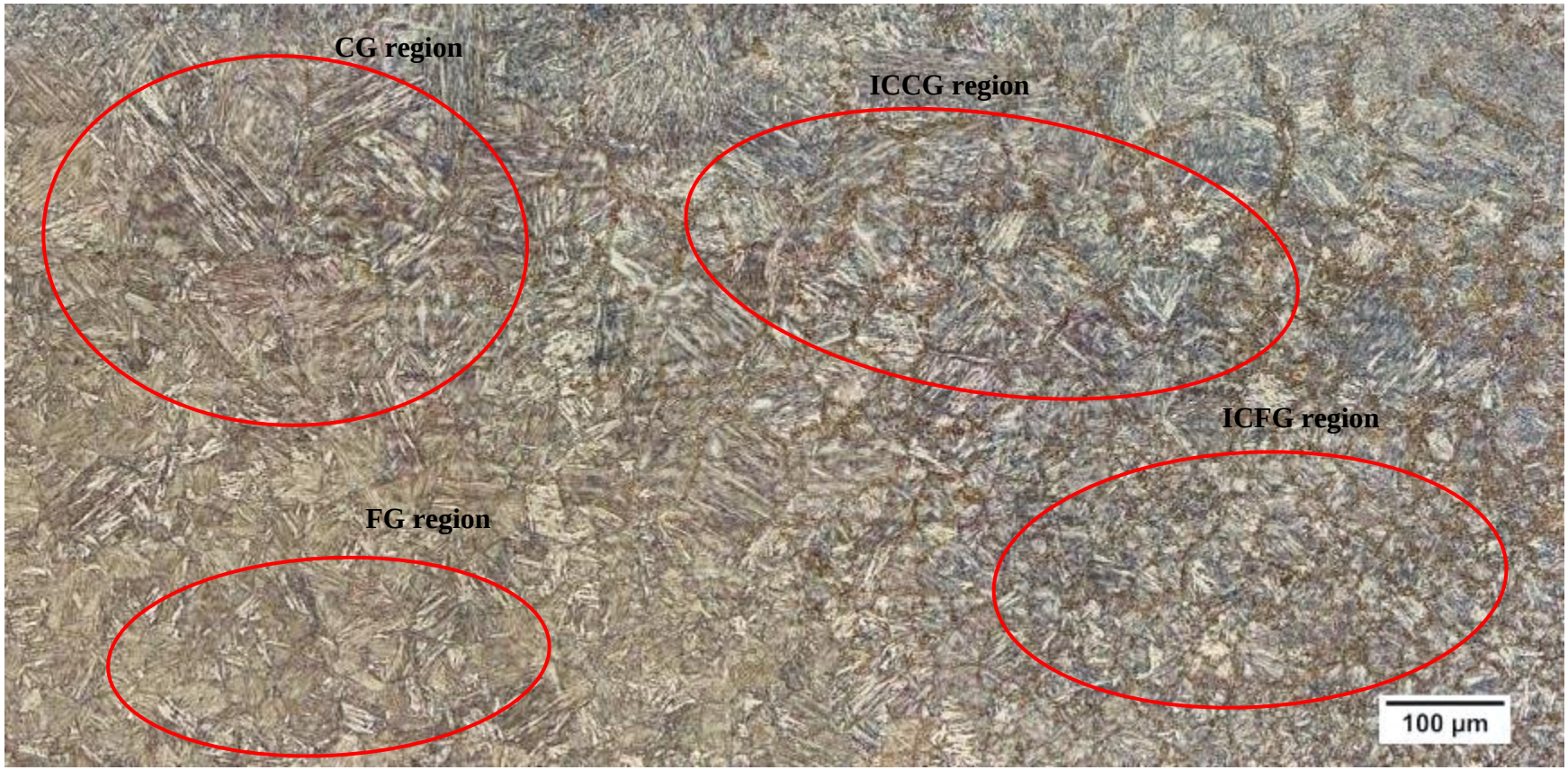

Figure 4-15: Stitched Micrograph showing the varying microstructure of a real HAZ, showing a transition from CG and CG-IC to FG and FG-IC microstructures, for BoP 1.

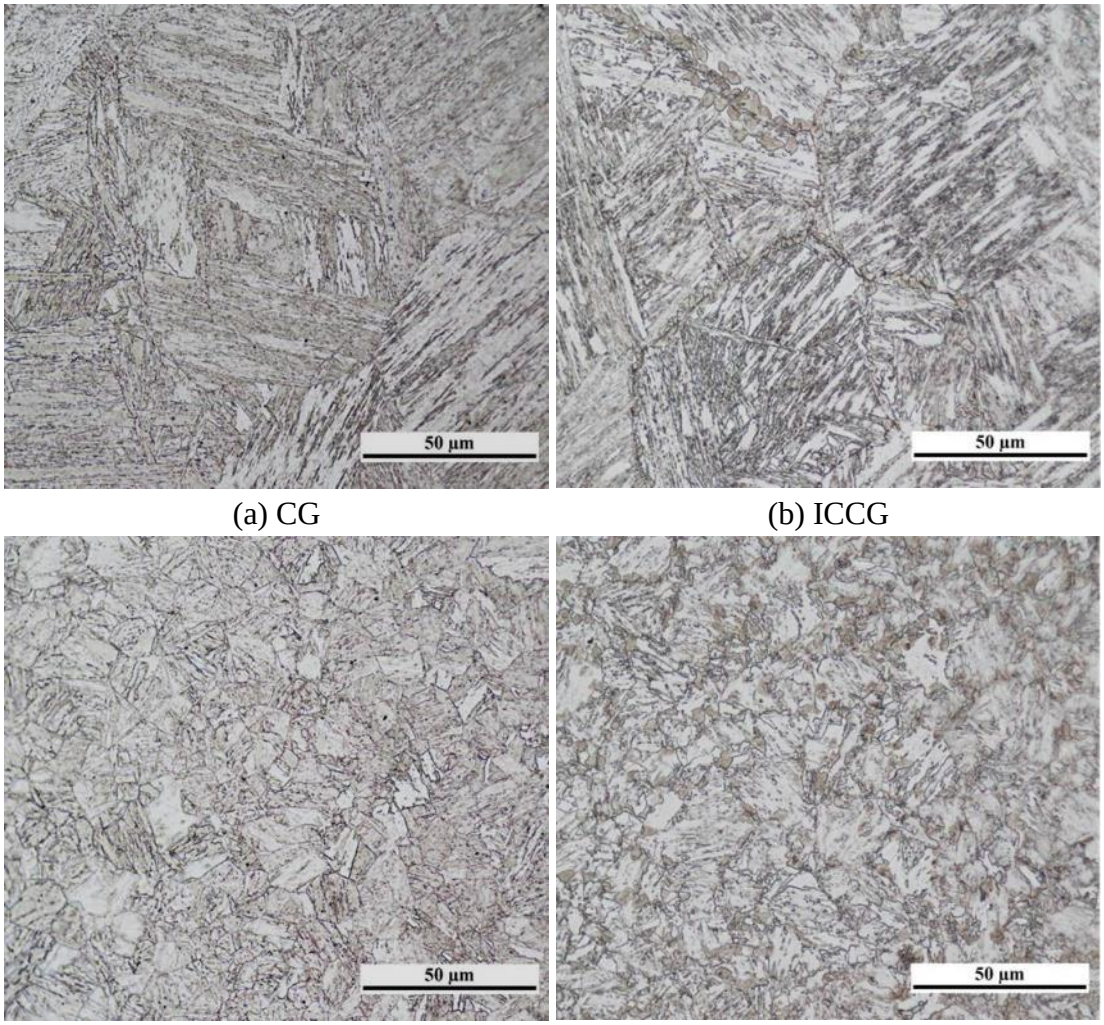

(a) CG (b) ICCG

(c) FG (d) ICFG

Figure 4-16: Typical optical images of specific HAZ microstructure for BoP 1 where; (a) CG region, (b) ICCG region, (c) FG region and (d) ICFG region.

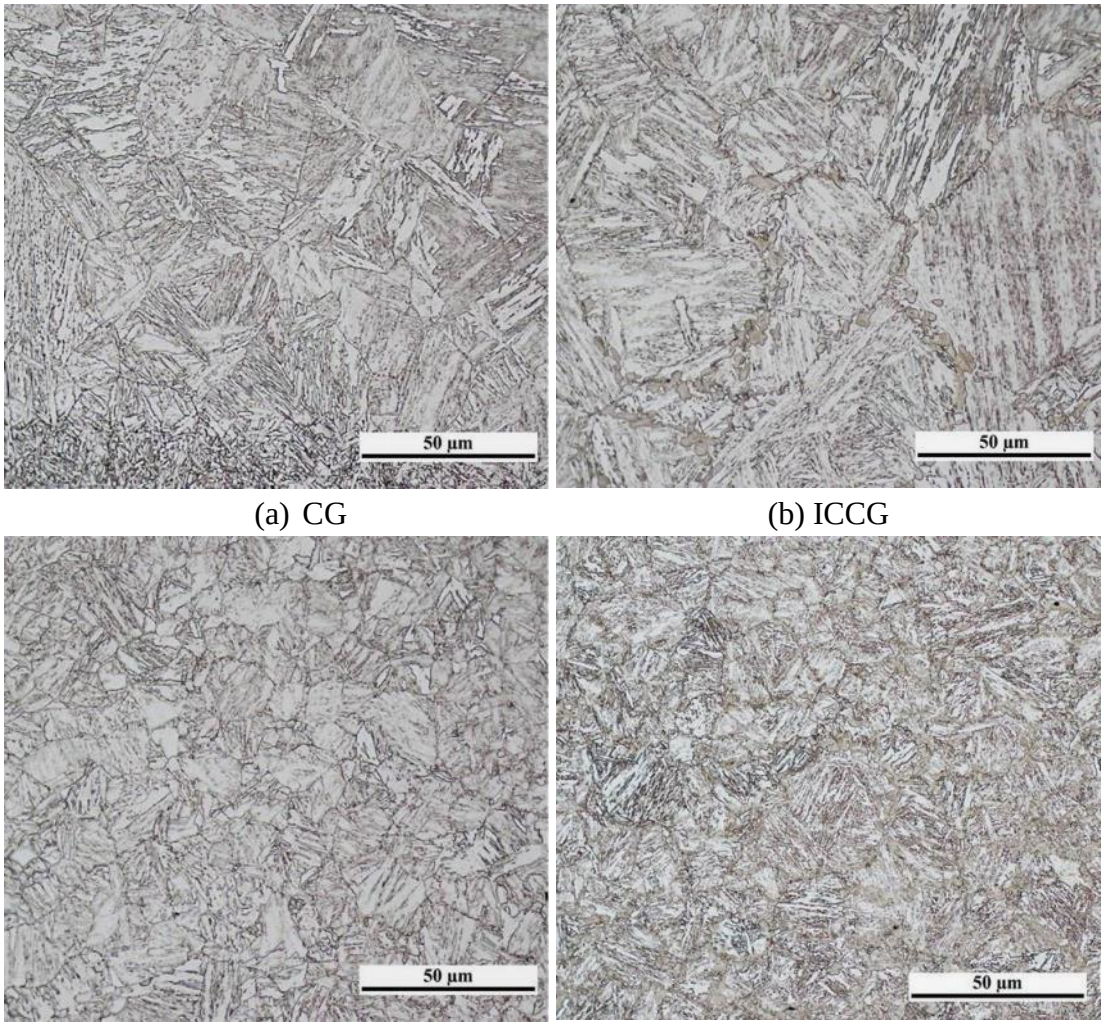

(a) CG (b) ICCG

(c) FG (d) ICFG

Figure 4-17: Typical optical images of specific HAZ microstructure for BoP 4 where; (a) CG region, (b) ICCG region, (c) FG region and (d) ICFG region.

4.5.2 Pad welds

Pad welds were sectioned, in the transverse direction, and analysed for microstructural changes from weld repair 1 to weld repair 4. For the ease of presentation, only repair 1 and 4 are compared.

Figure 4-18 shows a macro image of the HAZ for pad weld repair 1, where the complexity of the HAZ due to multi-pass welding can be seen. Figure 4-18 also shows two regions with the low toughness ICCG HAZ microstructures.

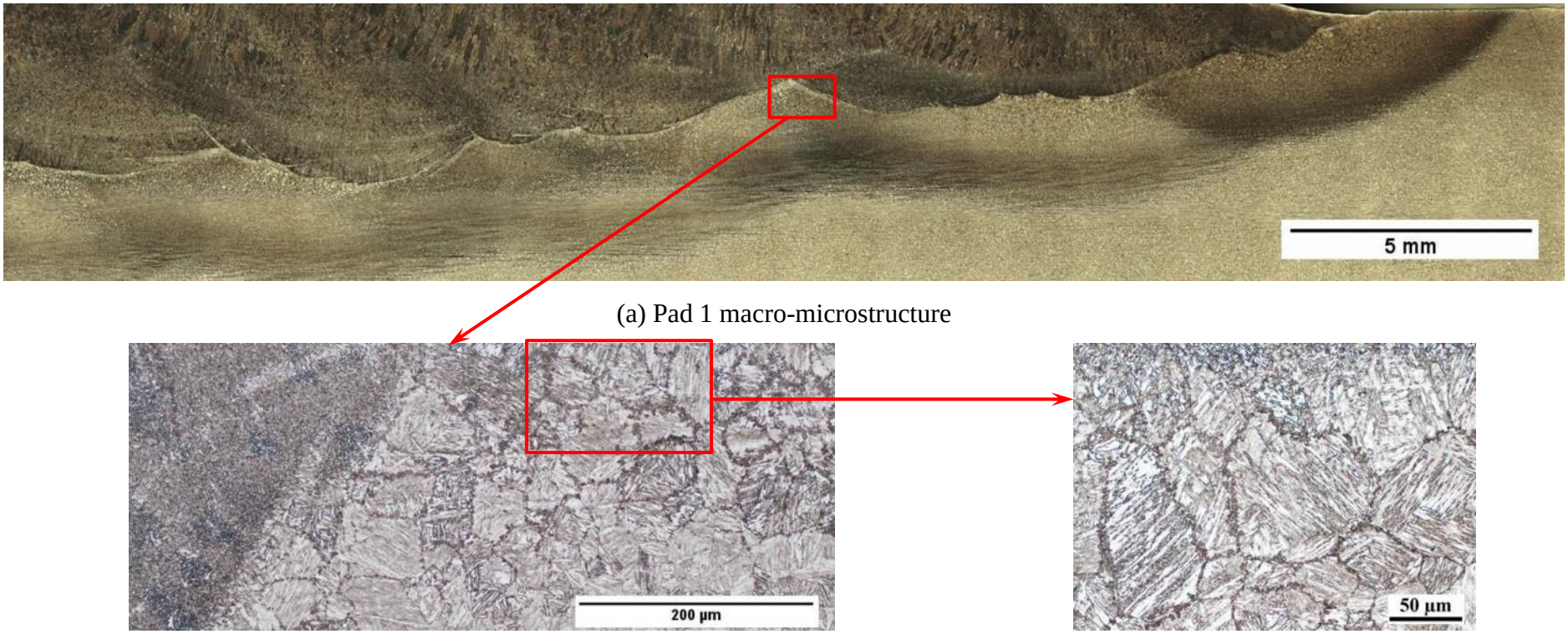

(a) Pad 1 macro-microstructure

(b) Region 1 showing ICCG microstructure.

(c) Region 2 showing ICCG microstructure.

Figure 4-18: Macro-image of the cross section of the HAZ in pad repair weld 1, where (b) and (c) show two regions comprised of the low toughness ICCG microstructure.

In Figure 4-19, typical examples of the different sub regions in the HAZ of pad weld repair 1 are shown.

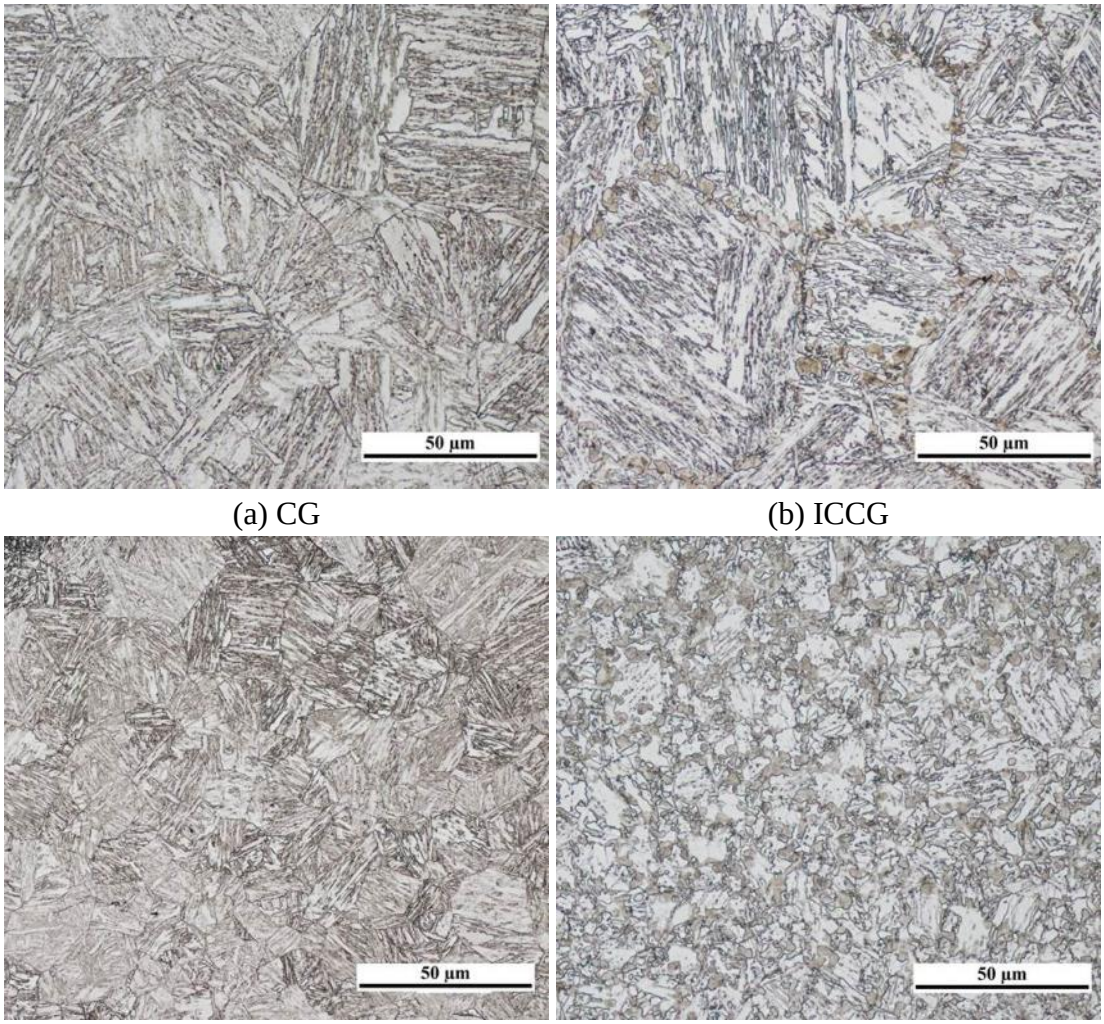

(a) CG (b) ICCG

(c) FG (d) ICFG

Figure 4-19: Typical examples of the different sub regions in the HAZ of pad weld repair 1, where (a) CG, (b) ICCG, (c) FG and (d) ICFG.

The macro images of pad weld repair 4, with typical images of the ICCG HAZ are shown in Figure 4-20. Typical optical images of the sub regions of the HAZ for pad weld repair 4 are shown in Figure 4-21.

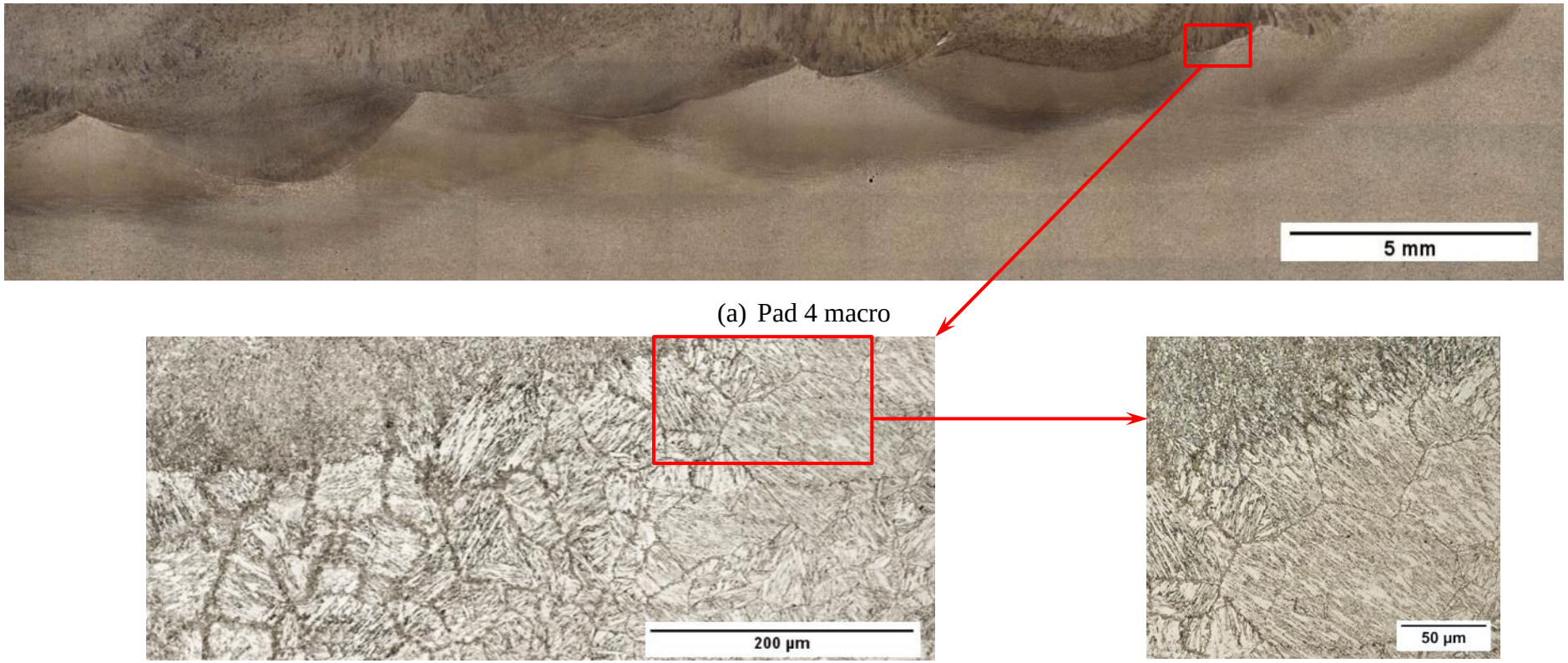

(a) Pad 4 macro

(b) Pad 4 ICCG transition region

(c) pad 4 ICCG region

Figure 4-20: Macro-image of the cross section of the HAZ in pad repair weld 4, where (b) and (c) show two regions comprised of the low toughness ICCG microstructure.

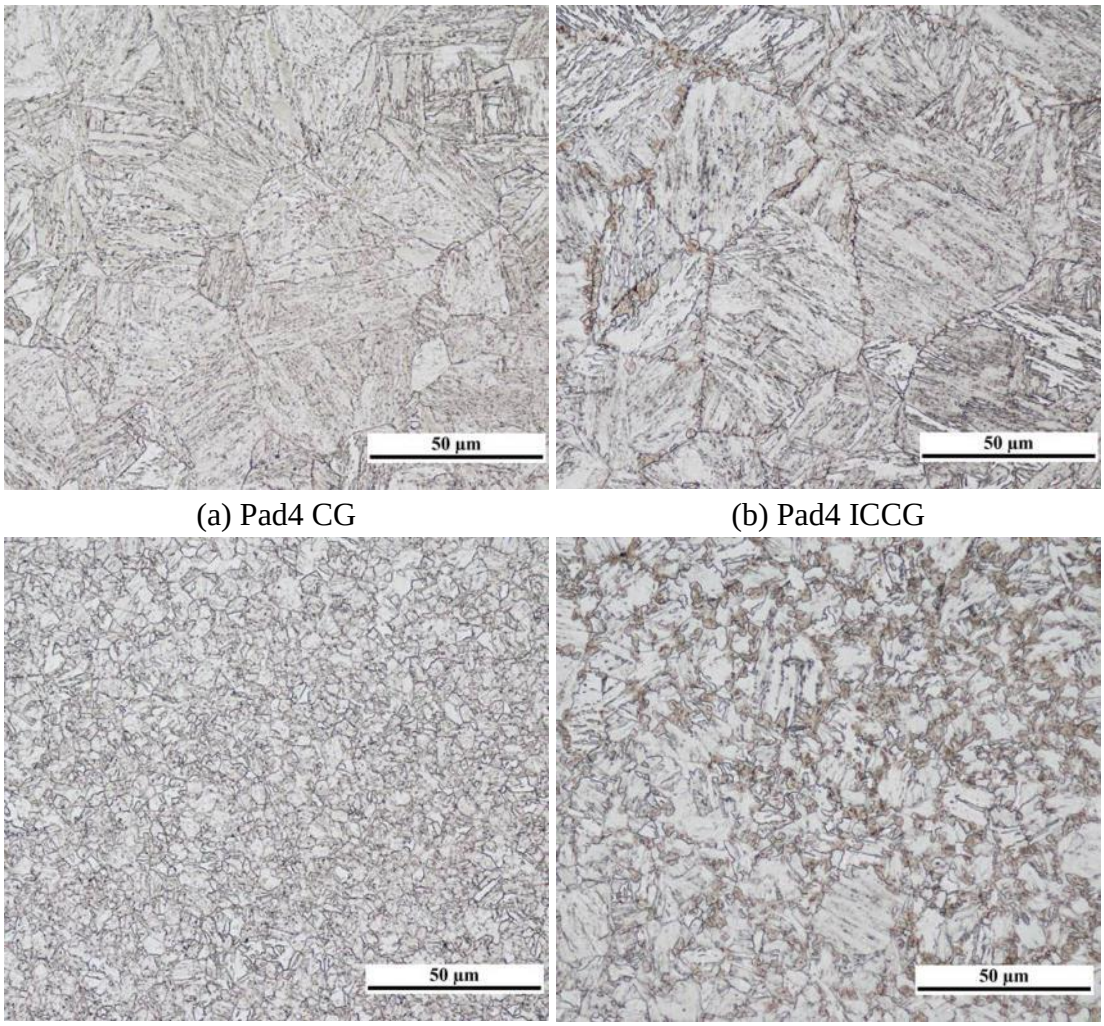

(a) Pad4 CG (b) Pad4 ICCG

(c) Pad4 FG (d) Pad4 ICFG

Figure 4-21: Typical examples of the different sub regions in the HAZ of pad weld repair 4, where (a) CG, (b) ICCG, (c) FG and (d) ICFG.

4.6 Variation of Charpy Impact toughness in simulated HAZ and real welds

Impact toughness was assessed on simulated welds and real welds with instrumented and non-instrumented Charpy impact tests, as described in Section 3.4.2. The results of single and multiple thermal cycle simulation tests and real weld HAZ results are discussed in the following sections.

4.6.1 Variation of Charpy impact toughness of single and double simulated HAZs

In Figure 4-22, the impact energy as a function of the peak temperature for single and double cycle HAZ simulations is shown. Toughness decreased as the peak temperature increased, due to the corresponding increase in the PAGS. The effect of PAGS on toughness is illustrated more clearly in upper x-axis. From Figure 4-22, it can be seen that the high intercritical (IC-850^{o}C) results showed similar toughness compared to the equivalent single HAZ cycles. However, with decreasing intercritical reheating temperature, the toughness deteriorated significantly.

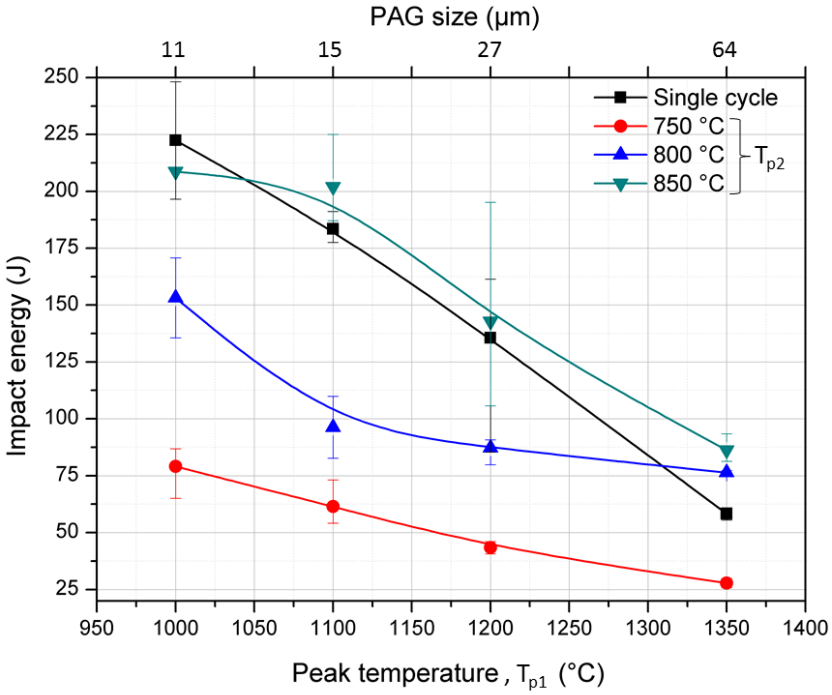

Figure 4-22: The variation of Charpy impact toughness with different peak temperatures, where the initial peak temperature, T_{p1} is shown on the bottom X-axis and the intercritical reheat temperature, T_{p2}, is shown in the legend. The upper X axis represents PAG sizes associated to peak temperatures on bottom axis. (test temperature was -20°C).

Load and displacement curves obtained from instrumented Charpy impact test samples for CGHAZ (1350°C), ICCGHAZ (1350-800°C and 1350-750°C) are shown in Figure 4-23. There were 3 tests per each thermal cycle.

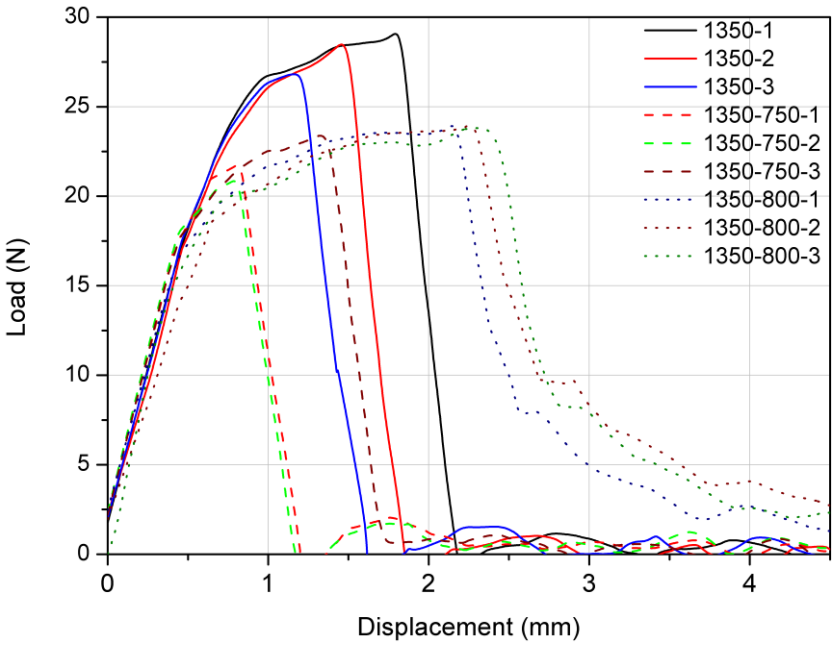

Figure 4-23: Instrumented impact test results (with curve smoothing) of simulated HAZ samples with single (1350°C) and double thermal cycles (1350-750°C and 1350-800°C), tested at -20°C. Curve soothing was applied to eliminate noise.

Instrumented tests enable calculation of initiation energy (E_i) and propagation energy (E_p) of fracture for the different samples [144]. Table 4-2 presents a summary of the instrumented Charpy data. The total energy calculated with the change in pendulum height is labelled as 'Fracta'. Due to smoothing of the instrumented data, total energy (E_t) was typically slightly less than the Fracta value. The average fracture propagation energy, E_p of both the CGHAZ and ICCGHAZ with lower IC (750°C) was very low. However, there was a significant increase in fracture propagation energy of ICCG HAZ with higher IC (800°C) sample, leading to a higher total energy value.

Table 4-2: Instrumented Charpy fracture energies of simulated HAZ samples with single and double thermal cycles, tested at -20°C

Simulation region	**Thermal cycle**	**Ave Fracta/J**	**Ave E_t/J**	**Ave E_i/J**	**Ave E_p/J**
CGHAZ	1350°C	37.8	35.6	30.1	5.5
ICCGHAZ	1350-750°C	24.2	20.5	16.0	4.5
ICCGHAZ	1350-800°C	69.0	57.8	26.2	31.7

4.6.2 Variation of Charpy impact toughness of multiple simulated thermal cycles

Samples that were simulated for three, four, five and six thermal cycles, to simulate specific sub-HAZ regions subjected to repeated welds, were tested for Charpy impact toughness. Figure 4-24 show the variation of toughness for multiple thermal cycles CG (1350^{o}C) HAZ (CG, CG×2, CG×3) and multiple CG cycles with a final IC (750°C) cycle (CG-IC, CG×2-IC, CG×3-IC). The result indicates that multiple thermal cycles (applied one after the other) had minimal influence on the toughness.

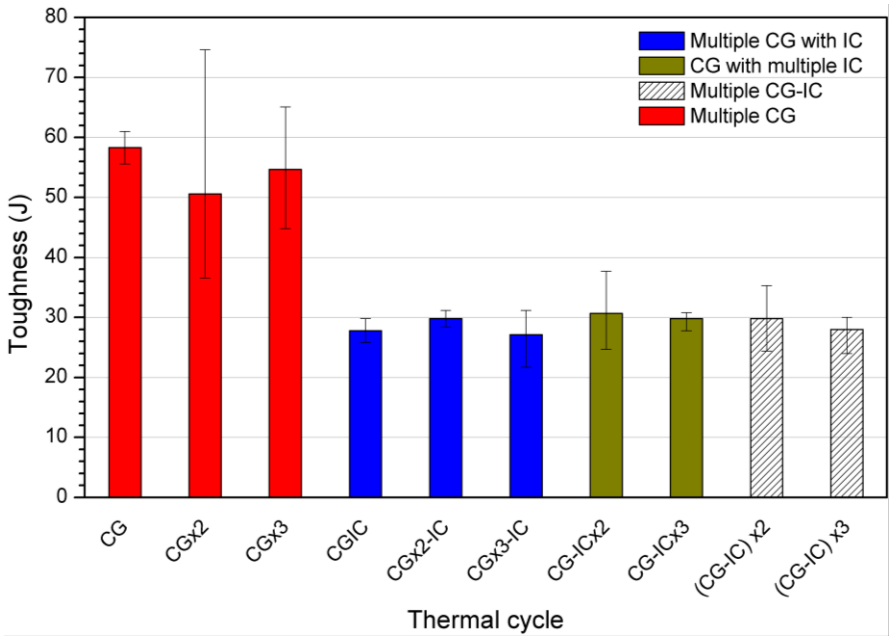

Figure 4-24: Effect of different thermal cycles on the toughness of simulated HAZ. Red columns are single, double and triple CG thermal cycles (1350°C) and blue columns are the samples with IC thermal cycle of 750°C followed by the previous respective combination of CG cycles.

A short tempering thermal cycle was applied on ICCG samples to identify toughness changes with tempering cycles. Table 4-3 shows the variation of toughness with different temperatures. The tempering cycles were similar to weld thermal cycles where 200 °C/s heating, 0.5 s at peak and extrapolated $t_{8/5}$ was 6 s. As shown in Table 4-3, a slight increase of toughness was noticed with 300°C and 400°C peak thermal cycles. There was a substantial increase in toughness was observed with 500°C peak temperature.

Table 4-3: Variation of toughness with short tempering cycle. (Tempering cycle was applied on ICCG (1350-750) sample.

Toughness of 1350-750 cycle/J	Tempering with 300°C max cycle/J	Tempering with 400°C max cycle/J	Tempering with 500°C max cycle/J
27.8	35.3	40.7	58.8

4.6.3 Variation of Charpy impact toughness of multiple repairs of real welds

Charpy impact test samples were prepared with real weld samples as described in Section 3.4.2. The notch was place at the fusion line and fusion line + 3 mm. The instrumented Charpy impact results for full penetration butt repair weld 1 and 4 are shown in Figure 4-25 and Figure 4-26, where test temperatures were -18°C and -51°C, respectively.

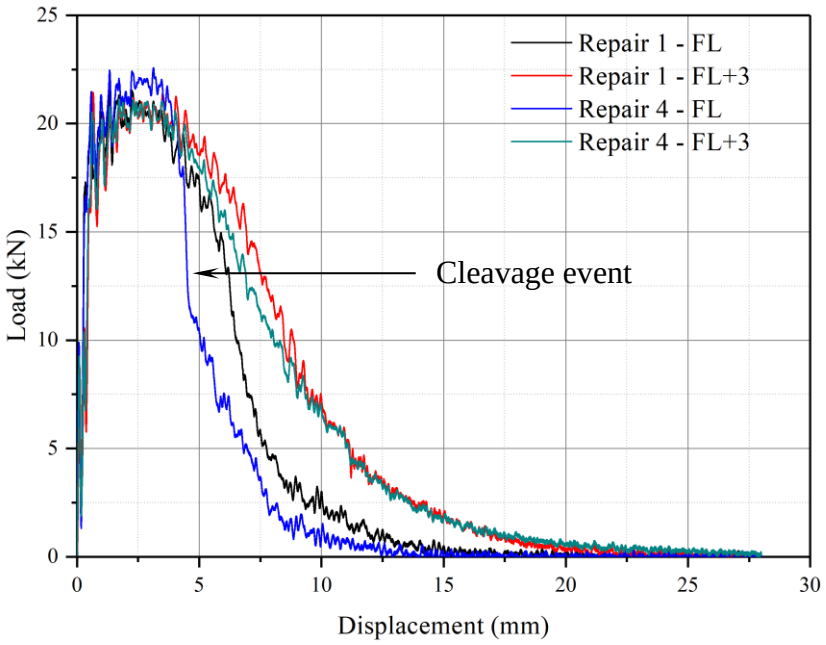

Figure 4-25: Load vs displacement curves from instrumented impact toughness testing for full penetration butt welds with weld 1 and weld 4, where samples were taken from fusion line (FL) and FL + 3 mm (FL+3). (tested at -18°C).

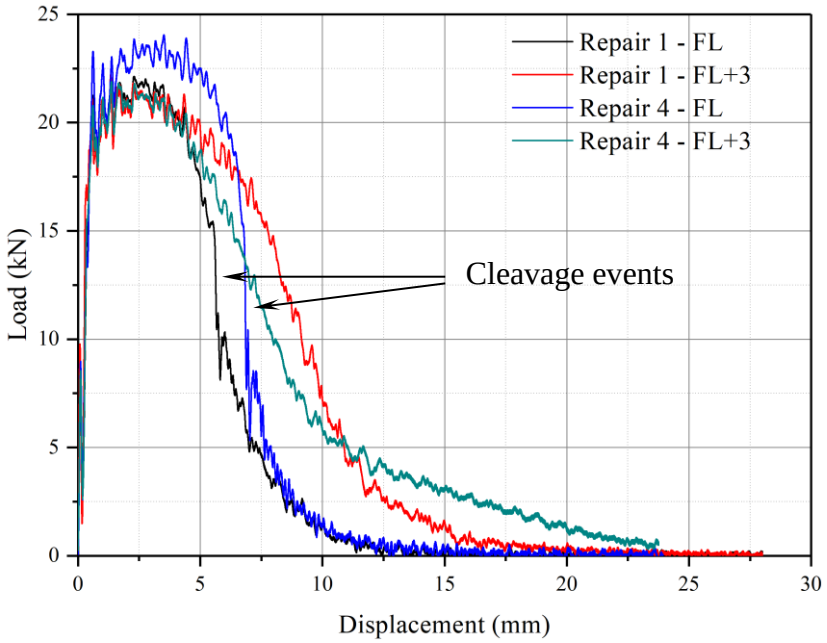

Figure 4-26: Load vs displacement curves from instrumented impact toughness testing for full penetration butt welds with weld 1 and weld 4 where samples were taken from fusion line (FL) and 3 mm into HAZ from FL (FL+3). (tested at -51°C).

In both test temperatures, FL+3 sample showed higher toughness and the fracture was more ductile as shown in load vs deflection graphs (See section 3.4.2 for instrumented Charpy test data analysis). For FL samples, tested at -51°C, a sudden vertical drop of the load (see Figure 4-26, black and blue curves) indicated cleavage fracture propagation occurred, which reduced the total energy recorded. Additionally, FL sample tested at -18°C also showed cleavage fracture (see Figure 4-25, blue line) with lower fracture energy. However, FL+3 showed ductile fracture curves at both test temperatures.

Table 4-4: Fracture initiation (E_i), propagation (E_p) and total (E_t) energies of real weld samples with different repair weld cycles.

Repair number	Test temperature (°C)	Impact toughness (J)					
		FL			FL+3 mm		
		E_i	E_p	E_t	E_i	E_p	E_t
1	-18	54.5	85.5	140	47.1	136	183
	-51	45.4	56.6	102	48.5	112	160
2	-18	36.0	77.0	113	43.1	86.9	130
	-51	58.9	61.1	120	58.2	134	192
3	-18	37.1	117	154	64.1	143	207
	-51	44.1	81.9	126	53.4	136	189
4	-18	68.6	113	182	53.7	127	181
	-51	59.5	100	159	53.1	133	186

Load vs displacement curves obtained from instrumented Charpy impact testing on full penetration butt repair welding show that substantially higher toughness than simulated weld results because of heterogeneous microstructure of real welds. All samples where the notch was placed at FL showed lower toughness and typically showed cleavage fracture propagations as shown in Table 4-4. FL+3 showed higher toughness and exhibited ductile fractures at -18°C and -51°C teats.

4.7 Variation in hardness

Vickers hardness testing was conducted on the simulated HAZ and real welds on polished samples. Figure 4-27 shows the changes in hardness of the simulated samples for single HAZ cycles and double HAZ cycles. For the single thermal cycle, hardness typically decreased as the peak temperature increased. The hardness of single thermal cycle was always higher than the hardness of double thermal cycles, when the second thermal cycle is in IC range. The lower intercritical temperatures, 750°C and 800°C, both showed lower hardness compared to the high intercritical temperature. For the larger grain size (at 1350°C), the 2nd phase is restricted to the PAGB's at 750 and 800°C, so overall hardness was similar. However, at the smallest grain size, an increased volume fraction of 2nd phase lowered the hardness.

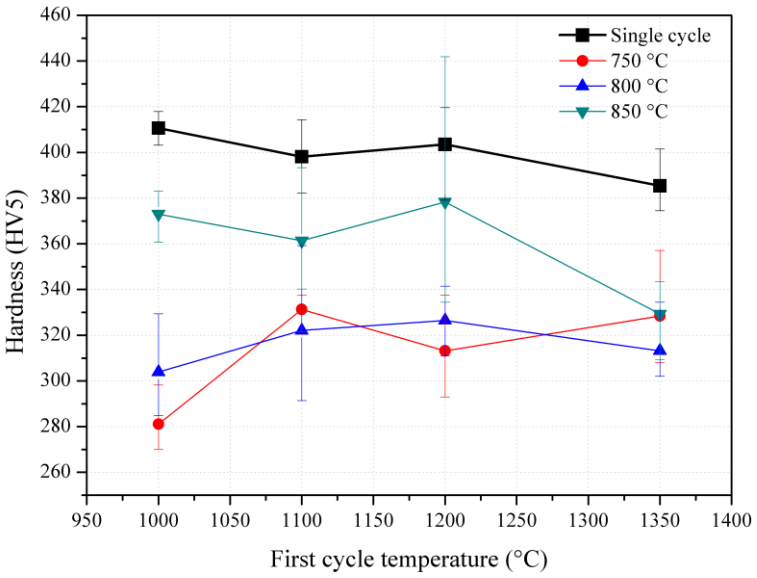

Figure 4-27: Variation of the hardness of single and double thermal cycles.

The variation of hardness with PAG size is shown in Figure 4-28 for different second IC cycle temperatures. The lowest hardness was evident in the sample which had the smallest PAG size and reheated to lower IC temperature (750°C).

Figure 4-29 graphs the hardness of multiple CG cycles and multiple CG cycles with an IC (750°C) cycle at the end. From the figure it can be seen that the hardness was relatively constant for multiple cycles.

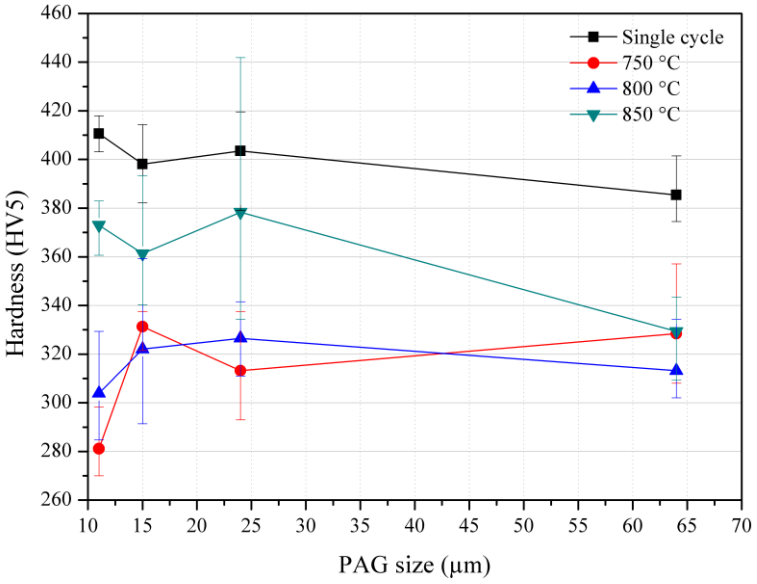

Figure 4-28: Variation of micro hardness of samples with different second cycle IC and PAG size temperatures for different PAG sizes.

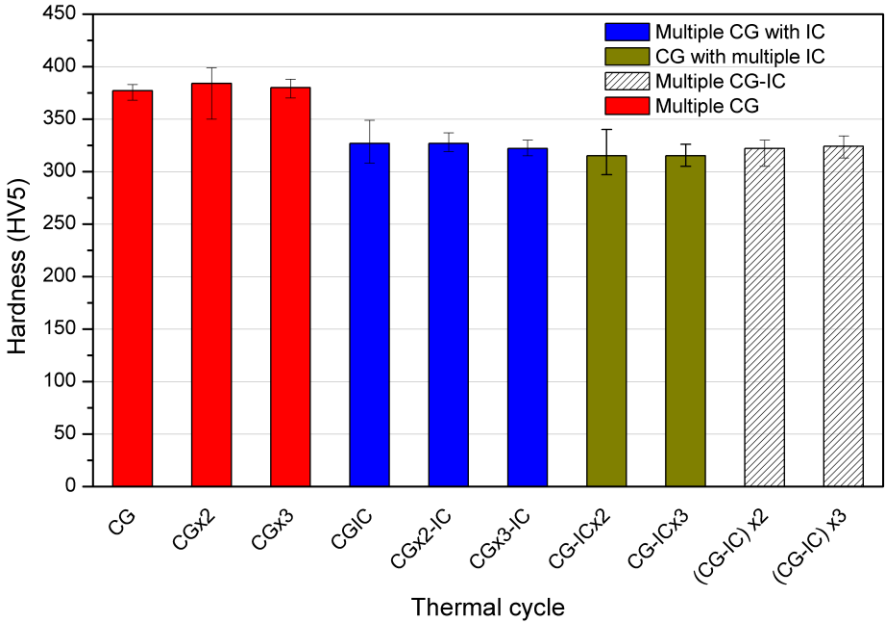

Figure 4-29: Variation of hardness with multiple CG (1350ºC) thermal cycles and multiple CG (1350ºC) cycles with a final IC (750ºC) cycle (HV5).

Hardness mapping was conducted on the real welds to characterise the variation in hardness for each HAZ. Figure 4-30 shows the variation of hardness from BoP 1 to BoP 4 welds, where hardness were mapped with 0.5 kg load. The hardness did not show any considerable variation within the HAZ, although the tempering effect of the second weld on the initial HAZ is clear for all welds.

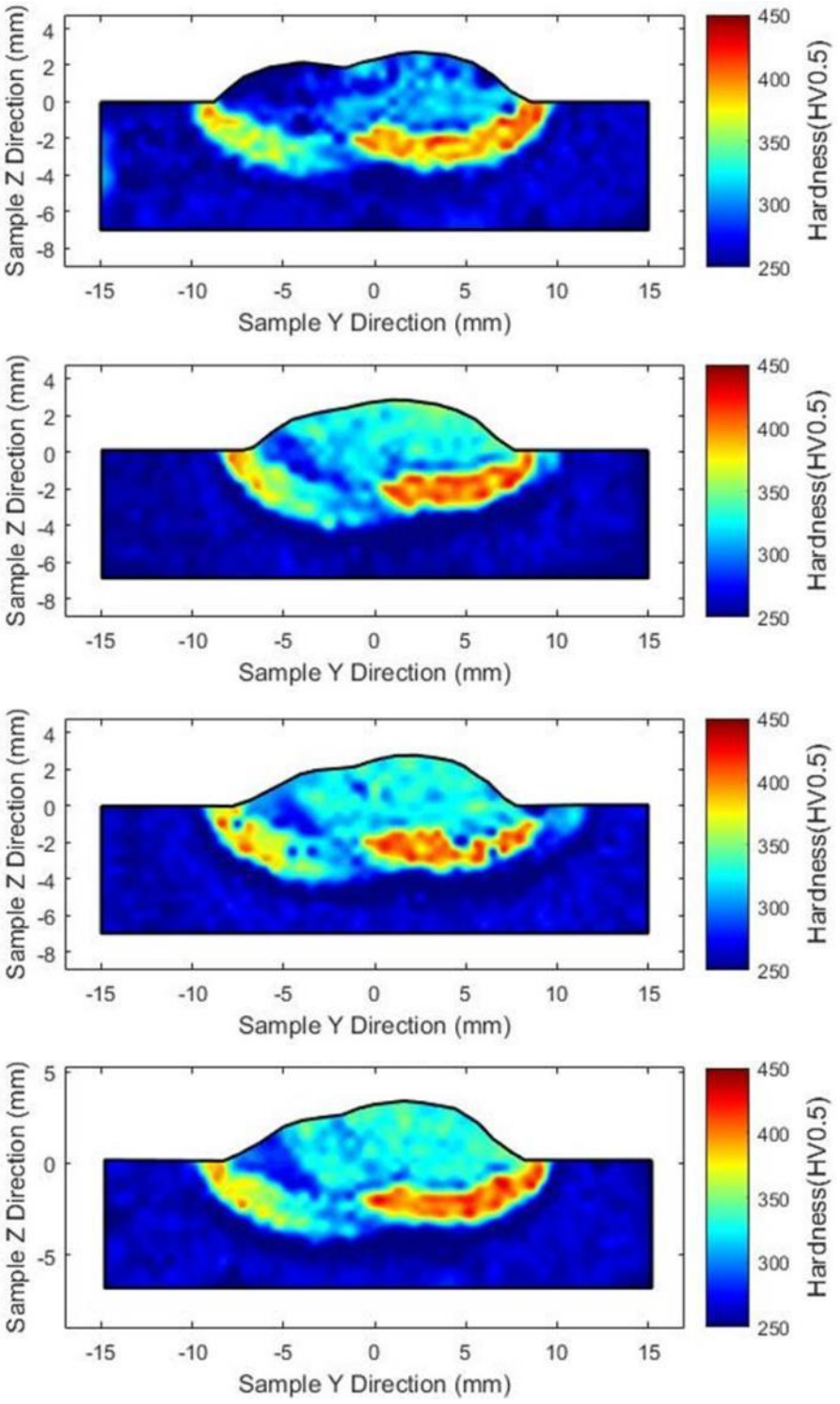

Figure 4-30: The variation of micro hardness of single and multiple repairs of BoP welds, where BoP 1 to 4 is from top to bottom (HV0.5).

Compared to the simple BoP welds, hardness of the pad welds showed a different pattern where the region of a high hardness was much localised, as shown in Figure 4-31 and Figure 4-32. The highest hardness was visible only at the toe of the last

weld, as this weld was only tempered using TIG dressing. Under the main body of the pad weld, the hardness is relatively low due to the tempering effect of multiple weld passes.

In full penetration butt welds, similar hardness behaviour to pad weld were observed as the regions of higher hardness was localised at the root of the weld and at the toe end as shown in Figure 4-33. Again, there were no noticeable differences in hardness (distribution and magnitude) between weld repair 4 and 1 of full penetration butt welds.

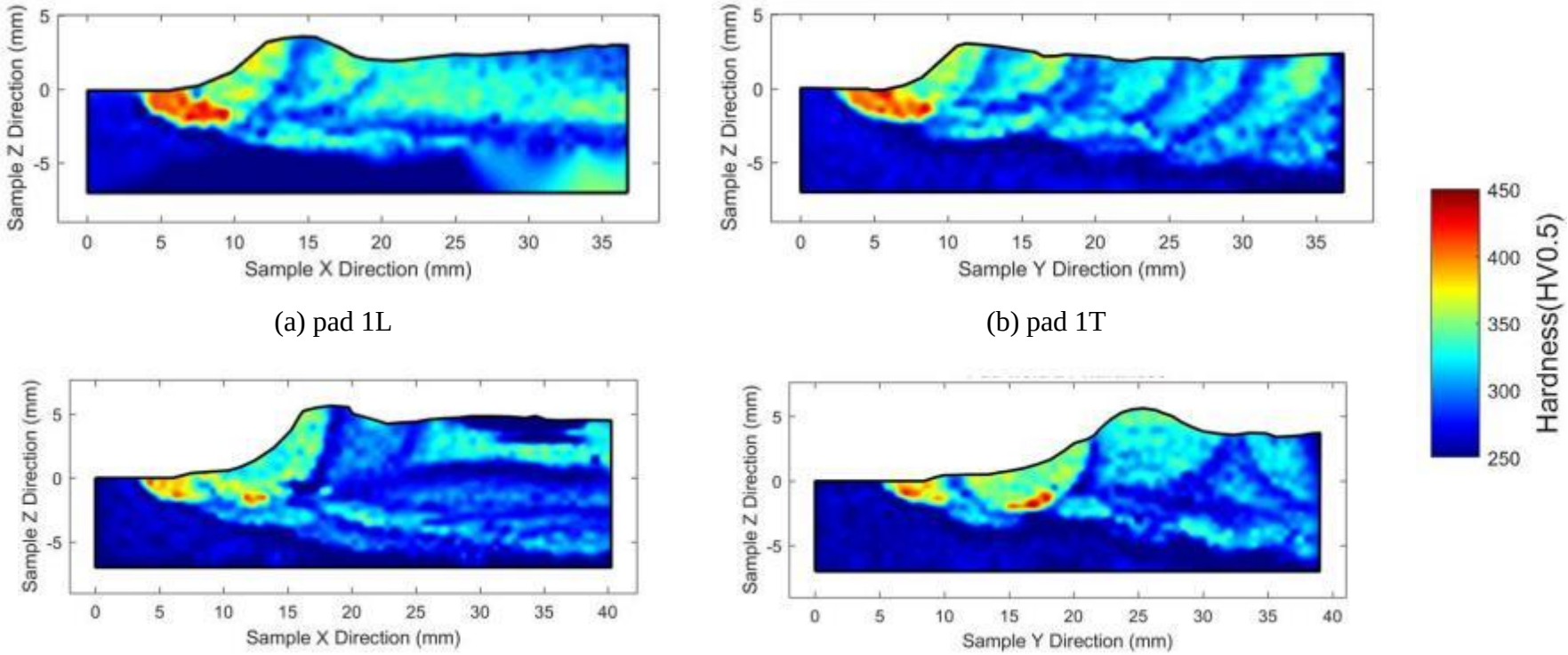

(a) pad 1L

(b) pad 1T

(c) pad 2L

(d) pad 2T

Figure 4-31: Hardness maps of pad repair welds. (a) and (c) are hardness in longitudinal direction to the weld from pad repair 1 and pad repair 2 respectively. (b) and (d) are hardness in transverse direction to the weld of pad 1 and pad 2, respectively (HV0.5).

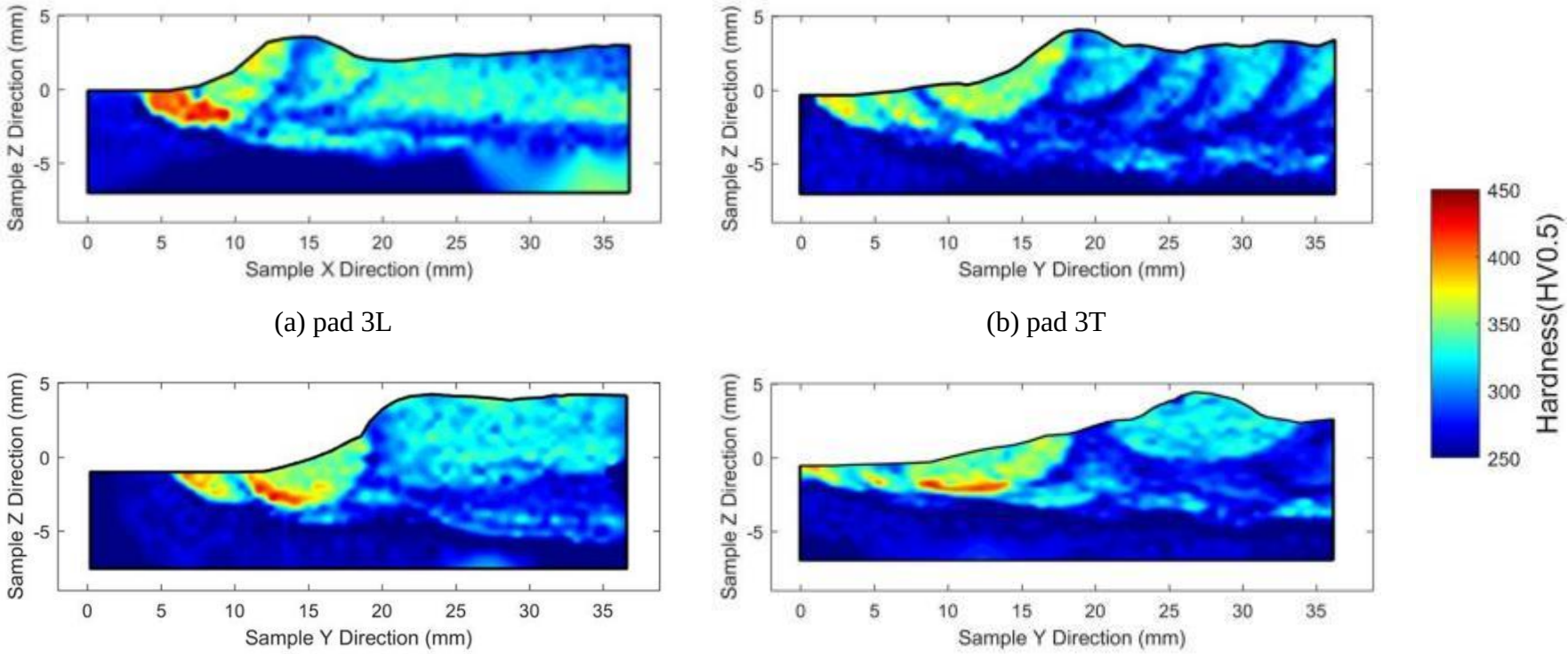

(a) pad 3L

(b) pad 3T

(c) pad 4L

(d) pad 4T

Figure 4-32: Hardness maps of pad repair welds. (a) and (c) are hardness in longitudinal direction to the weld from pad repair 3 and pad repair 4 respectively. (b) and (d) are hardness in transverse direction to the weld of pad 3 and pad 4, respectively (HV0.5).

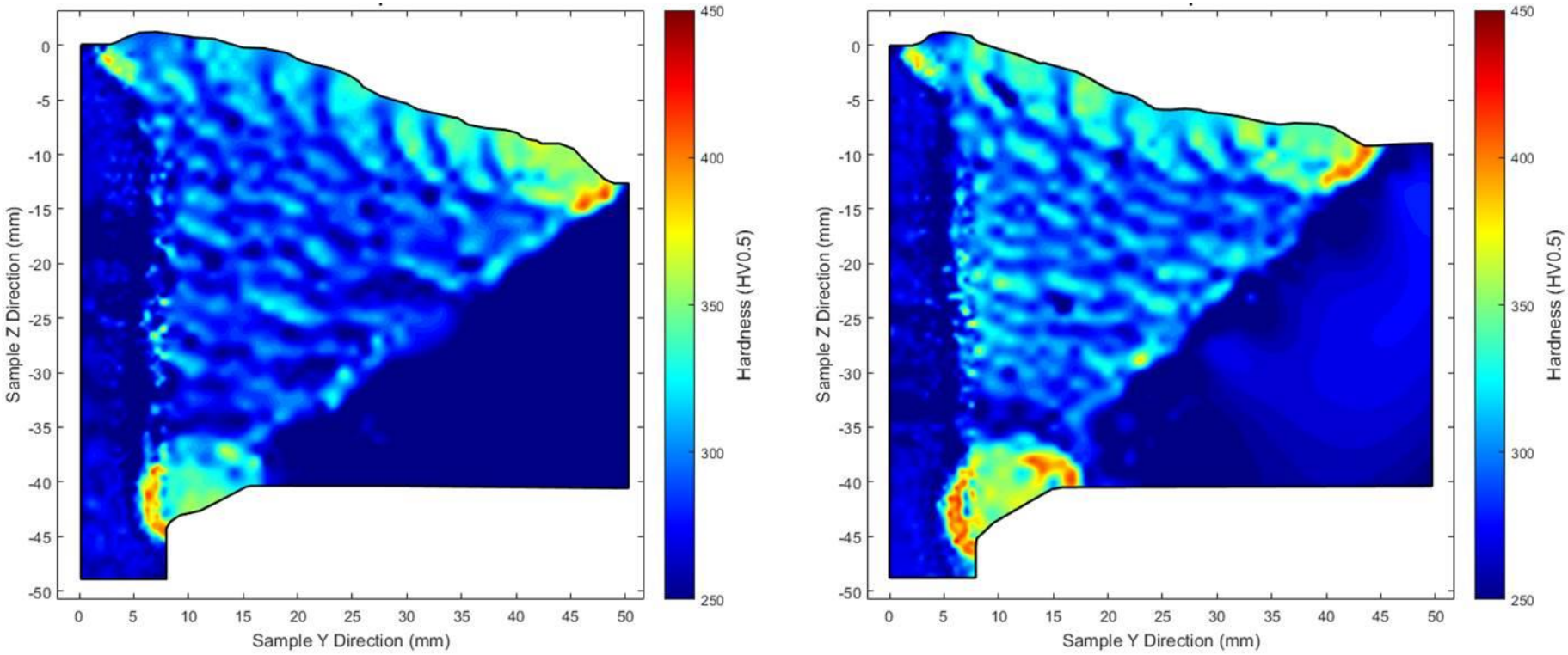

(a) Butt weld repair 1

(b) Butt weld repair 4

Figure 4-33: Comparison of hardness distribution between full penetration butt weld repair 1 and repair 4. The only 50 mm plate on left side of the weld have gone through all 4 weld cycles in the weld repair 4. The 30 mm plate was replaced with a new one in each weld repair.

Nano indentation hardness was measured on two specimens with different thermal cycles and indentation locations are shown in Figure 4-34. Indentations were placed on the MA constituents on the grin boundaries and on the rest of the matrix. Red crosses were placed over the indents to clearly indicate the location of each indent.

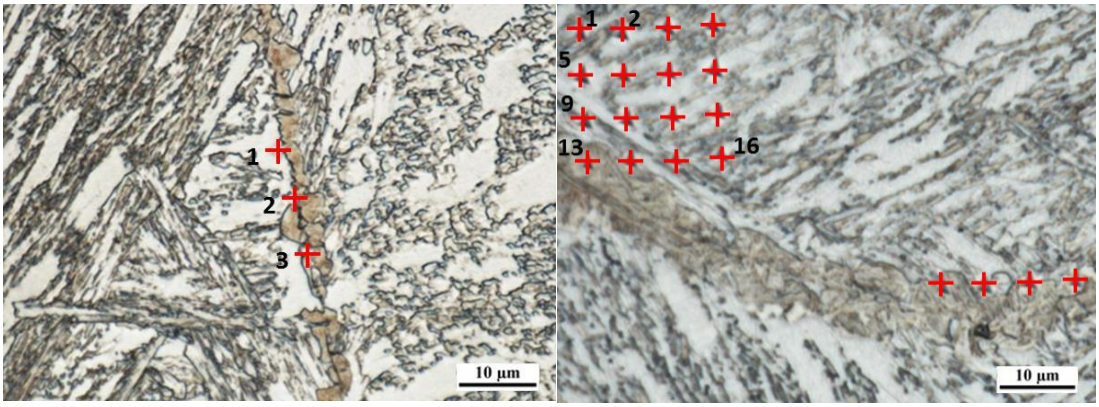

(a) (b)

Figure 4-34: Nano hardness indentations of (a) 1350-750°C and (b)1350-800°C specimens.

Hardness values obtained from above selected locations are tabulated in Table 4-5. The hardness on MA particles are slightly higher than the matrix.

Table 4-5: Nano indentation hardness measured on simulated HAZ specimens. Location numbers are corresponding to Figure 4-34.

Specimen	**Point Number**	**Hardness (GPa)**	**Location**
1350-750 °C	1	3.97	Matrix
	2	5.93	MA
	3	4.03	MA
1350-800 °C	1	3.89	Matrix
	2	2.81	Matrix
	5	4.12	Matrix
	9	3.49	Matrix
	13	4.81	MA

4.8 Fractography

The fracture surfaces of Charpy impact samples for the single cycle HAZ simulations, double HAZ simulations and multiple HAZ simulations are reviewed in this section.

Figure 4-35 (a) and (b) shows the fracture surface the single cycle FG HAZ (1100ºC), where the majority of surface exhibits ductile dimple formation, with the structure elongated towards the propagation direction of the fracture. For the double cycle FG-IC HAZ, 1100 - 750°C, cleavage-like fracture was predominant, as shown in Figure 4-35 (c) and (d) At the higher IC temperature, 1100 - 850°C, the fracture surface showed a mixture of ductile and cleavage cracks, as shown in Figure 4-35 (e) and (f).

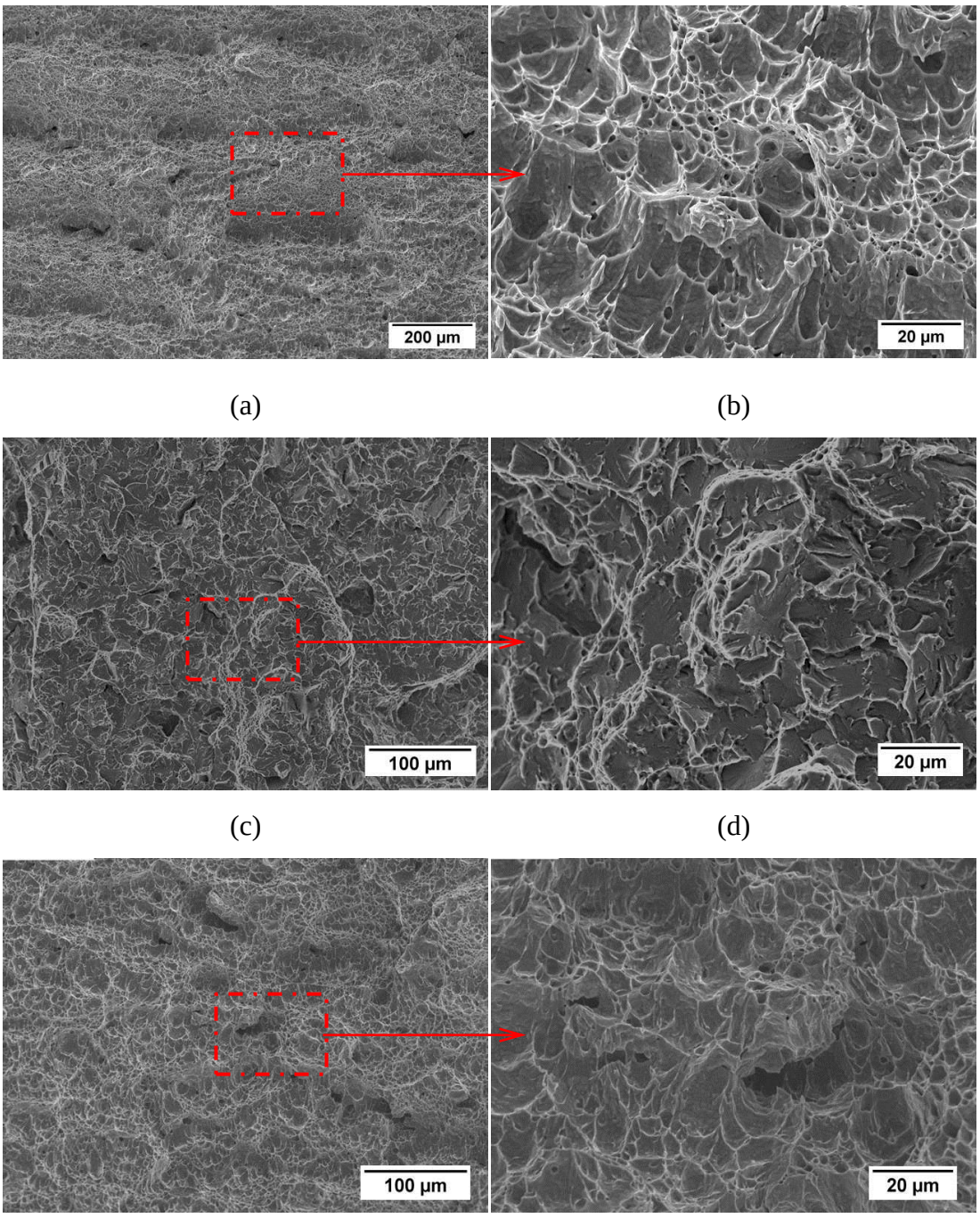

Figure 4-35: SEM fractograph of simulated HAZ where (a) and (b) are 1100°C peak temperature (FG HAZ), (c) and (d) 1100 - 750°C double cycle and (e) and (f) 1100 - 850°C double cycle.

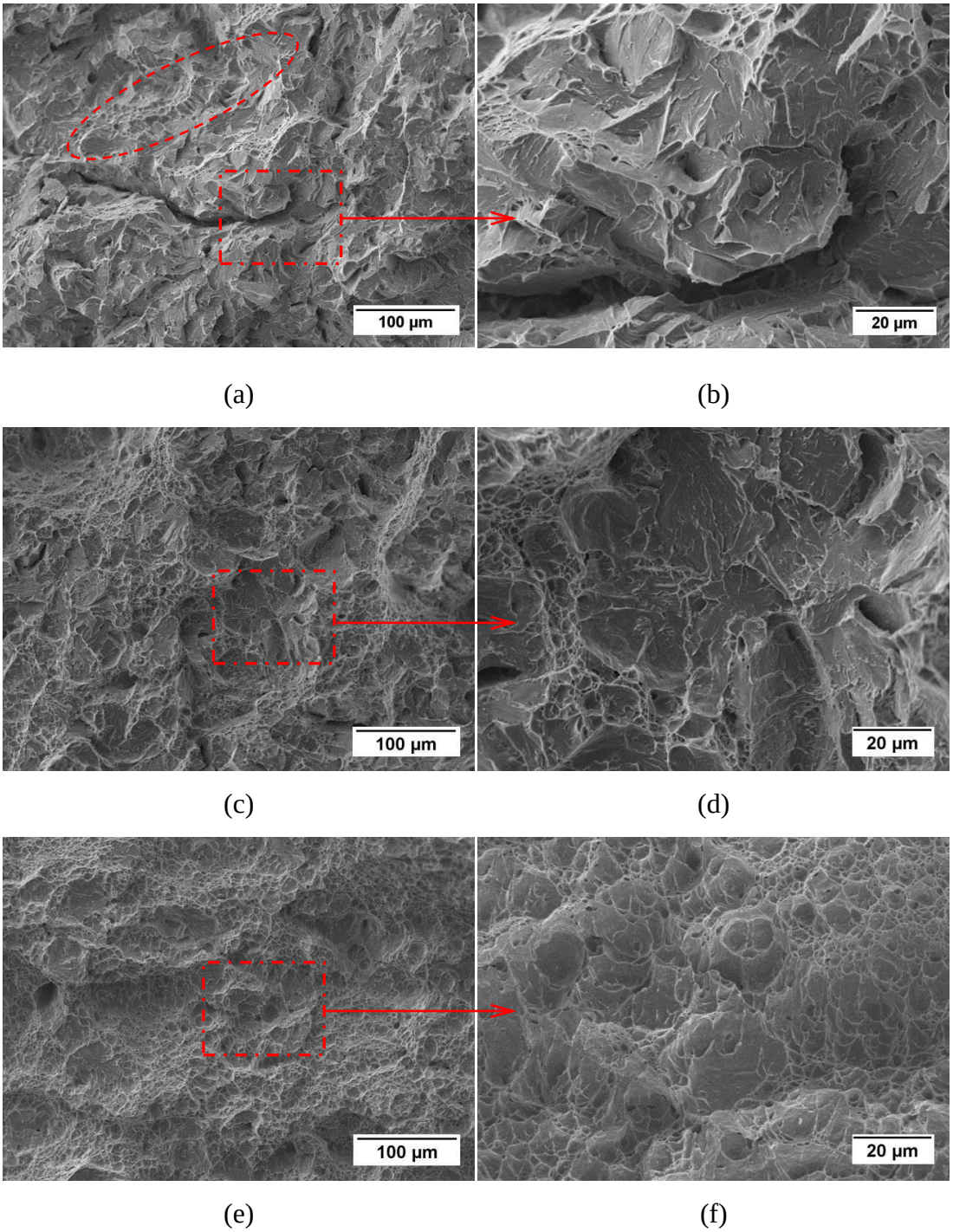

Figure 4-36: SEM fractographs of simulated HAZ, where (a) and (b) are 1200°C peak temperature (CG-HAZ), (c) and (d) 1200 - 750°C double cycle, (e) and (f) 1200 - 850°C double cycle.

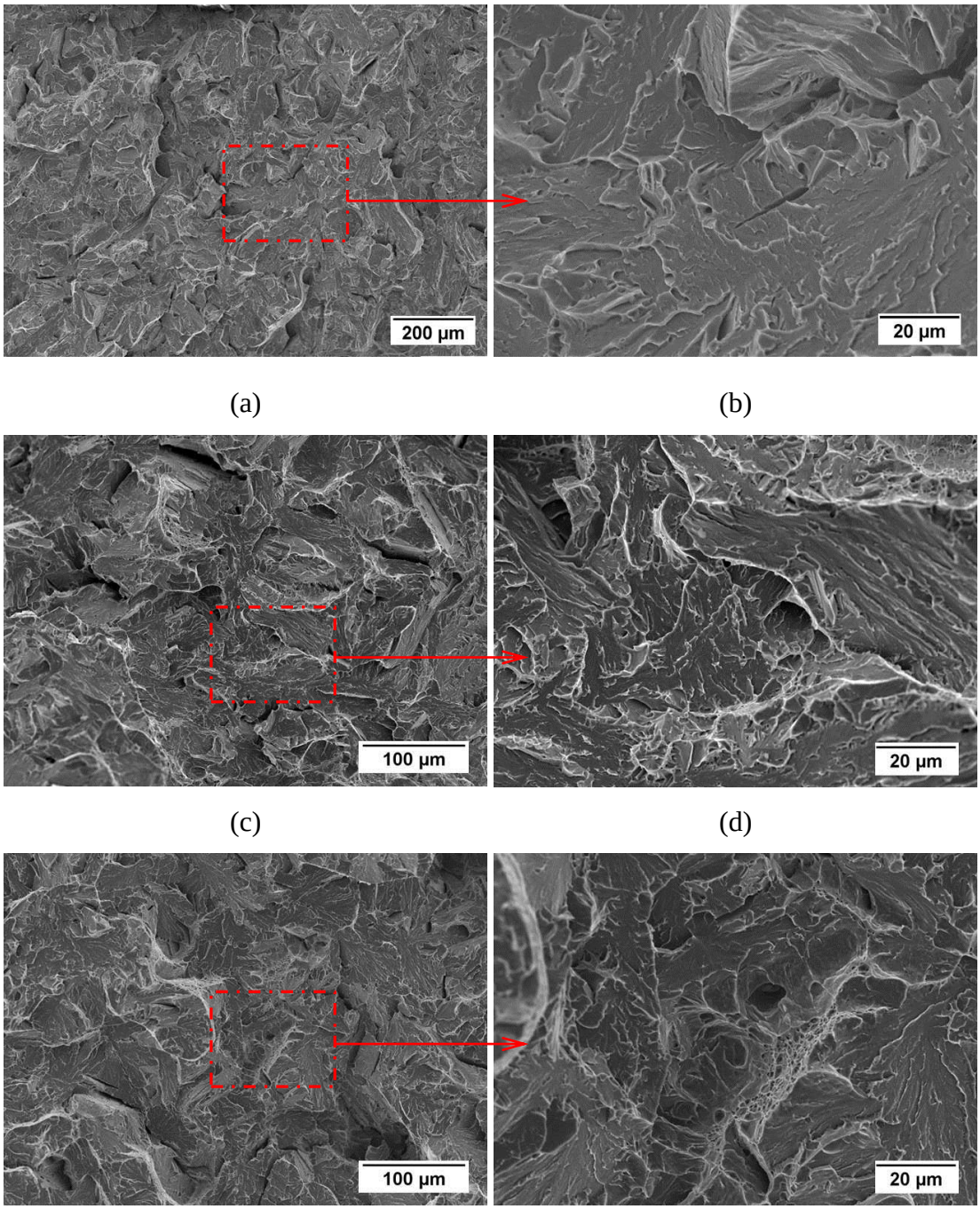

Figure 4-37: SEM fractographs of simulated HAZ where, (a) and (b) are peak temperature 1350°C (CG HAZ), (c) and (d) 1350 - 750°C double cycle, (e) and (f) 1350 - 850°C double cycle.

In coarse grained simulated HAZ, where the samples were heated close to the melting temperature (1350°C), the fracture surface showed clear quasi-cleavage fracture, with evidence of secondary cracks, as shown in Figure 4-37 (a) and (b).

Figure 4-37 (c) and (d) showed the fracture surface for the double cycle 1350-750°C HAZ and quasi-cleavage fracture facets dominated the fracture surface. At 1350-850°C, there was some areas of ductile regions, but the fracture surface was predominantly quasi-cleavage, as shown in Figure 4-37 (e) and (f).

The fracture appearance of the simulated double CG (1350-1350°C) samples showed quasi-cleavage fracture similar to single cycle CG (1350°C), as shown in Figure 4-38. Simulated samples with double CG cycles followed by single IC cycle (1350-1350-750°C) showed similar cleavage facets to the CGIC (1350-750°C) sample, as shown in the Figure 4-39. The fracture appearance of the both CGCGIC and CGIC samples was predominately brittle.

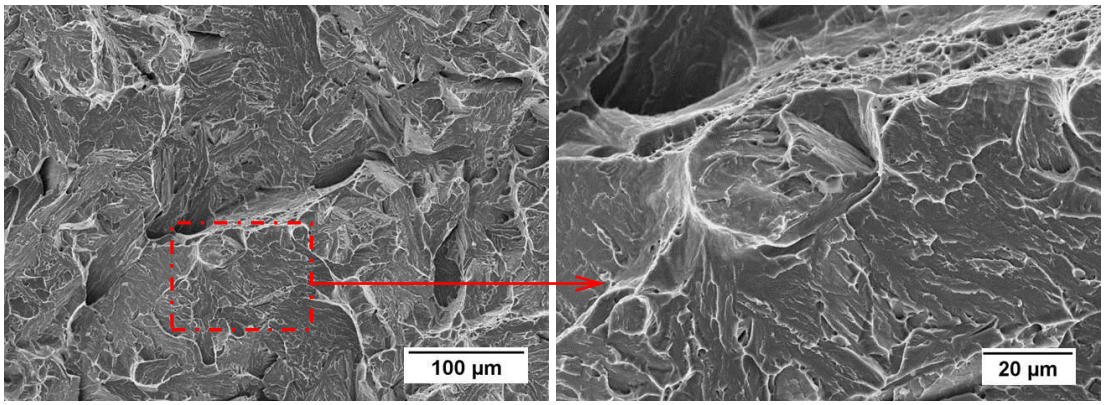

Figure 4-38: SEM fractographs of simulated HAZ of double CG thermal cycle (1350-1350°C)

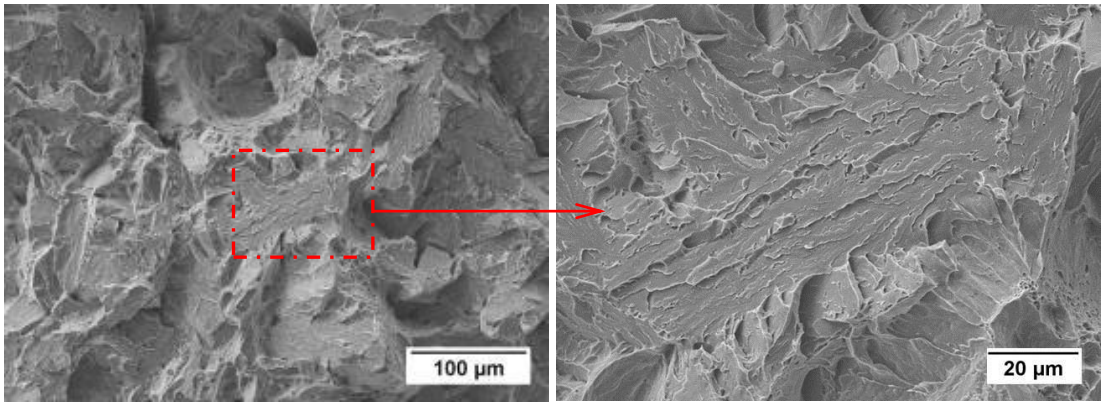

Figure 4-39: SEM fractographs of simulated HAZ with three thermal cycles, CG-CG-IC (1350-1350-750°C)

The multiple weld thermal cycles, CG-IC-IC (1350-750-750°C) and CG-CG-CG-IC (1350-1350-1350-750°C), both showed brittle fracture appearance and quasi-cleavage fracture facets, as shown in Figure 4-40 and Figure 4-41.

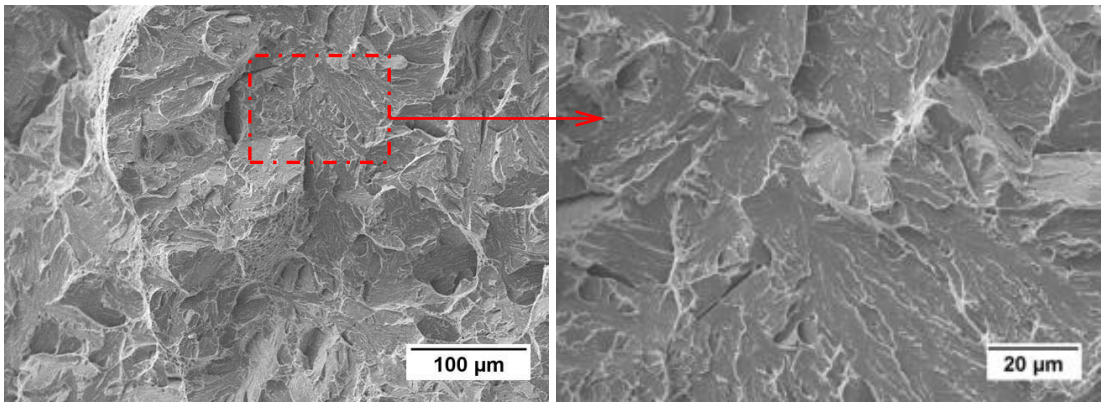

Figure 4-40: SEM fractographs of simulated HAZ with three thermal cycles CG-IC-IC (1350-750-750°C)

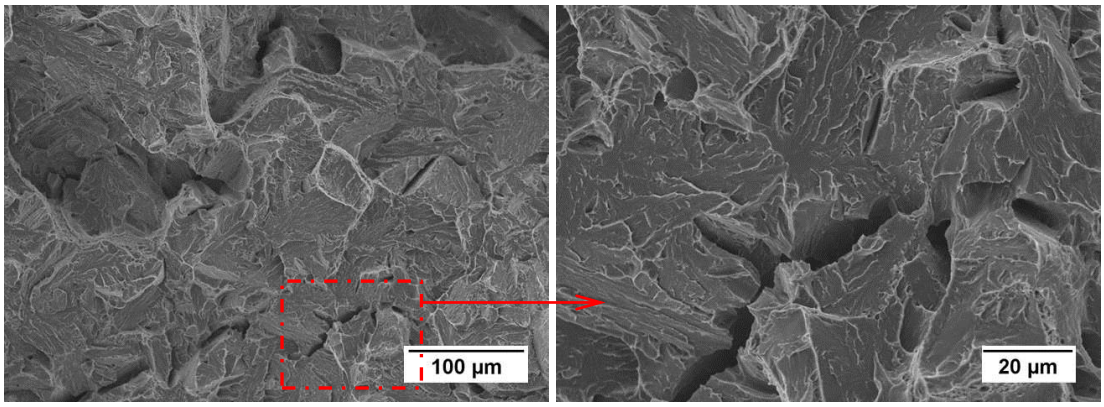

Figure 4-41: SEM fractographs of simulated HAZ with four thermal cycles CG-CG-CG-IC (1350-1350-1350-750°C)

Cross sections of fractured samples were observed under the optical microscope to identify the behaviour of fracture propagation. Cross sections of double-cycle simulated HAZ (1350-850°C and 1100-850°C) are shown in Figure 4-42. Both samples showed trans-granular fracture and minimal plastic deformation on 1350-850°C sample and considerable plastic deformation on 1100-850°C sample. The

1350-850°C sample showed several secondary cracks, as shown by the arrows in the Figure 4-42 (b).

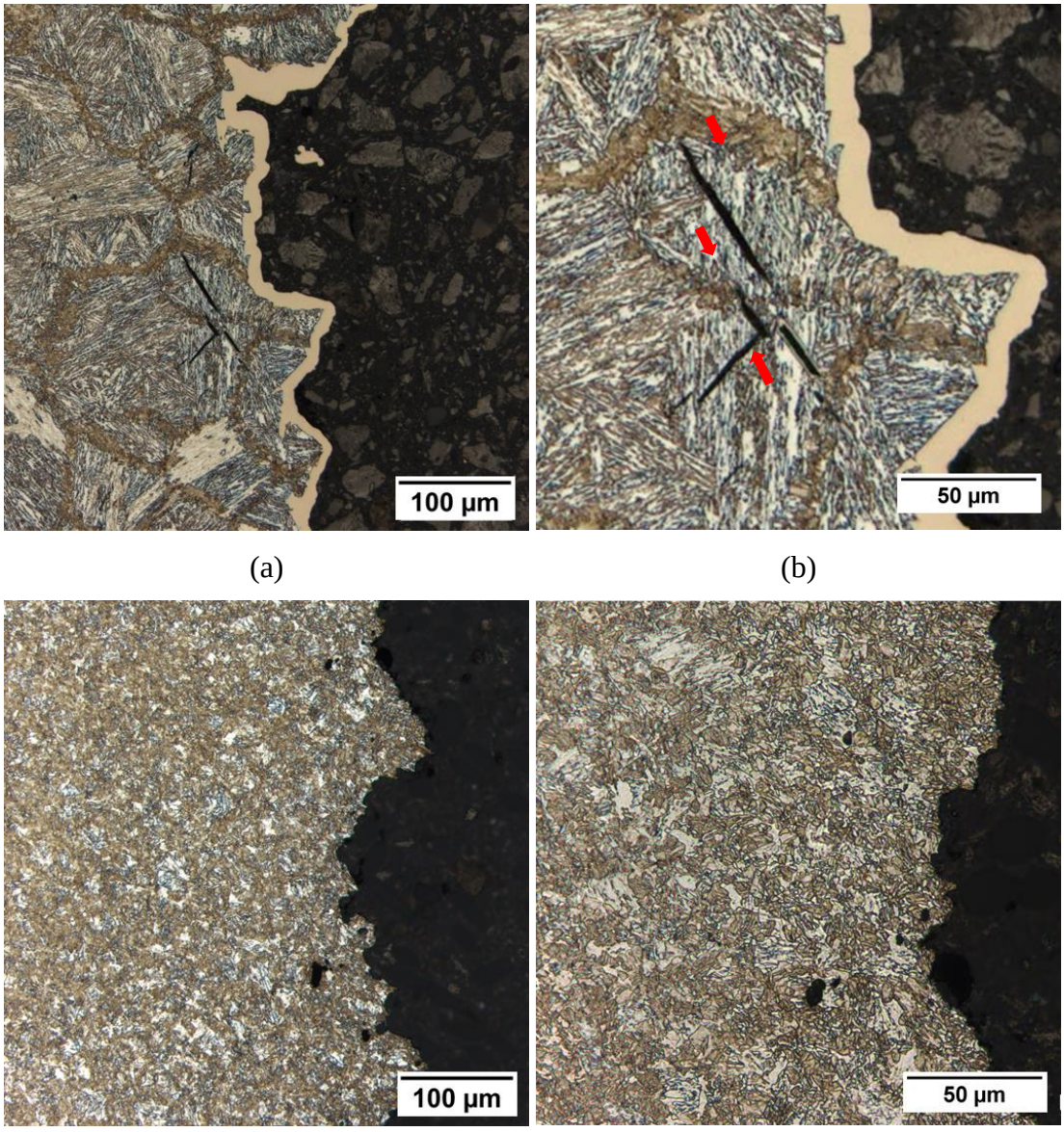

Figure 4-42: Metallography of fracture cross sections with 2% nital etch. (a) and (b) double cycle simulation 1350 - 850°C and (c) and (d) double cycle simulation 1100 - 850°C (Nickel coated on 1350-850°C to preserve the edge).

4.9 TEM analysis

The typical structure of base metal with lath martensite structure with carbide particles in between laths (see Figure 4-43). All TEM images are bright field images, unless otherwise stated. The TEM images reveal that the martensitic blocks can consist of finer laths, which typically range between 100 nm and 250 nm and some coarser laths, 1-2.5 μm were observed. The smaller laths generally had the same orientation, with the same habit plane [147].

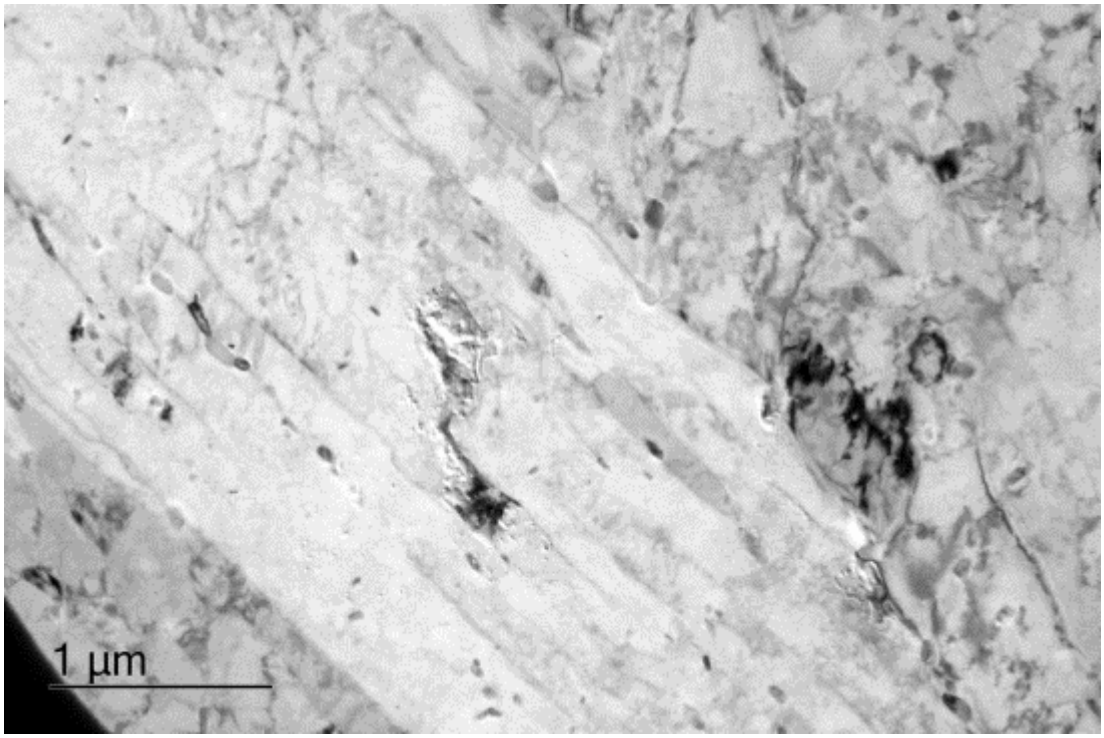

Figure 4-43: TEM micrograph of Martensite laths in the base metal

4.9.1 TEM foils for simulated welds

TEM images of simulated HAZ samples with single (1350ºC) and double (1350 - 750°C) thermal cycles are shown in Figure 4-44. Both samples showed similar lath-like structure with fine martensitic laths. With higher intercritical reheating, there was no microstructural changes evident in TEM samples (Figure 4-45). In fine-grain simulated samples, a lath microstructure, which was similar to the structure found in CG samples was observed as shown in Figure 4-46.

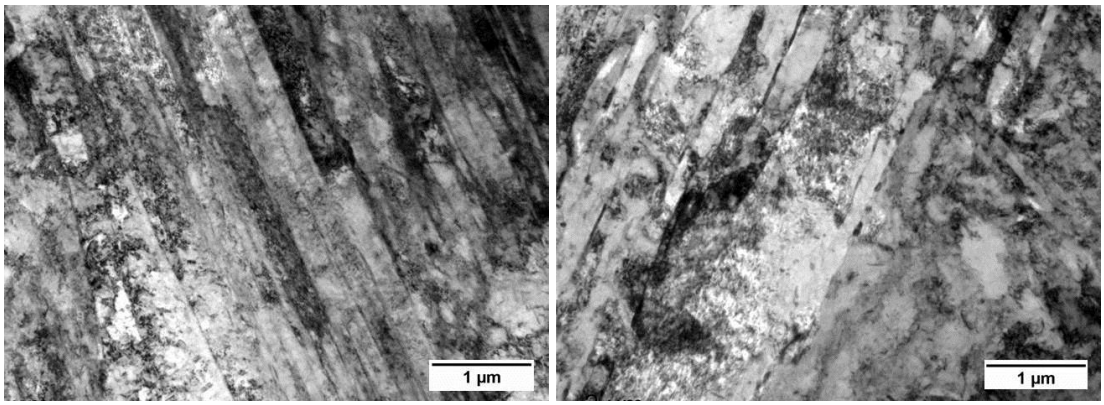

(a) (b)

Figure 4-44: TEM images of simulated HAZ of single and double thermal cycles (a) 1350ºC and (b) 1350 - 750°C

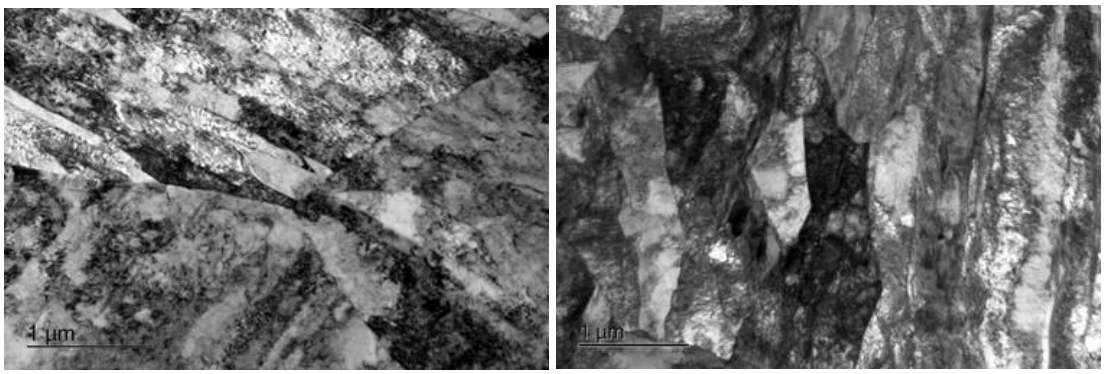

(a) (b)

Figure 4-45: TEM images of simulated HAZ. (a) 1350 - 750°C and (b) 1350 - 800°C

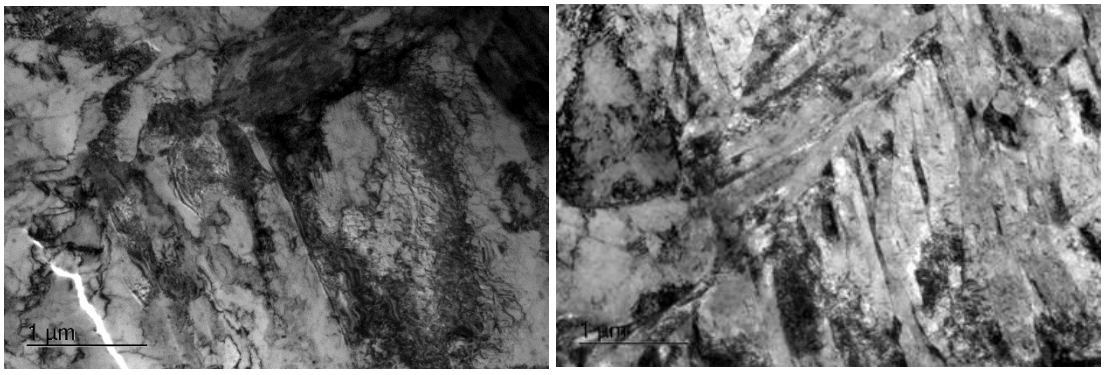

(a) (b)

Figure 4-46: TEM images of simulated HAZ. (a) 1100 - 750°C and (b) 1100 - 800°C

4.9.2 TEM FIB samples for simulated and real welds

To enable TEM specimens taken from site specific locations (at the MA phase), the FIB technique was used, as described in Section 3.5.6. TEM FIB specimens were taken from the ICCG HAZ region of single and four-times repaired pad welds. The lamellar sample was taken across a MA phase, located at a PAG boundary, with the martensite matrix sampled on either side, as shown in Figure 4-47 (a) and (b). Therefore, the centre part of the lamellar shown in Figure 4-47 (c) corresponds to the MA phase and the edges correspond to the martensite matrix. The microstructure of the centre region and the edge showed similar lath-like structure, however, smaller laths were observed in the centre region where MA was present. TEM images of the centre region are shown in Figure 4-48.

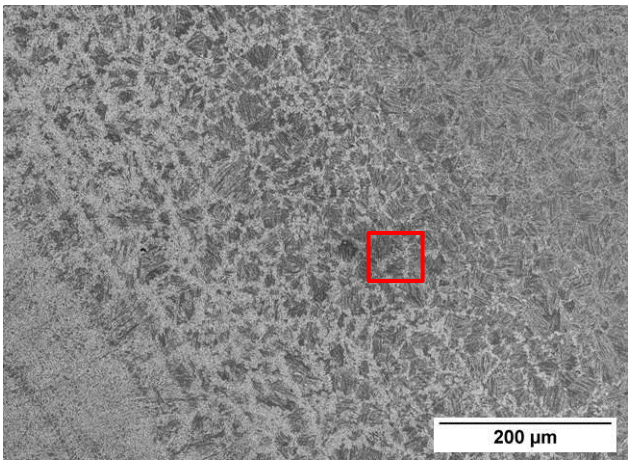

(a)

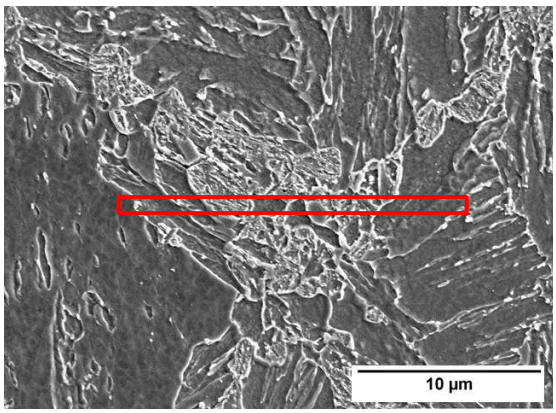

(b)

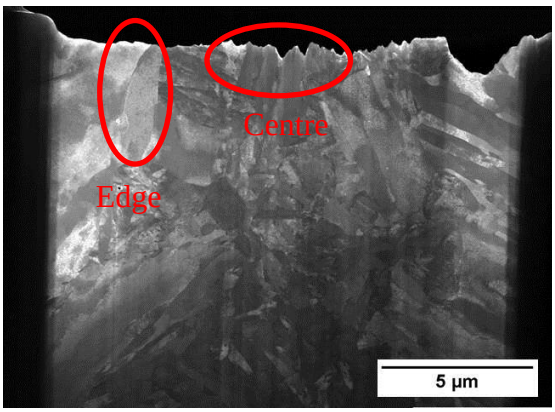

(c)

Figure 4-47: FIB sample taken from CGIC region on pad weld repair 1. (a) CGIC region where the fib sample was taken, (b) the magnified image of the location where sample cut out and (c) the FIB lamellar after final preparation.

Figure 4-48 (a) shows MA laths with high dislocation density and dark silvers of retained austenite. The corresponding region with dark field image (Figure 4-44 (b)), showed retained austenite in-between the laths, grey, and cementite particles, which are visible as white spots. The FCC diffraction pattern obtained from area "A" in Figure 4-44 (a), is shown in Figure 4-44 (c) and confirms the presence of austenite in MA.

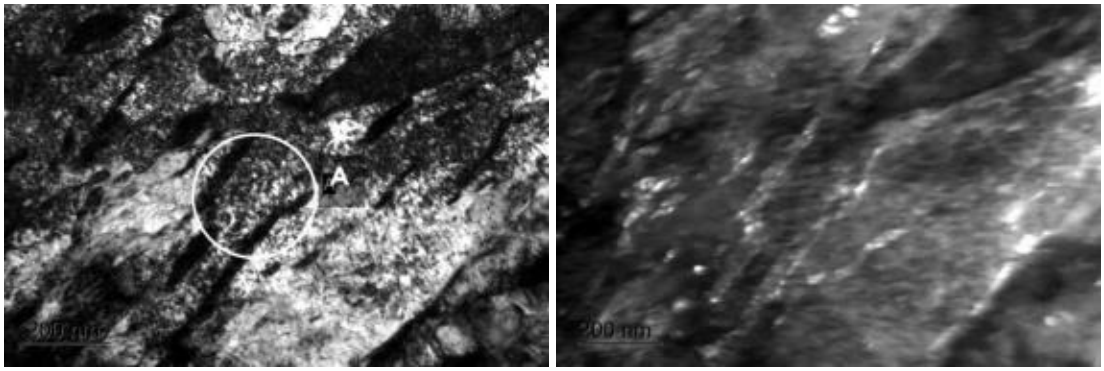

(a) (b)

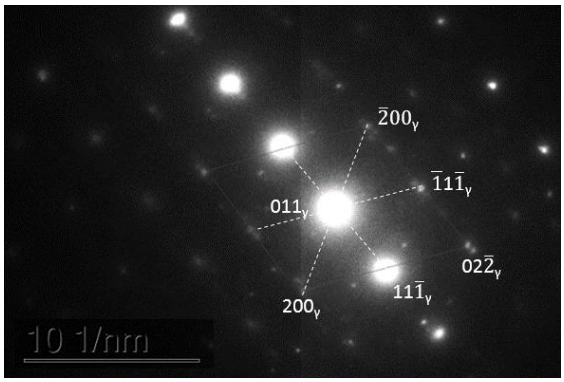

(c)

Figure 4-48: TEM images from the MA constituent in GCIC region of single repair pad weld sample. Where (a) Fine lath structure with high dislocations and retained austenite, (b) Dark field image of (a) where cementite particles can be seen in white and retained austenite as grey and (c) the diffraction pattern with FCC spots, obtained from location A, confirmed the presence of RA.

TEM images from the matrix region of pad repair 1 sample are shown in Figure 4-49, where (a) shows a large grain which was orientated to the [011] zone axis (c) and (b) shows the presence of carbides. In Figure 4-50, a higher magnification image

shows the high dislocation density of the grain shown in Figure 4-49. The grain was tilted slightly to show up the dislocations. The diffraction image in (b) shows a 011 BBC matrix with spots in between (arrowed) that confirms the presence of fine particles of cementite.

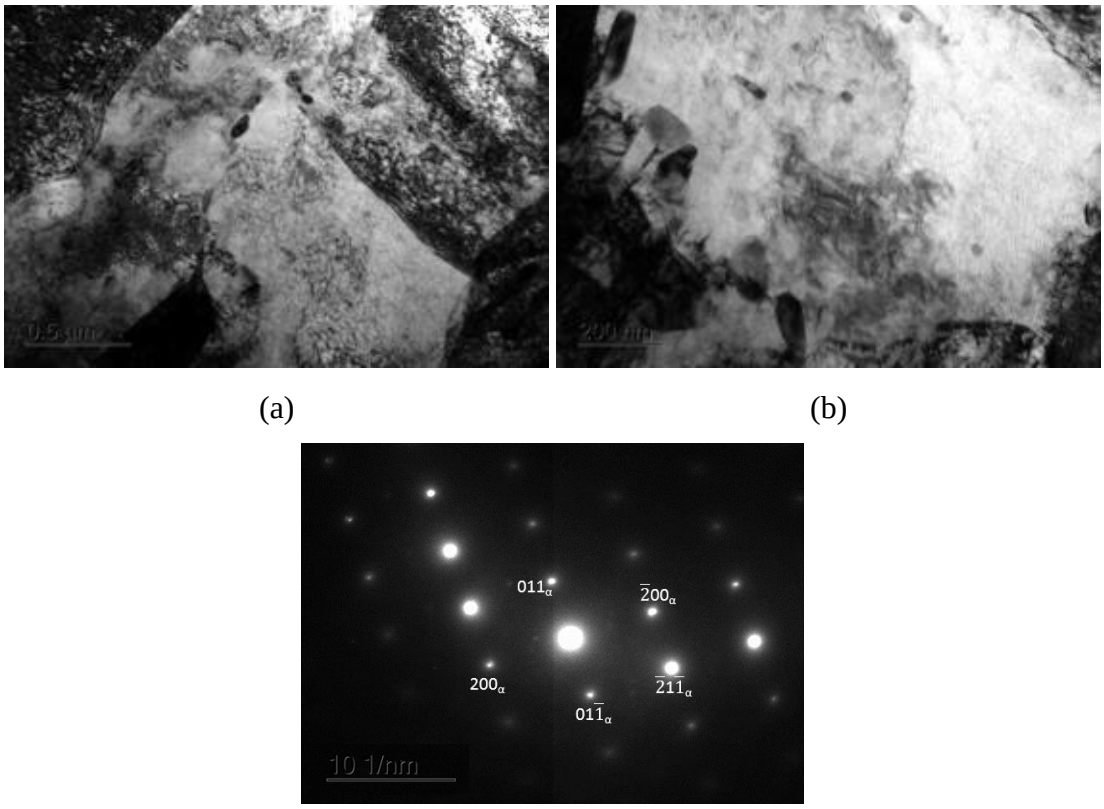

Figure 4-49: TEM images from the tempered matrix of pad repair 1. Where (a) a large grain with 011 orientation, (b) carbide particles along the grain boundaries and (c) Diffraction pattern from the large grain showing [011] zone axis orientation.

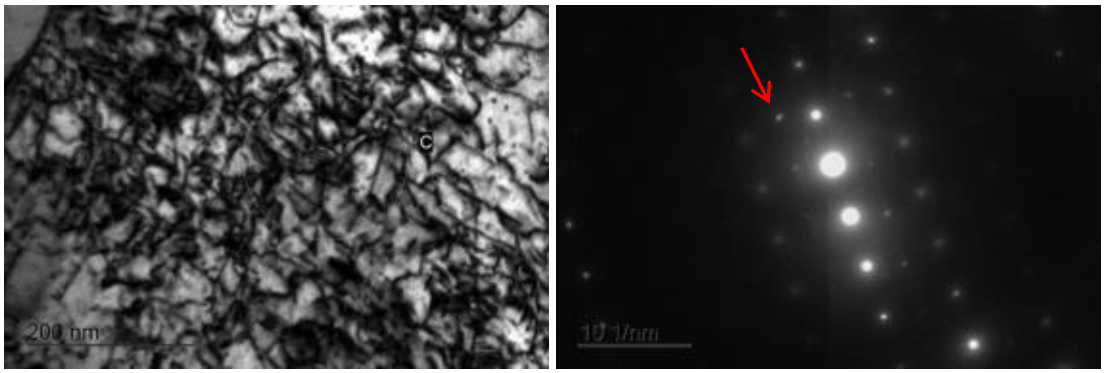

(a) (b)

Figure 4-50: TEM images from the same grain shown in Figure 4-49, showing (a) presence of high dislocation density and small carbide particles and (b) diffraction from area "C", showing 011 BCC matrix with spots in between (arrowed) from cementite.

A TEM FIB sample was taken from ICCG region of pad weld repair 4. A sequence of images is shown in Figure 4-51, where (a) shows the relation of the ICGC region to fusion line, (b) shows the location the TEM lamellar was taken and (c) shows the final TEM lamellar. The sample was taken so that the centre part of the lamellar included the middle of an MA phase and the edges were the matrix.

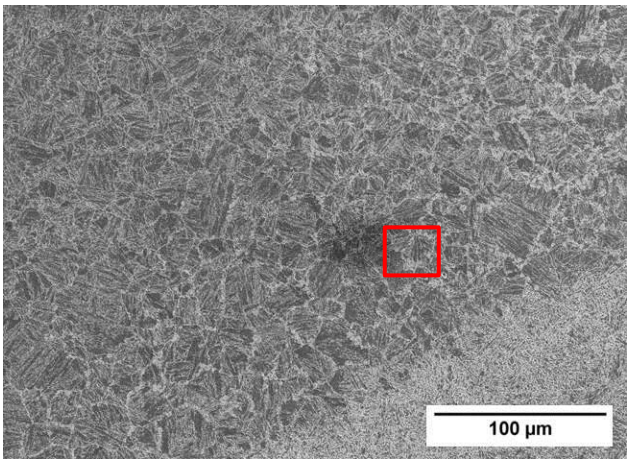

(a)

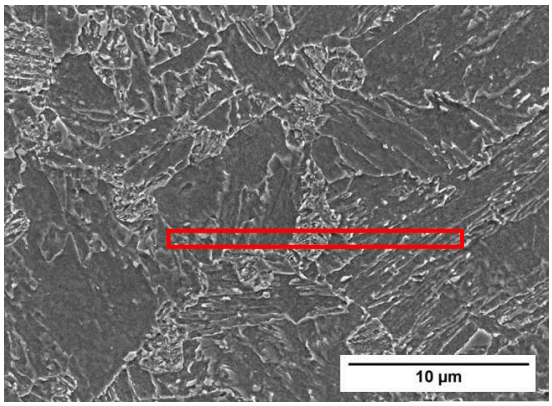

(b)

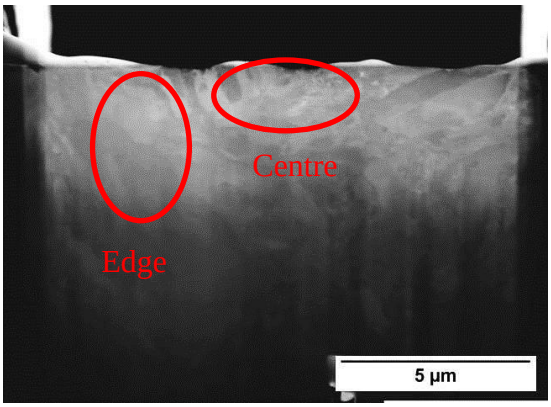

(c)

Figure 4-51: FIB sample taken from an ICCG region of repair 4, pad weld. Where (a) region of selected ICCG HAZ, (b) location of the FIB sample and (c) the FIB lamellar after final preparation. Image (c) is a 30 kV transmission electron image of where the centre is the second phase of ICCG and the edge is the matrix region.

The matrix consisted of larger laths compared to MA in the centre region and fine particles were observed inside the laths, as shown in Figure 4-52. The diffraction pattern showed these particles were not cementite. Figure 4-53 shows an example of particles of retained austenite found in the ICCG region of pad weld repair x4 sample, where the inset diffraction pattern indicated FCC structure was present. Retained austenite particles were in the range of size between 50-100 nm.

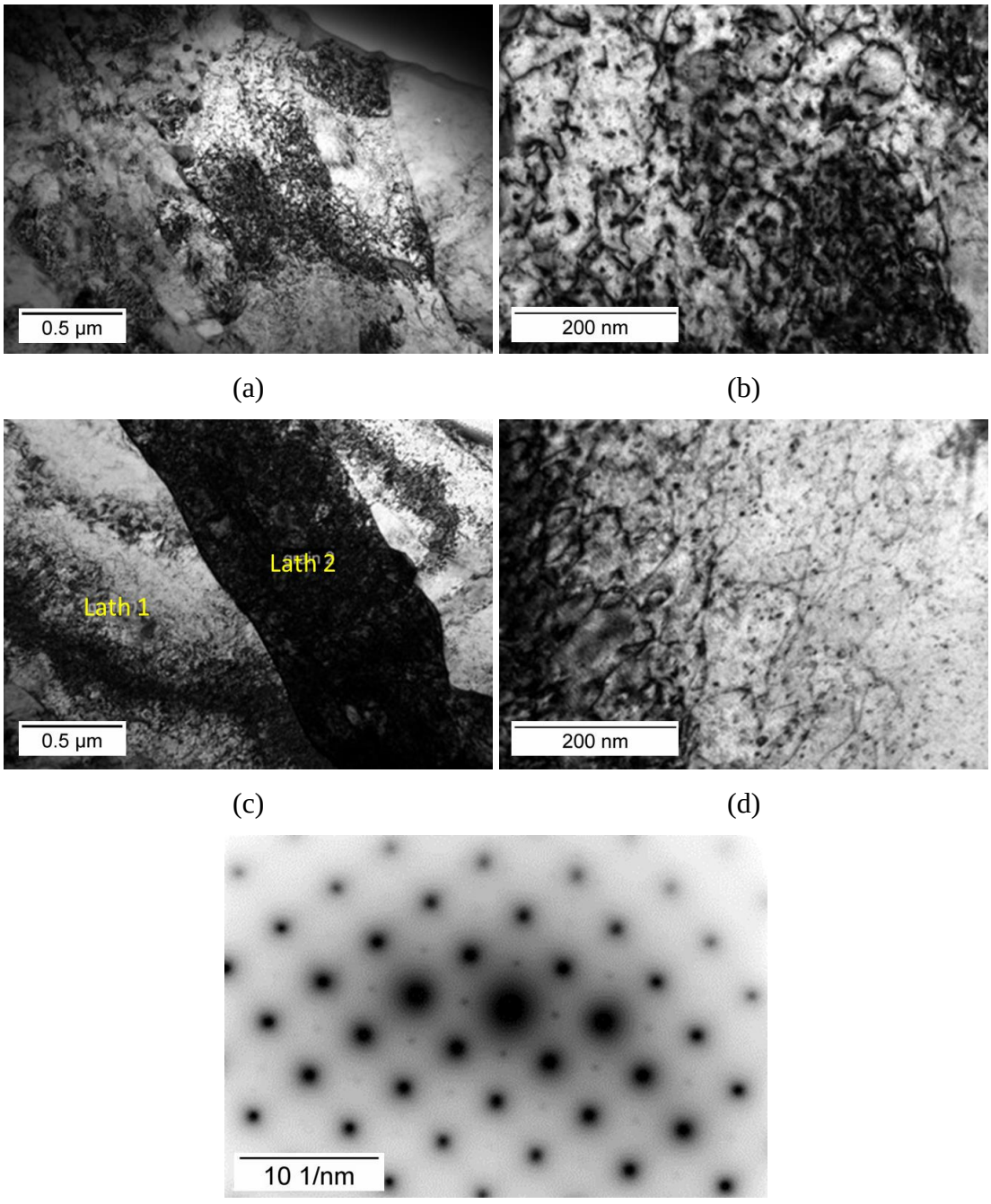

Figure 4-52: TEM images of pad 4. (a) low magnification image of centre ICCG region, (b) dislocations in ICCG region in 'a' tilted to 001 zone axis, (c) low magnification image of edge, (d) dislocations and cementite of lath 1 in 'c' tilted to 001 and (e) diffraction from above ‘d’ and extra spots are from cementite.

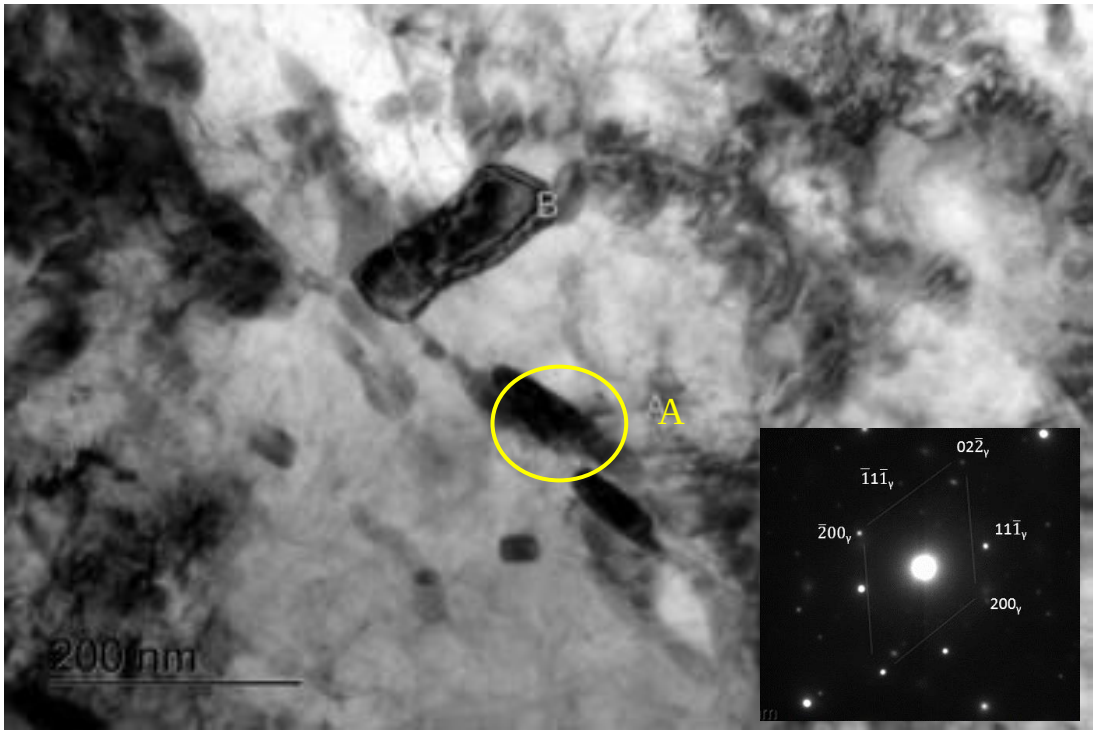

Figure 4-53: TEM image of retained austenite particles from the ICCG region of pad weld repair x4, where the diffraction pattern from "A" contains spots from an FCC phase, is shown in the inset.

Retained austenite particles were in the range of size between 50-100 nm. All retained austenite particles were presented along the lath boundaries (Figure 4-53). TEM image and selected area diffraction patterns taken from the matrix region of pad weld repair 4 is shown in the Figure 4-54. Diffraction patterns indicated the presence of an FCC phase, which identifies the particles as MA phase. The MA particles ranged between 10-100 nm in size.

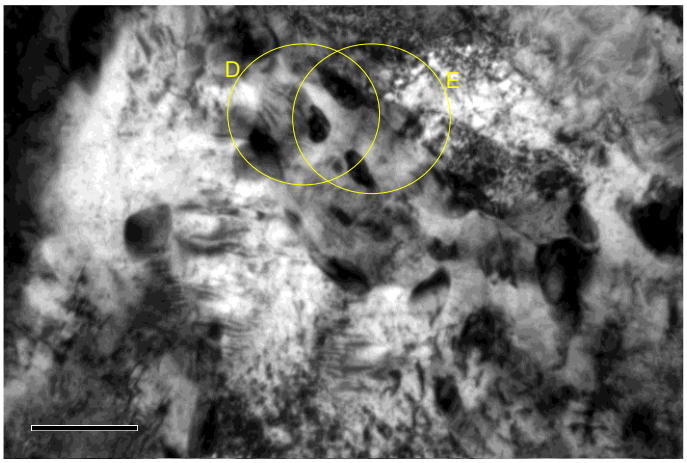

(a)

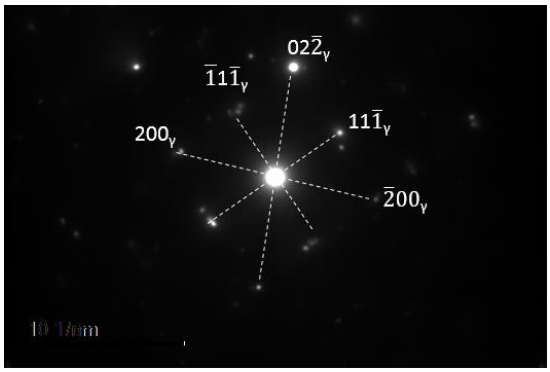

(b)

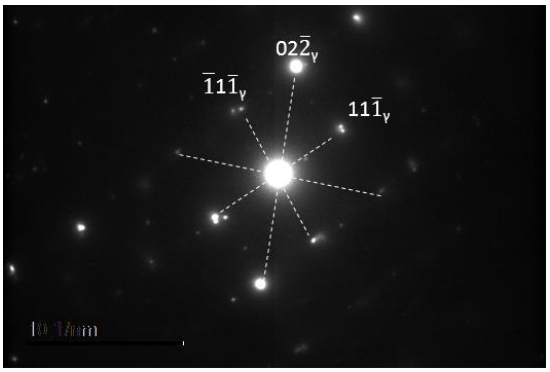

(c)

Figure 4-54: TEM image and diffraction patterns of the matrix region of pad repair weld ×4, where (a) TEM image from the matrix region showing dark grains of retained austenite and (b) and (c) show diffraction patterns from locations D and E, respectively, with evidence of FCC spots, indicating retained austenite.

4.10 Dynamic tear testing

The dynamic tear testing was conducted on full penetration butt weld samples, where the notch was located in the HAZ region as described in section 3.4.3. Tests were carried out with full-size specimens. The results are shown in Table 4-6 and macro images of fracture surfaces are shown in Figure 4-55. All samples exhibited large shear lips, comprising of approximately 60% of the cross-section area. As shown in Table 4-6, all samples except the DT4 showed dynamic tear values above 900 J at -29°C (-20.0°F). The minimum energy requirement is 680 J [7]

Table 4-6: Dynamic tear test results of HAZ samples taken from full penetration butt joints with four cycles of repair welding.

Sample No	Test sample orientation	Test temperature/°C	Drop height/m	Drop carriage weight/kg	DT Energy/J
DT1	LT	-29	2	171	945
DT2	LT	-29	2	171	903
DT3	LT	-29	2	171	945
DT4	LT	-29	2	171	717

Fracture face

Fracture side view

DT1

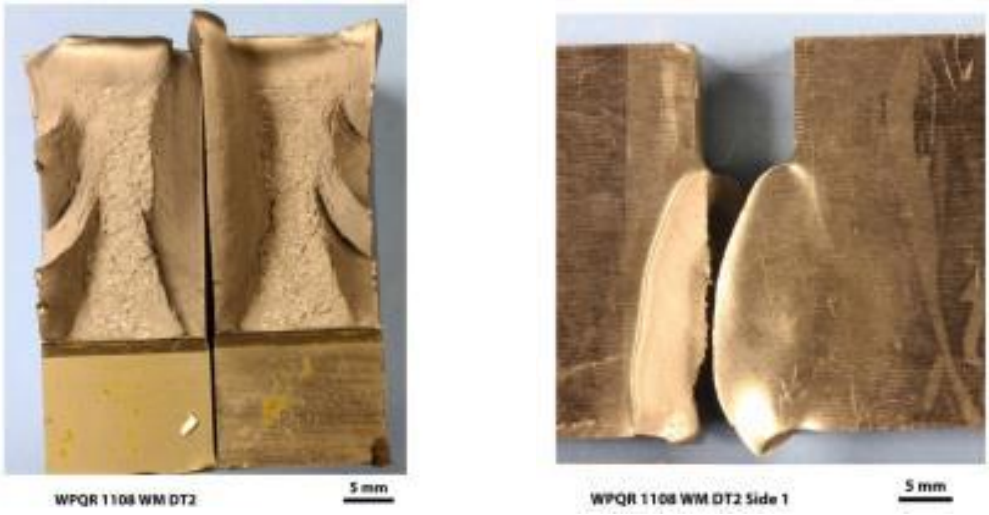

DT2

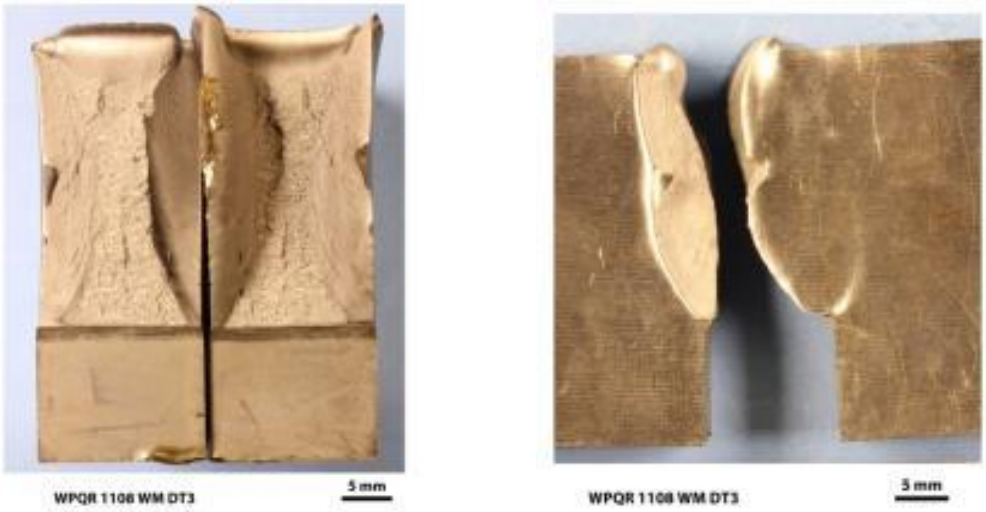

DT3

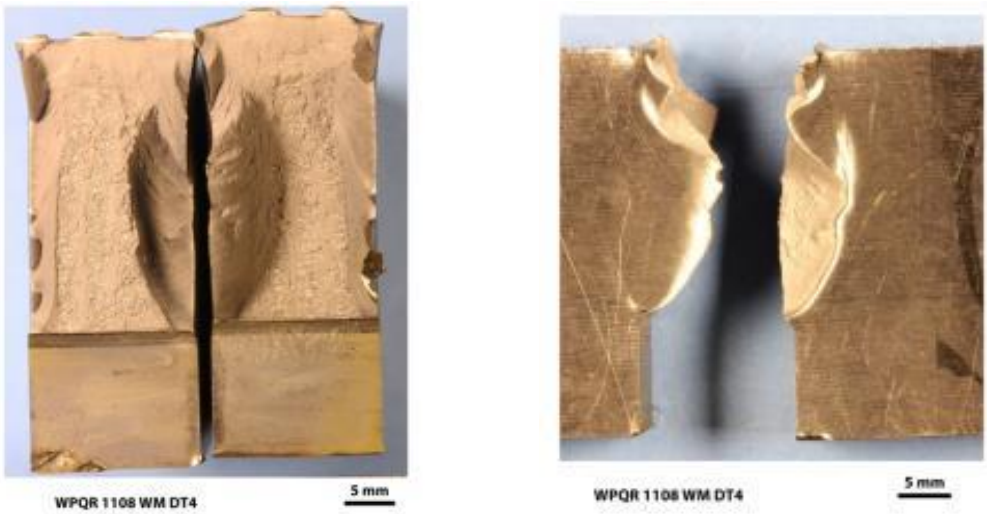

DT4

Figure 4-55: Macro images of dynamic tear test samples.

4.11 Residual stresses in pad welds

The residual stresses of pad welds were measured using neutron diffraction technique, as described in Section 3.4.4. The longitudinal, transverse and normal stress fields on all four samples of pad weld repairs were measured. There were higher tensile stresses underneath the pad weld, in both longitudinal and transverse direction, for all repair samples (repair 1 to repair 4). High longitudinal residual stresses quickly reduced to background levels, within 20 mm from the pad weld, as shown in Figure 4-56. High transverse residual stresses changed from tensile to compression stresses within 10 mm from the pad weld, as shown in Figure 4-57. The normal residual stresses, Figure 4-58, were quite variable and often above the background level of the plate. The longitudinal stresses typically showed higher values compared to the transverse stresses, where the maximum stress was 550 MPa in the weld repair 2 (80% of the minimum yield strength of the material). Longitudinal stresses remained as tensile stresses, even away from the pad weld, while transverse stress changed to compression just after the weld, compare Figure 4-56 to Figure 4-57.

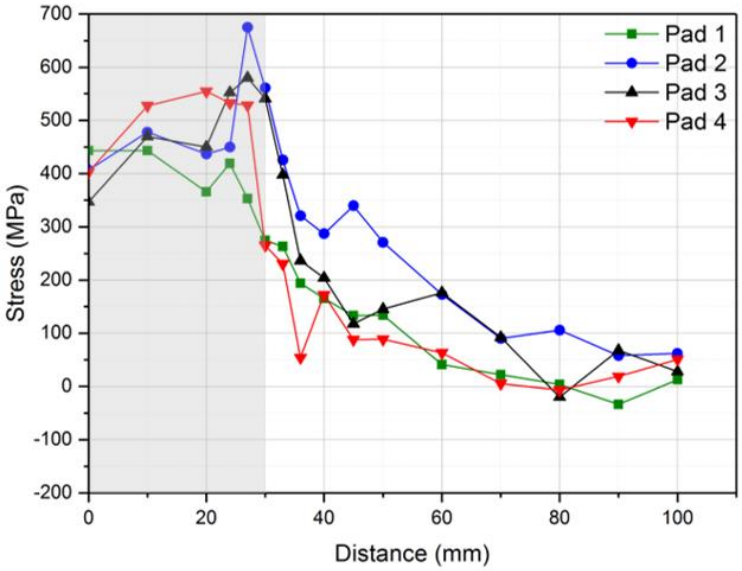

Figure 4-56: Longitudinal residual stress distribution along the longitudinal direction of the weld (shaded is weld region)

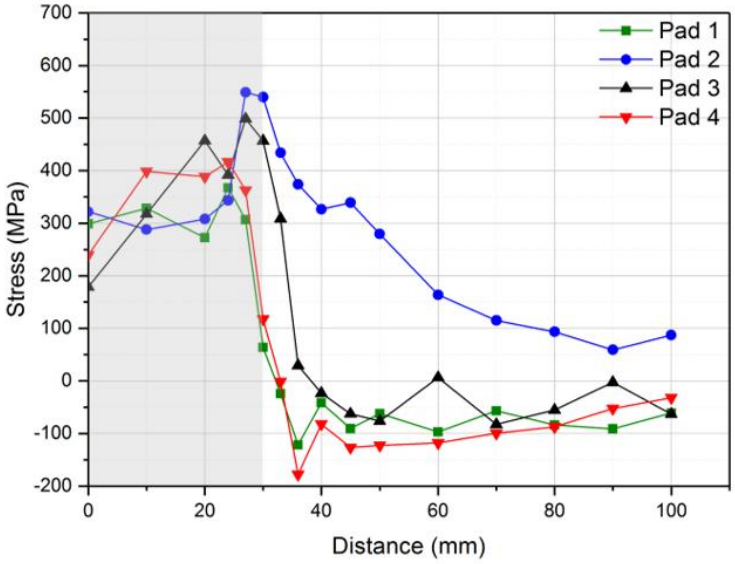

Figure 4-57: Transverse residual stress distribution along the longitudinal direction of the weld (shaded is weld region)

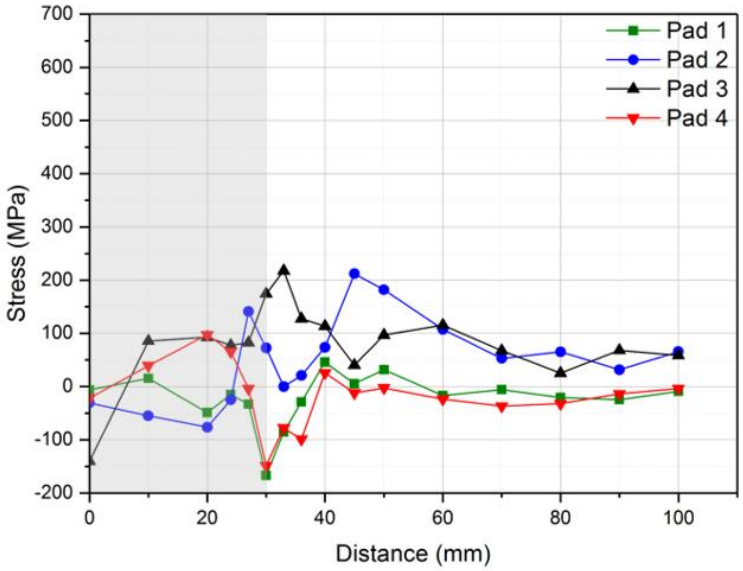

Figure 4-58: Normal residual stress distribution along the longitudinal direction of the weld

The variation of residual stresses in longitudinal and transverse directions of pad repair weld 1 and pad repair weld 4 measured along the weld direction measured 3 mm below the plate surface as shown in Figure 4-59. Both longitudinal and transverse stresses were slightly higher in pad 4 compared to pad 1. Longitudinal stress field was always higher than the transverse stresses in both pad weld repair 1 and 4 (see Figure 4-59).

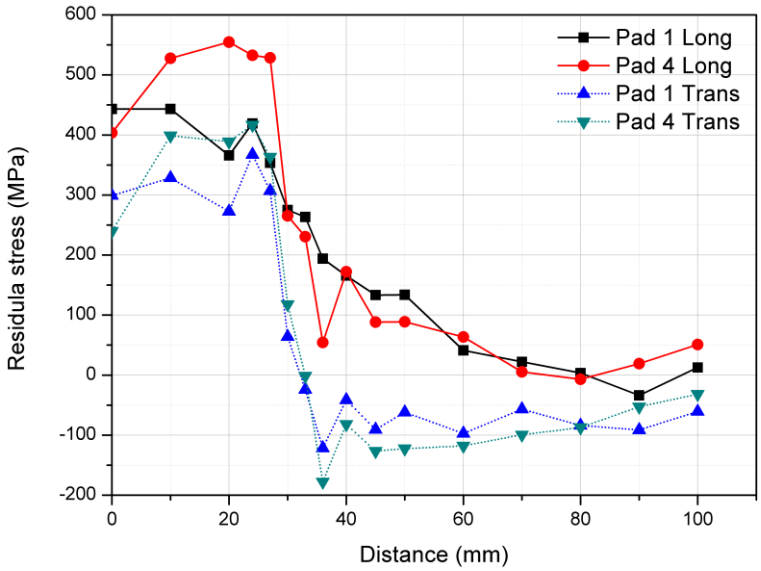

Figure 4-59: The variation of residual stresses in longitudinal and transverse directions of pad repair weld 1 and pad repair weld 4.

In some situations, it is required to grind off the capping of the pad weld because of functional reasons. To replicate the scenario, residual stresses were re-measured on pad repair weld 1 with the capping of the weld ground off. Figure 4-60 shows the variation of the three principal stresses with and without weld capping on. In the figure, dotted lines represent the stress fields with the weld ground off. It was observed that there were minimal changes to the residual stress profile after the weld capping was ground off. The notable exception was a sharp peak longitudinal stress, at 33 mm, corresponding to the edge of the pad weld. Furthermore, it appears that there was about a 5 mm peak shift for both the longitudinal and transverse stresses on the ground pad weld, compared to the original weld.

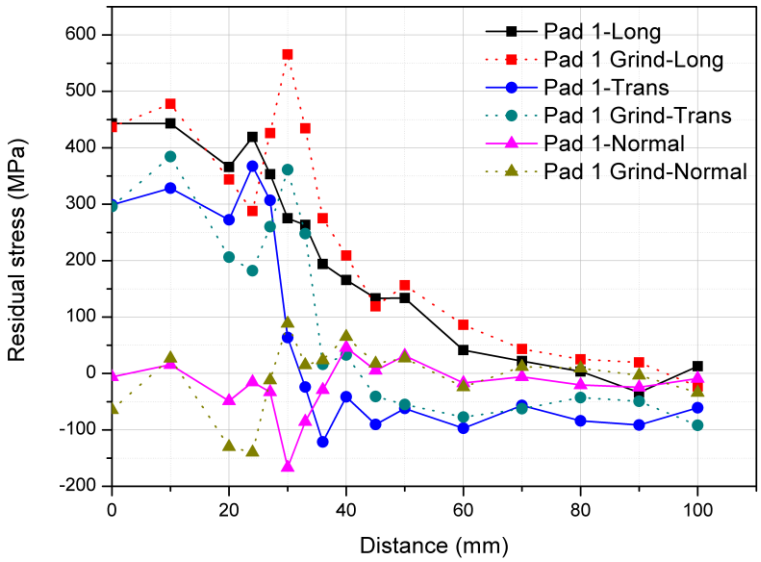

Figure 4-60: Comparison of residual stress changes in pad repair 1 between the original weld and after the weld capping was ground back to 1 mm above the plate surface.

4.11.1 Contour mapping of residual stresses in pad welds

Residual stress was measured in the through-thickness direction (z-direction) for pad welds 1 to 4, as described in section 3.4.4. These results were combined with the surface (3 mm below the surface) results to produce contour colour maps of the residual stress. The contour colour maps of the residual stress distribution of pad weld repairs 1 to 4 in both longitudinal and transverse directions are shown in Figure 4-61 to Figure 4-64. All four pad welds showed similar residual stress distributions, where the highest stresses were found beneath the pad, particularly at the toe of the weld. The transverse residual stresses appeared slightly lower in the weld repair 1 compared to the multiple weld repaired specimens.

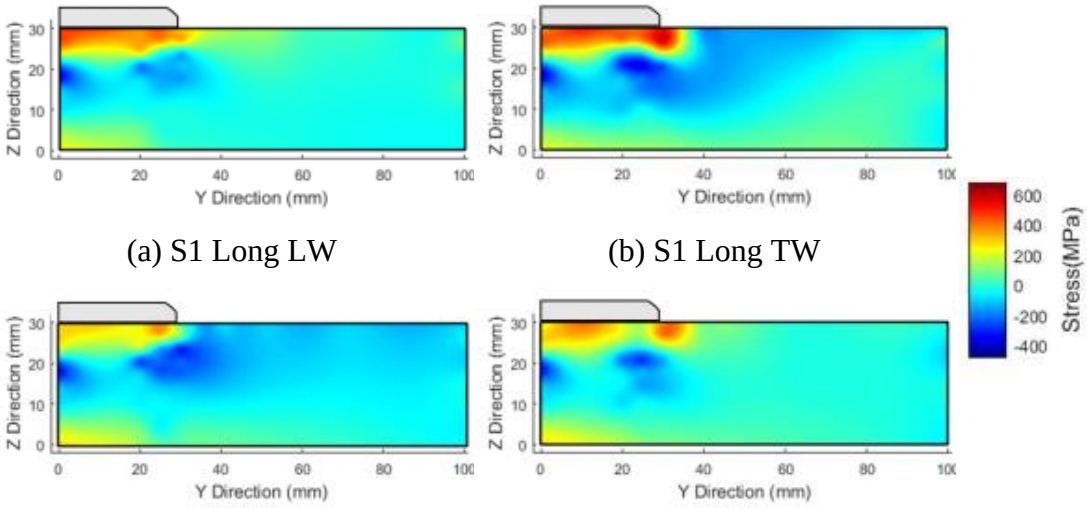

(a) S1 Long LW (b) S1 Long TW

(c) S1 Trans LW (d) S1 Trans TW

Figure 4-61: Distribution of residual stresses below the pad weld repair 1 (a) Longitudinal stresses longitudinal to the weld (b) longitudinal stresses transverse to the weld, (c) transverse stresses longitudinal to the weld and (d) transverse stresses transverse to the weld

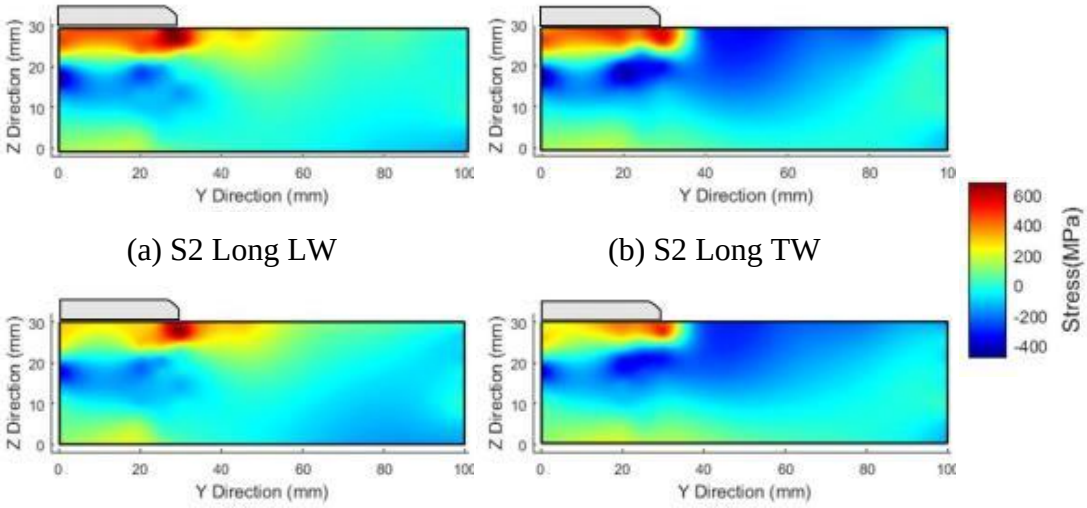

(a) S2 Long LW (b) S2 Long TW

(c) S2 Trans LW (d) S2 Trans TW

Figure 4-62: Distribution of residual stresses below the pad weld repair 2 (a) Longitudinal stresses longitudinal to the weld (b) longitudinal stresses transverse to the weld, (c) transverse stresses longitudinal to the weld and (d) transverse stresses transverse to the weld

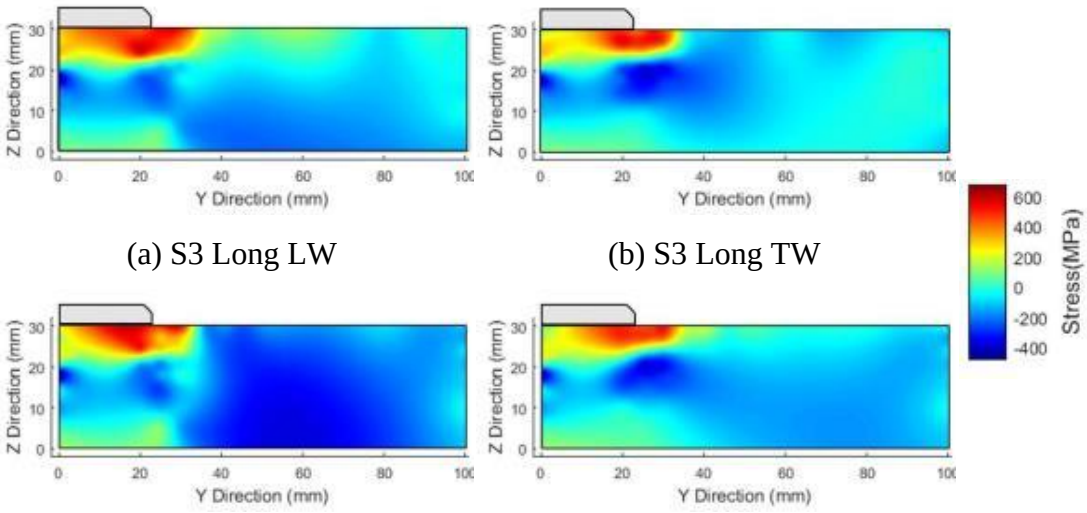

(a) S3 Long LW (b) S3 Long TW

(c) S3 Trans LW (d) S3 Trans TW

Figure 4-63: Distribution of residual stresses below the pad weld repair 3 (a) Longitudinal stresses longitudinal to the weld (b) longitudinal stresses transverse to the weld, (c) transverse stresses longitudinal to the weld and (d) transverse stresses transverse to the weld

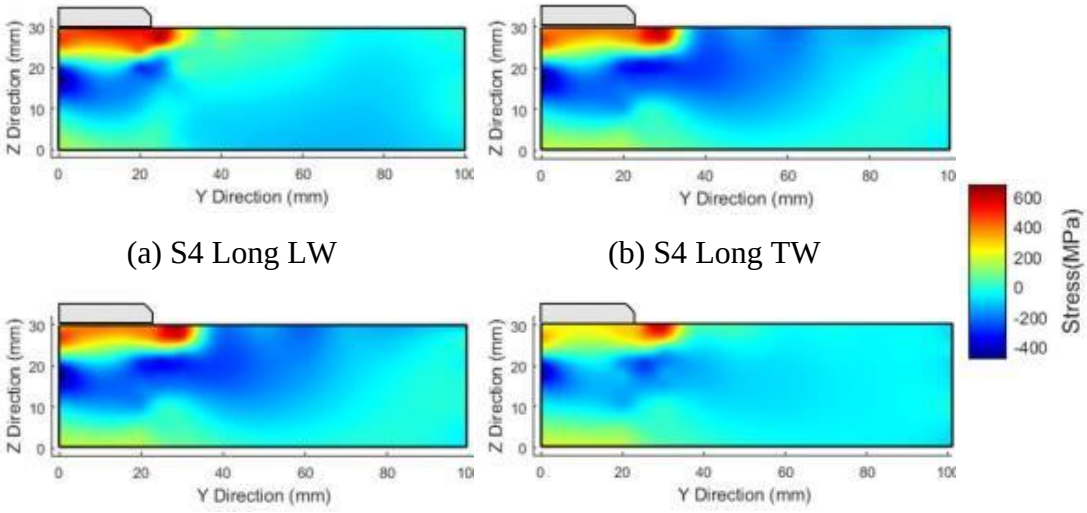

(a) S4 Long LW (b) S4 Long TW

(c) S4 Trans LW (d) S4 Trans TW

Figure 4-64: Distribution of residual stresses below the pad weld repair 4 (a) Longitudinal stresses longitudinal to the weld (b) longitudinal stresses transverse to the weld, (c) transverse stresses longitudinal to the weld and (d) transverse stresses transverse to the weld

4.12 EBSD Analysis

The Electron Backscattering Diffraction (EBSD) technique was used to characterise microstructural texture, grain size, lath orientation and to identify the preferred orientation along the fracture path. As discussed in Section 3.5.6, simulated HAZ samples were used for the characterisation of fracture propagation and real weld samples were used for texture and phase analysis.

4.12.1 EBSD of simulated HAZ specimens.

The focus of the EBSD work was investigating the simulated HAZ specimens that had the lowest toughness, (I.e. 1350°C, 1350-750°C) samples. For the 1350-750°C sample, the band contrast map clearly showed the location of MA phases on the prior austenite grain boundaries, as shown in Figure 4-65. This was useful as it was easy to distinguish between the MA particles and the matrix for the rest of the analysis.

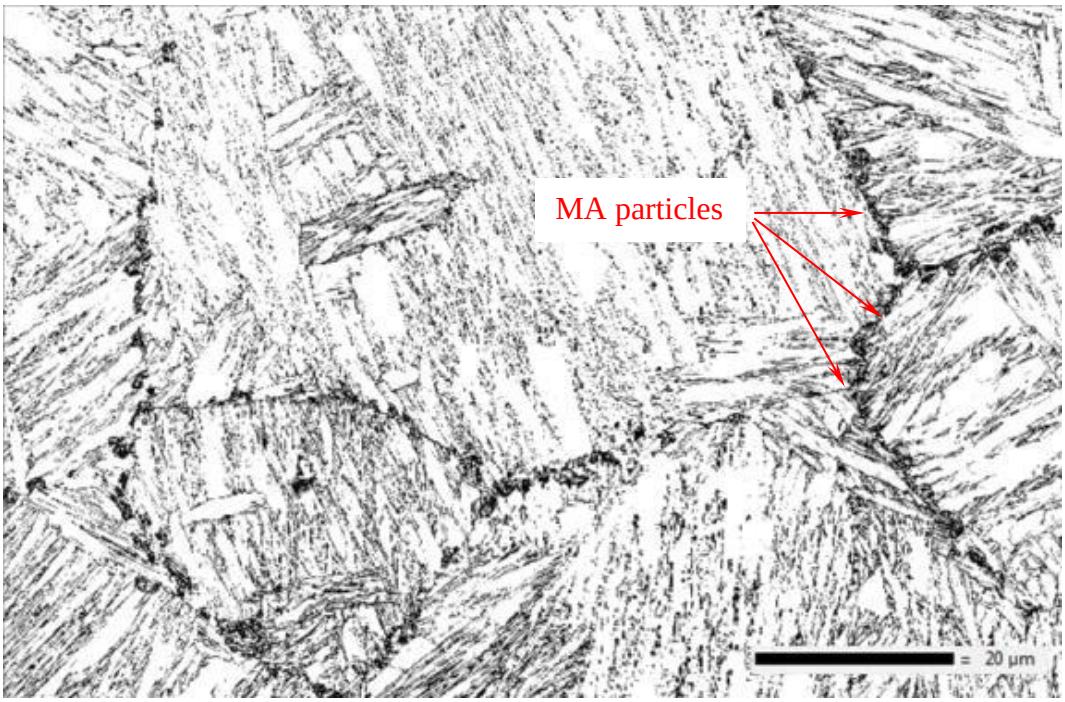

Figure 4-65: Band contrast map for the simulated HAZ of 1350-750°C sample. MA particles formed along the prior austenite grain boundaries during the second intercritical heating can be seen as darker regions.

Figure 4-66 shows the inverse pole figure colour map of the same region of Figure 4-65, showing there was no preferred orientation of the matrix. The magnified region in (b), shows that the newly formed MA does not have any preferred orientation.

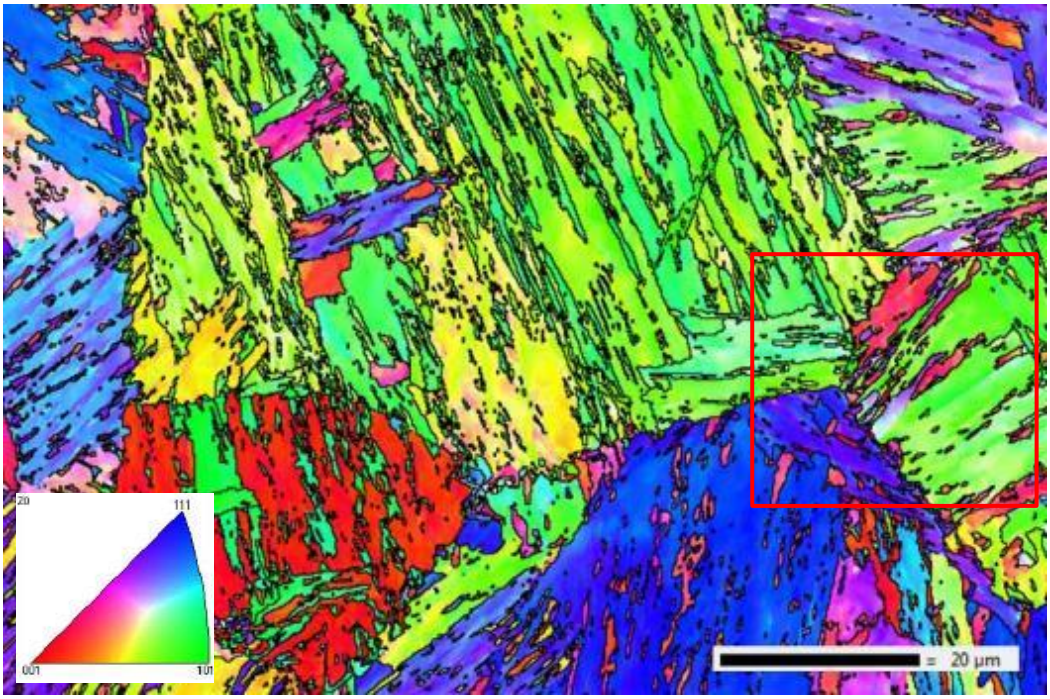

(a)

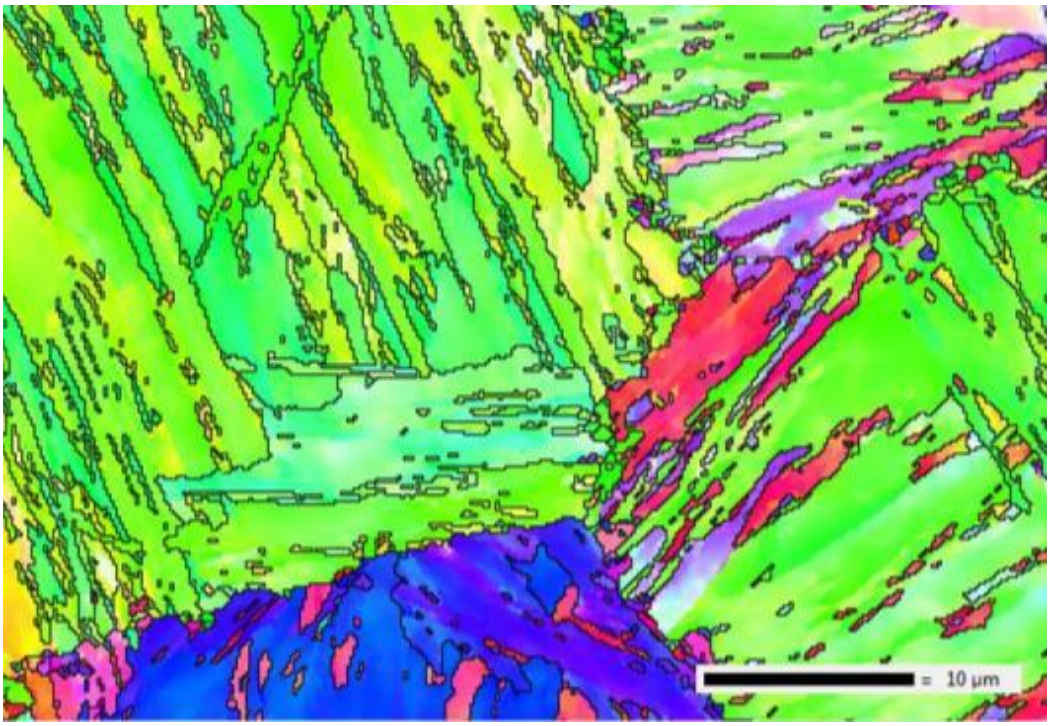

(b)

Figure 4-66: (a) IPF colour map for the simulated ICCG sample with 1350-750°C thermal cycles and (b) is the higher magnification from the inset of a. (Black lines are the grain boundaries with more than 15° of misorientation).

The band contrast map with grain boundaries added showed a high density of high angle grain boundaries in the MA phase compared to the rest of the matrix, for the simulated CGIC sample, as shown in Figure 4-67. The majority of the structure consisted of BCC (blue), with a very small amount of retained austenite (FCC- red), as shown in Figure 4-68.

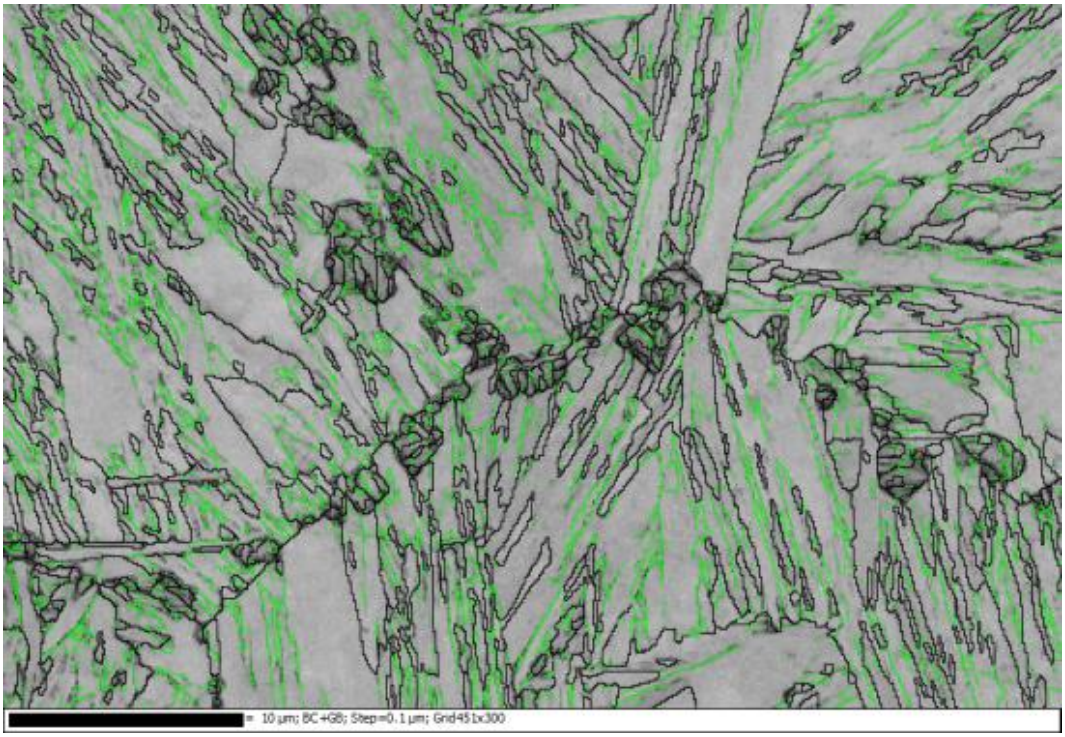

Figure 4-67: Band contrast map with grain boundaries of simulated HAZ with double thermal cycles (1350-750ºC). Darker grey areas represent newly formed MA constituents. Dark lines show high angle grain boundaries (θ>15º) and green lines are low angle grain boundaries (15º>θ>2º).

As indicated with TEM micrographs, EBSD also shows a smaller lath-like structure in the MA phase. There is a high density of high angle grain boundaries in the newly formed MA phase compared to the rest of the matrix.

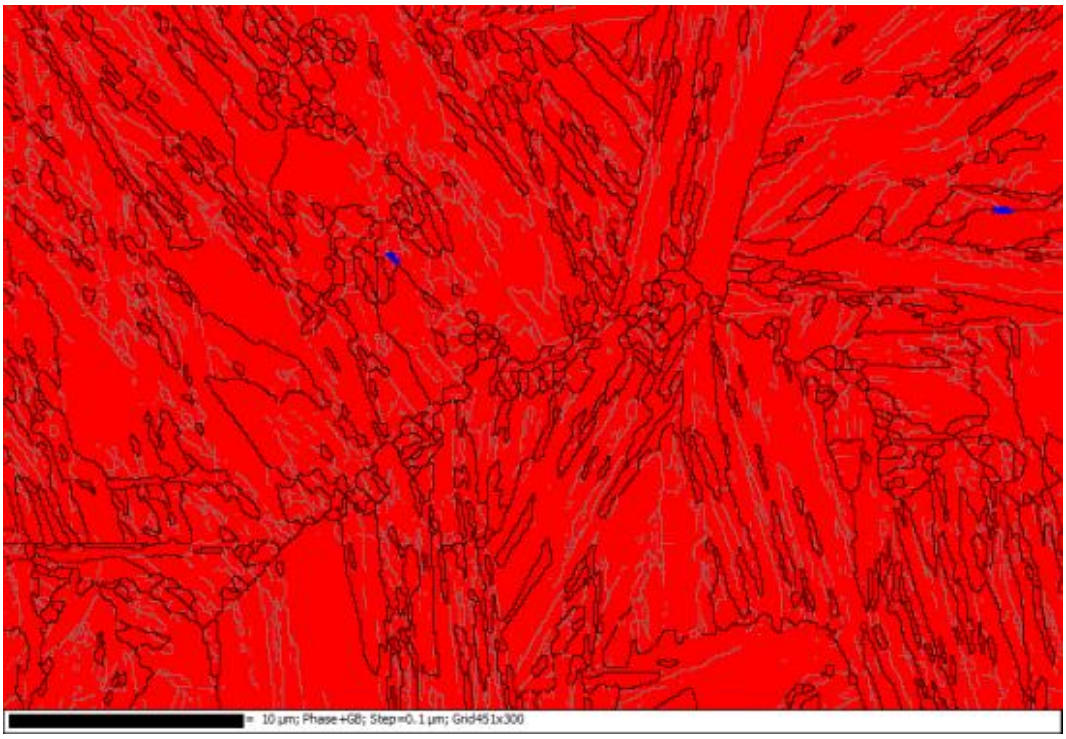

Figure 4-68: Phase map of simulated HAZ with double thermal cycles (1350-750°C). Red is BCC steel and Blue is FCC. Dark lines show high angle grain boundaries (θ>15º) and green lines are low angle grain boundaries (15º>θ>2º).

The band contrast map of the simulated HAZ sample with ICCG of 1350-800°C, is shown in Figure 4-69. MA phase at the grain boundaries were wider compared with the 1350-750°C sample, which matches the finding from optical images and with SEM images. The same region of the band contrast map is shown with IPF colour map in Figure 4-70(a), with the higher magnification image of the highlighted region shown in Figure 4-70(b). Both figures confirm that there was no specific preferred orientation to either MA phase or the rest of the matrix.

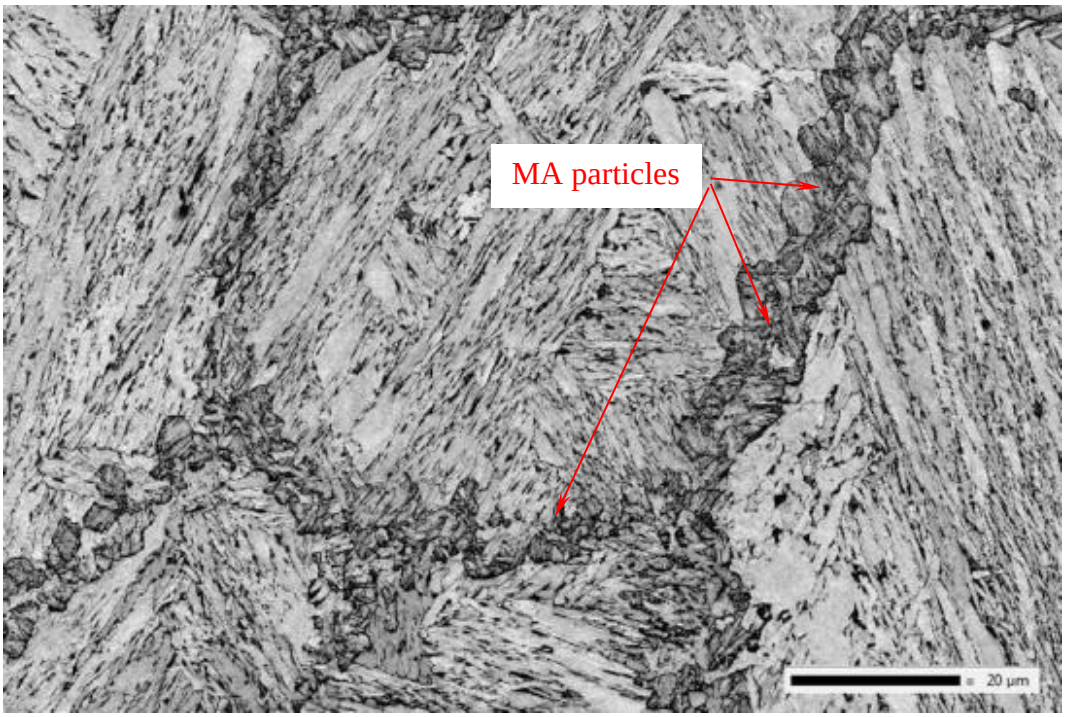

Figure 4-69: Band contrast map for the simulated HAZ of 1350-800°C sample. MA particles formed along the prior austenite grain boundaries during the second intercritical heating can be seen as darker regions.

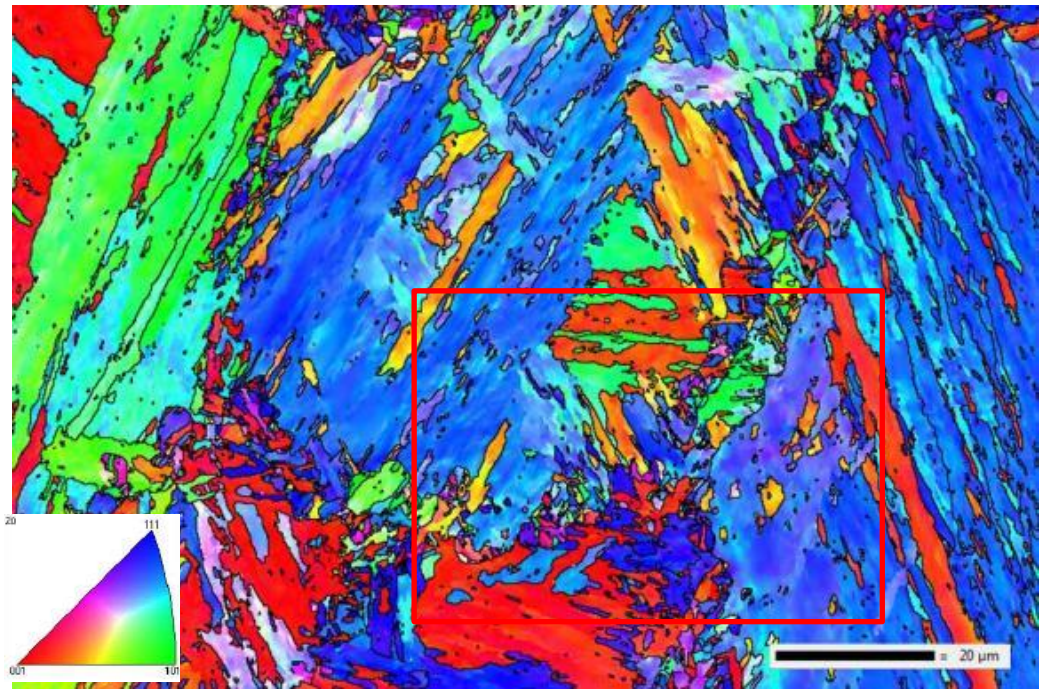

(a)

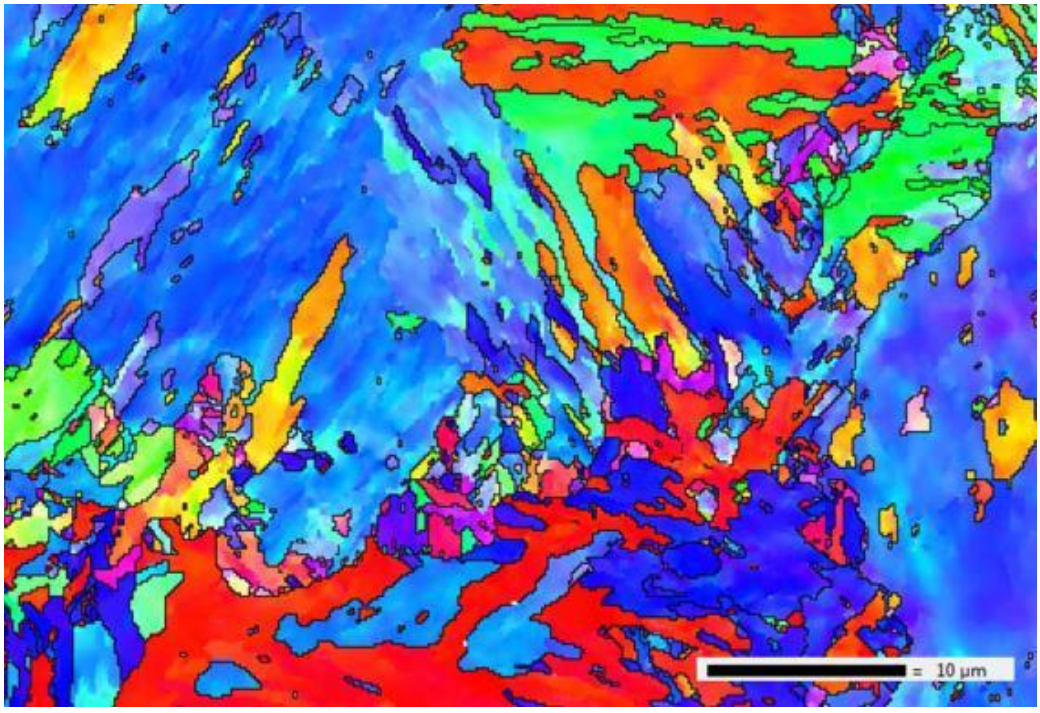

(b)

Figure 4-70: IPF colour map for the simulated ICCG sample with 1350-800°C thermal cycles. (Black lines are grain boundaries with more than 15° of misorientation).

4.13 Summary of Results

- Dilatometer experiments were completed to determine the upper and lower transformations on heating in order to establish the correct intercritical region for BIS812 EMA steel,
- Prior austenite grain size was measured, so its influence on toughness could be evaluated,
- Optical microscopy was performed to characterise the different microstructures formed in the HAZ, for single and multiple welds, and this data was used to understand the variation in properties of each sub-HAZ region,
- SEM microscopy was used to 1) characterise the microstructure at higher magnification (compared to optical) to reveal the internal structure of the MA phases and 2) to investigate the microstructure at the fracture face in cross-sections and 3) conduct fractography,
- The toughness of different simulated HAZ sub-regions and of the real weld, for single and multiple welds, was determined using Charpy impact testing.
- Instrumented Charpy impact testing was performed to gain an understanding of how the variation in microstructure of the different sub-HAZ regions influenced the initiation energy and propagation energy during fracture,
- The influence of multiple repair welds on hardness was determined using Vickers hardness mapping of the HAZ. Regions of high hardness can potentially indicate the region with lower toughness,
- Dynamic tear tests were performed to determine the effect of multiple repairs on the high strain rate toughness of the full penetration butt welds,
- TEM was used to characterise the lath morphology of the martensite, the MA phase and to determine the existence of retained austenite.

5 DISCUSSION

In the fabrication process of steel structures and components, welding is often required. Due to the thermal cycles of welds, the microstructure in the parent metal next to the weld is altered, producing a heterogeneous microstructure called a heat affect zone (HAZ). The properties of the HAZ is dependent on several variables, such as, composition of the parent metal, the welding conditions and resultant thermal cycle, alloying elements of welding consumable and, preheat and post weld heat treatments. As a result, the properties of the HAZ can vary widely, so it is important to establish the HAZ properties for specific welding conditions for a given steel type.

In this research, three types of welds, BoP, pad and full penetration butt welds, were used to investigate multiple repair welds on HAZ properties of a microalloyed quenched and tempered steel, BIS812 EMA. In each case, four weld repairs were conducted and the microstructure and, selected mechanical properties (toughness and hardness) were evaluated. Thermal HAZ simulations were conducted to study the effects of single and multiple thermal cycles and repeated single and multiple thermal cycles, to investigate the effects of recurring, multi-pass repair welds on specific sub-HAZ properties. The simulated specimens were made into Charpy impact samples, so the toughness of different sub-HAZ regions could be evaluated.

Microstructures of simulated samples compared with real weld HAZ's, confirming that the simulation accurately matched the weld conditions (see figure 4-8). Microstructural evolution for single and multiple simulated thermal cycles and repeated repair welds were studied and there were no visible changes from single cycle and multiple cycle HAZ observed with optical microscopy and SEM. The lowest toughness regions of the HAZ were the ICCG HAZ and CG HAZ (see figure 4-22). The reasons for the low toughness, the microstructural evolution and an evaluation of the mechanical properties of simulated HAZ specimens and repeated weld repaired samples will be reviewed in the discussion. A key emphasis of the discussion is to determine if the material properties are degraded with recurring multiple repair welds.

5.1 Microstructure evolution in multiple repair welds

The base material of BIS812 EMA steel was a martensitic structure with average planner grain size of 18 µm. After application of weld thermal cycles, with peak temperatures of 1000°C to 1350°C, the average PAG size varied from 11 µm to 64 µm, respectively (Table 4-1). In welding HAZ simulations, higher cooling rates often leads to martensite formation and slower cooling rates can lead to the formation of a mixture of martensite, bainite and ferritic products [15]. In this research, the cooling rate was relatively fast (because of 1 kJ/mm arc energy and 30 mm thick plate), which promoted lath martensite of both FGHAZ and CGHAZ regions (fig. 4-8). Furthermore, the moderate carbon level (~0.13%), macro alloying elements (e.g. Mn, Mo & Cr) and free boron increased the hardenability, which also promoted the formation of fully martensitic structures in HAZ regions, even at a fine PAG size. The calculated (from formula (10)) [14]) martensite start temperature (Ms) was 408°C and the CE (IIW) was 0.531. The final microstructure plays an important role in determining the mechanical properties of the HAZ. Hence, the steel type and its chemistry are important factors influencing the properties of the HAZ. The CCT diagram (Figure 5-1) shows fully martensitic microstructure can be achieved with even relatively slow cooling rates.

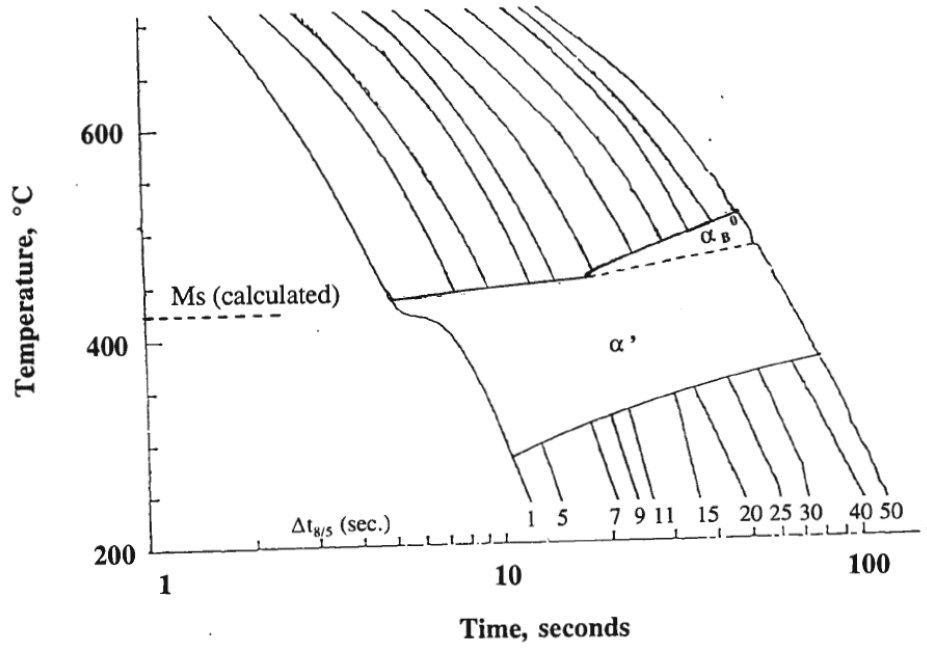

Figure 5-1 Continuous cooling transformation (CCT) diagram of BIS812 EMA steel with the sample austenised at 1250°C for 13 s before cooling [21].

$$M_s = 550 - 350C - 40Mn - 20Cr - 10Mo - 17Ni - 8W - 35V - 10Cu + 15Co + 30Al \quad (10)$$

When the microstructures of multiple CG thermal cycles were examined (Figure 4-11), the microstructures were similar to single CG thermal cycle. In multiple thermal cycles, the cumulative time at the maximum temperature did not affect the microstructure evolution, probably because of the short time at the peak of each cycle. As an example, the CG HAZ consisted of martensite with average PAG size of 64μm and the CGx4 thermal cycle exhibited 68μm, which is slightly increased at 7.8% of grain size.

Samples with an initial CG cycle and finished with an IC cycle showed lath martensite in main matrix and secondary MA constituent along grain boundaries. For multiple CG thermal cycles (1350°C), the previous microstructures were completely replaced with a new, similar coarse martensitic microstructure. As already stated, grain growth was negligible with multiple consecutive CG cycles due to the short hold time (0.5s) at the peak temperature. As the CG cycle replaced the previous IC cycle, only the final IC cycle counted for multiple CG-IC cycles, thus the microstructure remained the same. For repeated IC cycles (CG-IC-IC & CG-IC-IC-IC-IC), while the microstructure was not replaced, the very low intercritical temperature (750°C), limited the formation of MA constituent to the prior austenite grain boundaries and the short time at 750°C minimised any noticeable increase in the volume fraction of MA at the boundaries. It was observed that the application of multiple thermal cycles did not influence the increase prior austenite grain size, due to the application of high heating rates with short holding times. For example, an increase of the austenite grain size of 25% took 15 minutes at a peak temperature of 1120ºC, at 10°C/s heating rate, for 0.12% carbon HSLA steel [148].

In summary, the microstructures observed were predominantly dependent on the maximum temperature and the cooling rate rather than the number of thermal cycles. In Table 5-1, the grain size of repeated CG cycles can be seen to be stable. In Table 5-2, the volume fraction of MA formed for multiple CG-IC cycles, where the IC =

750°C, is shown and the volume fraction was similar. These observations from simulated cycles can be extended into the real welds since the thermal cycles for simulated HAZ were designed based on real weld thermal cycles. A review of the microstructures in the results section (section 4.4.1), found the above statement to be accurate, as the microstructures of the simulated and real HAZ specimens were similar. Due to the microstructural variation in a real HAZ, it is difficult to accurately measure any microstructural changes within different sub-zones, due to multiple thermal cycles, as there was significant microstructural variation within each zone.

Table 5-1: PAG sizes with single and consecutive multiple thermal cycles. All CG cycles were 1350ºC peak, 0.5 s at peak and 4.3 s to cool from 800 to 500ºC.

Thermal cycle	CG	CGx2	CGx3	CGx4
PAG size (µm)	64	69	66	68

Table 5-2: Percentage of MA measured in different thermal cycles.

Notation	**Thermal cycle**	**% of MA**
CG	1350°C	0
CG-IC	1350-750°C	4.4
CG-ICx2	1350-750-750°C	5.4
CG-ICx3	1350-750-750-750°C	5.3
CGx2-IC	1350-1350-750°C	4.8
CGx3-IC	1350-1350-1350-750°C	4.6
(CG-IC)x2	1350-750-1350-750°C	3.9
CGx2-ICx2	1350-1350-750-750°C	4.3

To show the importance of time at peak temperature, research conducted by Deng, et al. [33] on X80 pipeline steel, showed a noticeable increase of PAG size in simulated double cycle CG samples, compared to the single cycle (i.e. Average grain size was 30-50 µm in single cycles and increased to more than 50 µm in double cycles). The grain growth in X80 steel was higher compared to the steel in current research due to the increased holding time at maximum temperature (5 s vs 0.5s).

5.1.1 Characterisation of martensite matrix

In single and multiple thermal cycles, the smallest unit size of martensite, the lath size, remained relatively consistent, within the main matrix, in all samples. The matrix lath size varied between 0.15 µm to 2.8 µm with average lath size of 0.61 µm. The lath size within the MA phase along the prior austenite grain boundaries showed smaller sizes. This observation can be backed up with the finding by Wang, et al. [38], who showed that the martensitic lath size (~0.3 µm) was almost independent of PAG size. Hanamura, et al. [149] noted that martensite lath dimensions were not varying much with PAG size. However, as the PAG size decreases, both the packet size (PS) and block width (BW) become smaller [11].

Wang showed that the martensite packet size linearly increased with the increase of the prior austenite grain size [38]. The current study showed a similar trend of increasing martensitic packet size with increasing PAG size. For multiple identical thermal cycles, there was minimal variation in the microstructures (packets, PAGs and MA). Research by Hidaldo [11], on a martensitic steel (0.3C-1.6Si-3.5Mn), found that grain, packets and block sizes become more homogeneous with an increasing number of thermal cycles which were above A_{c3} temperature with same peak temperature.

All samples tested with simulated thermal cycles and real weld thermal cycled showed fully martensitic structure in the HAZ. The CCT curves of BIS812 EMA showed for both cooling rates used in the current experiment ($t_{8/5}$ 4.3 and 6.7s) the microstructure transforms to fully martensite, as shown in Figure 4-8.

5.1.2 Formation of MA constituents

The microstructure of the intercritically reheated HAZ varied with increasing intercritical temperature. MA constituents formed at lower IC temperature, which is commonly observed in the literature. However, at higher IC reheating, the structure formed on grain boundaries can be classified as secondary lath martensite, rather than MA constituents. That is, grains of martensite formed, without any evidence of RA, as was noted in the TEM results section. Therefore, it should be referred to as

secondary martensite phase, rather than MA constituent. An example of the lath structure observable within the secondary martensite phase, formed at higher intercritical temperatures, is shown in high magnification SEM images in Figure 5-2 (a & b). In Figure 5-2 (c), the second phase formed at lower IC temperatures of 750°C, showed minimal internal structure, so will be referred to as MA constituent.

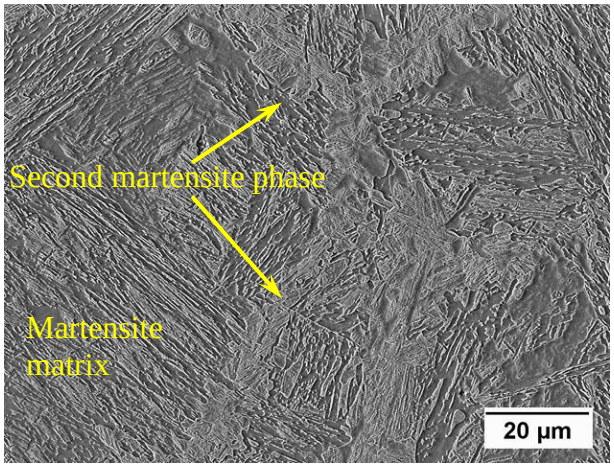

(a)

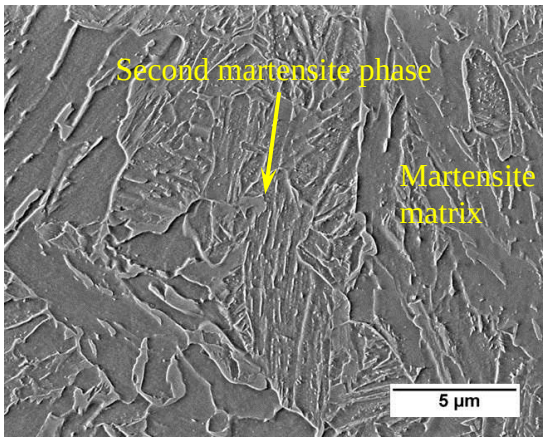

(b)

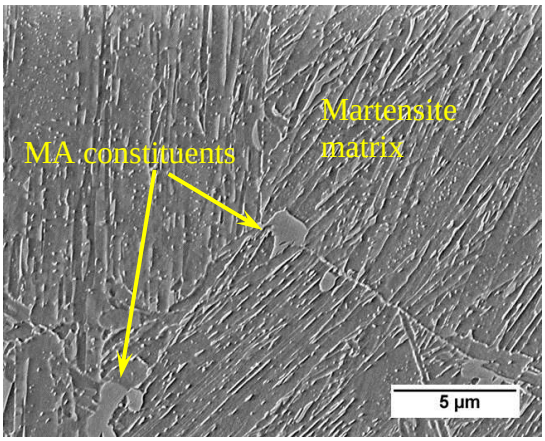

(c)

Figure 5-2 SEM images showing (a) low magnification image of 1350-850°C, showing second phase formed on grain boundaries, (b) higher magnification image of (a) and (c) image of 1350-750°C specimen at the same magnification as (b).

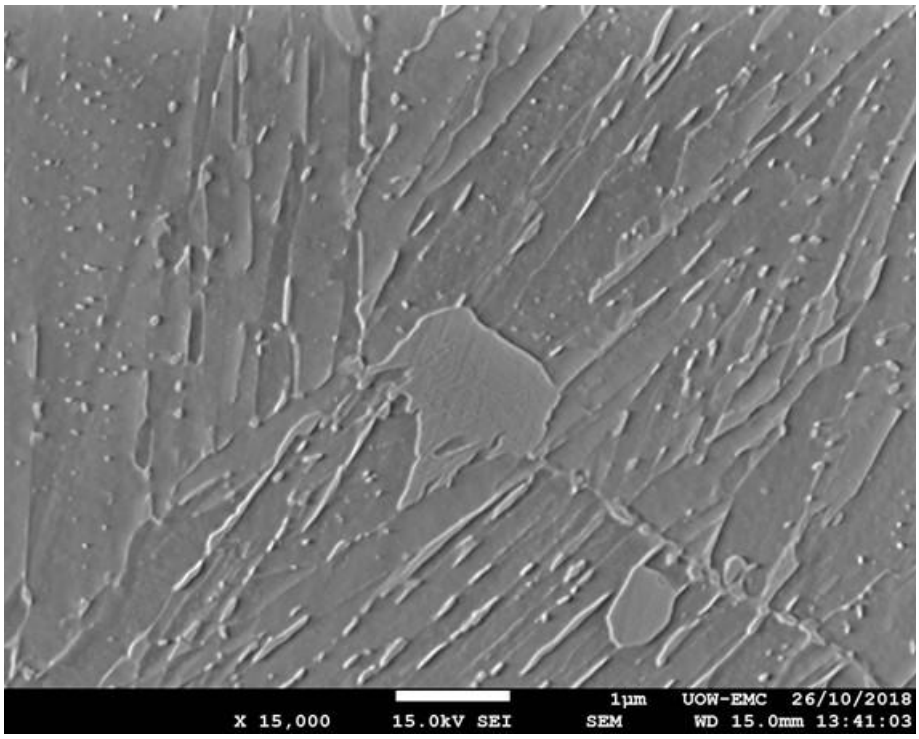

Figure 5-3: High magnification secondary electron image of an MA particle in above Figure 5-2(c) image shows lath structure inside MA.

However, at a high magnification, internal lath structure of MA was visible as shown in Figure 5-3. As indicated in Section 4.9, these laths formed inside MA particles were significantly smaller than those in the matrix (average lath size was 260 nm in MA vs 610 nm in matrix).

The study of the formation of MA with intercritical reheating provided important information on the origin and growth of MA constituent with IC temperature. In the sample with ICCG cycle with lower IC temperature (1350-750°C), the MA particles were nucleated at PAG boundaries and grew into neighbouring martensite grains, as showed in Figure 5-4. The parent austenite of the MA phase was observed to grow only in to one side of neighbouring grain, while maintaining a specific orientation relationship (OR) to the opposite grain.

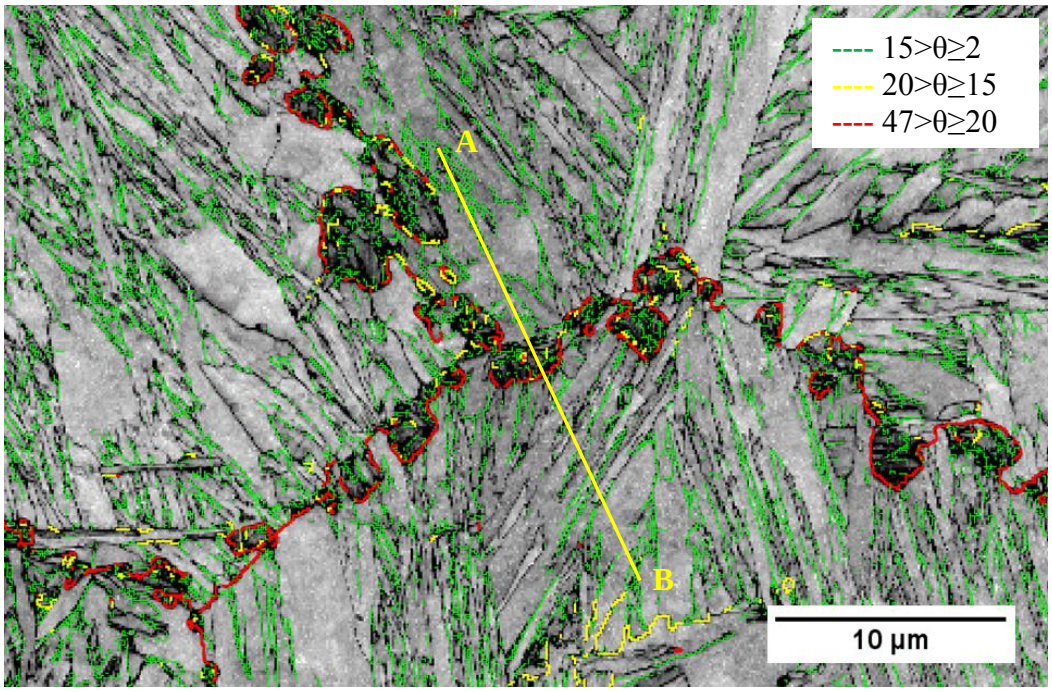

Figure 5-4: Grain misorientation map of simulated 1350-750°C sample. Confirming that MA grows into neighbouring grain while keeping specific OR. θ is the misorientation angle. (misorientation along line AB presented in Figure 5-5).

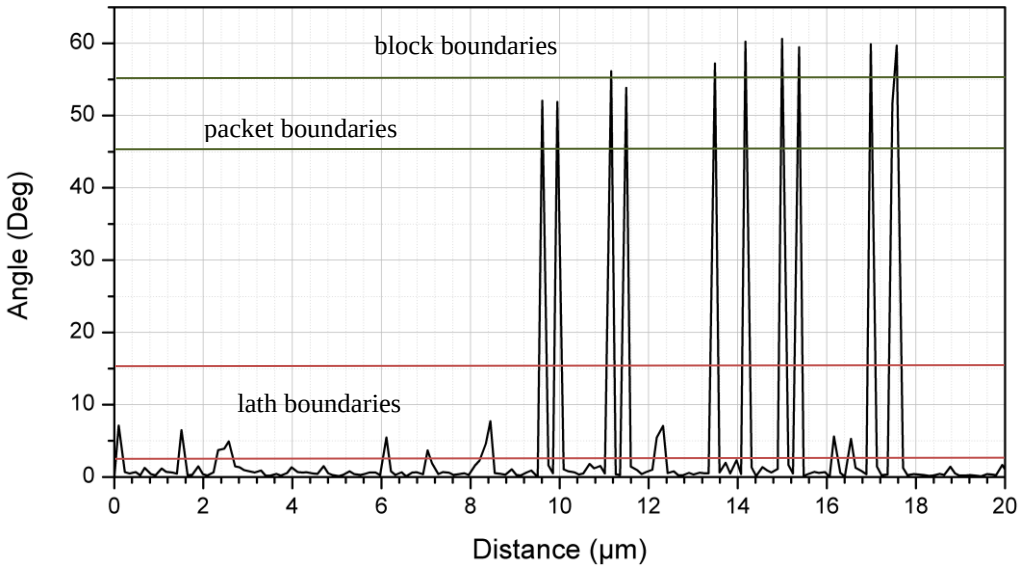

Figure 5-5: Misorientation profile of 1350-750ºC sample through a MA particle along the line A to B shown in Figure 5-4.

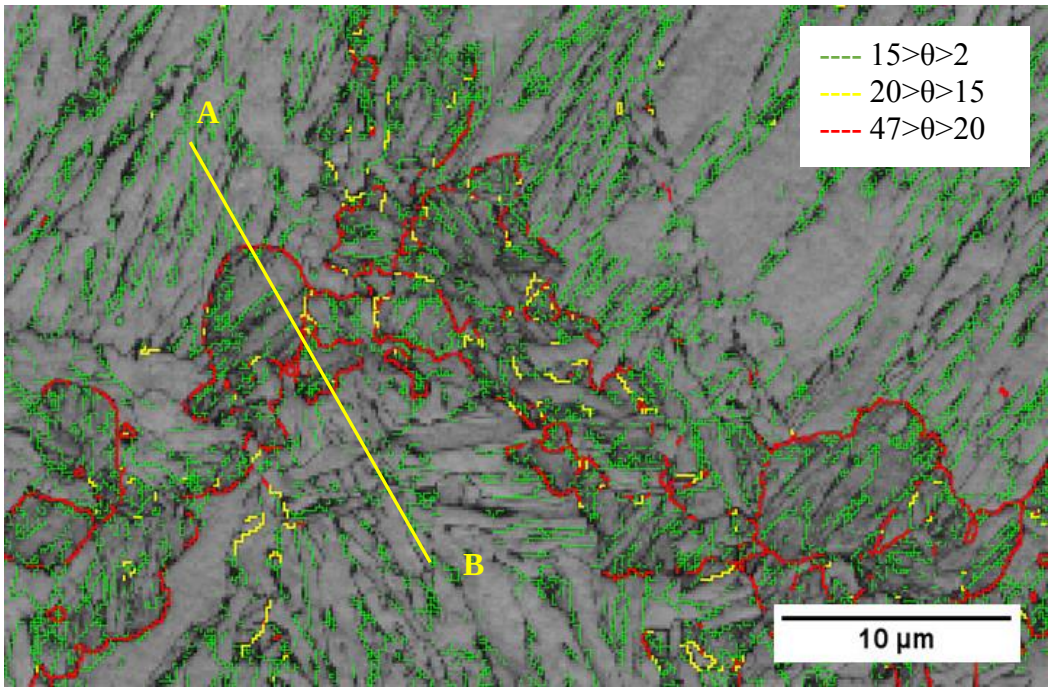

Figure 5-6: Grain misorientation map of simulated 1350-800°C sample. Confirming that MA grows into neighbouring grain while keeping specific OR. θ is the misorientation angle. (misorientation along line AB presented in Figure 5-7).

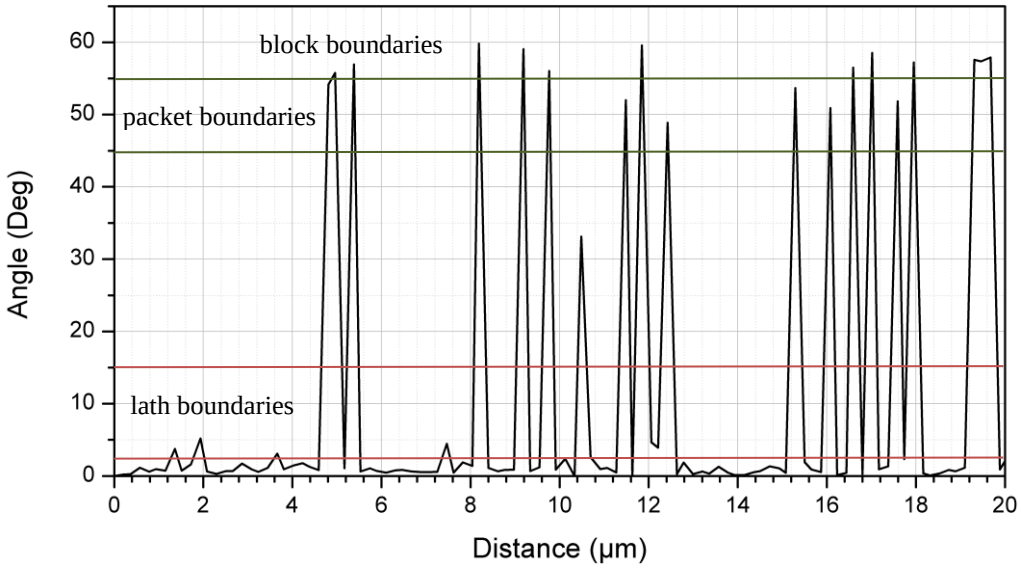

Figure 5-7: Misorientation profile of 1350-800ºC sample through a MA particle along the line A to B shown in Figure 5-6.

Orientation relationships between final martensite boundaries and parent austenite, varies between approximately 10° to 20° or 47° to 57° in packets and around 50° to 60° in blocks [11, 150]. Therefore, misorientation between 20° to 47° can be considered as PAG boundaries [11]. At high IC temperature, the growth of the new austenite was much more extensive, covering both sides of grain, as shown in Figure 5-6. This effectively formed a new set of PAG boundaries, formed along the PAGB, as shown by the red lines in Figure 5-6.

5.2 Effect on PAG size on toughness in single cycle welds

The effects of PAG size on Charpy impact toughness for single cycle HAZ simulations were shown in Fig 4-21 and toughness was an inverse function of PAG size. In single cycle simulated samples, lath martensite was the dominate microstructure for all peak temperatures, so toughness was directly related to PAG size. Grain size is one of the main microstructural properties, which determine mechanical properties such as strength, hardness, toughness etc. [151-155].

As shown in the results section 4.2, a larger PAG size, resulted in larger packets and block sizes. As already mentioned, the martensite lath sizes stayed relatively stable, which was similar to the investigation by Hidalgo and Santofimia [11]. Therefore, the variation of block and packet size with PAG size controls the toughness, rather than lath size. Other researchers have found similar findings. Dunder, et al. [15] found that sizes of blocks and packets decreased with reduction of PAG size in the fully martensitic CG region, as shown in Figure 5-10 (microalloyed Q&T steel with 0.17% carbon, cooling time $t_{8/5}$ up to 12s) [156]. Decreasing the block size, increases the number of block boundaries, which are high angle grain boundaries (50°-60°). Therefore, high angle grain boundaries increase with a decrease of PAG size. Tomita [157], in 0.2 %C martensitic steels, showed that the primary microstructural feature that affected yield strength and DBTT was the packet size.

Fractography of the CG HAZ samples showed that the cleavage facets sizes were similar to the packet size which confirms that the controlling factor for the toughness in martensite was the packet size. This agrees with a similar finding by Dunder, et al. [15], where the cleavage facet size was similar to the martensite packet size in

simulated CG HAZ specimens. Similar Charpy impact toughness was also recorded, 65J at -20°C for Dunder's work, 58 J at -20°C for current research and both fractures were quasi-cleavage. The relationship between toughness and PAG size and martensite packets size agrees with the classical Hall-Petch relationship, where yield strength and also toughness, increases with decreasing grain size [38]. Clearly, the PAG size and corresponding martensitic packet and block size, strongly controls the toughness.

5.3 Effects of PAG size on double cycle ICCG HAZ

In the case of the intercritically reheated HAZ cycles, the formation of MA constituents or new martensite grains at the prior austenite grain boundaries, added a second layer of complexity for the influence on toughness, on top of the change in PAG size.

At the low intercritical reheat temperature, IC-750^{o}C, a discontinuous necklace-like microstructure of MA constituent, as shown in Figure 4-5, formed along the prior austenite grain boundaries. The size of the MA constituents were typically between 0.5-10 µm. Specimens with this type of microstructure showed the lowest toughness; always much less compared to the corresponding single cycle tests. At the IC temperature of 800°C, the MA constituents, or new martensite grains, that formed along the prior austenite grain boundaries were wider and more continuous and toughness improved compared to IC-750^{o}C results. However, toughness was still considerably lower compared to the equivalent single cycles, except at 1350°C, where toughness was marginally improved. Research on low carbon bainitic steels by Kumar, et al. [26], also found that the ICCG HAZ subjected to a mid-intercritical reheat temperature had improved toughness compared to the CG HAZ (1300°C peak temperature). This was attributed to a refinement of the final grain size of the regions that cycled through the austenite transformation. Kumar did not investigate the influence of lower intercritical peak temperatures on the toughness of the ICHAZ. At the high intercritical temperature of 850°C, the majority of the matrix had transformed to new martensite phase, so that the toughness was similar or better compared to single cycles. The MA size, or extent of new martensite grain formation, and hence the inter-critical reheating temperature, is a critical factor

controlling the toughness of intercritically reheated HAZ microstructures. MA constituent in the size range of 0.5-10 μm, decorating the PAGB's, substantially reduced toughness. This agrees with previous research, where low toughness was related to the formation of MA constituents in a necklace-like structure, along the PAG boundaries [10, 70, 92, 158].

There was no evidence of MA particles at cleavage fracture sites, or debonding at MA constituents at the fracture face of the polished cross-sections in current research. Analysis of the TEM data (section 4.9) explains why MA constituents were not observed at cleavage fracture sites in our research, as the MA phase was 'coherent' with the surrounding martensitic matrix. Distinct, separate MA constituents, which appear like a particle in the TEM, did not form, as was the case in other research [92, 95, 159]. An example of MA constituent with a particle-like appearance is shown in Figure 5-8.

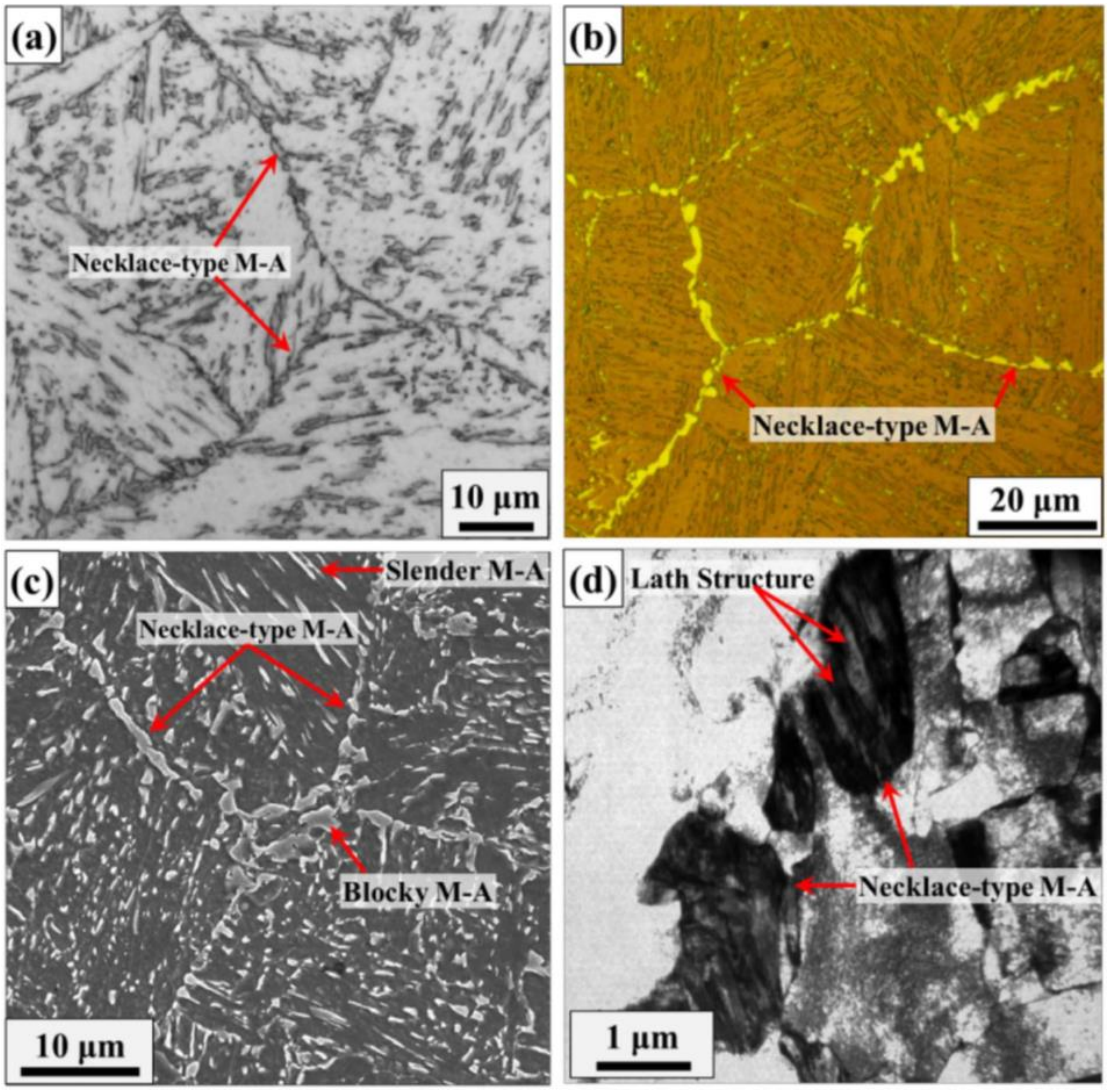

Figure 5-8: Characterization of the microstructure of ICCG HAZ and M-A constituent. (a) OM micrograph (etched by 4% nital), (b) OM micrograph (etched by LePera etchant), (c) SEM micrograph and (d) TEM micrograph of blocky type M-A constituent

High magnification images of the MA constituents in Figure 5-2 showed sub-structure features, indicating new martensite grains, rather than hard and brittle MA constituents, which fits with the debonding mechanism (phase is unlikely to crack). This would explain why toughness improves with increasing IC temperature, as the new martensite grains provide high angle grain boundaries as barriers to crack propagation. Evidence of secondary cracks arrested at MA phase was shown in Figure 4-40. However, the toughness of the IC-800°C cycles at peak temperatures of 1000 to 1200°C, were significantly lower compared to single cycle tests. It is

believed that the reason for this decrease in toughness is the new grains of martensite would be more highly dislocated and harder compared to the tempered martensite of the matrix .Hence, the lower toughness of the new martensite grains is expected to reduce the total toughness, compared to single cycle structure. The instrumented Charpy impact test result as shown in Figure 5-9 indicates that the fracture initiation energy reduced with lower intercritical reheating (750°C). Formation of MA resulted to change the fracture mode from ductile to cleavage in FG region.

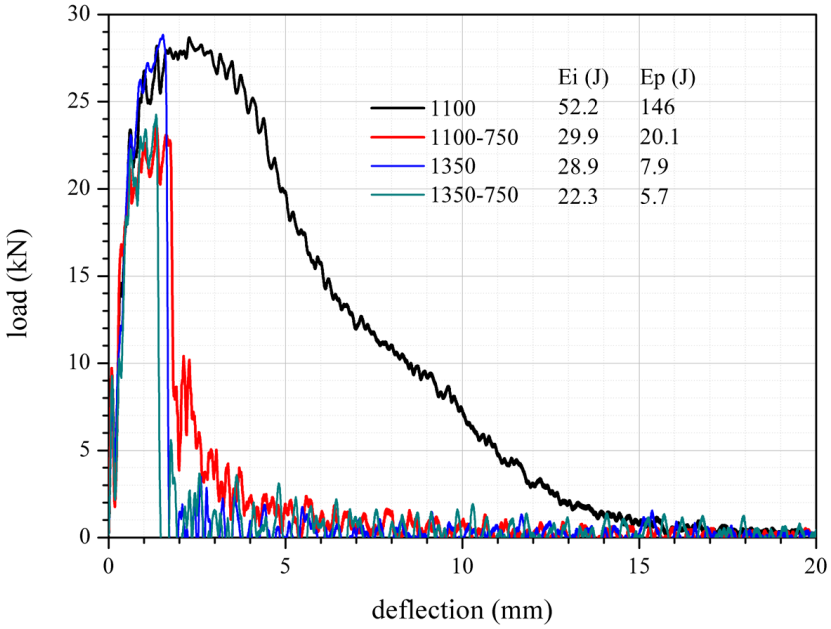

Figure 5-9: Instrumented Charpy impact energies of single cycle FG (1100°C) and CG (1350°C) samples and, double cycle ICFG (1100-750°C) and ICCG (1350-750°C) samples.

5.4 Effect of IC temperature on toughness

The intercritical temperature was identified as a critical variable for the toughness for all PAG sizes, which represented the FG and CG HAZ regions. In all cases, the lowest toughness was measured on specimens where the intercritical temperature was close to the lower transformation temperature (A_{c1}). As the PAG size decreased, the toughness at IC-750°C increased (28 J to 65 J), showing there is a positive benefit to refining the grain size. However, as the PAG size decreased, the relative reduction of toughness compared to the equivalent single cycle toughness became larger, as shown in Figure 5-10. The highest loss of toughness was found for the smallest grain size (11 µm which is corresponds to 1000°C sample) with 143 J difference,

compared to a reduction of toughness of 30 J for largest PAG size (1350°C). This highlights the detrimental effect due to the formation of a 'necklace' like structure of MA constituents along the PAGB's. Furthermore, the MA constituent produced at low IC temperatures is likely to have a higher carbon concentration because of the high diffusivity and higher concentration for saturation of carbon in austenite. Research conducted by Lee, et al. [160] in 0.07% carbon HSLA steels, found that the hardness of MA particles was higher than the rest of the matrix. These harder MA particles were acting as fracture initiation sites. As shown in Figure 5-9 the fracture initiation energy of the ICCG specimen was lower than that of the CG specimen but the propagation energies were almost similar. On the other hand, for the ICFG sample, both fracture initiation and propagation energies were lower than the single cycle FG sample. This indicates how detrimental a significant reduction in fracture initiation resistance is to the overall toughness of the HAZ in steel, as even with a finer matrix grain size which is typically beneficial for improving crack propagation resistance, the propagation energy was still relatively low. The propagation energy of the ICFG HAZ was improved over that of the ICCG HAZ, so the reduction of grain size did offer some resistance to the cleavage fracture. This evident in the fractography images, where tear ridges are observed at grain boundaries (see Figure 4-35(d)). It is possible that the relatively low propagation energy of the ICFG HAZ was also influenced by the network of MA particles along the PAGB's by hindering the grain boundaries ability to arrest a propagating cleavage crack. However, this would be difficult to prove. The significant reduction of the energy required for cleavage cracking to initiate appears to be the chief reason for the low toughness observed when MA constituent decorates the PAGB's.

With upper IC reheating (850°C), it was found that the toughness was higher than the toughness without IC cycle in all PAG sizes except the smallest PAG size. Secondly, the percentage decrease of toughness from single cycle to double cycle with IC (850°C) reheating remained consistent. At this higher IC temperature, the second phase is no longer MA, but new grains of martensite. As such, these grains no longer act as cleavage fracture initiation sites, so toughness reflected the change in PAG

size. The improvement in toughness of the double cycles at IC 850°C, over that of the single cycle specimens is likely due to the overall refinement of the martensite grain size during high intercritical reheating.

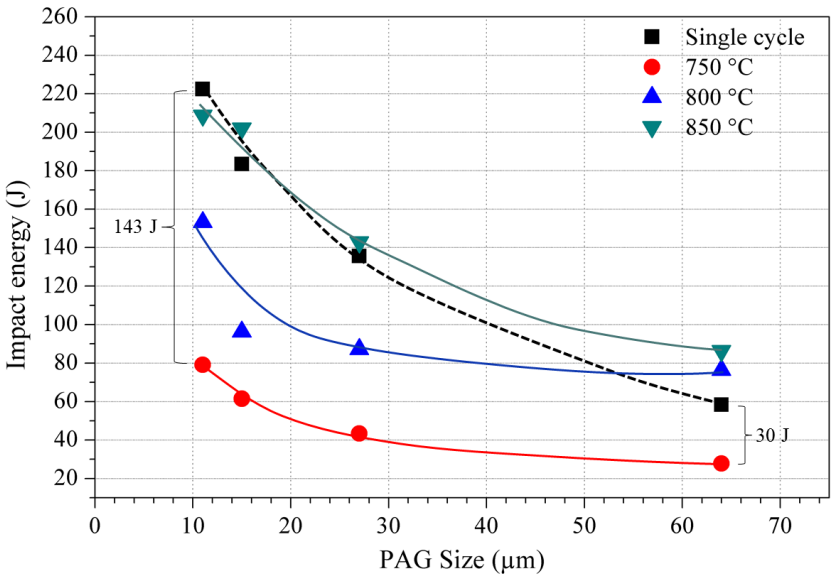

Figure 5-10: The variation of toughness due to IC cycle compared with single thermal cycle for different PAG sizes.

This research has shown that there was a significant toughness gradient within the ICCG HAZ. This is important as it effectively reduces the size of the LBZ in real welds to the CG HAZ and ICCG HAZ, when the reheating temperature is close to the A_{C1}. These lowest toughness regions in real welds are limited to a very small region. Furthermore, such low toughness regions are surrounded by regions with higher toughness (weld metal or FG HAZ). In cross sections of BOP welds, the regions with the lowest toughness was 0.5 mm^2 for the area 120 mm^2 of total HAZ. In Pad welds, there were multiple locations of low toughness regions between 0.06 and 0.38 mm^2 with total area of 1.52 mm^2 for total HAZ of 74 mm^2. There was no trend between the number of repair cycles and size of LBZs in real welds. The regions with toughness less than the toughness of mid IC toughness was around 0.0016 mm^2 in BOP weld repair 1 and the value remained similar throughout repair 2 to 4. This indicates that the there is no change in low toughness areas with multiple

repair welding up to 4 repair welds because these regions were effectively replaced by new and similar microstructures following the next weld cycle.

As the intercritical temperature increased, 1350-750°C to 1350-800°C, toughness increased from 27 J to 76 J (180%), which is better than the CGHAZ (58 J). Instrumented Charpy results for 1350-800°C showed E_i was much higher compared with 1350-750°C and slightly lower compared to the CGHAZ. This indicates that the growth of the MA phase at IC 800°C significantly reduced its effectiveness for triggering cleavage fracture. The improvement in toughness compared with the CG HAZ was linked to improved propagation energy, E_p, which was probably due to the positive influence of tempering on the matrix during the intercritical reheat (800°C).

This research showed that the toughness of the ICCG zone increased substantially with increased IC temperatures. Research by Zhu, et al. [10] on X70 pipeline steels, found only a small improvement in toughness with increasing inter-critical temperatures. This dissimilarity is attributed to the steel type; especially the large difference in hardenability. For the pipeline steel, large MA particles, within a bainitic ferrite microstructure, persisted even at high IC temperatures, resulting in low toughness, while the steel in the current work was much more harden-able and new martensite grains formed in a martensitic matrix. As MA particles are detrimental to toughness, only a small improvement in toughness was observed for the X70 steel.

It is proposed that the new grains of martensite produced at higher IC temperatures provide high angle grain boundary barriers to hinder crack propagation and improve toughness. Secondary cracks inside the grains were observed to terminate at these new grain boundary phases. The new grains of martensite would have lower hardness compared to MA constituents, which would also contribute to the observed improved toughness. At the highest IC temperature, the majority of the matrix had transformed into new martensite laths and the toughness was similar, or slightly better, compared to single HAZ cycles with the same peak temperatures.

As previously discussed, the ICCG HAZ is considered to be a local brittle zone in steels. However, in this research it was found that, for high strength, quench and tempered steels, the low toughness of the IC reheated HAZ was restricted to low IC temperatures, thus effectively decreasing the area of the local brittle zone in this steel type. The low toughness of the IC-750^{o}C cycles persisted well into the fine-grained region. It is generally accepted that toughness is acceptable in the FG HAZ region due to the beneficial effects of small grain size. However, a local brittle zone can exist, even in the FG HAZ, if it is reheated to an intercritical temperature just above the Ac_1 temperature.

5.5 HAZ Toughness with Multiple thermal cycles

The toughness of specific sub-regions of the HAZ was subjected to multiple thermal cycles and results were presented in sections 4.6.2. Charpy toughness results showed that the simulated multiple thermal cycles had similar toughness compared to the equivalent single or double cycle tests. Only the CG-1350°C HAZ showed a noticeable drop for the 4x cycles, but was stable for 1×, 2× and 3×. Due to the transformation of similar microstructures after each cycle, as previously explained, toughness remained stable. This finding matches the findings of Duch and Dupont [91], where toughness did not degrade with multiple simulated CG HAZ cycles (up to three cycles) for a HSLA-100 steel.

The 1350-750°C multiple cycles had an increase in toughness for the 4x cycle, the 1350-800°C cycles showed a slight decrease with consecutive multiple cycles, but the 1350-850°C cycles increased in toughness with multiple cycles. The 1100-750, 1100-800 and 1100-850°C multiple cycles showed a mixture of higher or lower toughness. Essentially, no significant change in toughness occurred due to multiple repeat cycles of the different sub-HAZ regions studied. Within the studied range of welding arc energy, there was no noticeable grain growth with application of multiple consecutive thermal cycles, nor significant change in MA volume fraction, as discussed in the Section 6.1. As the final microstructures of the multiple cycle HAZ specimens were always, similar, it is no surprise the toughness was shown to be similar, as the microstructure controls the toughness.

Due to the similarity of microstructure and toughness of multiple repair HAZ cycles, they can be simplified by alignment with the appropriate single or double cycle HAZ, as shown in Table 5-3. If the temperature of most recent thermal cycle is higher than Ac_3 temperature, the resultant microstructure is similar to single thermal cycle with that temperature because any previous microstructures are replaced by a new CG or FG microstructure. If the last thermal cycle temperature is between Ac_1 and Ac_3 (i.e. in IC region), the resultant microstructure and hence the toughness was equivalent to two-cycle simulated CG-IC or FG-IC microstructure with MA regions corresponds to the highest IC temperature.

Table 5-3: toughness of samples with multiple thermal simulations and similarities to single and double thermal simulations in terms of toughness.

Thermal cycle	**Impact energy (J)**	**Equivalent thermal cycle in terms of toughness and microstructure**	**Impact energy (J)**
CG-CG CG-CG-CG	50.6 54.7	CG	58.3
CG-CG-IC CG-IC-IC FG-CG-IC CG-CG-CG-IC	24.4 33.9 28.5 27.1	CG-IC	27.8
CG-IC-CG-IC FG-IC-CG-IC CG-IC-IC-IC	27.1 28.5 29.8	CG-IC	27.8

However, the introduction of a third thermal cycle which was below the A_{c1} temperature (a sub-critical or tempering cycle) on samples with the lowest toughness (ICCG samples with 1350-750ºC), showed an improvement of toughness as shown in Table 4-3. This improvement was probably due to the tempering effect on the matrix microstructure. The short time at peak temperature led to only a slight improvement in toughness.

Toughness of the HAZ is generally linked to hardness, where higher hardness typically corresponds to lower toughness. This was not the case for intercritically reheated specimens, where toughness decreased significantly (see figures 4-21 and 4-

23) in spite of the decrease in hardness. Toughness reduction by IC cycle was attributed to developing MA phase along grain boundaries [54, 80], which had an overriding influence on toughness, despite the decrease in hardness. Thus, it is important to assess both hardness and the microstructure for multi-pass welded structures.

Fractography (Section 4.8) showed quasi-cleavage fracture facets for both multiple CG HAZ cycles and multiple CG-IC HAZ cycles, typical for low toughness conditions. The fracture facet sizes appeared similar for both the multiple CG cycle samples and CG-IC samples. Research carried out on martensitic steel by Luo, et al. [161] reported that fracture facet sizes were similar to the size of martensite blocks. As the matrix microstructure remained similar for all multi-cycles, it is reasonable to assume that the typical martensite block size was not altered with multiple thermal cycles. Due to the similar coarse grain size of all specimens, cleavage crack propagation behaviour was similar. The instrumented load versus deflection curves for the CG and CG-IC HAZ samples all had cleavage events, which matched the observed cleavage facture behaviour. As discussed previously, MA constituents forming at PAG boundaries decrease toughness by acting as cleavage initiation sites. Therefore, the addition of an intercritical cycle to a CG HAZ lowers toughness by decreasing cleavage initiation resistance.

5.6 Fracture behaviour of ICCG HAZ and CG HAZ

There are two main mechanisms proposed as to why MA constituents cause a reduction in toughness; 1) A microcrack is formed due to the harder, brittle MA constituent cracking under the applied stress during impact testing [22, 81, 139] and 2) a microcrack is formed due to debonding (interfacial decohesion) of the MA constituent with the matrix [28, 70, 76, 77, 95, 102]. This microcrack then propagates into the matrix. In mechanism one, the size of the MA constituents is important [28, 87, 101], where coarser particles were related to lower toughness. This was explained [32, 96] using Griffith crack theory, where the critical stress value required to propagate fracture will decrease as the crack size (cracked MA constituent) increases. When the critical stress value is below the applied stress, then the existing microcrack will propagate, leading to failure. In the second mechanism, researchers

[28, 70, 76, 95, 102] have observed MA constituent at the fracture initiation sites for cleavage decohesion. This research agrees with findings by Lan, et al. [100], who stated that MA constituents larger than 3 μm contributed to the initiation of micro cracking, which substantially reduced the toughness.

Instrumented Charpy test results conducted for 1350^{o}C, 1350-750^{o}C and 1350-800^{o}C HAZ cycles (see Figure 4-22) showing that the fracture initiation and propagation energies were varied between samples with different thermal cycles. It has been proposed by many researchers the reasons for loss of the toughness of ICCG HAZ was due to the formation of M/A constituents along the PAGB [22, 28, 77, 87]. Results for 1350-750^{o}C indicated that the introduction of fine MA constituent along the PAGB's substantially reduced the fracture initiation energy (E_i), but the fracture propagation energy (E_p) was similar to the 1350^{o}C results. Therefore, it can be established that the MA constituents formed at IC-750^{o}C act as fracture initiation sites, but do not contribute to cleavage fracture propagation. Instrumented results for the 1350-800^{o}C samples showed similar fracture initiation energy (E_i), but much higher fracture propagation energy (E_p), compared to results at 1350^{o}C, indicating that the coarser MA constituent (or new martensite grains), now act as a barrier to crack propagation, but have grown too large to act as a crack initiation defect (see the graphical illustration in Figure 5-11). Furthermore, the tempering of the untransformed matrix will also contribute to the improved toughness due to reduced hardness. Toughness was further improved at 1350-850°C, where the volume fraction of new martensite grains growing along the PAGB's had increased, providing additional barriers to crack propagation.

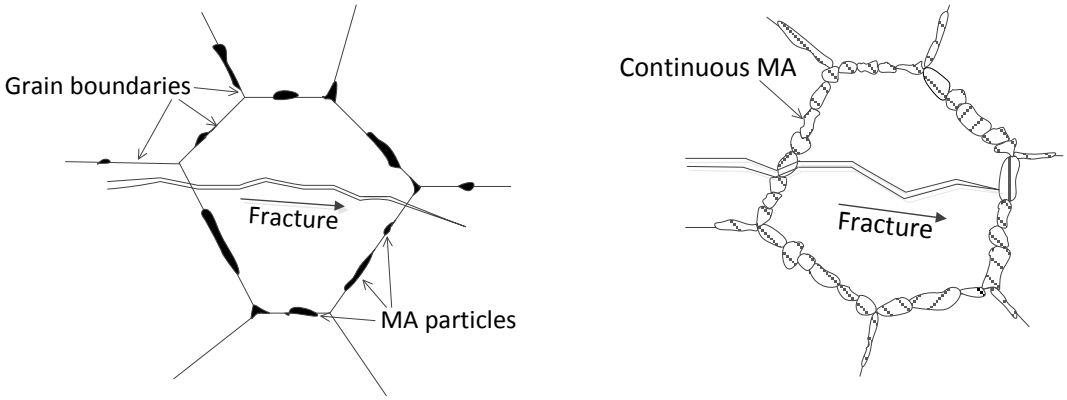

Figure 5-11: The proposed mechanism of fracture behaviour in low and high IC reheating where; (a) at low IC temperature (750ºC) and (b) at high IC temperature (800ºC).

At lower IC temperature, the MA particles were 1.3 to 6.6µm in size which were act as cleavage initiation sites. MA formed at lower IC temperature typically possess higher hardness because of higher carbon concentration [80]. Cracks can initiate along the interface of MA particles and the matrix due to localised stress differential caused by the difference in yield strength of the two phases [100]. At higher IC temperatures (800°C), the MA size was larger and initiation of fracture was much more difficult, as shown in table 4-2; the fracture initiation energies for CG and ICCG (with IC-800°C) was 30.1 J and 26.2 J respectively. Due to the growth of the MA phase at higher IC, it should have lower carbon content and hardness would be similar to the rest of the matrix, so the MA phase does not act as defects or particles with high hardness. That is, the hardness/yield strength difference between the MA phase and matrix diminishes.

5.6.1 Influence by hardness

Nano indentation hardness provided vital information about the hardness variation in different phases in the HAZ. The summery of hardness on MA and rest of the matrix of two deferent specimens are shown in Table 5-4. The hardness on MA was slightly higher than the hardness of the matrix in both specimens. Moreover, hardness of MA on 1350-750°C is higher than 1350-800°C. The deference of hardness indicates that a higher concentration of carbon is possible in MA compared to the rest of the matrix. Also, higher MA hardness on 1350-750°C specimen indicates that the

particles with higher hardness may influence a lower toughness by providing fracture initiation sites.

Table 5-4: Summery of average hardness on the MA and the matrix measured with nano indentation.

Specimen	Average hardness (GPa)	
	MA	Matrix
1350-750 °C	5.10	3.41
1350-800 °C	4.18	3.67

5.6.2 Influence by grain boundaries

The distribution of grain, packet and block boundaries plays an important role in controlling fracture propagation; especially in brittle samples. For example, the fracture path of cleavage fracture has been observed to change the direction at the packet boundaries [162]. The grain boundary misorientation has a very strong influence on strength and toughness [14]. In the current research, the grain boundary misorientation played a vital role in controlling the impact toughness.

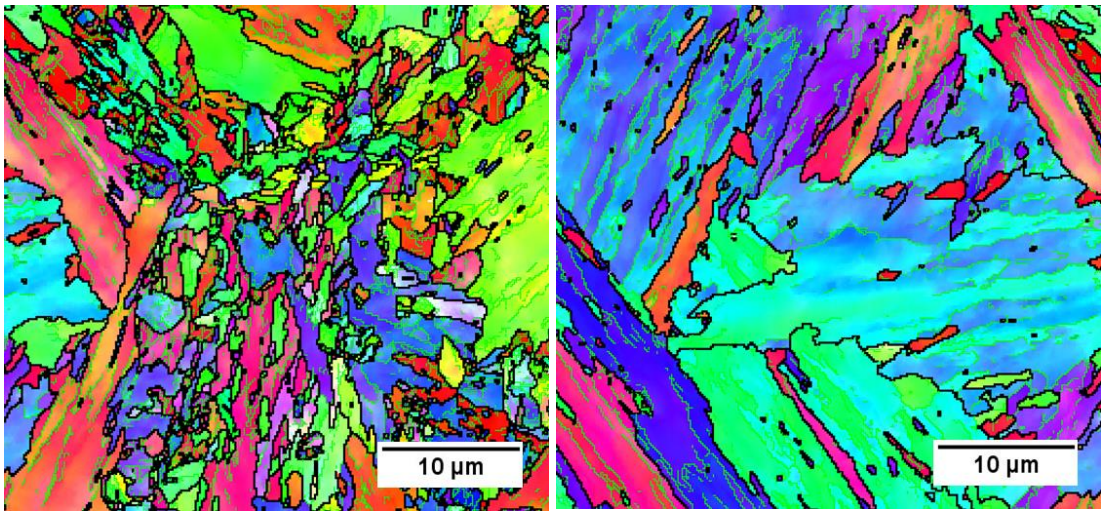

(a) (b)

Figure 5-12: Evidence of high density of HAGB in MA at higher IC temperature. (a) region with MA at PAGB and (b) matrix. Dark lines – High angle grain boundaries (>15°) and Green lines – Low angle grain boundaries (2°<θ<15°). Simulated HAZ sample with 1350-800°C thermal cycle.

EBSD analysis showed a large number of martensite packets were created within the MA formed at the mid IC temperature (IC-800°C), as shown in Figure 5-12 (a). Such HAGBs are known to effectively arrest cleavage fracture propagation, through martensite laths. The increase in the Ep energy for the 1350-800°C and 1350-850°C specimens concur with this mechanism. Figure 5-13 shows evidence of a secondary fracture that was arrested at HAGB of the MA phase. Both fractures in Figure 5-13 were identified as following the 001 cleavage plane. Lan, et al. [32] reported that when cracks propagate, only high misorientation boundaries are effective in impeding crack propagation. In Figure 5-12(b), the matrix region is shown at the same magnification as the MA region in a. The matrix region shows aligned packets with limited HAGB's, so provided limited resistance to cleavage propagation. As already stated, instrumented Charpy curves showed significant cleavage events. Therefore, the toughness of the 1350-800°C specimens was still poor due to the influence of the coarse PAG size.

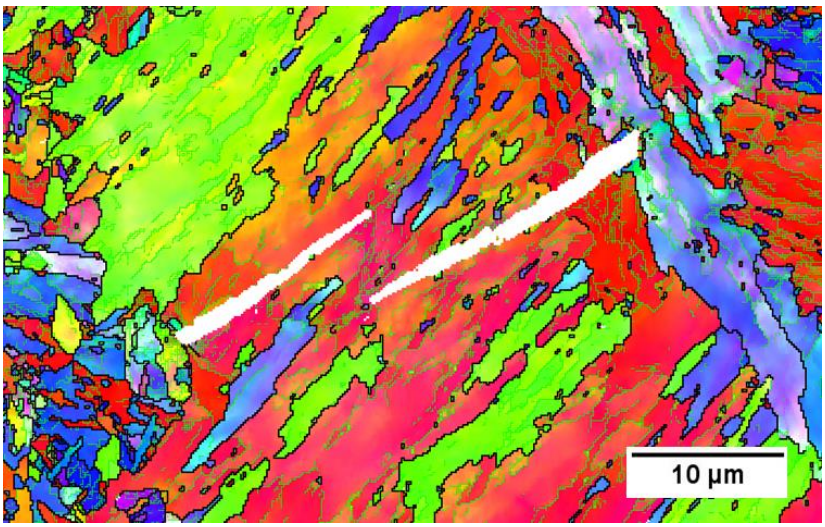

Figure 5-13: Evidence of fracture arrests by high angle grain boundaries (HAGB's) of MA produced in high IC thermal cycles. Simulated sample with 1350-800°C thermal cycle. Grain boundaries with misorientation >15° shown in black lines.

5.7 Mechanism of fracture propagation in ICCG

All tested impact samples with a coarse grain size showed trans-granular fracture propagation. Some researchers suggest that the fracture in ICCG region initiate due to the de-bonding mechanism, where the high hardness MA particles de-bond from

the rest of the matrix [100]. If the energy to occur debonding of MA particles is lower than the energy to fracture the martensite matrix, it can be suggested that the majority of fracture could propagated by debonding; so, mainly along grain boundaries as inter-granular fracture. However, in current research there was not adequate evidence to support the suggestion of de-bonding mechanism of MA from the rest of the matrix in ICCG region which supports fracture propagation.

In both cases of lower IC and higher IC, there were high densities of high angle grain boundaries in MA phase. As shown in Figure 5-5 and Figure 5-7 from lower IC to higher IC, the high angle grain boundary density increased in MA phase. However, the fraction of high angle grain boundaries (>15°) were higher in ICCG with low IC (for 1350-750, 0.393 and for 1350-800, 0.232). However, as shown in Figure 4-72, majority of these boundaries belongs to Σ3 grain boundaries. This indicates that higher density of HAGBs does not always improve the toughness. Similar findings were reported by Zeng, et al. [90] which concluded that the low temperature toughness was not depended on the fraction of HAGBs on X70 grade.

All tested impact samples with a coarse grain size showed trans-granular fracture propagation. The primary cleavage planes for iron are {100} planes [38, 163] so the majority of cleavage fractures should follow this set of planes which is confirmed by the current research as indicated in the Table 4-6. The primary slip planes of iron are {110} set of planes, so the toughness should increase with increase of misorientation in {110} planes across boundaries. Martensite lath boundaries tends to lie parallel to {110} planes [38]. Therefore, martensite laths can act as barriers for slip so that to propagation of fracture. In addition, with the increase of HAGBs, the probability of misorientation of slip planes in neighbouring packets gets higher which eventually contributing to higher toughness.

The dislocation densities of MA and the matrix may have contributed in fracture propagation but there was not adequate evidence found in TEM analysis in this research. However, Pešička, et al. [164] stated that for martensitic steels, dislocation densities vary from place to place within the grain. Therefore, localised high dislocation densities can alter fracture behaviour.

5.8 Effect of weld repair cycle on residual stresses

Residual stresses are unavoidable in welds due to volume changes in phase transformation, microstructural changes in HAZ and weld metal shrinkage. Residual stress distribution of multiple repairs of pad welds was determined using the neutron diffraction technique. For all pad weld repairs in this research, stresses were typically higher for longitudinal stress component, compared to the transverse component. For example, beneath the centre of the pad weld, in the longitudinal direction, longitudinal stresses were between 350-450 MPa, while transverse stresses were between 180-320 MPa. In the transverse direction, longitudinal stresses were between 300-390 MPa, while transverse stresses were between 120-200 MPa. The maximum tensile stresses were found just beneath the weld toe, typically between 500-600 MPa; which is 87% of the minimum tensile strength of the material. The highest stress recorded was for Pad 2, at 674 MPa. Just beyond the toe regions of the weld, stresses substantially reduced to a maximum of around 400 MPa. The longitudinal stress distribution was always tensile and decreased to almost zero stress beyond 50 mm from the end of the weld, on the other hand, changed from tensile to compression soon after the toe of the weld. Normal stresses were varied between compression and tensile fluctuating around zero as shown in figure 4-54.

Similar outcomes were found by Dong [136], who used FEA modelling on repair welds on stainless steel to show that the highest tensile stresses were below the start-end locations. Dong also found that beyond the start-end locations, residual stresses dropped into compression, to balance out the high tensile stresses. [136].

However, the effect of weld start and stop was not prominent in current research as it showed a similar stress distribution under the pad weld with first repair weld of 60×60 mm pad and forth repair weld of 40×40 mm pad. The stop and start effect for the residual stress were eliminated in this research by carrying out a tempering weld run which covers all starts-stops of pad weld and with a TIG dressing to smooth-out the toe region of pad welds. However, repair welds of pipeline girth welds showed that in longer repair welds, the effect of start and the end of arc are isolated and axial residual stress distribution is uniform at the mid portion of the weld repair length

compared to shorter repair welds [136] and no effect of start-stop of original welds were considered and these results were taken from FEA modelling.

Longitudinal residual stress can be considered the most detrimental for the mechanical properties and fracture behaviour of welds because 1) the high stresses generated are close to the yield point of the parent material and 2) tensile stresses enhances fracture propagation as opposed to compressive forces which tend to push a crack closed. The high tensile stress below the weld toe can be potentially detrimental, as high hardness was also found in the same region, as shown in Figure 5-14. The combination of high hardness with high tensile stresses would make this region more susceptible to failure if a weld defect was present.

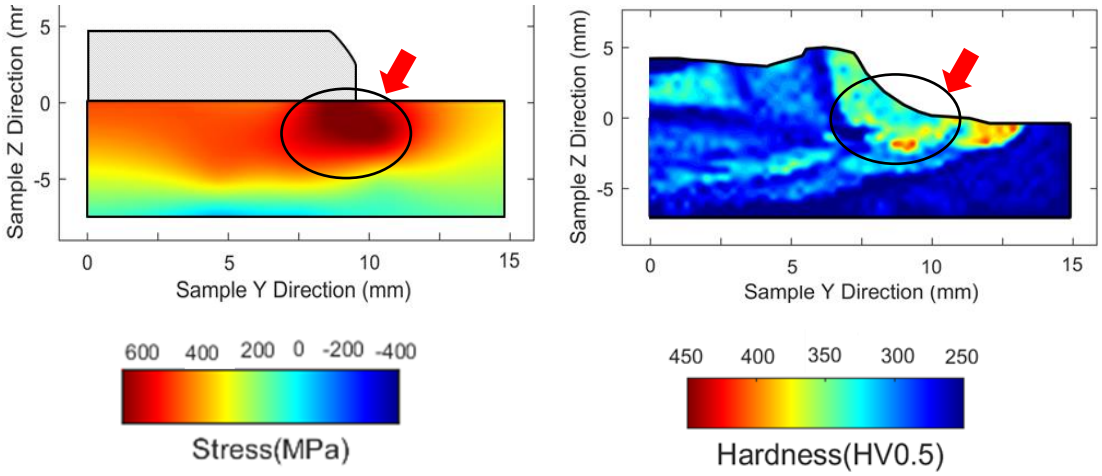

(a) Pad weld 2 longitudinal stress (b) Pad weld 2 hardness

Figure 5-14: Distribution of residual stress field and hardness in longitudinal direction of weld under the toe of pad weld repair 2. Circled areas show regions with high tensile stress and higher hardness.

All repair welds showed a similar trend of residual stress which is comparable with the hardness distribution. The highest hardness was observed under the toe region of the weld pad and highest residual stress was observed in the same region.

The effect of weld reinforcement on residual stress was minimal in pad welds as show in Figure 4-58. There were slightly lower stresses were observed on the weld plate after removing the reinforcement of the pad.

5.9 Variation of hardness and hardness profile with weld repair cycles

The hardness of the CG cycles (cycle 1 to 4) was similar for each cycle, which corresponded with the similar microstructures that were observed for single and multiple cycles. The hardness of samples finished with a lower IC cycle (750°C) was lower in average by 14% compared to the CG samples (see Figure 4-26), even though the hardness of MA constituents is expected to be high. Research by Kim, et al. [80] found that the carbon concentration in MA was significantly higher than the rest of the matrix, which would result in higher hardness of MA constituents, compared to matrix. Carbon has higher solubility in austenite, so diffuses into the newly formed austenite, but it is trapped there due to the rapid welding cycle and a higher carbon martensite, austenite complex forms [34]. The higher hardness of the MA constituent did not result in higher hardness of the microstructure. This can be explained by 1) the increased carbon concentration in the MA constituent would slightly decrease the carbon in the adjacent matrix and 2) more importantly, the IC cycle would have tempered the existing matrix martensite and this would significantly decrease the hardness.

At higher IC temperature at 850°C, the sample showed increased hardness compared to lower IC but still lower than the hardness of single thermal cycle sample. As discussed earlier, with the growth of MA phase at higher IC temperature, the carbon distribution in the matrix and MA expected to be more equalised compared to lower IC. Therefore, the higher hardness was reported with high IC reheating.

In comparing the hardness between the single cycles and intercritically reheated cycles (see Figure 4-26), maximum hardness was always recorded for the single cycles. Hardness within the single cycles increased slightly with decreased grain size, this can be attributed to the presence of a higher number of grain boundaries and higher number of martensite packets compared to CGHAZ. The decreased hardness of the intercritically reheated samples, compared with the equivalent single cycle, was due to the tempering effect of the reheating as well as the slower cooling rate of the IC cycles. Higher cooling rates are well known to increase the hardness of martensite. The lowest hardness for the intercritically reheated samples was at lower IC temperature (IC-750°C). This indicates that the tempering effect on the matrix

martensite had a stronger effect in lowering hardness compared to the change in cooling rate. As the intercritical temperature increased, the matrix martensite was progressively replaced by new martensite, which had higher hardness than the existing matrix, as it was not tempered. However due to the decreased cooling rate, the hardness of samples heated to the highest IC temperature (850°C), was lower compared with the single cycle tests. Hardness results showed that there was lower hardness in ICCG HAZ compared to CG HAZ which confirms that higher hardness does not always associate with low toughness.

The maximum hardness for pad welds was 410HV0.5 and 400HV5. The highest hardness occurred beneath the final weld run as there was no tempering effect of subsequent weld runs. Due to the tempering effect of multi-pass weld runs, the hardness beneath the pad was relatively low. In this region, the hardness did not exceed 370HV0.5. There were no noticeable effects from recurring pad repair welds (weld repair 1 to 4), on the magnitude of hardness nor for the distribution of hardness, as shown in the figures 4-30 and 4-31.

The cross-section area of the edge regions, with HV more than 400HV, was 4.4 mm^2 in the first weld and was only 2.3 mm^2 in 4^{th} weld. The average area of the higher hardness edge regions (>400HV0.5) are shown in Table 6-4, where the largest region was for the original weld. In the subsequent weld cycles, the harder regions were tempered thermal cycle and therefore the region with higher hardness becomes smaller.

Table 5-5: Average area of the hardness higher than 400HV0.5 with different repair weld cycles in pad weld repairs. (The average area is the average hardness of longitudinal and transverse sections). See figures 4-30 and 4-31 for visual representation of hardness.

Weld repair cycle	**Average area where the hardness higher than 400HV0.5/(mm^2)**
First	4.4 ±0.21
Second	1.8 ±0.30
Third	2.6 ±0.19
Forth	2.3 ±0.20

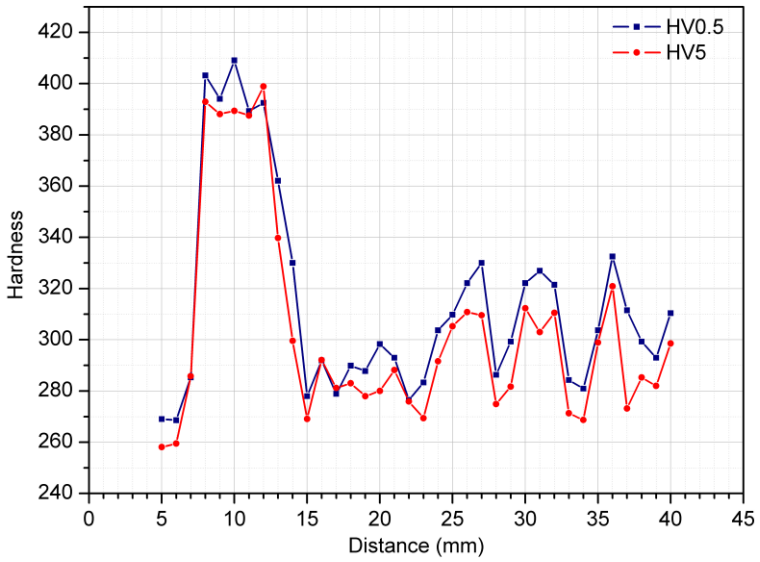

Figure 5-15: The comparison of variation of hardness across the HAZ region on pad weld 1

In real weld repairs of BoP, pad welds and full penetration butt welds, the hardness profiles were shown in Figures 4-31, 4-32 & 4-33 respectively. Even with four repair weld cycles, there were no noticeable hardness changes. This was due to the HAZ of the previous repair, being replaced by the following repair weld, as the subsequent weld was in the same place as the previous weld. Therefore, similar final microstructures and hardness's were obtained. Most importantly, the hardness distribution and the maximum hardness stayed similar throughout all weld repair cycles, indicating that multiple repairs had minimal effect on the parent plate properties

6 CONCLUSIONS

The present study provides a comprehensive assessment of changes in mechanical properties and microstructure evolution with multiple recurring repair welds on a high strength steel (BIS812 EMA). The findings of this research made several contributions to the current literature and more importantly, provided practical applications, for the long-term sustainment of Collins class submarines. Conclusions made from this investigation are presented below.

6.1 Effect of PAG size on toughness in single cycle welds

The effect of the PAG size of single-pass welds were investigated with HAZ simulations on a Gleeble thermo-mechanical simulator, as discussed in sections 3.3.2, 4.4 and 5.2. Specimens with larger PAG sizes showed lower toughness compared to specimens with smaller PAG sizes. For single-cycle HAZ simulations, PAG size was the main contributing factor for the variation of toughness. The link between large grain size and reduced toughness is a well-established relationship. The largest average PAG size of 64 µm showed the lowest toughness of 58 J at -20ºC for any single-cycle simulated sample. The smallest PAG size of 11 µm showed higher toughness than the parent material at 222 J at -20ºC. The impact toughness reached a plateau when the PAG size was around 20 µm. There was no further improvement of the toughness for PAG sizes smaller than 20 µm.

6.2 Effect of PAG size on toughness for double thermal cycles with intercritical reheating

Double thermal cycles are defined as; the first cycle was heated in the range of 1000 to 1350°C, and the second cycle heated within the intercritical range, 750 to 850°C. Toughness improved as the PAG size decreased. The degree of improvement of the toughness with decreasing PAG size depended on the temperature of the second intercritical thermal cycle. IC at 750°C, close to the A_{C1} temperature, was found to have the most detrimental effect on toughness due to the fine MA phase, located along the PAG boundaries as well as MA between martensitic laths, reducing the fracture initiation energy, thereby reducing the total toughness. At IC at 800°C, the growth of the MA phase diminished its influence on initiation of fracture and

toughness improved. At IC at 850°C, toughness increased due to significant growth of the MA phase, which also can be classified as fresh martensite grains.

6.3 Effect on IC temperature on toughness

Samples with the lowest IC temperature (750°C), close to the Ac_1 temperature, showed the lowest toughness for all PAG sizes. For the mid-IC temperature (800°C) results, there was a significant improvement in toughness compared to the 750°C results, particularly at the finest PAG size. For the high IC temperature (850°C) results, close to the Ac_3 temperature, toughness was as high or higher than the equivalent single cycle results. Therefore, once the IC temperature passed the mid-IC temperature, the toughness had recovered and mostly depended on the PAG size. For the 1350-800 and 1350-850 cycles, the toughness was higher than that for the single CG cycle, due to the tempering effect of the second cycle on the existing martensitic microstructure.

6.4 Effect of multiple thermal cycles on the toughness of simulated HAZ specimens

The toughness of multiple thermal cycle, simulated HAZ samples was relatively consistent and results were predictable based on the thermal history. As expected, any CG heating cycles fully re-austenised the material, so the PAG size could be predicted by considering the last CG thermal cycle. In the coarse grain region, multiple simulated CG cycles displayed a similar microstructure to the single simulated CG cycle, hence, toughness was similar. Multiple CG cycles did not lead to a progressive coarsening of the PAG size. When a CG-IC cycle was repeated multiple times, a similar toughness and microstructure to the single-time CG-IC cycle was obtained, for up to six thermal cycles (i.e. three times CG-IC cycles). Metallography showed that there was minimal variation of the volume fraction of the second phase formed due to the IC cycle, for multiple IC cycles. Table 6-1 shows what the equivalent single or double cycle was for the tested multiple thermal cycles.

Table 6-1 The toughness equivalent of the multiple thermal cycles to a single or double thermal cycle.

Characteristics of multiple thermal cycles	Equivalent toughness of single or double thermal cycle
CG-CG-CG-CG	CG
CG-CG-CG-IC	CG-IC
CG-IC-CG-IC	CG-IC
CG-CG-IC-IC	CG-IC
FG-CG-IC	CG-IC
CG-FG-IC	FG-IC
CG-IC-CG	CG

6.5 Factors affecting the toughness of intercritically reheated specimens

The ICCG HAZ (CG-IC thermal cycles) with an IC temperature close to the Ac_1 (1350-750 and 1200-750) showed the lowest toughness compared to all other HAZ regions tested. The main factor for the reduction of toughness in the ICCG region, compared to the CG-HAZ, was the presence of a fine distribution of the MA phase along the prior austenite grain boundaries, as well as inside the grains. This MA phase acted as fracture initiation sites and thereby lowered the toughness. The fracture initiation mechanism appeared to be due to decohesion (debonding) between the MA phase and matrix. As already stated, the MA phase in the ICCG region showed no effect on fracture propagation (for low IC temperatures). The fracture propagation energy was low for both CG HAZ and ICGC HAZ, as shown by instrumented impact toughness tests.

At higher IC reheating temperatures, the volume fraction and thickness of the MA phase, located along the PAG boundaries, increased. Due to this increased thickness/volume fraction, the stress concentration between the MA phase and matrix diminished, so decohesion was more difficult. Correspondingly, instrumented impact data showed a significant increase in the fracture initiation energy. Furthermore, instrumented impact toughness results also indicated that the coarsening of grains of the MA phase at higher IC temperatures increased the fracture propagation energy. EBSD data proved that these grains had high angle grain boundaries, which are known to hinder fracture propagation.

6.6 Influence of MA constituent on toughness

As discussed in Section 2.4.2.3, the literature suggested that higher fraction of MA constituent was detrimental to the toughness. However, current research exposed that the fraction of MA does not solely contribute to the toughness. The distribution and the size of MA in the matrix are more critical to the determination of toughness. Discrete MA constituents on the grain boundaries reduces the toughness more than large and interconnected MA, growing away from the prior austenite grain boundaries. As the interconnected MA size increases, effectively becoming fresh grains of martensite, a higher toughness can be expected.

6.7 Difference between the simulated and real weld microstructures

The corresponding sub-HAZ regions of the simulated HAZ and real weld HAZ were similar in morphology, hardness and toughness. Therefore, simulated HAZ samples adequately captured the real weld HAZ for investigation of mechanical properties and microstructure of the simulated sub-HAZ specimens. For multiple HAZ cycles, there were no obvious changes in the microstructure of the HAZ for repair weld 1 to repair weld 4, in both real and simulated welds.

6.8 Hardness of multiple repair welds for the real welds

The hardness values of the HAZ for BoP, pad and full penetration welds, did not deviate by any significant amount between the single repair weld results and the four-times repair weld results. The maximum hardness was measured as 420 HV0.5 for the hardness mapping data and 415 HV5 for the line trace. The area of higher hardness (>400 HV0.5), varied depending on the welding sequence, but the average size was 2.8 mm^2 and the maximum and minimum sizes were 4.4 and 1.8 mm^2. Consequently, the higher hardness regions of the welds were restricted to very small regions.

6.9 The effects of multiple repairs on the mechanical properties of real welds

Charpy impact toughness of real welds was conducted with instrumented Charpy impact testing technique. The analysed results were provided in Section 4.6.3. Impact toughness of real welds was considerably higher than simulated samples, such as the CG and GC-IC regions (see Table 4-2 and 4-4). The higher toughness in the real welds was due to the heterogeneity of microstructure in the sample. Unlike simulated

HAZ, where the entire Charpy sample consisted of the microstructure of the simulated sub-zone, real HAZ Charpy samples consists of different sub-HAZ regions due to the steep gradient change of the microstructure between the fusion zone and base metal. As such, even for a fusion line (FL) Charpy sample, the low toughness CG HAZ is surrounded by higher toughness FG HAZ, so the overall toughness of the specimen is much higher compared to a simulated CG HAZ specimen.

The effects of recurring weld repairs on HAZ toughness was shown to be minimal, Table 4-4. Due to the heterogeneous nature of the microstructure of a real weld HAZ Charpy sample, there was scatter between the results for recurring repair welds, but there was no trend of worsening HAZ toughness.

The resistance to rapid progressive fracture was evaluated using the dynamic tear test. Acceptable toughness results were obtained which surpassed the minimum energy requirement for the application of 680 J. Thus, recurring full penetration repair welds did not compromise the fracture toughness of the welds, as measured by the DT test.

6.10 Effect of recurring repair welds on residual stresses

The residual stresses were measured with neutron diffraction and results showed that there were minimal variations in the residual stress behaviour between the single repair weld and four-times repair weld. There was a slight increase in the residual stresses recorded for all of the recurring repair welds. However, the residual stresses did not progressively worsen as the number of recurring repair welds increased.

The transverse stresses were on average around 27% higher than the longitudinal stresses in all repair welds. The maximum tensile stress was approximately 87% of the minimum tensile strength of the material. All repair welds showed a similar trend of residual stress distribution. The effect of removing the weld reinforcement of the pad weld on the residual stress behaviour was negligible.

6.11 Summary of the effects of recurring repair welds on the properties of BIS812EMA steel

This research confirmed that the low toughness region of multi-pass welds was substantially narrow (~2% of the total HAZ). Even though researchers pointed out the ICCG region has the lowest toughness, only a small region within the ICCG HAZ, namely, the region which was reheated to just above A_{c1} temperature, showed

low toughness. The low toughness at low intercritical reheat temperatures was due to the formation of MA particles at the prior austenite boundaries acting as fracture initiation sites and substantially reducing the fracture initiation energy. At higher IC temperatures, increased toughness was observed, where the fracture initiation energy and propagation energy increased. This was due to the increased width of MA phase minimising the stress concentration around the MA phase, thus improving fracture initiation energy. Secondly, the larger MA phase consisted of high angle grain boundaries, which contributed to improving fracture propagation energy. Finally, as the PAG size decreased, toughness of both single cycle tests and intercritically reheated cycles improved. This effectively restricted low toughness to coarse grained microstructures, with the noted exception of when the intercritically reheated temperature was just above the A_{c1} temperature, were toughness remained relatively low, even at fine PAG sizes.

The toughness of ICCG region was not affected by the number of repair weld cycles, up to four weld repairs. Correspondingly, the hardness, toughness and residual stresses were not affected, to any noticeable degree, with real multiple repair welds, for up to four weld repairs. Therefore, multiple recurring repair welds can be carried out on BIS812 EMA steel, with minimal risks in regards to the loss of toughness, adverse changes of hardness and with minimal changes in residual stresses, for up to four repair cycles.

6.12 Feasibility of multiple recurring weld repairs on BIS812 EMA steel

The effect of multiple recurring weld repairs on the microstructure and mechanical properties was studied. The hardness, toughness, and residual stresses were not adversely affected by the multiple recurring weld repairs up to four recurring welds. The microstructures were similar to single multi-pass weld microstructures. The lowest toughness was noted in ICCG region in all single and recurred weld repairs and did not deteriorate with multiple weld cycles. Therefore, multiple recurring weld repairs on BIS812 EMA steel can be done without adversely affecting toughness, hardness and residual stresses in the HAZ within the studied weld parameters and conditions.

7 RECOMMENDATIONS

7.1 Careful control of the weld sequence

In real welds, the region with the lowest toughness (LBZ) was measured between 1.9 and 2.4 mm^2, which was around 2% of the total HAZ. However, the size of this region varied depending on the variation of welding sequence, distance between each weld bead, weld heat input and preheat and interpass temperature. Therefore, there is potential to minimise the size of LBZs to improve the overall toughness by careful control of the welding parameters and sequencing. However, careful control of some of these parameters may be difficult, or already optimised.

7.2 The effect of post-weld heat treatment (PWHT) for residual stress

With current welding procedures of weld repairs, there are no PWHT procedures for the given repair welds. Application of PWHT may significantly alter the residual stress fields in and around repair welds. Few comprehensive studies have been conducted on the effect of PWHT for recurring repair welds on the residual stresses of high strength steels. The methodologies applied in this research program can be extended to investigate the effects of PWHT on residual stresses.

7.3 In-situ studies of fracture behaviour of the ICCG region

To understand the exact mechanism of fracture initiation and propagation, it can be studied with in-situ tensile testing in a TEM and an SEM, equipped with EBSD. This will provide a better understanding of fracture initiation and propagation behaviour of the steel with regards to the low-toughness HAZ regions. Careful planning and sample preparation will be required to carry out such an investigation.

REFERENCES

[1] B. Dixon and J. Taylor, "Welding of collins submarine hulls," presented at the 42nd National welding conference, Melbourne, 1994.

[2] B. F. Dixon, "Evaluation of Welding Consumables and Procedures for Submarine Construction," DSTOFebruary 1994 1994.

[3] K. Hakansson, Doctoral thesis, Royal Institute of Technology (KTH), 2002.

[4] J. C. Ritter and B. F. Dixon, "Welding of Quenched and Tempered Steels for Submarine Construction," presented at the 34th National Conference of the Australian Welding Institute, Adelaide, November 1986, 1986.

[5] Z. Sterjovski, "Pad-weld repairs of in-service high-strength steel plate used in seawater environments," *Welding in the World,* Article vol. 54, no. 7-8, pp. R173-R181, 2010.

[6] I. Samardzic and T. Siewert, "Reliability Improvements in Repair Welding of High Strength Steels," *IIW Doc. IX-2002-01,* 2001.

[7] D. Miller, description of existing repair procedure ed. Adelaide: ASC pty ltd, 2017.

[8] S. Pearce, "Breakdown of residual stress in highly restrained thick section steel welds," PhD, School of Mechanical Engineering, The University of Adelaide, South Australia, 2009.

[9] J. R. Loureiro and A. A. Fernandes, *Toughness of CG HAZs of Welds in Q-and-T Steels*. American Welding Society, 1994.

[10] Z. Zhu, L. Kuzmikova, H. Li, and F. Barbaro, "Effect of inter-critically reheating temperature on microstructure and properties of simulated inter-critically reheated coarse grained heat affected zone in X70 steel," *Materials Science and Engineering: A,* vol. 605, no. Supplement C, pp. 8-13, 2014/05/27/ 2014.

[11] J. Hidalgo and M. J. Santofimia, "Effect of Prior Austenite Grain Size Refinement by Thermal Cycling on the Microstructural Features of As-Quenched Lath Martensite," *Metallurgical and Materials Transactions A,* journal article vol. 47, no. 11, pp. 5288-5301, November 01 2016.

[12] Y. Prawoto, N. Jasmawati, and K. Sumeru, "Effect of Prior Austenite Grain Size on the Morphology and Mechanical Properties of Martensite in Medium Carbon Steel," *Journal of Materials Science and Technology,* Article vol. 28, no. 5, pp. 461-466, 2012.

[13] G. Krauss, *Steels-Heat Treatment and Processing Principles*. Ohio: ASM international, 1990.

[14] P. P. Suikkanen, C. Cayron, A. J. DeArdo, and L. P. Karjalainen, "Crystallographic Analysis of Martensite in 0.2C-2.0Mn-1.5Si-0.6Cr Steel using EBSD," *Journal of Materials Science & Technology,* vol. 27, no. 10, pp. 920-930, 2011/10/01/ 2011.

[15] M. Dunder, T. Vuherer, and I. Samardžić, "Impact energy analysis of quenched and tempered fine grain structural steel specimens after weld thermal cycle simulation," *Metalurgija,* Note vol. 53, no. 4, pp. 637-640, 2014.

[16] Welding and Fabrication of Quenched and Tempered Steel, WTIA Technical Note No.15, 1999, W. T. i. o. Australia.

[17] H. K. D. H. Bhadeshia and R. W. K. Honeycombe, *Steels : Microstructure and Properties,* Third edition ed. Oxford, UK: Elsevier Ltd., 2006.

[18] H. K. Sung, S. Y. Shin, B. Hwang, C. G. Lee, N. J. Kim, and S. Lee, "Effects of carbon equivalent and cooling rate on tensile and Charpy impact properties of high-strength bainitic steels," *Materials Science and Engineering A,* Article vol. 530, no. 1, pp. 530-538, 2011.

[19] T. Kasuya, K. Ichikawa, and M. Fuji, "Derivation of carbon equivalent to assess hardenability of steel," *Science and Technology of Welding and Joining,* Article vol. 3, no. 6, pp. 317-320, 1998.

[20] V. B. Ginzburg and R. Ballas, *Flat rolling fundamentals*. New York: Marcel Dekker, 2000.

[21] Y. Ito and K. Bessyo, "Weldability formula of high strength steel related to heat affected zone cracking," *Sumitomo Search,* Article no. 1, pp. 59-70, 1969.

[22] S. Lee, B. C. Kim, and D. Kwon, "Fracture toughness analysis of heat-affected zones in high-strength low-alloy steel welds," *Metallurgical Transactions A,* Article vol. 24, no. 5, pp. 1133-1141, 1993.

[23] J. Hu, L.-X. Du, J.-J. Wang, H. Xie, C.-R. Gao, and R. D. K. Misra, "High toughness in the intercritically reheated coarse-grained (ICRCG) heat-affected zone (HAZ) of low carbon microalloyed steel," *Materials Science and Engineering: A,* vol. 590, pp. 323-328, 1/10/ 2014.

[24] A. Ramazani *et al.*, "Micro-macro-characterisation and modelling of mechanical properties of gas metal arc welded(GMAW)DP600 steel," *Materials Science and Engineering A,* vol. 589, pp. 1-14, 2014.

[25] P. R. Vishu, J. R. D. Kelly Ferjutz, Nikki D. Wheaton, Ed. *Solid-state transformations in weldments* (ASM handbook of welding, brazing and soldering). ASM International, 1993.

[26] S. Kumar, S. K. Nath, and V. Kumar, "Effect of single and multiple thermal cycles on microstructure and mechanical properties of simulated HAZ in low carbon bainitic steel," *Materials Performance and Characterization,* vol. 4, no. 3, pp. 365-380, 2015.

[27] J. I. Jang, J. B. Ju, B. W. Lee, D. Kwon, and W. S. Kim, "Effects of microstructural change on fracture characteristics in coarse-grained heat-affected zones of QLT-processed 9% Ni steel," *Materials Science and Engineering A,* vol. 340, no. 1-2, pp. 68-79, 2003.

[28] C. L. Davis and J. E. King, "Cleavage initiation in the intercritically reheated coarse-grained heat-affected zone: Part I. Fractographic evidence," *Metallurgical and Materials Transactions A,* vol. 25, no. 3, pp. 563-573, 1994.

[29] M. Hamada, "Control of strength and toughness at the heat affected zone," (in English), *Yosetsu Gakkai Shi/Journal of the Japan Welding Society,* Article vol. 71, no. 7, pp. 22-26, 10 / 01 / 2002.

[30] O. M. Akselsen, J. K. Solberg, and O. Grong, "Effects of martensite-austenite (M-A) islands on intercritical heat-affected zone toughness of low carbon microalloyed steels," (in English), *Scandinavian Journal of Metallurgy,* Article vol. 17, no. 5, pp. 194-200, 01 / 01 / 1988.

[31] X. J. Di, X. An, F. J. Cheng, D. P. Wang, X. J. Guo, and Z. K. Xue, "Effect of martensite–austenite constituent on toughness of simulated inter-critically reheated coarse-grained heat-affected zone in X70 pipeline steel," *Science and Technology of Welding and Joining,* Article vol. 21, no. 5, pp. 366-373, 2016.

[32] L. Lan, C. Qiu, D. Zhao, X. Gao, and L. Du, "Microstructural characteristics and toughness of the simulated coarse grained heat affected zone of high strength low carbon bainitic steel," *Materials Science and Engineering A*, Article vol. 529, no. 1, pp. 192-200, 2011.
[33] Q. Deng, W. Zhao, W. Jiang, T. Zhang, T. Li, and Y. Zhao, "Hydrogen Embrittlement Susceptibility and Safety Control of Reheated CGHAZ in X80 Welded Pipeline," *Journal of Materials Engineering and Performance*, Article vol. 27, no. 4, pp. 1654-1663, 2018.
[34] H. K. D. H. Bhadeshia, "About calculating the characteristics of the martensite–austenite constituent," presented at the Proc. Int. seminar on Welding of high strength pipeline steels, Araxa, Brazil, 2013.
[35] W. C. Leslie, *The Physical Metallurgy of Steels*. McGraw-Hill, 1981.
[36] G. Krauss, *Steels : processing, structure and performence*. Ohio: ASM International, 2005.
[37] P. Lehto, H. Remes, T. Saukkonen, H. Hänninen, and J. Romanoff, "Influence of grain size distribution on the Hall-Petch relationship of welded structural steel," *Materials Science and Engineering A*, Article vol. 592, pp. 28-39, 2014.
[38] C. Wang, M. Wang, J. Shi, W. Hui, and H. Dong, "Effect of microstructure refinement on the strength and toughness of low alloy martensitic steel," *Journal of Materials Science and Technology*, Article vol. 23, no. 5, pp. 659-664, 2007.
[39] S. C. Kennett, G. Krauss, and K. O. Findley, "Prior austenite grain size and tempering effects on the dislocation density of low-C Nb–Ti microalloyed lath martensite," *Scripta Materialia*, vol. 107, pp. 123-126, 2015/10/01/ 2015.
[40] B. K. Agrawal, *Introduction to Engineering Materials*. New Delhi: Tata McGraw-Hill Publishing Company Limited, 1988.
[41] B. Ralph, "Grain growth," *Materials Science and Technology (United Kingdom)*, Article vol. 6, no. 11, pp. 1136-1144, 1990.
[42] T. Falkenreck, A. Kromm, and T. Böllinghaus, "Investigation of physically simulated weld HAZ and CCT diagram of HSLA armour steel," *Welding in the World*, Article vol. 62, no. 1, pp. 47-54, 2018.
[43] M. Shome, O. P. Gupta, and O. N. Mohanty, "Effect of simulated thermal cycles on the microstructure of the heat-affected zone in HSLA-80 and HSLA-100 steel plates," *Metallurgical and Materials Transactions A: Physical Metallurgy and Materials Science*, Article vol. 35, no. 13, pp. 985-996, 2004.
[44] B. Loberg, A. Nordgren, J. Strid, and K. E. Easterling, "Role of alloy composition on the stability of nitrides in Ti-microalloyed steel during weld thermal cycles," *Metallurgical transactions. A, Physical metallurgy and materials science*, Article vol. 15 A, no. 1, pp. 33-41, 1984.
[45] M. F. Ashby and K. E. Easterling, "A first report on diagrams for grain growth in welds," *Acta Metallurgica*, Article vol. 30, no. 11, pp. 1969-1978, 1982.
[46] W. G. Welland, *Welding international*, p. 55, March 1989.
[47] W. Pang, N. Ahmed, and D. Dunne, "Hardness and microstructural gradients in the heat affected zone of welded low-carbon quenched and tempered steels," *Australasian Welding Journal*, vol. 50, no. 2, pp. 36-48, 2011.

[48] M. Shome, "Effect of heat-input on austenite grain size in the heat-affected zone of HSLA-100 steel," *Materials Science and Engineering A*, Article vol. 445-446, pp. 454-460, 2007.
[49] L. Zhang, "Microstructure-property relationship in microalloyed high-strength steel welds," PhD, Fakultaet fuer Maschinenbau, Magdeburg Univ. (Germany), Berlin, 2017.
[50] N. Yurioka and H. Suzuki, "Hydrogen assisted cracking in C—Mn and low alloy steel weldments," *International Materials Reviews*, Article vol. 35, no. 1, pp. 217-249, 1990.
[51] L. Kuzmikova, H. Li, J. Norrish, Z. S. Pan, and N. Larkin, "Development of safe optimized welding procedures for high strength Q&T steel welded with austenitic consumables," *Revista Soldagem e Inspecao*, vol. 18, no. 2, pp. 169-175, 2013.
[52] X. Li *et al.*, "Elemental distribution in the martensite–austenite constituent in intercritically reheated coarse-grained heat-affected zone of a high-strength pipeline steel," *Scripta Materialia*, vol. 139, pp. 67-70, 2017/10/01/ 2017.
[53] E. Bayraktar and D. Kaplan, "Mechanical and metallurgical investigation of martensite-austenite constituents in simulated welding conditions," *Journal of Materials Processing Technology*, Article vol. 153-154, no. 1-3, pp. 87-92, 2004.
[54] H. Ikawa, H. Oshige, and T. Tanoue, "Effect of Martensite-Austenite constetuent on HAZ toughness of a high strength steel," *Transactions of the Japan Welding Society*, vol. 11, no. 2, pp. 87-96, 1980.
[55] AS 1554.4, Structural steel welding, Part 4: Welding of high strength quenched and tempered steel, 2014, S. A. International.
[56] AS/NZS 1554.1, Structural steel welding, Part 1: Welding of steel structures, 2014, S. A. International.
[57] AS/NZS 3992, Pressure equipment - Welding and brazing qualification, 2015, S. A. International.
[58] AS 3597, Structural and pressure vessel steel - Quenched and tempered plate, 2008, S. A. International.
[59] AS/NZS 2885.2, Pipelines-Gas and liquid petroleum, Welding, 2016, S. A. International.
[60] MIL-STD-1689A (SH), Fabrication, welding and inspection of ships structure, 1990,
[61] Offshore standard, Submarine pipeline systems, 2013, D. N. Veritas.
[62] (2019, 1st of August). *FAQ - How many times can a weld be re-welded?* Available: https://www.twi-global.com/technical-knowledge/faqs/faq-how-many-times-can-a-weld-be-re-welded
[63] O. E. Vega, J. M. Hallen, A. Villagomez, and A. Contreras, "Effect of multiple repairs in girth welds of pipelines on the mechanical properties," *Materials Characterization*, vol. Volume 59, no. Issue 10, pp. 1498–1507, October 2008 2008.
[64] P. Dong, "On repair weld residual stresses and significance to structural integrity," *Welding in the World*, Article vol. 62, no. 2, pp. 351-362, 2018.
[65] S. Song and P. Dong, "Residual stresses at weld repairs and effects of repair geometry," *Science and Technology of Welding and Joining*, Article vol. 22, no. 4, pp. 265-277, 2017.
[66] P. Dong, J. K. Hong, J. Zhang, P. Rogers, J. Bynum, and S. Shah, "Effects of repair weld residual stresses on wide-panel specimens loaded in tension,"

Journal of Pressure Vessel Technology, Transactions of the ASME, Article vol. 120, no. 2, pp. 122-128, 1998.

[67] P. J. Bouchard *et al.*, "Measurement of the residual stresses in a stainless steel pipe girth weld containing long and short repairs," *International Journal of Pressure Vessels and Piping,* Article vol. 82, no. 4, pp. 299-310, 2005.

[68] M. Zeinoddini, S. Arnavaz, A. P. Zandi, and Y. A. Vaghasloo, "Repair welding influence on offshore pipelines residual stress fields: An experimental study," *Journal of Constructional Steel Research,* Article vol. 86, pp. 31-41, 2013.

[69] O. M. Akselsen, O. Grong, and J. K. Solberg, "Structure-property relationships in intercritical heat affected zone of low-carbon microalloyed steels," (in English), *Materials Science and Technology,* Article vol. 3, no. 8, pp. 649-655, 1987.

[70] C. L. Davis and J. E. King, "Effect of cooling rate on intercritically reheated microstructure and toughness in high strength low alloy steel," *Materials Science & Technology,* vol. 9, no. 1, pp. 8-15, 1993.

[71] V. Gliha, T. Vuherer, B. Ule, and J. Vojvodič-Tuma, "Fracture resistance of simulated heat affected zone areas in HSLA structural steel," (in English), *Science and Technology of Welding and Joining,* Article vol. 9, no. 5, pp. 399-406, 10 / 01 / 2004.

[72] L. Lan, C. Qiu, D. Zhao, X. Gao, and L. Du, "Analysis of microstructural variation and mechanical behaviors in submerged arc welded joint of high strength low carbon bainitic steel," *Materials Science and Engineering A,* vol. 558, pp. 592-601, 2012.

[73] L. Lan, C. Qiu, D. Zhao, C. Li, X. Gao, and L. Du, "Microstructural characters and toughness of different sub-regions in the welding heat affected zone of low carbon bainitic steel," (in English), *Jinshu Xuebao/Acta Metallurgica Sinica,* Article vol. 47, no. 8, pp. 1046-1054, 08 / 01 / 2011.

[74] A. Loureiro, "HAZ toughness of multipass welded joints: Influence of brittle zones," *Advanced Materials Forum I,* vol. 230-2, pp. 31-35, 2002.

[75] S. Moeinifar, *Microstructure and toughness properties of subcritically, intercritically and supercritically heat affected zones in x80 pipeline steel* (Advanced Materials Research). 2011, pp. 1850-1854.

[76] S. Moeinifar, A. H. Kokabi, and H. R. Madaah Hosseini, "Influence of peak temperature during simulation and real thermal cycles on microstructure and fracture properties of the reheated zones," *Materials and Design,* Article vol. 31, no. 6, pp. 2948-2955, 2010.

[77] P. Mohseni, J. K. Solberg, M. Karlsen, O. M. Akselsen, and E. Østby, "Investigation of mechanism of cleavage fracture initiation in intercritically coarse grained heat affected zone of HSLA steel," *Materials Science and Technology (United Kingdom),* Article vol. 28, no. 11, pp. 1261-1268, 2012.

[78] H. Qiu, H. Mori, M. Enoki, and T. Kishi, "Fracture mechanism and toughness of the welding heat-affected zone in structural steel under static and dynamic loading," *Metallurgical and Materials Transactions A: Physical Metallurgy and Materials Science,* Article vol. 31, no. 11, pp. 2785-2791, 2000.

[79] Y. You, C. Shang, N. Wenjin, and S. Subramanian, "Investigation on the microstructure and toughness of coarse grained heat affected zone in X-100 multi-phase pipeline steel with high Nb content," *Materials Science and Engineering A,* Article vol. 558, pp. 692-701, 2012.

[80] I. Kim, H. Nam, M. Lee, D. Nam, Y. Park, and N. Kang, "Effect of Martensite–Austenite Constituent on Low-Temperature Toughness in YS 500 MPa Grade Steel Welds," *Metals*, vol. 8, no. 8, p. 638, 2018.

[81] A. Lambert, J. Drillet, A. F. Gourgues, T. Sturel, and A. Pineau, "Microstructure of martensite-austenite constituents in heat affected zones of high strength low alloy steel welds in relation to toughness properties," *Science and Technology of Welding and Joining*, Article vol. 5, no. 3, pp. 168-173, 2000.

[82] D. A. Curry and J. F. Knott, "Effect of microstructure on cleavage fracture toughness of quenched and tempered steels," *Met Sci*, vol. Volume 13, no. Issue 6, pp. Pages 341-345, 1979.

[83] C. J. McMahon Jr and M. Cohen, "Initiation of cleavage in polycrystalline iron," *Acta Metallurgica*, Article vol. 13, no. 6, pp. 591-604, 1965.

[84] S. Imamura, H. Muramoto, Y. Murata, Y. Shimada, Y. Kayamori, and T. Tagawa, "Crystallographic orientation analysis of cleavage facets adjacent to a fracture trigger in low carbon steel," *International Journal of Fracture*, Article vol. 192, no. 2, pp. 253-257, 2015.

[85] G. E. Dieter, *Mechanical Metallurgy*, 3 ed. New York: Mc Graw-Hill Book Co, 1988.

[86] K. A. Macdonald, *Fracture and fatigue of welded joints and structures*. Cambridge: Woodhead publishing limited, 2011.

[87] J. H. Chen, Y. Kikuta, T. Araki, M. Yoneda, and Y. Matsuda, "Micro-fracture behaviour induced by M-A constituent (Island Martensite) in simulated welding heat affected zone of HT80 high strength low alloyed steel," *Acta Metallurgica*, vol. 32, no. 10, pp. 1779-1788, 1984/10/01 1984.

[88] X. Li, Y. Fan, X. Ma, S. V. Subramanian, and C. Shang, "Influence of Martensite-Austenite constituents formed at different intercritical temperatures on toughness," *Materials and Design*, Article vol. 67, pp. 457-463, 2015.

[89] X. Li, C. Shang, X. Ma, and S. V. Subramanian, "Study on the toughness of X100 pipeline steel heat affected zone," in *Energy Materials 2014, Conference Proceedings*, 2014, pp. 597-604.

[90] Y. P. Zeng, P. Y. Zhu, and K. Tong, "Effect of microstructure on the low temperature toughness of high strength pipeline steels," *International Journal of Minerals, Metallurgy and Materials*, Article vol. 22, no. 3, pp. 254-261, 2015.

[91] E. Duch and J. N. Dupont, "Effect of multiple weld thermal cycles on hsla-100 steel," *Welding Journal*, Article vol. 98, no. 3, pp. 88-S-98-S, 2019.

[92] X. Li, X. Ma, S. V. Subramanian, C. Shang, and R. D. K. Misra, "Influence of prior austenite grain size on martensite-austenite constituent and toughness in the heat affected zone of 700MPa high strength linepipe steel," *Materials Science and Engineering A*, Article vol. 616, pp. 141-147, 2014.

[93] B. Białobrzeska, Ł. Konat, and R. Jasiński, "The influence of austenite grain size on the mechanical properties of low-alloy steel with boron," *Metals*, Article vol. 7, no. 1, 2017, Art. no. 26.

[94] S. Takebayashi, K. Ushioda, N. Yoshinaga, and S. Ogata, "Effect of carbide size distribution on the impact toughness of tempered martensitic steels with two different prior austenite grain sizes evaluated by instrumented charpy test," *Materials Transactions*, Article vol. 54, no. 7, pp. 1110-1119, 2013.

[95] Y. Li and T. N. Baker, "Effect of morphology of martensite–austenite phase on fracture of weld heat affected zone in vanadium and niobium microalloyed steels," *Materials Science and Technology,* vol. 26, no. 9, pp. 1029-1040, 2010/09/01 2010.

[96] T. Jia, Y. Zhou, X. Jia, and Z. Wang, "Effects of Microstructure on CVN Impact Toughness in Thermomechanically Processed High Strength Microalloyed Steel," *Metallurgical and Materials Transactions A: Physical Metallurgy and Materials Science,* Article vol. 48, no. 2, pp. 685-696, 2017.

[97] L. Lan, C. Qiu, D. Zhao, X. Gao, and L. Du, "Analysis of martensite-austenite constituent and its effect on toughness in submerged arc welded joint of low carbon bainitic steel," (in English), *Journal of Materials Science,* Article vol. 47, no. 11, pp. 4732-4742, 06 / 01 / 2012.

[98] W. W. Xu, Q. F. Wang, T. Pan, H. Su, and C. F. Yang, "Effect of Welding Heat Input on Simulated HAZ Microstructure and Toughness of a V-N Microalloyed Steel," *Journal of Iron and Steel Research International,* Article vol. 14, no. 5 SUPPL. 1, pp. 234-239, 2007.

[99] Z. S. Li, S. L. Li, X. D. Zhu, and H. Q. Xu, "Effects of weld thermal cycle modes on microstructure and properties of coarse-grained heat-affected zone of Q690 steel processed by TMCP," (in English), *Cailiao Rechuli Xuebao/Transactions of Materials and Heat Treatment,* vol. 35, no. 2, pp. 121-125, 2014.

[100] H. F. Lan, L. X. Du, and R. D. K. Misra, "Effect of microstructural constituents on strength-toughness combination in a low carbon bainitic steel," *Materials Science and Engineering A,* Article vol. 611, pp. 194-200, 2014.

[101] C. L. Davis and J. E. King, "Cleavage initiation in the intercritically reheated coarse-grained heat affected zone: Part II. Failure criteria and statistical effects," *Metallurgical and Materials Transactions A: Physical Metallurgy and Materials Science,* Article vol. 27 A, no. 10, pp. 3019-3029, 1996.

[102] L. Lan, C. Qiu, H. Song, and D. Zhao, "Correlation of martensite-austenite constituent and cleavage crack initiation in welding heat affected zone of low carbon bainitic steel," (in English), *Materials Letters,* Article vol. 125, pp. 86-88, 06 / 15 / 2014.

[103] M. Mandal, W. J. Poole, T. Garcin, M. Militzer, and L. Collins, "Mechanical behaviour of intercritically reheated coarse-grained heat affected zone in high strength line pipe steels," in *Proceedings of the Biennial International Pipeline Conference, IPC*, 2018, vol. 3.

[104] A. Lambert-Perlade, A. F. Gourgues, J. Besson, T. Sturel, and A. Pineau, "Mechanisms and modeling of cleavage fracture in simulated heat-affected zone microstructures of a high-strength low alloy steel," *Metallurgical and Materials Transactions A: Physical Metallurgy and Materials Science,* Article vol. 35, no. 13, pp. 1039-1053, 2004.

[105] F. Matsuda *et al.,* "Review of mechanical and metallurgical investigations of martensite-austenite constituent in welded joints in Japan," *Welding in the World, Le Soudage Dans Le Monde,* Article vol. 37, no. 3, pp. 134-154, 1996.

[106] B. Hwang, S. Lee, Y. M. Kim, N. J. Kim, and J. Y. Yoo, "Correlation of rolling condition, microstructure, and low-temperature toughness of X70 pipeline steels," *Metallurgical and Materials Transactions A: Physical Metallurgy and Materials Science,* Conference Paper vol. 36, no. 7, pp. 1793-1805, 2005.

[107] Y. M. Kim, S. K. Kim, Y. J. Lim, and N. J. Kim, "Effect of microstructure on the yield ratio and low temperature toughness of linepipe steels," *ISIJ International,* Article vol. 42, no. 12 SPEC., pp. 1571-1577, 2002.
[108] W. Wang, W. Yan, L. Zhu, P. Hu, Y. Shan, and K. Yang, "Relation among rolling parameters, microstructures and mechanical properties in an acicular ferrite pipeline steel," *Materials and Design,* Article vol. 30, no. 9, pp. 3436-3443, 2009.
[109] B. Hwang, Y. G. Kim, S. Lee, Y. M. Kim, N. J. Kim, and J. Y. Yoo, "Effective grain size and Charpy impact properties of high-toughness X70 pipeline steels," *Metallurgical and Materials Transactions A: Physical Metallurgy and Materials Science,* Article vol. 36, no. 8, pp. 2107-2114, 2005.
[110] M. Díaz-Fuentes, A. Iza-Mendia, and I. Gutiérrez, "Analysis of different acicular ferrite microstructures in low-carbon steels by electron backscattered diffraction. Study of their toughness behavior," *Metallurgical and Materials Transactions A: Physical Metallurgy and Materials Science,* Article vol. 34 A, no. 11, pp. 2505-2516, 2003.
[111] B. B. Wu *et al.*, "Crystallography analysis of toughness in high strength ultra-heavy plate steel," *Materials Letters,* Article vol. 250, pp. 55-59, 2019.
[112] S. Morito, X. Huang, T. Furuhara, T. Maki, and N. Hansen, "The morphology and crystallography of lath martensite in alloy steels," *Acta Materialia,* vol. 54, no. 19, pp. 5323-5331, 2006/11/01/ 2006.
[113] S. Morito, H. Tanaka, R. Konishi, T. Furuhara, and T. Maki, "The morphology and crystallography of lath martensite in Fe-C alloys," *Acta Materialia,* vol. 51, no. 6, pp. 1789-1799, 2003/04/02/ 2003.
[114] Y. Murata, "Formation mechanism of lath martensite in steels," *Materials Transactions,* Article vol. 59, no. 2, pp. 151-164, 2018.
[115] H. Kitahara, R. Ueji, N. Tsuji, and Y. Minamino, "Crystallographic features of lath martensite in low-carbon steel," *Acta Materialia,* Article vol. 54, no. 5, pp. 1279-1288, 2006.
[116] K. Verbeken, L. Barbé, and D. Raabe, "Evaluation of the crystallographic orientation relationships between FCC and BCC phases in TRIP steels," *ISIJ International,* Article vol. 49, no. 10, pp. 1601-1609, 2009.
[117] N. Takayama, G. Miyamoto, and T. Furuhara, "Effects of transformation temperature on variant pairing of bainitic ferrite in low carbon steel," *Acta Materialia,* Article vol. 60, no. 5, pp. 2387-2396, 2012.
[118] X. L. Wang, Z. Q. Wang, L. L. Dong, C. J. Shang, X. P. Ma, and S. V. Subramanian, "New insights into the mechanism of cooling rate on the impact toughness of coarse grained heat affected zone from the aspect of variant selection," *Materials Science and Engineering A,* Article vol. 704, pp. 448-458, 2017.
[119] Y. T. Pan and J. L. Lee, "Development of TiOx-bearing steels with superior heat-affected zone toughness," *Materials and Design,* Article vol. 15, no. 6, pp. 331-338, 1994.
[120] I. Andersen and Ø. Grong, "Analytical modelling of grain growth in metals and alloys in the presence of growing and dissolving precipitates-I. Normal grain growth," *Acta Metallurgica Et Materialia,* Article vol. 43, no. 7, pp. 2673-2688, 1995.

[121] A. D. Batte, P. J. Boothby, and A. B. Rothwell, "Understanding the weldability of niobium-bearing HSLA steels," *Niobium, Science and Technology,* Conference Paper pp. 931-958, 2001.
[122] A. G. Fox and D. G. Brothers, "The role of titanium in the non-metallic inclusions which nucleate acicular ferrite in the Submerged ARC Weld (Saw) fusion zones of Navy HY-100 steel," *Scripta Metallurgica et Materiala,* Article vol. 32, no. 7, pp. 1061-1066, 1995.
[123] M. Fattahi, N. Nabhani, M. Hosseini, N. Arabian, and E. Rahimi, "Effect of Ti-containing inclusions on the nucleation of acicular ferrite and mechanical properties of multipass weld metals," *Micron,* Article vol. 45, pp. 107-114, 2013.
[124] K. Nakashima, K. Hase, and T. Eto, "Development of shipbuilding steel plate with superior low temperature toughness for large heat input welding," *JFE Technical Report,* Article no. 20, pp. 8-13, 2015.
[125] H. W. Lee *et al.*, "Effect of boron contents on weldability in high strength steel," *Journal of Mechanical Science and Technology,* Article vol. 21, no. 5, pp. 772-778, 2007.
[126] Volume 6: Welding, Brazing, and Soldering, ASM Handbook, 1993, A. International.
[127] Y. Ueda, H. Murakawa, and N. Ma, "Chapter 1 - Introduction to Welding Mechanics," in *Welding Deformation and Residual Stress Prevention*, Y. Ueda, H. Murakawa, and N. Ma, Eds. Boston: Butterworth-Heinemann, 2012, pp. 1-34.
[128] B. L. Josefson, "Prediction of residual stresses and distortions in welded structures," *Journal of Offshore Mechanics and Arctic Engineering,* Article vol. 115, no. 1, pp. 52-57, 1993.
[129] G. S. Schajer, *Practical Residual Stress Measurement Methods*. West Sussex, PO19 8SQ, United Kingdom: John Wiley & Sons Ltd, 2013.
[130] N. Hoye, "Characterisation of Ti-6Al-4V deposits produced by arc-wire based additive manufacture," PhD, Department of mechanical, materials and machatronics engineering, University of Wollongong, 2015.
[131] P. Colegrove *et al.*, "Welding process impact on residual stress and distortion," *Science and Technology of Welding and Joining,* Article vol. 14, no. 8, pp. 717-725, 2009.
[132] H. Alipooramirabad, R. Ghomashchi, A. Paradowska, and M. Reid, "Residual stress- microstructure- mechanical property interrelationships in multipass HSLA steel welds," *Journal of Materials Processing Technology,* Article vol. 231, pp. 456-467, 2016.
[133] E. Van Puymbroeck, G. Van Staen, N. Iqbal, and H. De Backer, "Residual weld stresses in stiffener-to-deck plate weld of an orthotropic steel deck," *Journal of Constructional Steel Research,* Article vol. 159, pp. 534-547, 2019.
[134] D. W. Rathod *et al.*, "Residual stresses in arc and electron-beam welds in 130 mm thick SA508 steel: Part 1 - Manufacture," *International Journal of Pressure Vessels and Piping,* Article vol. 172, pp. 313-328, 2019.
[135] P. J. Withers, "Residual stress and its role in failure," *Reports on Progress in Physics,* Article vol. 70, no. 12, pp. 2211-2264, 2007.
[136] P. Dong, J. Zhang, and P. J. Bouchard, "Effects of repair weld length on residual stress distribution," *Journal of Pressure Vessel Technology, Transactions of the ASME,* Article vol. 124, no. 1, pp. 74-80, 2002.

[137] D. George, D. J. Smith, and P. Bouchard, *Evaluation of Through Wall Residual Stresses in Stainless Steel Weld Repairs*. 1999.
[138] I. Robertson, "Electron microscope study of the microstructure of BIS812EMA submarine steel," DSTO Materials Research Laboratory1991.
[139] L. Chen, "Characterisation of transverse cold cracking in weld metal of a high strength quenched and tempered steel," Doctor of Philosophy, Department of materials engineering, University of Wollongong, Australia, 2000.
[140] Weld joint hardness test, Methods for destructive testing of welds in metal 2003, Standards Australia International.
[141] Metallic materials - Vickers hardness test, Method 1: Test method (ISO 6507-1:1997, MOD), 2003, S. A. International.
[142] Part 2: Charpy V-notch, Method for impact tests on metals, 2003, S. A. International.
[143] N. Lane, "A study of the toughness and weldability of HSLA-65 for naval surface ships," PhD thesis, 2015.
[144] Instrumented test method, Metallic materials-Charpy V-notch pendulum impact test, 2015, The International Organization for Standardization.
[145] Standard test method for dynamic tear testing of metalic materials, 2008, Amarican Society of Testing and Materials.
[146] M. E. Fitzpatrick and A. Lodini, *Analysis of residual stress by diffraction using Neutron and Synchrotrone radiation*. London: Taylor & Francis, 2003.
[147] T. Maki, "Morphology and substructure of martensite in steels," in *Phase Transformations in Steels*, vol. 2, 2012, pp. 34-58.
[148] R. A. M. Napitupulu, "Influence of heating rate and temperature on austenite grain size during reheating steel," in *IOP Conference Series: Materials Science and Engineering*, 2017, vol. 237.
[149] T. Hanamura, S. Torizuka, S. Tamura, S. Enokida, and H. Takechi, "Effect of Austenite Grain Size on Transformation Behavior, Microstructure and Mechanical Properties of 0.1C–5Mn Martensitic Steel," *ISIJ International,* vol. 53, no. 12, pp. 2218-2225, 2013.
[150] T. Karthikeyan, M. K. Dash, S. Saroja, and M. Vijayalakshmi, "Estimation of martensite feature size in a low-carbon alloy steel by microtexture analysis of boundaries," *Micron,* vol. 68, pp. 77-90, 2015/01/01/ 2015.
[151] P. Lehto, J. Romanoff, H. Remes, and T. Sarikka, "Characterisation of local grain size variation of welded structural steel," *Welding in the World,* journal article vol. 60, no. 4, pp. 673-688, July 01 2016.
[152] E. O. Hall, "Variation of Hardness of Metals with Grain Size," *Nature,* vol. 173, no. 4411, pp. 948-949, 1954/05/01 1954.
[153] R. W. Armstrong, "The influence of polycrystal grain size on several mechanical properties of materials," *Metallurgical and Materials Transactions B,* journal article vol. 1, no. 5, pp. 1169-1176, May 01 1970.
[154] M. Furukawa, Z. Horita, M. Nemoto, R. Z. Valiev, and T. G. Langdon, "Microhardness measurements and the hall-petch relationship in an Al-Mg alloy with submicrometer grain size," *Acta Materialia,* Article vol. 44, no. 11, pp. 4619-4629, 1996.
[155] N. Hansen, "Hall-petch relation and boundary strengthening," *Scripta Materialia,* Article vol. 51, no. 8 SPEC. ISS., pp. 801-806, 2004.
[156] T. Furuhara *et al.*, "Phase Transformation from Fine-grained Austenite," *ISIJ International,* vol. 48, no. 8, pp. 1038-1045, 2008.

[157] Y. Tomita and K. Okabayashi, "Effect of microstructure on strength and toughness of heat-treated low alloy structural steels," *Metallurgical Transactions A*, Article vol. 17, no. 7, pp. 1203-1209, 1986.
[158] S. Moeinifar, A. H. Kokabi, and H. R. M. Hosseini, "Effect of tandem submerged arc welding process and parameters of Gleeble simulator thermal cycles on properties of the intercritically reheated heat affected zone," *Materials & design*, vol. 32, no. 2, pp. 869-876, 2011.
[159] Y. Li *et al.*, "Investigation of local brittle zone in multipass welded joint of NiCrMoV steel with heavy section," *Journal of Materials Research*, Article vol. 33, no. 8, pp. 923-934, 2018.
[160] S. G. Lee, S. S. Sohn, B. Kim, W. G. Kim, K. K. Um, and S. Lee, "Effects of martensite-austenite constituent on crack initiation and propagation in inter-critical heat-affected zone of high-strength low-alloy (HSLA) steel," *Materials Science and Engineering A*, Article vol. 715, pp. 332-339, 2018.
[161] Z. J. Luo, J. C. Shen, H. Su, Y. H. Ding, C. F. Yang, and X. Zhu, "Effect of substructure on toughness of lath martensite/bainite mixed structure in low-carbon steels," *Journal of Iron and Steel Research International*, Article vol. 17, no. 11, pp. 40-48, 2010.
[162] C. Wen, X. Deng, Y. Tian, Z. Wang, and R. D. K. Misra, "Microstructural Evolution and Toughness of the Various HAZs in 1300-MPa-Grade Ultrahigh-Strength Structural Steel," *Journal of Materials Engineering and Performance*, Article vol. 28, no. 3, pp. 1301-1311, 2019.
[163] R. Ayer, R. R. Mueller, and T. Neeraj, "Electron backscattered diffraction study of cleavage fracture in pure iron," *Materials Science and Engineering: A*, vol. 417, no. 1, pp. 243-248, 2006/02/15/ 2006.
[164] J. Pešička, R. Kužel, A. Dronhofer, and G. Eggeler, "The evolution of dislocation density during heat treatment and creep of tempered martensite ferritic steels," *Acta Materialia*, vol. 51, no. 16, pp. 4847-4862, 2003/09/15/ 2003.

APPENDIX A: DILATOMETER MEASUREMENTS

Dilatometer data

Typical dilatometer curves for BIS812 EMA upon heating with different heating rates starting from 5°C/s to 200°C/s.

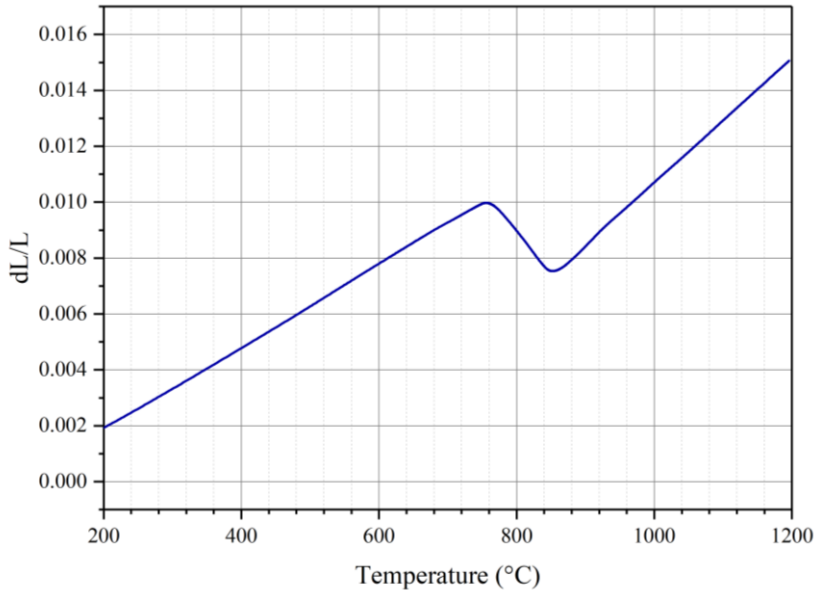

Figure A-1: Heating rate - 5°C/s

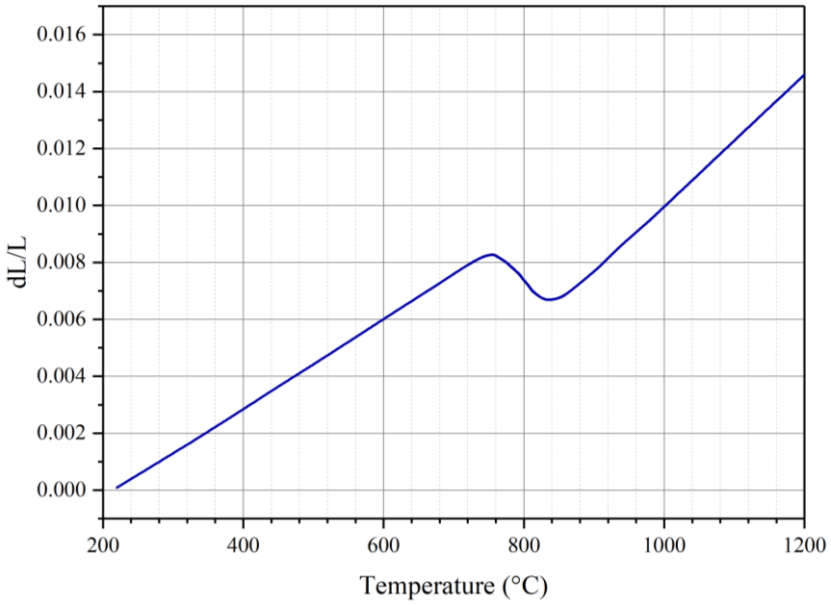

Figure A-2: Heating rate - 50°C/s

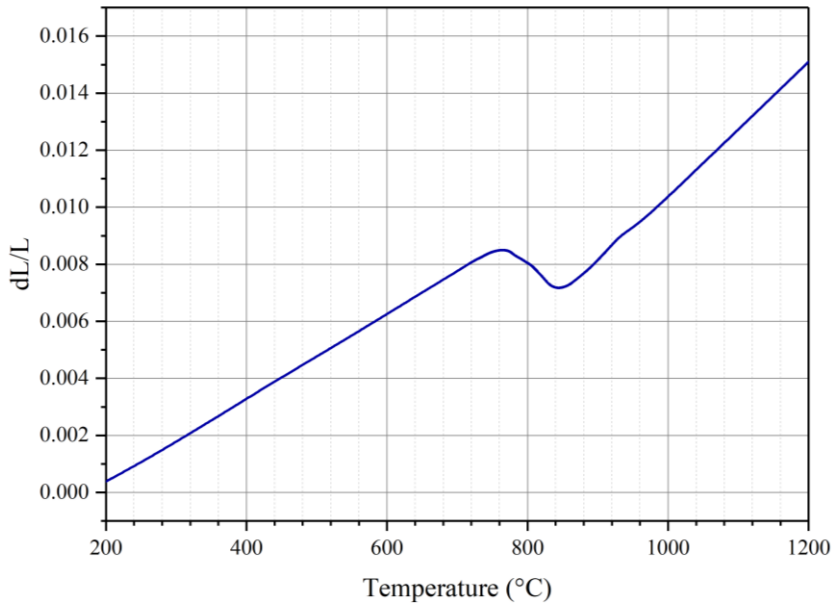

Figure A-3: Heating rate - 100°C/s

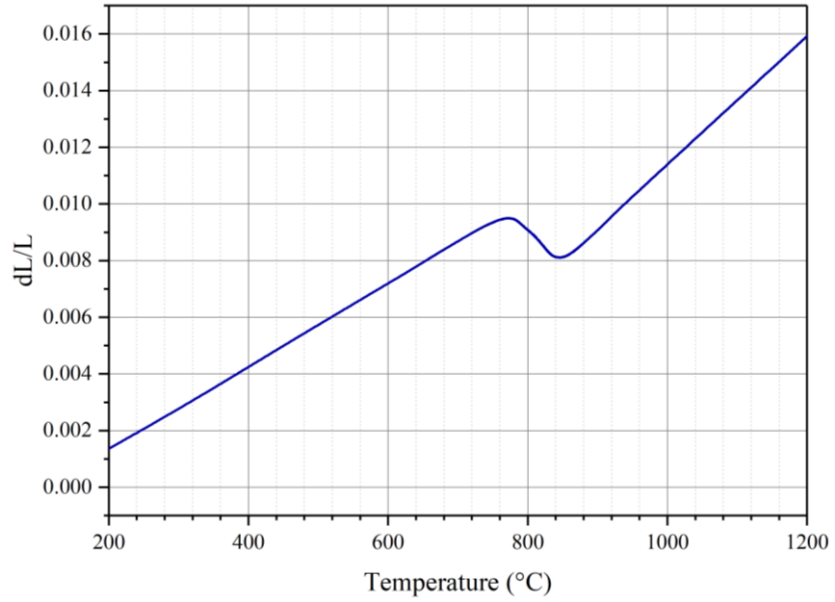

Figure A-4: Heating rate - 150°C/s

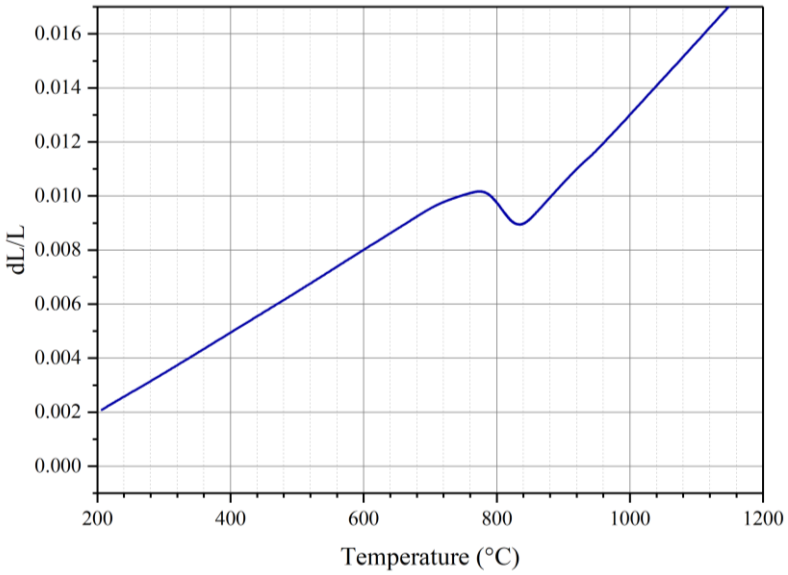

Figure A-5: Heating rate - 200°C/s

APPENDIX B: REAL WELD THERMAL CYCLES

Weld parameters of BoP welds

BoP welds were carried out with imbedded thermocouples to measure thermal histories of real welds. Welds were atarted from weld run 1 and progressed to run 8. Then last three weld beads were ground back to the base pate and rewelded starting from run 9 to 14. The last two weld beads were ground and rewelded. Below figure shows the weld run sequence and thermo couple locations. The table shows the weld parameters for each weld run.

Weld consumable : Atomarc E120.18.M2

Diameter : 3.2 mm

Preheat temperature : 150°C

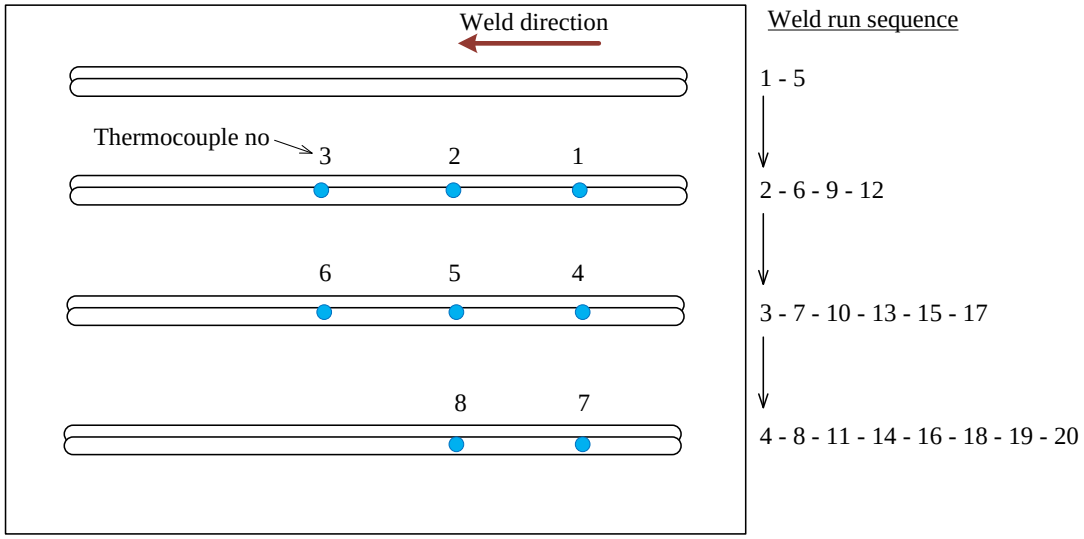

Figure B-1: BoP weld test plate with imbedded thermocouples

Thermocouple 1, 4 and 7 - 2.5 mm away from tne weld surface

Thermocouple 2, 5 and 8 - 4 mm away from the weld surface

Thermocouple 3 and 6 - 5 mm awat from the weld surface

Above distances (2.5, 4 and 5 mm) were from the top of the weld plate. Therefore, when weld was conducted, the real distance from the fution line to the thermocouple was diferent. Cross section of the samples through thermocouple locations were used for accurate distance measurement.

Note : Thermocouple 3 was malfuntioned and data was not recorded

Table B-1: Welding parameters of BoP welds shown in figure B-1.

Run Number	Current (A)	Voltage (V)	Weld length (mm)	Time/s
1	135	24	152	56
2	135	24	160	57
3	135	24	160	60
4	136	24	159	57
5	135	24	160	60
6	135	24	160	60
7	134	24	157	56
8	136	24	158	60
9	137	24	161	58
10	135	24	161	60
11	135	24	160	60
12	136	24	158	57
13	135	24	158	58
14	134	24	162	60
15	134	24	157	58
16	134	24	158	58
17	136	24	160	59
18	135	24	159	60
19	135	24	162	60
20	134	24	156	57

Real weld thermal histories of BOP welds

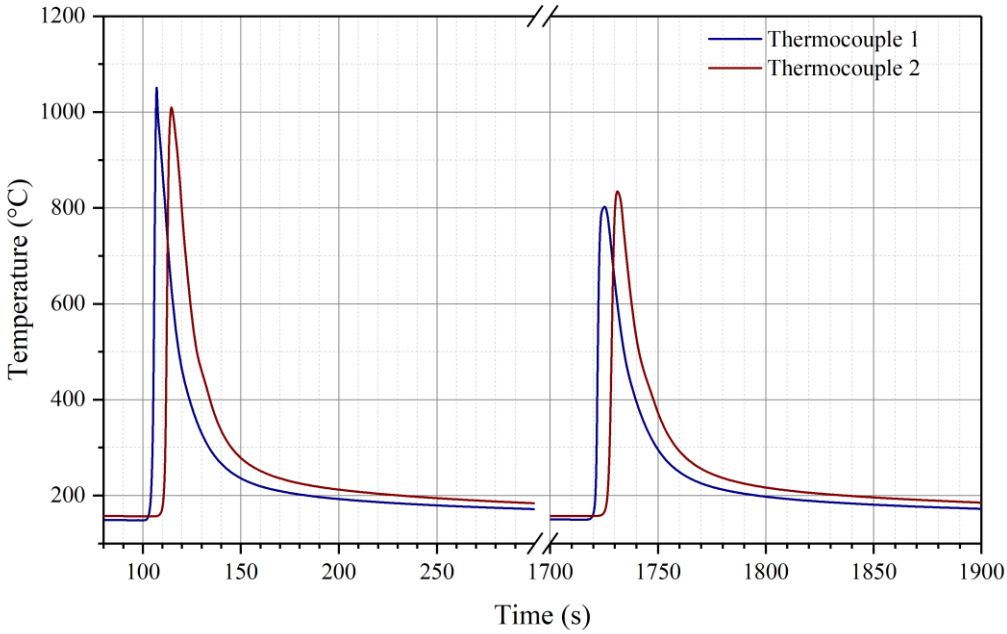

Figure B-2: Thermal cycles of BoP weld runs 2 and 6 obtained from thermocouples 1 and 2

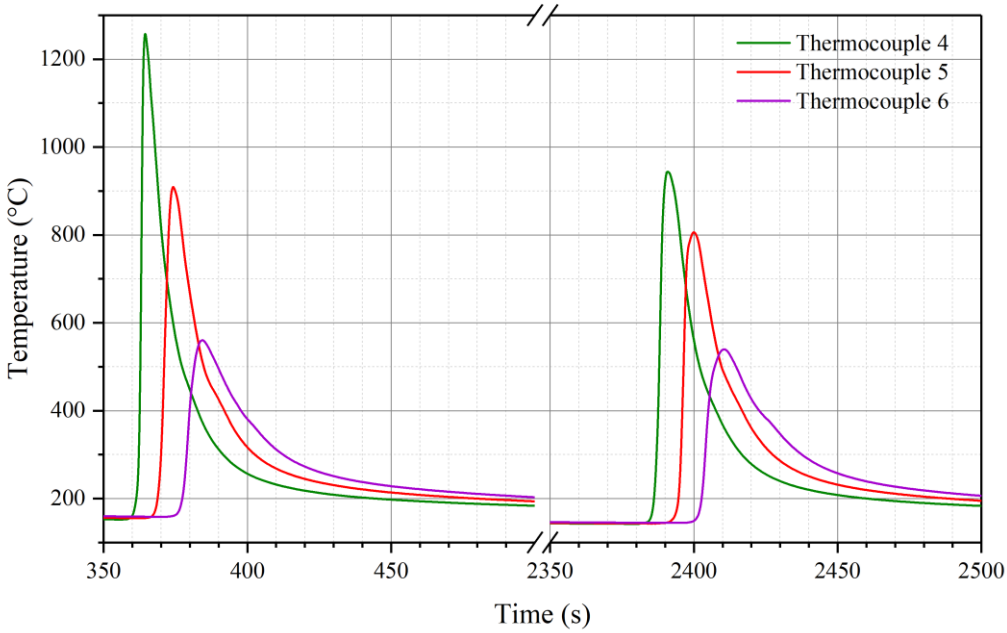

Figure B-3: Thermal cycles of BoP weld runs 3 and 7 obtained from thermocouples 4, 5 and 6

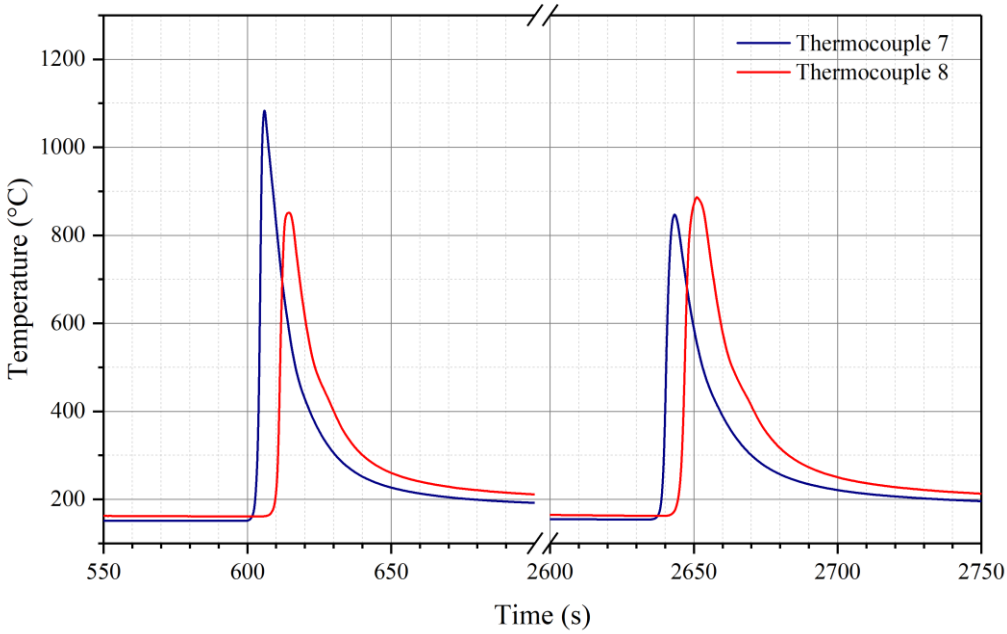

Figure B-4: Thermal cycles of BoP weld runs 4 and 8 obtained from thermocouples 7 and 8

APPENDIX C: SIMULATED THERMAL CYCLES

Simulated weld thermal histories

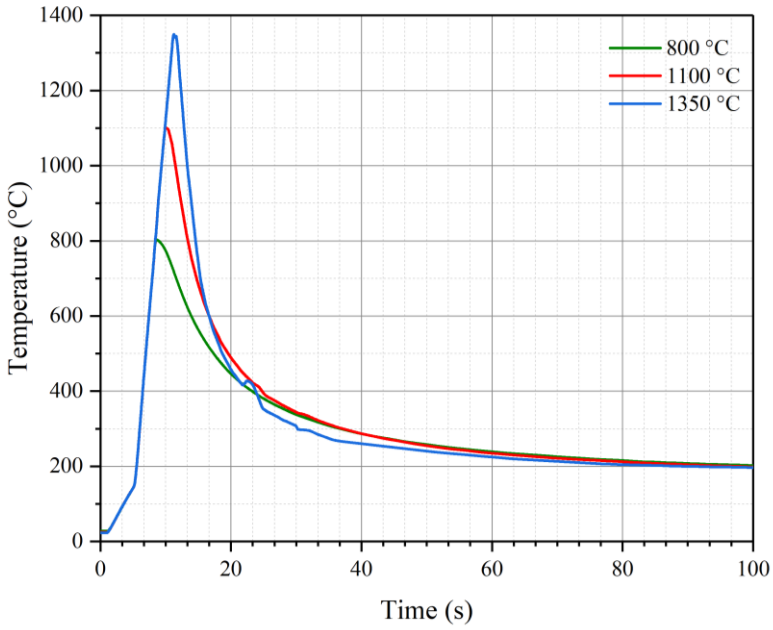

Figure C-1: Single thermal cycles with maximum temperature 1350°C (CG), 1100°C (FG) and 800°C (mid IC). All samples cooled down to 160º at around 150 s.

Double thermal cycles

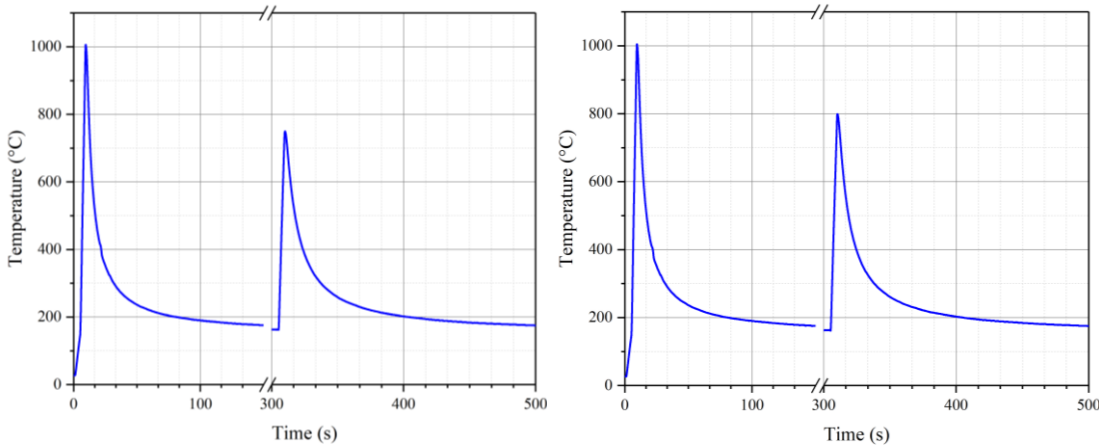

1000-750°C

1000-800°C

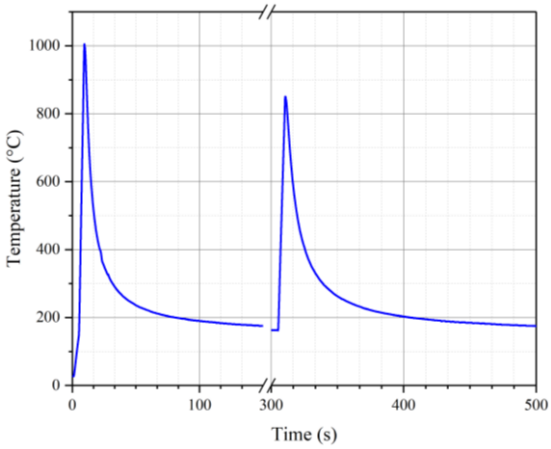

1000-850°C

Figure C-2: Double thermal cycles of FG-IC. First thermal cycle was at 1000°C and three diferent IC thermal cycles at 750°C, 800°C and 850°C.

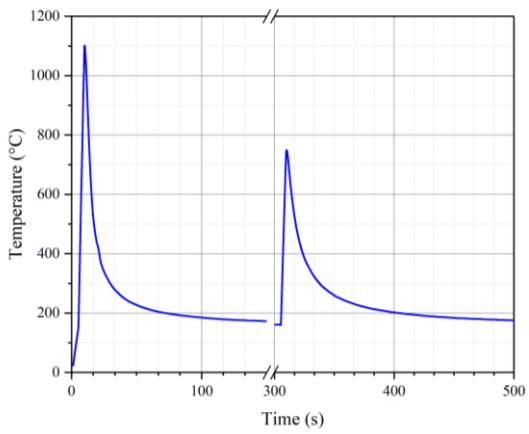

1100-750°C

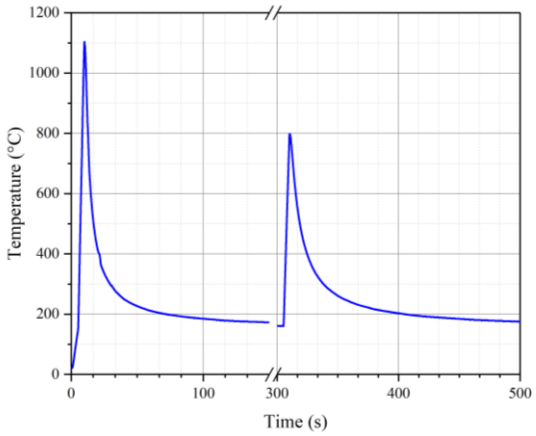

1100-800°C

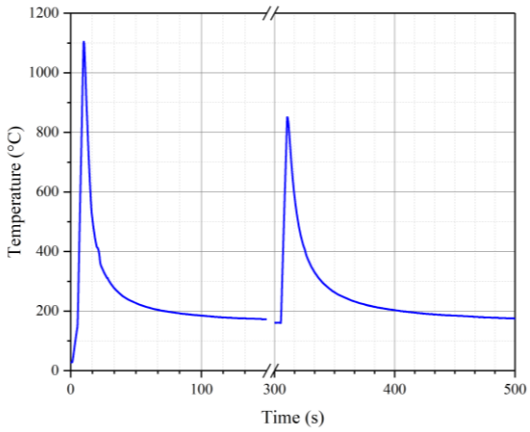

1100-850°C

Figure C-3: Double thermal cycles of FG-IC. First thermal cycle was at 1100°C and three diferent IC thermal cycles at 750°C, 800°C and 850°C.

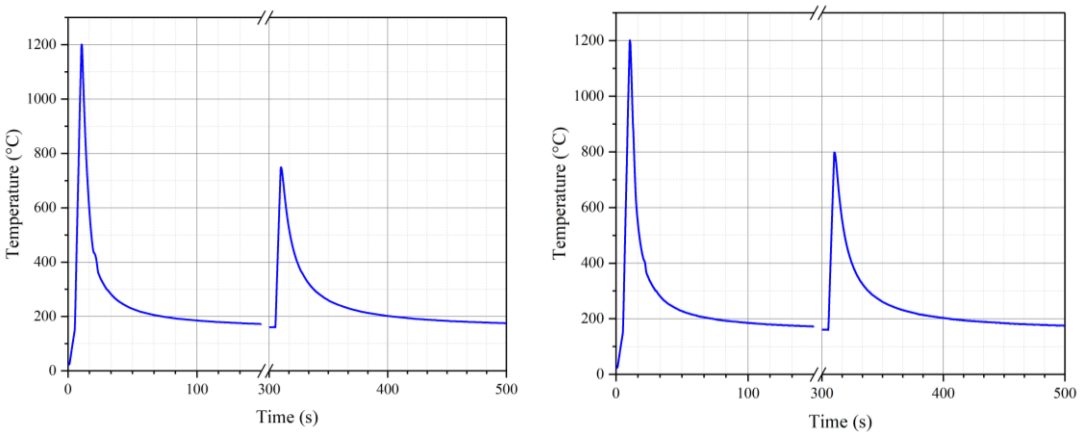

1200-750°C

1200-800°C

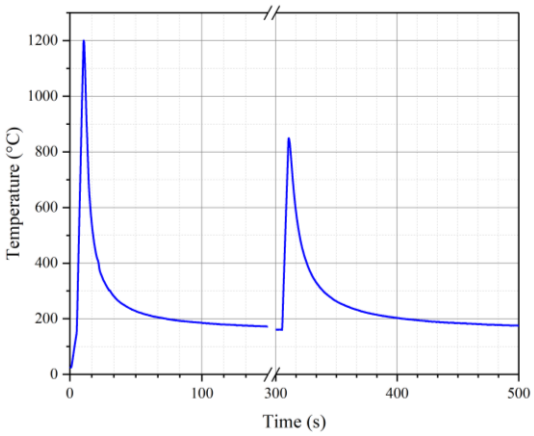

1200-850°C

Figure C-4: Double thermal cycles of CG-IC. First thermal cycle was at 1200°C and three diferent IC thermal cycles at 750°C, 800°C and 850°C.

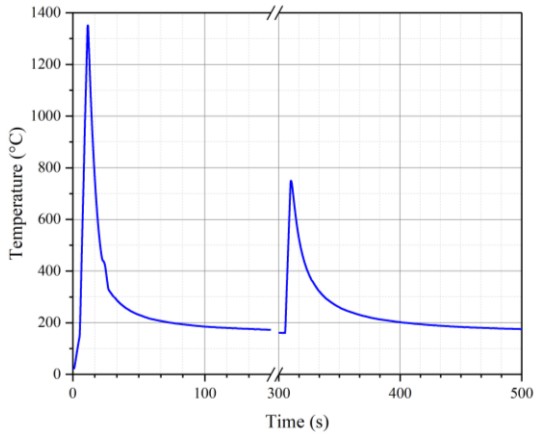

1350-750°C

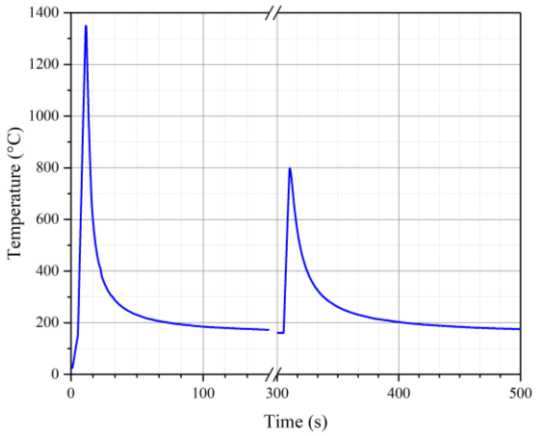

1350-800°C

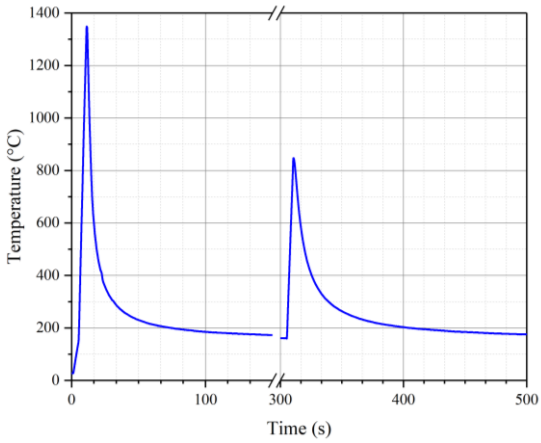

1350-850°C

Figure C-5: Double thermal cycles of CG-IC. First thermal cycle was at 1350°C and three diferent IC thermal cycles at 750°C, 800°C and 850°C.

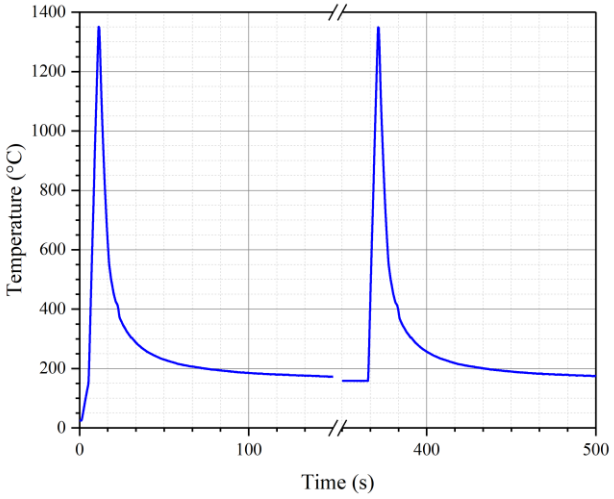

1350-1350°C (CG×2)

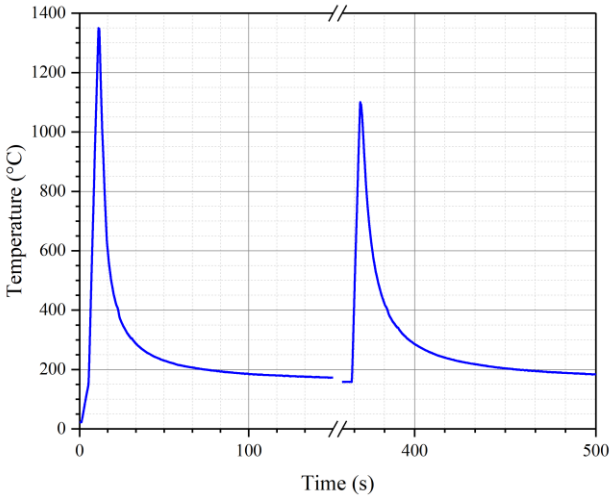

1350-1100°C (CGFG)

Figure C-6: Double thermal cycles of CG-CG and CG-FG. First thermal cycle was at 1350°C and two diferent second thermal cycles at 1350°C and 1100°C.

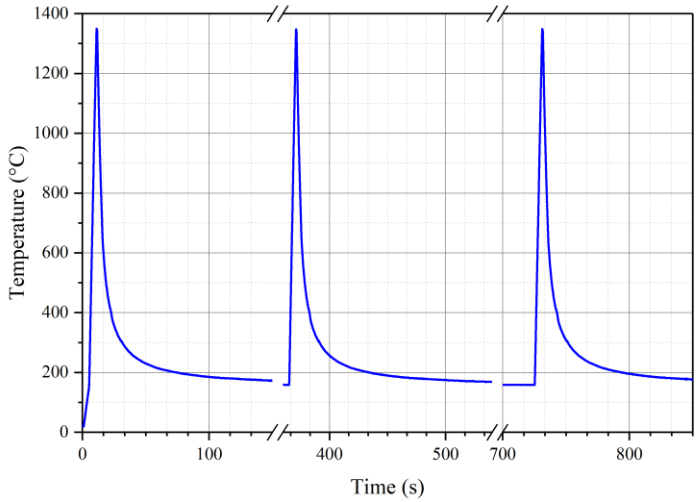

1350-1350-1350°C (CG×3)

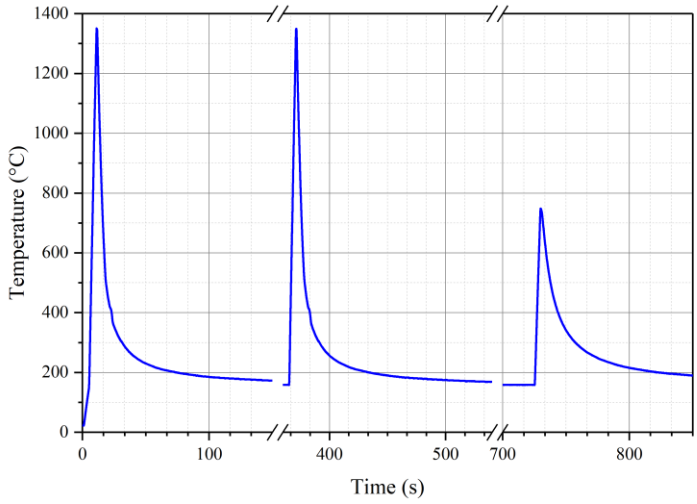

1350-1350-750°C (CG×2-IC)

Figure C-7: Three thermal cycles of CG-CG-CG and CG-CG-IC.

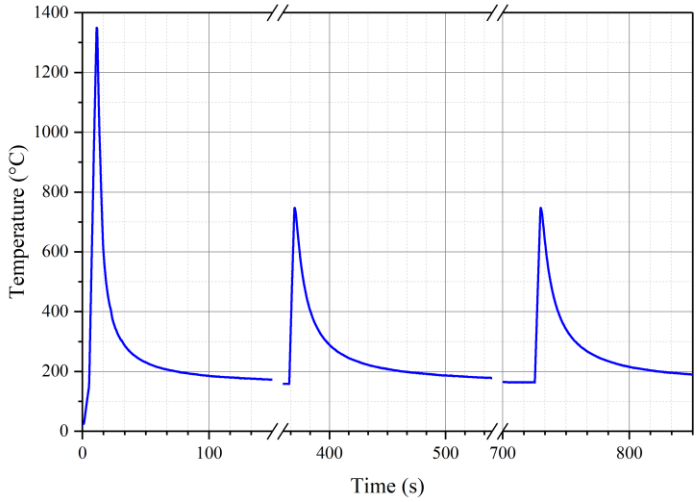

1350-750-750°C (CG-IC×2)

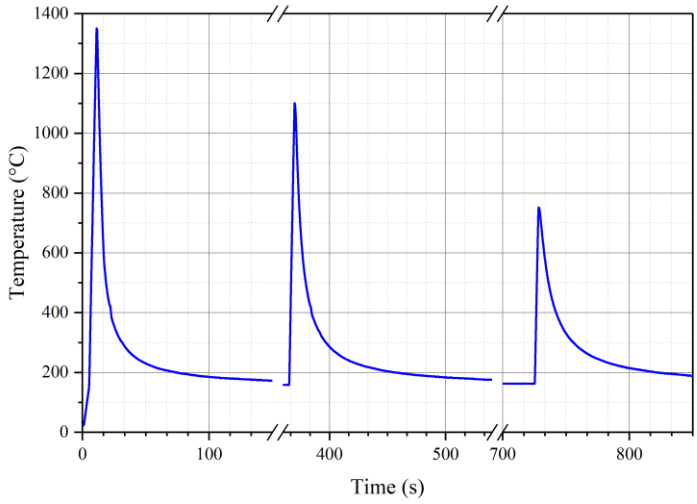

1350-1100-750°C (CGFGIC)

Figure C-8: Three thermal cycles of CG-IC-IC and CG-FG-IC.

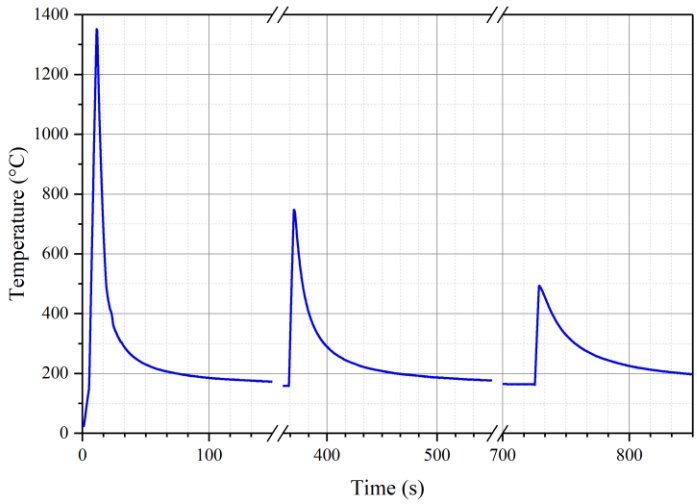

1350-750-500°C (CGICTM50)

Figure C-9: Three thermal cycles with tempering cycle at the end (CG-IC-TM)

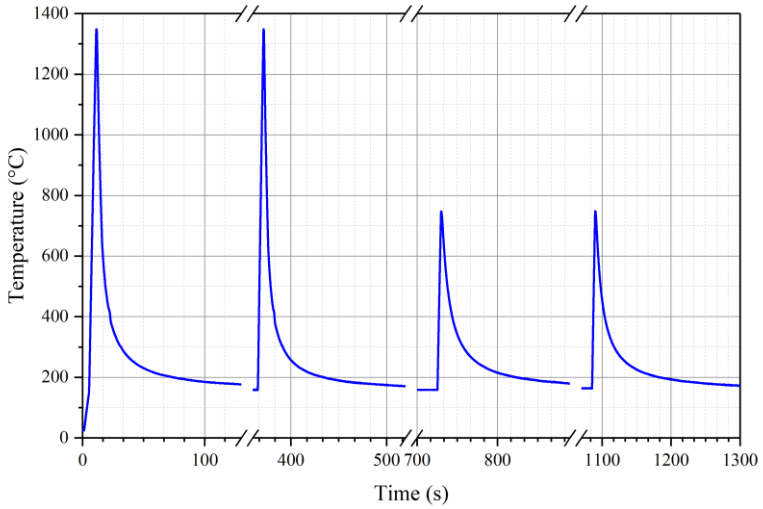

1350-1350-750-750°C (CG×2-IC×2)

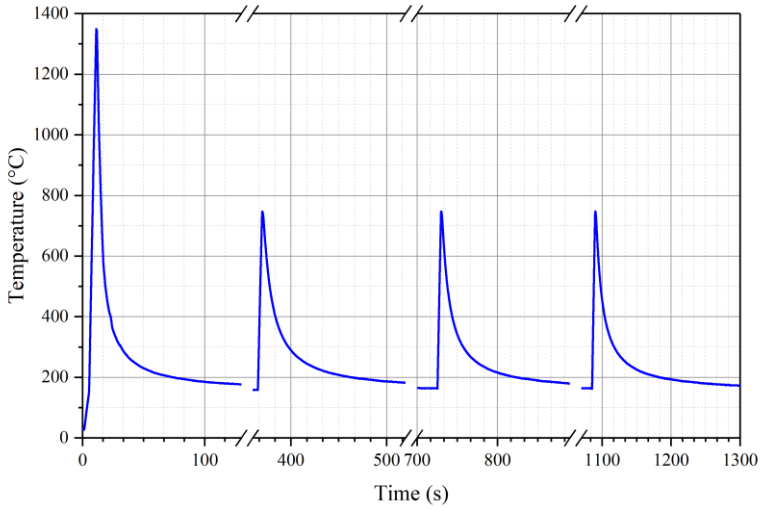

1350-750-750-750°C (CG-IC×3)

Figure C-10: Four thermal cycles with combination of CG and IC thermal cycles.

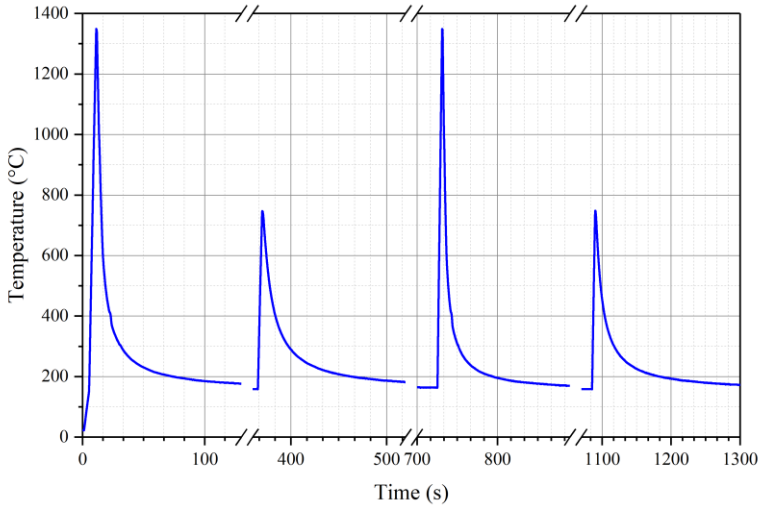

1350-750-1350-750°C ((CGIC)×2)

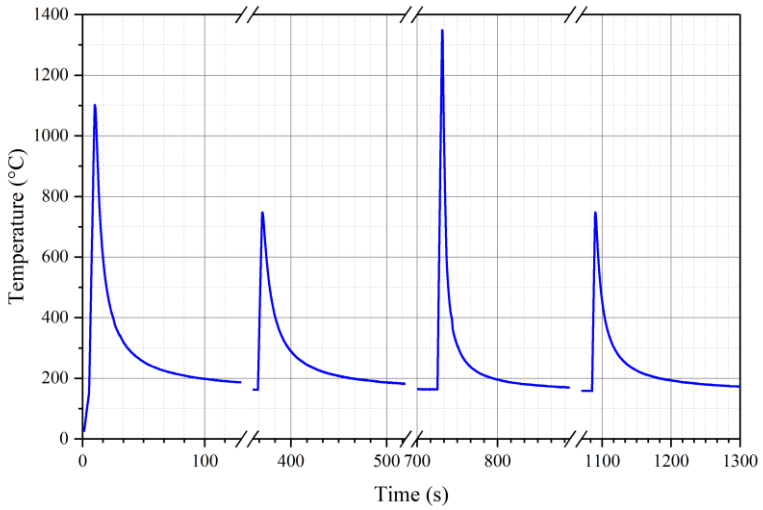

1100-750-1350-750°C (FGICCGIC)

Figure C-11: Four thermal cycles with combination of CG and IC thermal cycles.

APPENDIX D: FRACTURE SURFACES

Fracture surface of Charpy impact test samples with simulated thermal cycles

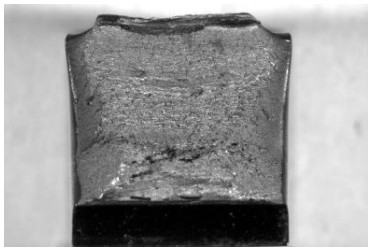

HAZ1000

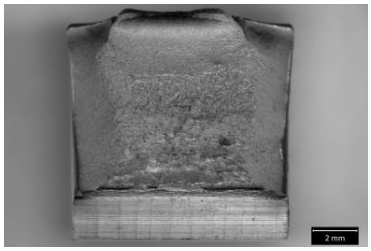

HAZ1200

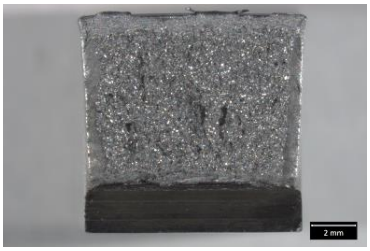

HAZ1350

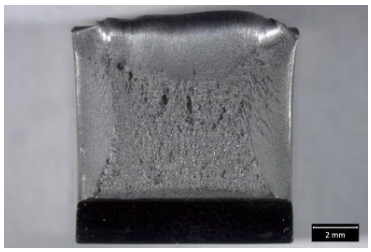

1000-750°C

1000-800°C

1000-850°C

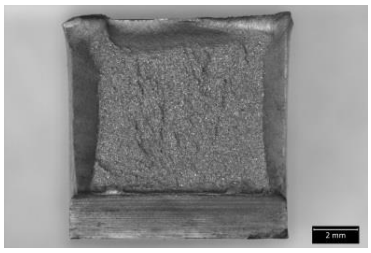

1200-750°C

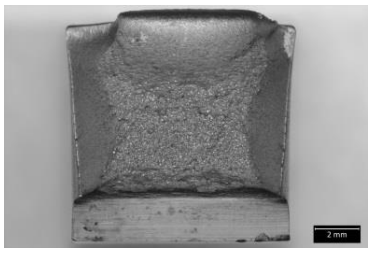

1200-800°C

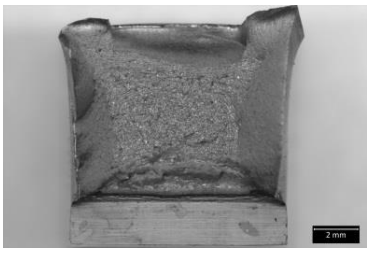

1200-850°C

1350-750°C

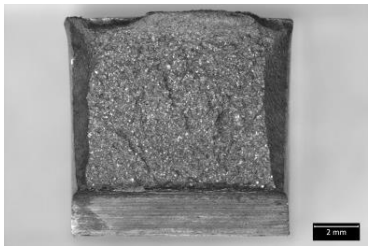

1350-800°C

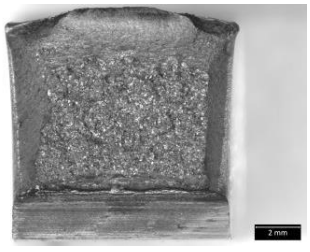

1350-850°C

Base metal

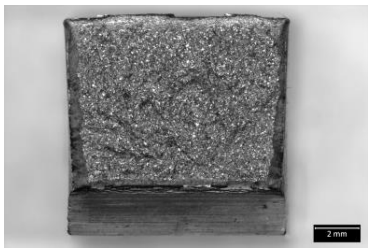

1350°C×2

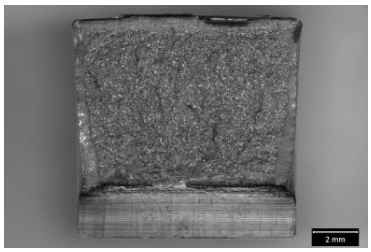

1350°C×3

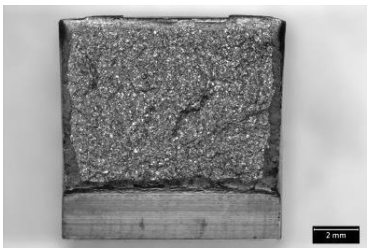

1350°C×4

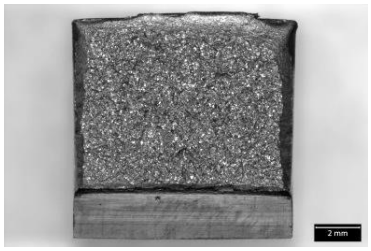

(1350×3)-750°C

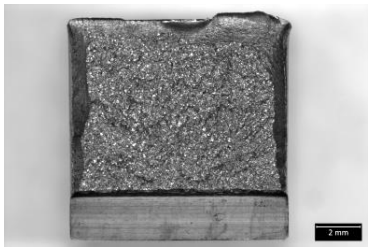

(1350×2)-750°C

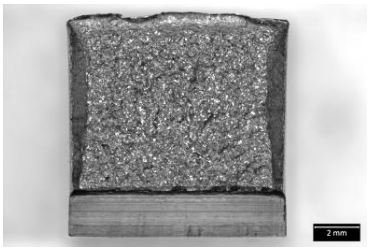

(1350-750°C)×2

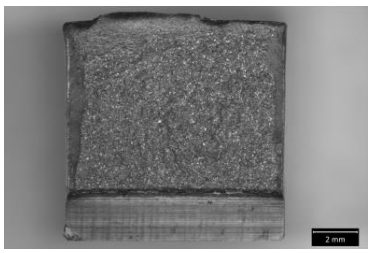

1350-(750°C×2)

Charpy test samples of real welds with first repair weld and forth repair weld.

Repair 1 - WM

Repair 1 - WM

Repair 1 - WM

Repair 1 - FL

Repair 1 - FL

Repair 1 - FL

Repair 1 – FL+3 mm

Repair 1 – FL+3 mm

Repair 1 – FL+3 mm

Repair 4 - WM

Repair 4 - WM

Repair 4 - WM

Repair 4 - FL

Repair 4 - FL

Repair 4 - FL

Repair 4 – FL+3 mm

Repair 4 – FL+3 mm

Repair 4 – FL+3 mm